UCONN LIBRARY

University of Connecticut
OpenCommons@UConn

Doctoral Dissertations

University of Connecticut Graduate School

9-14-2015

Experimental & Computational Approaches Towards Improving Mesoscale Understanding of Particle Interactions in Pharmaceutical Systems

Saurabh Sarkar
saurabh.sarkar@uconn.edu

Follow this and additional works at: https://opencommons.uconn.edu/dissertations

Recommended Citation
Sarkar, Saurabh, "Experimental & Computational Approaches Towards Improving Mesoscale Understanding of Particle Interactions in Pharmaceutical Systems" (2015). *Doctoral Dissertations*. 928.
https://opencommons.uconn.edu/dissertations/928

Experimental & Computational Approaches Towards Improving Mesoscale Understanding of Particle Interactions in Pharmaceutical Systems

Saurabh Sarkar, Ph.D.
University of Connecticut, 2015

ABSTRACT

Despite solid oral and inhaled dosage forms making a significant proportion of marketed pharmaceutical products, a better understanding of particulate processes will enable more science-based product optimization and scale up. A combination of experimental and computational approaches can be used to improve our current understanding of particulate processes. The current dissertation aims at improving understanding of particulate systems by investigating applications in several multiphase multicomponent flow regimes, each capturing a fundamental force, by systematic experiments and computational modeling.

Computational Fluid Dynamics (CFD) modeling of aerosol flow through pressurized metered dose inhaler (pMDI) – spacer systems and correlation of fluid flow patterns with drug transport and deposition through the Recirculation Index (RCI), a dimensionless variable developed during the course of our studies, improved our understanding in the dilute flow regime. Increased discharge of co-flow air and the smaller spacer were associated with smaller spacer deposition.

In the dense flow regime, the effect of material (cohesion/adhesion) and process variables on formation ordered mixtures were investigated in low shear and high shear double cone (DCN) and a high shear mixer (HSM) using experiments and Discrete Element Method (DEM) based modeling. Segregation of ordered mixtures was studied upon flow from hoppers in both mass

and funnel flow regimes. Ordered mixtures formed quickly in the HSM, however the high velocity in the HSM also caused greater sticking of fines and abrasion of carrier fines compared to DCN. DEM studies demonstrated different flow fields for the blenders, which also responded differently to change in adhesive properties of the mixture components. Press-on forces holding the carrier and the fines decreased as a function of drug load but not differentiated between the blenders .No segregation of ordered mixtures was observed upon discharge from either hopper.

The impact of electrostatic forces was investigated during tribocharging of binary mixtures in a hopper-chute assembly. The work function difference, determined computationally from Molecular Dynamics (MD) simulations for chemically pure materials, between contacting materials was tested as a predictor for tribocharging of insulators. The work function difference model was found to be a good predictor for pure systems, but not for binary mixtures where the system net charge was additionally influenced by material hygroscopicity and segregation patterns.

Capillary forces impacting high shear wet granulation (HSWG) performance were investigated in a simple lactose-water system. This was done through experiments and a dynamic 3D DEM model capable of including dynamic process variables and incorporating material property changes upon liquid addition. The effects of liquid addition rate and impeller speed were well-correlated with experimental observations. The DEM model also predicted poor agglomeration for a cohesive material in contrast with a non-cohesive powder. The importance of incorporating modification of material properties of granular material with binder addition was also elucidated.

Experimental & Computational Approaches Towards Improving Mesoscale Understanding of Particle Interactions in Pharmaceutical Systems

Saurabh Sarkar

B.Pharm, University of Delhi, 2008

M.S., University of Kentucky, 2010

A Dissertation

Submitted in Partial Fulfillment of the

Requirements for the Degree of

Doctor of Philosophy

at the

University of Connecticut

2015

Copyright by

Saurabh Sarkar

2015

APPROVAL PAGE

Doctor of Philosophy Dissertation

Experimental & Computational Approaches Towards Improving Mesoscale Understanding of Particle Interactions in Pharmaceutical Systems

Presented by

Saurabh Sarkar, B.Pharm., M.S.

Major Advisor

_____

Bodhisattwa Chaudhuri, Ph.D.

Associate Advisor

_____

Michael J. Pikal, Ph.D.

Associate Advisor

_____

Robin H. Bogner, Ph.D.

Associate Advisor

_____

Bruno C. Hancock, Ph.D.

University of Connecticut
2015

DEDICATION

To all my grandparents, for their affection and blessings

ACKNOWLEDGEMENTS

The doctoral dissertation work presented in this thesis was made possible due to the contribution of many people, to all of whom I am indebted. My first vote of thanks goes to my major advisor, Dr. Bodhisattwa Chaudhuri, for providing me an opportunity to pursue the Ph.D. degree under his supervision. Throughout the course of this research work, he has been immensely helpful, supportive and has given me great encouragement to pursue my research interests. His advice, support, guidance and enthusiasm towards my dissertation have been invaluable. He has always encouraged me to perform and present, and boosted my self - confidence over the years. At a personal level, he has gone out of the way to support me on multiple occasions. It has been an honor to work with him and I would certainly cherish this experience and our close personal rapport for the rest of my life.

I am also grateful to my thesis committee members; Dr. Mike Pikal, Dr. Robin Bogner and Dr. Bruno Hancock who have encouraged, guided and helped me meet several challenges I have encountered through my course of the dissertation. I would especially like to acknowledge Dr. Hancock for giving me an opportunity to a summer internship with him at Pfizer Inc., and travelling to the UConn campus whenever needed .My discussions with them during graduate courses and one-on-meetings were one of the most satisfying experiences of my graduate life at University of Connecticut. I am also thankful to my collaborators, particularly Dr. Maziar Kakhi (USFDA) and Dr. Kyrre Thalberg (AstraZeneca Inc.), whose insightful comments, suggestions and careful assessment of project progress have helped me develop a better understanding of the subject matter and direct my perspective towards regulatory and industrially important aspects.

I am also indebted to all Pharmaceutics faculty members for running a very competitive curriculum at UConn, especially with regards to coursework and seminars which were critical to building a strong foundation of my research area. I have been lucky to receive prudent advice and support from them at several instances during my academic carrier.

The University of Connecticut AAPS student chapter is deeply acknowledged, along with its current and past members. The activities, particularly guest talks, have been intellectually very stimulating and provided an opportunity to meet and share the views of successful experts in our area. This chapter also helped me hone my leadership skills by discharging various responsibilities during my term in the executive committee.

I would also like to acknowledge the stellar role played by the associate staff at UConn towards my dissertation research. I must mention Mark Drobney and Joseph Csiki at UConn Dept. of Mechanical Technology for helping me fabricate several equipment through the course of the Ph.D. program. Ms. Laura Pinnati, Dr. Na Li and Dr. B.V. Mahesh are thanked at the Institute of Material Sciences for helping me to characterize samples.

I would like to convey my deepest gratitude to the administrative staff at UConn School of Pharmacy- Mark Armati, Laura Burnett, Leslie Lebel and Kathy Koji, Liz Anderson, Skip Copeland for helping me with day to day activities, and their continued support and cooperation.

Special thanks are due to my labmates – Shivangi and Ekneet for sharpening my skills on the DEM code; Raj, Apurva, Vipul and Bruna for being always there and helping me with some experiments. I am thankful to my department colleagues for their support and thoughtful discussions. At this point, I must thank dear friends outside of the Dept. who helped me with my multidisciplinary research interests, most notably Dr. Vinit Sharma and Dr. Subhas Ghosal who

went taught me computational chemistry and have been just like elder brothers in sprit; Dr. Deep Mukherjee, Mr. Abhishek Saha and Mr. Debrishi Bose for helping me with statistics. These friends have been nothing short of a family to me during my stay at UConn and have provided strong moral and emotional support. Finally, no thanks are enough for my childhood friends Ms Anupriya, Dr. Pushkar Tripathi and Dr. Sonali Gupta, who have always stood by my side as far as I can remember. I feel blessed to have friends like these.

Family plays a fundamental role in the success of any individual, and it is no different for me. Words cannot suffice in expressing my gratitude for my parents, Mr. Tapan Kumar Sarkar and Mrs. Kalpana Sarkar, who have dedicated their lives in an endeavor to ensure quality education for me. Even as I was outside of the household while they grew older, they have always supported and encouraged me to pursue my goals. I am sure my grandparents would be proud wherever they are, for this work could not have been completed without their blessings. I am also really grateful to my sister, Mrs. Mahua Sarkar Kundu and brother in law, Dr. Samrat Kundu for their unending care and affection. I want to express my deep love to my baby niece Tanisha, who always manages to put up a smile on my face.

Finally, the financial support of the sponsors of this dissertation – Department of Pharmaceutical Sciences & Graduate School at UConn, UCRF (University of Connecticut Research Foundation), CPPR (Center of Pharmaceutical Processing Research), PhRMA (Pharmaceutical Researchers and Manufacturers Association), NIPTE (National Institute for Pharmaceutical Training & Education), is gratefully acknowledged.

TABLE OF CONTENTS

ABSTRACT .....

Experimental & Computational Approaches Towards Improving Mesoscale Understanding of Particle Interactions in Pharmaceutical Systems i

APPROVAL PAGE iii

DEDICATION iv

ACKNOWLEDGEMENTS v

TABLE OF CONTENTS viii

Chapter 1 1

Introduction, Aims, and Organization of the Dissertation 1

1. Introduction 2
2. Objectives and Aims 4
3. Chapter Organization and Outline 7
4. References 10

Chapter 2 12

On the Role of Forces Governing Particulate Interactions in Pharmaceutical Systems: A Review 12

Abstract 13

1. Introduction 14

1.1 Motivation 14

1.2 Granular Flow regimes in Pharmaceutical Processes 15

1.3 Process Modeling Techniques 18

2. Particle-Fluid Forces 26

2.1 Origin 26

2.2 Factors affecting Drag 27

2.3 Measurement of Drag Force 29

2.4 Applications & Numerical Modeling 30

3. Van der Waals (VDW) Force 32

3.1 Origin 32

3.2 Factors influencing VDW forces 33

3.3 Estimating VDW forces: Material Characterization 34

3.4 Numerical Modeling in Pharmaceutical applications 37
4. Capillary Forces 38
4.1 Origin 38
4.2 Factors influencing Capillary forces 41
4.3 Measurement of Capillary Force 42
4.4 Applications & Numerical Modeling in Pharmaceutical Systems 42
5. Electrostatic Forces 44
5.1 Origin 44
5.2 Factors Influencing Electrostatic Force 47
5.3 Determination of Relevant Material properties 48
5.4 Applications and Numerical Modeling 50
6. Conclusions 51
7. References 53
List of Tables 74
List of Figures 79
Chapter 3 91
Investigation of Multiphase Multicomponent Aerosol Flow Dictating pMDI-spacer Interactions 91
Abstract 92
1. Introduction 93
2. Materials and Methods 95
2.1 Geometry 96
2.2 Simulation Set Up 97
3. Results & Discussion 101
3.1 Spray in Unconfined Surrounds 101
3.2 Case Studies involving Spacer & USP Throat Systems 101
4. Conclusions 105
5. Acknowledgments 106
6. References 106
List of Tables 108
List of Figures 110
Chapter 4 121
Investigation of Mixing & Segregation of Ordered Mixtures for DPI formulations 121

Abstract 122
1. Introduction 123
2. Materials & Methods 125
2.1 Materials 125
2.2 Experimental Procedure 125
2.3 Characterization of Quality Attributes 127
2.4 Statistical Analysis 129
3. Discrete Element Method (DEM) 129
4. Results & Discussion 131
4.1 Formation of Ordered mixtures 131
4.2 Segregation of Ordered mixtures from Hoppers 137
5. Conclusions 138
6. Acknowledgements 139
7. References 139
List of Tables 143
List of Figures 147
Chapter 5 166
Triboelectrification of Binary Mixtures 166
Abstract 167
1. Introduction 168
2. Experimental Method, Materials and Characterization Techniques 171
2.1 Experimental Method 171
2.2 Materials 172
2.3 Characterization of Materials 173
3. Multi-Scale Modeling 173
3.1 Atomistic Scale: Work Function Determination based on Semi-Emperical Quantum Mechanics 173
3.2 Particle Scale: Discrete Element Method 174
4. Results & Discussion 176
4.1 Electrostatic charging of Primary Spherical Particles 176
4.2 Charge Reduction with additives 178
4.3 Computational Results 182

5. Conclusions 184
6. Acknowledgements 186
7. References 186
List of Tables 189
List of Figures 192
Chapter 6 202
Optimization of High Shear Wet Granulation of a Simple System 202
Abstract 203
1. Introduction 204
2. Materials & Methods 206
2.1 Materials 206
2.2 Procedure 207
3. Discrete Element Method (DEM) 208
3.1 Liquid Bridge Model 208
3.2 Post Processing & Visualization 210
4. Results & Discussion 211
4.1 Effect of Impeller Speed 211
4.2 Effect of Liquid addition Rate 212
4.3 Effect of Material Properties 212
5. Conclusions 213
6. Acknowledgement 214
7. References 214
List of Tables 216
List of figures 217
Chapter 7 223
Summary and Future Directions 223
NOMENCLATURE 230
Appendix 234

Chapter 1

Introduction, Aims, and Organization of the Dissertation

1. Introduction

With over 75% of pharmaceutical products formulated as solid dosage forms, particulate processing forms the cornerstone of the pharmaceutical industry.[1,2] Current understanding of these processes at a fundamental level, and their consequent optimization and scale-up of, is widely recognized to be inadequate.[3,4] This leads to process inefficiency, batch rejection, product recalls and translates to high manufacturing costs. It is true that some of these processes have been practiced for more than half a century, but often as an art than as a purely scientific exercise. Given a rapidly changing pharmaceutical landscape largely driven by economic constraints wherein repurposing of existing products, expanding current process capacities and developing novel process paradigms (e.g., continuous manufacturing) are commercially viable strategies, the need for better understanding of fundamental particulate interactions cannot be overstated. It is with this view that the increasing focus on bettering process understanding can be appreciated, which is highlighted by Quality by Design[5] and Process Analytical Technology[6] initiatives by the regulatory bodies in alliance with industrial and the academic community. Fortunately, the 21st century allows us privileges of superior analytical and computational tools, when compared to resources available to our predecessors, and these must be utilized towards achieving our general objective of improving process and product understanding.

The processing of pharmaceutical solid dosage forms often involves powder flow, an area of physics which is generally regarded to be poorly understood.[7] Powders may behave as solids or fluids under different conditions; this simple observation alone forms a basis for conducting basic research into powder physics especially given its economic importance. However, the pharmaceutical sector relies on engineering powder flows to an end objective of delivering the right drug in the right amount safely, and repeatedly without compromising on product elegance.

Reliable control of powder flow is a rather difficult task, especially for an industry which is known to be conservative by nature and is under great economic pressure and regulatory oversight.

Considering the challenges facing pharmaceutical product development, the research in pharmaceutics is increasingly becoming multidisciplinary in nature with significant thrust on importing knowledge from other allied (food, chemical etc.) and sometimes, non-allied industries. Prime examples of importing tools is process modeling techniques at different length and time scales, which is accredited to advances in engineering, mathematics and physics*: atomistic/molecular (micro) scale*-Density Functional Theory (DFT), Molecular Dynamics (MD), *particle (meso) scale*: Discrete Element Method (DEM), *continuum (macro) scale* : Computational Fluid Dynamics (CFD),Engineering Design. As scientists working in the areas of formulation and process development, we are quite interested in the meso scale effects, which lies in between the macro and micro scales representing inter-particulate forces having a molecular origin which impact the bulk process and formulation behavior. A better meso-scale understanding would ideally lead to improving our understanding of interaction of material and process variables, consequently enabling development of efficient, robust and scalable processes.

Particulate flows are a subclass of multiphase multicomponent flows and are governed by particle interactions which in turn are mediated through the fundamental forces (particle-fluid, particle-particle (van der Waals (VDW), electrostatic, capillary)), which have long been well known. The contribution of each force is dependent upon the interparticle spacing.[8] Depending upon the particle volume fraction and hence the interparticle spacing, these flows can be classified as dense or dilute, in which the particle-particle or particle –fluid forces dominate, respectively. Even when the most important forces impacting a given process are known, the

dynamic interplay of material, process, geometric and environmental variables at different length and time scales which is not well mapped. Dynamic interaction of these variables can be mapped through systematic experiments, developing a hypothesis explaining the results and testing the hypothesis in first principle computational models. This procedure, done iteratively, can indeed improve our basic understanding, and this forms the guiding principle for the current thesis.

2. Objectives and Aims

The overall objective was to improve the fundamental understanding of meso-scale particle interactions in several flow regimes. This was accomplished through experimental and numerical simulations of several cases of 'poorly understood' pharmaceutical processes whose performance is governed by particulate interactions. Each case focused on capturing relevant forces numerically and verifying the resulting predictions against systematic experiments. The cases are chosen so as to study each fundamental particulate force (fluid, VDW, electrostatic, capillary) in a pharmaceutically relevant application.

Following cases were studied:

<u>Dilute Flow Regime (CFD Simulations)</u>

1) **Fluid forces: Investigation of Multiphase Multicomponent Aerosol Flow pressurized metered dose inhaler (pMDI)-spacer interactions**

Goal: To improve the mechanistic understanding of complex multiphase flow patterns, distribution and deposition of aerosols in the pMDI-spacer assembly by developing a CFD based predictive model.

Specific aims:

I. To develop a multiphase CFD model of spray from a suspension based pMDI and compare it against known experimental results in open air.

II. To apply the CFD model to predict aerosol flow and deposition behavior within a pMDI-spacer assembly in combination with a USP Mouth-Throat assembly and compare CFD model results against experimental results.

Dense Flow Regime (DEM Simulations)

2) Cohesive forces: Investigation of Mixing and segregation of Adhesive Mixtures for Dry Powder Inhalers (DPI) formulations

Goal: To improve the understanding of particle-particle and particle-wall interactions during mixing and handling operations with the goal of formulating robust and high performing ordered mixtures, and to develop quantitative approaches for optimizing the processes.

Specific Aims:

I. To determine the effects of particle size and other characteristics, vessel speed, fill level and loading configuration on mixing performance in a double cone and high shear mixer.

II. To determine the effects of particle size and other characteristics, hopper angle and orifice diameter on granular flow and segregation of ordered mixtures

III. To develop experimental and computational methods suitable for performing quantitative examination of flow, mixing and segregation in geometries of interest.

3) **Electrostatic forces: Triboelectrification of binary powder mixtures**

Goal: To enhance the understanding of tribocharging of binary mixtures experimentally and numerically.

Specific Aims:

I. To study tribocharging of binary mixture in a hopper-chute assembly

II. To model by DEM the tribocharging of binary mixtures in a hopper –chute assembly

4) Capillary forces: Optimization of High Shear Wet Granulation (HSWG)

Goal: To develop experimental and computational methods suitable for performing a quantitative examination of granular flow, agglomeration patterns and rates in a granulation vessel.

Specific Aims:

I. To study the effect of different material and process variables on HSWG performance in a lactose-water system

II. To develop a first principle DEM model which can be used to predict HSWG performance

3. Chapter Organization and Outline

Chapter 2 is a review of the basics of granular flow regimes and theoretical models used to understand powder flow. The principles of process modeling techniques, and their applications are presented. In addition, the origin and some commonly used numerical formalisms of the fundamental forces are evaluated. The influence of process and environmental variables in modulating these forces, and determination of relevant material properties, are also reviewed to provide a holistic background of particulate interactions before commencing with the thesis research objectives.

Chapter 3 describes particle-fluid interactions in a dilute flow regime in context of modeling multiphase multicomponent aerosol flow through pMDI-spacer geometries. Previous studies concluded that the performance of these systems was largely unpredictable,[9-11] thus driving the regulatory initiative to seek better understanding of these systems for efficient spacer design and labelled instructions for patient use. The effect of volumetric rate of coaxially flowing air, spacer geometry and delay time were studied experimentally for two spacer (Aerochamber Plus™, Optichamber Advantage™) –pMDI(Proventil HFA™) combinations to characterize particle deposition behavior in terms of percentage drug deposition of the actuated aerosol within the spacer, and aerodynamic size at the end of a model USP Throat apparatus.[11] The experimental studies were computationally modeled using CFD to improve the basic understanding of transient local 3D flow structures with the spacers. Fluid flow was correlated to particle deposition behavior through a dimensionless parameter which furthers the goal of rational spacer design.

Chapter 4 describes experimental and computational studies to investigate formation of ordered mixtures for DPI formulations by focusing on inter-particle cohesion. Ordered mixtures

are special structured units wherein fine particles coat a coarse particle so that uniform API dispersal is achieved.[12] Such a structural unit also provides for greater lift forces aiding API entrainment in air upon patient inspiration[13], thus improving the flow and processibility of the formulation. The critical formulation requirement is a fine balance of cohesive (API-API) and adhesive (API-carrier) forces. When adhesive forces are too weak, the API dispersal on the carrier is poor. In contrast, when the strength of the adhesive forces is too high, the API does not release from the ordered mixtures upon patient inspiration.[14] The performance of ordered mixtures, as judged by the fine particle fraction (FPF) is known to be impacted by surface and bulk properties of both the drug and carrier and the mixing process itself .[15] However, drug delivery from DPIs is considered to be largely inefficient[16].Prediction of the performance of ordered mixtures requires systematic research. The effect of carrier and drug material properties has been well studied, but the mixing process itself has received less attention. The mixing of fine lactose (AZFL), used to represent the API, and carrier lactose (Lactohale100 ™ (LH100)) were studied in a low shear Double Cone (DCN) blender and in a high shear mixer (HSM) as a function of process variables (rotation speed, fill, drug load, loading configuration). Process and product metrics were identified (press-on forces, wall adhesion of fines, static charging, abrasion of carrier fines) which can aid the formulation and process scientists to facilitate the selection of blender and process parameters to make ordered mixtures. Segregation of ordered mixtures was studied in hoppers in both mass flow and funnel flow regimes. Numerical DEM simulations used interparticle cohesion, modeled through Bond numbers (K)[17], to represent the ratio of particle cohesion to particle weight. These numerical modeling studies provided further insight into the mixing process for several process and material properties.

Chapter 5 discusses interparticle electrostatic forces and tribocharging in detail, with a focus on the origin and effect of process and environmental factors modulating electrostatic forces. Particle tribocharging in the pharmaceutical sector results in flow instabilities leading to processing and drug release difficulties, sticking during tableting and a risk of fire and explosion.[18-20] Despite known results, tribocharging remains poorly understood as the academic community is divided based on support for several theoretical models (i.e., work function difference/electron transfer, ion transfer, impurity adsorption) [21] governing tribocharging of insulator systems. The current thesis examines the work function differential as a predictor for insulator tribocharging in a hopper-chute assembly. Tribocharging of binary mixtures were studied in a hopper-chute system to examine the effect of excipient load, chute angle, and material properties (work function of equipment and particles, hygroscopicity) in dictating particle flow and charge. DEM simulations incorporating the work function difference model, where the work functions were computed from MD simulations, were used to quantitatively test the theoretical model by comparison with experimental results for both pure and mixed systems.

Chapter 6 presents studies designed to determine the effects of capillary forces on performance of wet granulation in a high shear granulator. High shear wet granulation (HSWG) can described in terms of three competing processes: (a) wetting of particles to create nuclei, (b) consolidation and coalescence of these nuclei to give growth and agglomeration, and (c) breakage and attrition of these nuclei under high shear.[22] Control of these processes produces granules with acceptable properties. Because the interplay of material, geometric and process variables at different length scales is still incompletely understood, HSWG processes are empirically developed, especially with regards to end point determination and scale up.[23] The effect of process variables and material properties on the HSWG performance was studied both

experimentally and computationally. A novel, dynamic 3D DEM based model was developed which captured dynamic capillary and viscous forces, along with modification of material properties as a function of binder content..

Chapter 7 provides a summary of the present research work and gives future directions to advance the studies described in the current thesis.

4. References

1. Muzzio FJ, Shinbrot T, Glasser BJ. 2002. Powder technology in the pharmaceutical industry: the need to catch up fast. *Powder Technology* **124**(1): 1-7.
2. Bridgwater J. 2003. The dynamics of granular materials–towards grasping the fundamentals. *Granular Matter* **4**(4):175-181.
3. Gernaey KV, Cervera-Padrell AE, Woodley JM. 2012. A perspective on PSE in pharmaceutical process development and innovation. *Computers & Chemical Engineering* **42**:15-29.
4. Federsel H. 2003. Searching for scalable processes: addressing the challenges in times of increasing complexity. *Current Opinion in Drug Discovery & Development* **6**(6):838-847.
5. FDA. 2006. Guidance for industry: Q8 pharmaceutical development. ed., Rockville, MD.
6. FDA. 2004. Guidance for industry: PAT—A framework for innovative pharmaceutical development, manufacturing, and quality assurance. ed., DHHS, Rockville, MD.
7. Campbell CS. 2006. Granular material flows–an overview. *Powder Technology* **162**(3):208-229.
8. Crowe CT, Schwarzkopf JD, Sommerfeld M, Tsuji Y. 2011. Multiphase flows with droplets and particles. CRC press.
9. Barry PW, O'Callaghan C. 1996. Inhalational drug delivery from seven different spacer devices. *Thorax* **51**(8): 835-840.
10. Berg E, Madsen J, Bisgaard H. 1998. In vitro performance of three combinations of spacers and pressurized metered dose inhalers for treatment in children. *European Respiratory Journal* **12**(2): 472-476.
11. Liu X,Guo C,Doub W,Chowdhury B,Starke P,Limb S,Peri P,Lostritto R,Schroeder A. 2011. Assessment of Effects of VHCs on In Vitro MDI Performance Characteristics Using the Andersen Cascade Impactor, Annual Meeting of AAPS, Washington, DC.

12. Staniforth JN, Rees JE. 1981. Powder mixing by triboelectrification. *Powder Technology* **30**(2):255–256.
13. W.H. Finlay. 2001. The Mechanics of Inhaled Pharmaceutical Aerosols: An Introduction. Academic Press.
14. Apte SP. 2012. Excipient-API interactions in dry powder inhalers, *Journal of Excipients and Food Chemistry* **3**(4):129-142.
15. De Boer AH, Chan HK, Price R. 2012. A critical view on lactose –based drug formulation and device studies for dry powder inhalation: Which are relevant and what interactions to expect? *Advanced Drug Delivery Reviews* **64**(3):257-274.
16. Labiris NR, Dolovich MB. 2003. Pulmonary drug delivery. Part II: The role of inhalant delivery devices and drug formulations in therapeutic effectiveness of aerosolized medications. *British Journal of Clinical Pharmacology* **56**(6):600-612.
17. Faqih AN, Chaudhuri B, Mehrotra A, Tomassone MS, Muzzio F. 2010. Constitutive model to predict flow of cohesive powders in bench scale hoppers. *Chemical Engineering Science* **65**(10):3341-3351.
18. Pingali KC, Hammond SV, Muzzio FJ, Shinbrot T. 2009. Use of static charge eliminator to improve powder flow. *International Journal of Pharmaceutics* **369**(1):2-4.
19. Hearn G. 1998. Static electricity: concern in the pharmaceutical industry? *Pharmaceutical Science and Technology Today* **1**(7):286-287.
20. Bailey AG. 1993. Charging of solids and powders .*Journal of Electrostatics* **30**:167-180.
21. McCarty LS, Winkleman A, Whitesides GM 2007. Ionic Electrets:Electrostatic charging of surfaces by transferring mobile ions upon contact. *Journal of the American Chemical Society* **129**(13):4075-4088.
22. Iveson SM, Litster JD, Kapgood K,Ennis K. 2001. Nucleation, growth and breakage phenomena in agitated wet granulation processes: a review. *Powder Technology* **117**(1):3-39.
23. Lister JD. 2003. Scale up of wet granulation processes: science not art. *Powder Technology*. **130**(1):35-40.

Chapter 2

On the Role of Forces Governing Particulate Interactions in Pharmaceutical Systems: A Review

Abstract

Process understanding for designing, optimizing and scaling of pharmaceutical unit operations is fundamentally important to address concerns of high risks, monumental costs, and productivity decline in the pharmaceutical industry. This is especially important in the rapidly changing landscape of the pharmaceutical industry. Pharmaceutical processes majorly deal with multiphase multicomponent flows, basics of which are reviewed ion the current article. In addition, basics of multiphase flow regimes, powder flow, and pertinent process modeling techniques pertinent to pharmaceutical unit operations are discussed. The most fundamental contact and non-contact forces are then reviewed in detail with respect to their molecular or physical origin, factors which influence these forces, numerical formalisms and modeling strategies to simulate flows and processes of pharmaceutical interest.

Keywords: Fundamental forces, multiphase multi-component flows, pharmaceutical processing, discrete element method, computational fluid dynamics, material characterization

1. Introduction

1.1 Motivation

Particulate processing is widely encountered across a range of industries, where more than 60% of all manufactured products [1] and more than 80% of pharmaceutical products (designed for US consumption) involve some particulate process.[2] Despite widespread use of these particulate processes and dosage forms, there exists a considerable scope of improving manufacturability and versatility while complying with strict regulatory controls. Research and development costs of introducing a new drug in the market have increased over the past decade and a half,[3] with an attrition rate of new molecular entities (NMEs) estimated at 66% and 30% for phase II and phase III respectively.[4] Manufacturing costs contribute to a significant portion of the total cost of a pharmaceutical product, which could be as high as 27-30% of the sales for brand name pharmaceuticals.[5] Suresh and Basu projected possible avenues of cost saving in manufacturing in the range of 20-50 billion dollars every year.[6] These statistics are of concern to both the regulatory bodies, who aspire for a science based understanding of manufacturing processes as reflected in their Process Analytical Technology (PAT)[7] and Quality by Design (QbD) initiatives;[8] and thus the pharmaceutical industry which is under high pressure to develop and manufacture drugs more efficiently.[9,10] Figure 1 highlights the decreasing productivity of the pharmaceutical industry. This backdrop is the motivation for critically examining and improving our fundamental understanding of particulate interactions towards rational process design, optimization and scale–up. The aim of the current article is to fundamentally review our basic understanding of granular flow, process simulation techniques and review fundamental forces with respect to their physical origin, factors which affect them and approaches to model them in common pharmaceutical applications.

1.2 Granular Flow regimes in Pharmaceutical Processes

Manufacturing of pharmaceutical products, especially oral and inhaled solids, involves processing of particulates, which requires reliable flow. From a strict physics perspective, particle laden flows can be considered to be a subcategory of multiphase multicomponent flows. Quantitative description of such flows requires deep understanding and evaluation of the various forces which produce the particle motion. Particle motion is produced by the action of forces, depending upon the volume fraction of the discrete phase. Particulate flows can thus be naturally classified into *dense* or *dilute* regimes and the ratio of the momentum response time (t_v) to the time between collisions (t_c) can be used to qualitatively assess the flow regime.[11] If $\frac{t_V}{t_C} < 1$, the flow can be considered *dilute* implying that the particle has sufficient time to relax to the local fluid dynamic forces before the next collision. Hence the particle trajectory is primarily dictated by the fluid forces. In contrast, in *dense* flow particles do not have sufficient time to relax to fluid forces before the next collision. Dense flows are further classified into collision dominated where time during contact is small relative that between contacts while in contact dominated flows, particles are in continuous contact and contact forces primarily determine particle's trajectory. Figure 2 shows the different multiphase flow regimes based on interparticle spacing. Solid state unit operations like granular mixing, transport, milling, granulation etc. are contact dominated dense flows in which enduring contact between the particles dictate the spatial and temporal evolution of the granular bed. However, flow fields in a given process equipment may include both flow regimes at a given time instant. The final pharmaceutical product typically undergoes a series of unit operations, and thus is affected by, any of these flow regimes during its production cycle. A thorough understanding of the process under consideration must ideally address all the

flow regimes, but it is not always feasible to do so whereupon simplified models can be applied to the critical length and time scales for optimal process understanding.

Modeling of granular flows from a continuum point of view for studying failure in soil for civil engineering applications began with Coulomb [12] who developed the Mohr Coulomb failure criteria based on friction, cohesion and the applied normal (σ) and shear stresses (τ) ; while modeling from an individual particle point of view was heralded by Bagnold [13] who concluded that stresses vary as square of the shear rate (γ).Powders were classified on the basis of their flowability at ambient temperature and pressure, as determined by fluidization behavior by Geldart[14] into 4 types : A (aeratable, 30-100 μm), B (bubbling,100-1000 μm), C (cohesive,0-30 μm) and D (spoutable >1000 μm).While beds from type A particles (e.g. catalyst beds) typically expand upto 2-3 times at incipient fluidization, Type B particles are free flowing demonstrate bubbling behavior directly. Pharmaceutical powders typically fall into the Type C category, and are difficult to fluidize on account of their high cohesivity which suppresses free particle motion. Type D is associated with large dense particles (e.g. metal ores, coal, coffee beans etc.) which are abrasive and require high dynamic pressures and are frequently operated in the spouting mode. Recently, Yang et al[15] expanded the original Geldart's classification based on new data at modified temperature and pressure. Castellanos et al.[16] identified 4 flow regimes for cohesive powders: (a) *plastic*: interparticle spacing and velocities are very small, (b) *inertial*: interparticle spacing is larger than in the plastic regime but much smaller than the particle diameter so that momentum is dictated by interparticle collisions. (c) *fluidization*: interparticle distance is of the order of magnitude of particle size and momentum transfer takes place through the interstitial fluid, and (d) *suspension*: large interparticle distance so that the mean velocity of particles approaches the fluid velocity due to negligible interparticle interactions. The transition

between plastic and inertial regimes for a particle with density ρ_p and diameter d_p, is dictated by $\rho_p {d_p}^2 v^2/(P\delta^2) \geq 0.1$, where v represents common gas and particle velocities, P is the total normal stress and δ is the shear layer thickness. For very fine cohesive powders, the gas flow must balance the weight of the powder and the tensile strength and the minimum velocity needed to fluidize the particles is independent of particle diameter. The upper limit of the fluidization zone is dictated by the Stokes drag law. Campbell[17] further classified cohesionless dense granular flows into *Inertial* and *Elastic* regimes depending whether the force is transported by inertia or force chains, which are quasi linear structures which support bulk of internal stresses.[18,19] In the *Elastic* regime, the natural stress scaling was identified to be $\tau d/k$ (k is the stiffness and d the particle diameter) which represents the ratio of particle deformation as a fraction of particle diameter. Formation of force chains are proportional to the shear rate at low to moderate shear rates, but the lifetime of the force chain is inversely related to the shear rate and so the product of formation rate and time of a force chain is shear rate independent as observed in *Elastic-Quasistatic* flows. On further increasing the shear rate, the elastic forces in the chain absorb the particle inertia which increases proportionally with increasing shear rate ; thus transitioning the flow into the *Elastic-Inertial* regime in which the stresses are proportional to the shear rate. The natural stress scaling factor in this regime is $k/\rho d^3 \gamma^2$, which is a measure of inertially induced deformation. *Inertial* flows denote cases when force chains are not formed and momentum is largely transported through particle inertia. The *Elastic –Inertial* regime transitions into an *Inertial* regime at low shear rates, as high shear rates promote formation of force chains at smaller concentrations; or by a reduction in concentration. The Inertial regime was further classified into *Inertial-non-Collisional* or *Inertial-Collisional (Rapid Flow)* sub-regimes depending on whether the dominant particle interaction is binary collisions. At constant

volume in which force chains are almost always present, granular flow is in the *Elastic* regime is as the forces chains can support much larger forces than particle inertia. In free surface flows, such as in hopper or landslides, the materials can dilate towards the free surface to balance the applied stress transitioning the flow from quastistatic to rapid flow. Figure 3 describes the granular flow regimes outlined by Castellanos et al.[16] and Campbell.[17]

The flow regimes described above were identified considering spherical particles, but pharmaceutical applications rarely involve ideal spheres. Force chains were observed to form at much lower solid fractions with high aspect ratio ellipsoids than with spheres.[20] In contrast to spherical particles, ellipsoids had a larger solid fraction resulting in larger pressure drops so that slugs were destabilized and the flow in a pneumatic conveyor transitioned early into relatively dilute collision dominated flow.[21] Guo et al.[22] pointed that stresses in collision dominated flows decrease with increasing aspect ratio of the particles as the projected area in direction perpendicular to the flow increases which in turn increases collision frequency and thereby decreases velocity fluctuations. In contact dominated dense flows, particles were found to align with their largest and smallest dimensions in the shear flow and velocity gradient directions respectively.[23] Sharp increases in stress were obtained for high aspect ratio particles as the solid fraction increases facilitating interparticle contacts and rotation. Smaller stresses were observed for flexible chains, modeled as chains of spheres.[24]

1.3 Process Modeling Techniques

From the above discussion, it can be gathered that pharmaceutically relevant flows are complicated and all modes of particle interactions need to be critically analyzed for a given system to map the *design space,* defined as the "multi-dimensional combination of critical input variables and critical process parameters that lead to the right critical quality attributes".[7]This has

been attempted traditionally through experiments. Numerical simulations, widely popular across other process-centric industries, also could be used to supplement process insight. The major advantages of a verified and validated *in silico* model are its ability to both test conventional process understanding dynamically and lend novel insights into a process not readily obtained by experiments, while saving expensive resources. Computational models are only recently gaining momentum within the pharmaceutical industry, but it still lags significantly behind in terms of process systems engineering when compared to other chemical process industries.[25] Techniques to model particle laden flows can be loosely classified into the length –time scales they consider. Macro-scale techniques capture only large scale particle population behavior thereby capturing large systems at a moderate computational expense, whereas micro scale techniques resolve the details of the individual particle phenomena to provide a detailed view of a small system. Meso-scale lies in between the macro and micro scales representing inter-particulate forces having a molecular origin which impact the bulk process behavior. Figure 4 outlines the several length and time scales considered for process modeling.

Forces considered for process modelling include the contact (normal and tangential) and non-contact forces. These non-contact forces involve a combination of the following fundamental forces : (a) Van der Waal's (VDW) attractive forces between "like" bodies (*auto-adhesion)* and "unlike" bodies (*adhesion*) which represent the integrated van der Waals (VDW) and hydrogen bonding interactions between molecules making up the particles, (b) capillary forces which pull particles together, are also represented in this class which originate due to preferential condensation of vapor molecules across a curved surface owing to interfacial tension effects, and (c) electrostatic forces which arise due to Columbic interactions between charged particles. Figure 5 plots the importance of fundamental forces with respect to particle size. The

importance of body forces, which scale proportionally to the cube of particle diameter decrease rapidly with decreasing size while VDW forces increase in importance at smaller particle sizes. The sum of VDW, capillary and electrostatic forces would be referred to as cohesive force throughout the article. In addition to these contact forces, particles are also subject to forces from the local (fluid) medium which are referred to as fluid forces. Fluid, VDW, capillary and electrostatic forces would be referred to as fundamental forces for the purposes of this article. In addition to these fundamental forces, real non-spherical particles also are subject to mechanical interlocking due to geometric entanglement and solid bridges due to surface reactions, dissolution etc. which bring particles together. Process modeling efforts within the pharmaceutical industry can be broadly classified to those for continuous (Computational Fluid Dynamics, Finite Element Method) or discrete phase (Discrete Element Method, Population Balance Method). Kremer and Hancock[26] published an excellent review of basic physical models used in the pharmaceutical industry for process simulations to highlight different applications of process modeling techniques.

1.3.1 Computational Fluid Dynamics (CFD)

CFD is an Eulerian technique that treats material as a continuum and is often relevant in the dilute flow regime. The governing equations for fluid flow – mass, momentum (Navier-Stokes) and energy are solved to determine the evolution of flow field in the simulation volume. Direct Numerical Simulation (DNS) of these equations is not feasible for real systems, and hence a number of numerical formalisms are used. Such formalisms, one of the most popular being RANS (Reynolds Averaged Navier Stokes equations)[27] are based on the energy cascade, which treat the generation of kinetic energy from mean flow at the largest (integral) length scales which cascade down to the smallest (Kolmogorov) length scales where viscous dissipation of energy

takes place. Turbulence is modeled as deviations around the mean flow. CFD codes are good approximations of physical reality in dilute flows (dissolution, inhalation etc.) and contact dominated flows (fluidization etc.). Particles can be included in a CFD simulation in dilute flows without enduring contact in the *Eulerian-Eulerian* ,where both phases are treated as interpenetrating continuum such as in Two Fluid Model (TFM) ,or *the Eulerian-Lagrangian* framework, with the latter modeling discrete particle behavior thereby offering a closer approximation of physical reality by incorporating particle effects like cohesion[28] and consequently being more computationally expensive.[29] The former approach is restricted by validity of the empirical constitutive relations, and can ideally be applied for dilute flows of monodisperse hard spheres undergoing elastic collisions where size distribution and stress states do not change rapidly upon exposure to high shear forces;[26] conditions which are too simplistic for pharmaceutically relevant flows.

In most CFD codes, representative computational geometry is discretized (meshed) into a number of elements or 'control volumes' which represents an infinitesimally small region in the fluid through which some property of the flow is transported. The variable of interest is located at the center of the control volume. A finite volume model numerically solves a coupled set of partial differential equations governing fluid flow (conservation of mass, momentum and energy) in conjunction with appropriate physical models in each control volume. Integration profiles are then assumed in order to describe the variation of concerned variable between cell centroids to give an accurate representation of the flow field subject to appropriate boundary conditions. Particles can be included by the Discrete Particle Model (DPM) approach where point masses are considered and interparticle forces are directly calculated, or by the Particle Cloud Model (PCM) where one representative particle represents many physically similar particles.[30] Figure 6 shows

some representative CFD simulation pictures which have yielded in improved process understanding.

1.3.2 Discrete Element Method (DEM)

In contrast to CFD, DEM takes a Lagrangian approach and treats particles individually which is relevant for processes in the dense flow regime. In DEM, the granular material is considered as a collection of frictional inelastic spherical particles, which resembles powder. Each particle interacts with its neighbors or with the boundary only at contact points through normal and tangential forces. Ideally, all the forces acting on the particle are accounted and are used to compute the net normal and tangential forces to compute the acceleration, which upon numerical integration gives the updated velocities and positions of the particles. The corresponding torque on each particle is the sum of the moment of the tangential forces. The normal and tangential forces (also called collisional forces, are calculated using an appropriate contact mechanics model. Hertz theory[31] considered elastic deformation of contacts and determined the relationship between normal force and normal displacement to be non-linear. Without considering adhesion, Hertz calculated the normal force f_n between two particles of radius R with a Young's modulus E and Poisson's ratio v to be $f_n = \frac{4}{3} R^{1/2} \frac{E}{1-v^{1/2}} \delta^{3/2}$, where δ is the depth of contact deformation. Mindlin and Deresiewicz[32] presented a detailed contact mechanics model demonstrating that loading history and instantaneous rate of change of the normal and tangential forces dictate the force-displacement relationship. In contrast with the classical Hertz theory, the JKR theory[33] also considers adhesion but it is evaluated within the contact area, so it is more appropriate for soft materials with a high surface energy. On the other hand DMT theory[34] considers Hertzian contact profile but with adhesive interactions outside the zone of contact which is appropriate for hard particles. The Tabor coefficient μ_T, defined as the

ratio between the gap outside the contact zone and equilibrium distance between atoms, to develop a unified theory parametrized with μ_T with JKR (high μ_T) and DMT (low μ_T) theories as limiting conditions.

Implementation of contact mechanics modeling in numerical simulations began with Cundall and Stack[35] who implemented Hertzian contact mechanics in their DEM model, which proposed a linear spring and dashpot (LSD) model to capture the normal force by accounting for the elastic deformation and viscous dissipation during an enduring contact. The tangential force in the LSD model is limited by the Coulomb criterion which specifies the maximum frictional force to be dependent upon the normal force. Walton and Braun[36] later incorporated Mindlin and Dereseiwicz contact mechanics in the partially latching spring model in which the normal force was calculated as a function of the overlap value. They used a linear spring to model the repulsive force during loading and a stiffer spring during unloading (Figure 7). Unlike Cundall & Stack's model, which specified a velocity dependent coefficient of restitution, Walton & Braun's model specified a velocity independent coefficient of restitution. The JKR model was incorporated into tangential contact mechanics by Thornton and Yin[37] who varied the contact radius till the onset of sliding

DEM models have grown more in complexity and scope over the past 2 decades to offer a great possibility for dynamic modeling of meso scale processes as evidenced by increasing number of publications in this area.[38] However, the use and scope of DEM its use is often restricted by computational limitations which scale as NlogN with N being the number of particles and a time step which is of the order of microseconds, so that true particle size and real process times are hard to simulate. This makes the choice of simulation parameters like stiffness coefficient critical in order to obtain maximum information from the simulation. Several articles

discuss the determination of contact parameters for practical DEM simulations.[39-41] Zhu et al.[42],Lu et al [38],Guo and Curtis[24] provide some excellent reviews which comprehensively discuss theoretical developments for DEM simulations.

DEM has been used to simulate a wide range of dense particulate flow systems relevant to the pharmaceutical systems. Zhu et al.[43] & Ketterhagen et al.[44] review a range of pharmaceutical applications which have been modeled using DEM.

For realistic representation of pharmaceutically relevant flows, both the continuous and discrete phases need to be coupled, i.e. CFD-DEM coupling, which could be done by either of 3 ways[42,45] (a) force from fluid phase is calculated separately for each particle according to its velocity while the force from the discrete phase on the fluid is calculated as per an averaging rule. Newton's third law might not be satisfied in this approach; (b) force from the fluid phase on the particles is distributed according an averaging rule while the force on the fluid by particles is still calculated be a local average, but this is not an accurate representation of reality (c) individual particle-fluid interaction is calculated at each time step in a grid element and all interactions are summed to produce a net force, and it is the most accurate of the schemes. Coupled CFD-DEM studies have been extensively used for in a number of applications, some of which are discussed later. Figure 8 showcases a range of applications studied using DEM while Table 1 lists some DEM based publications investigating a range of unit operations within the pharmaceutical industry.

1.3.3 Population Balance Modeling

Population Balance Modeling (PBM) which groups particles into different classes based on size and other properties and tracks changes in each class as they undergo rate processes. Ramkrishna[46] defined the population balance equation as an "equation in the number density and

may be regarded as representing a number of particles of a particular state. The equation is often coupled with conservation equation for entities in the particles' environmental (or continuous) phase." Processes can be tracked by following changes in internal (e.g shape, size, porosity, composition etc.) and external (Eucledian) coordinates for different particle classes.[47] The basic PBM equation (Eq.1) can be represented[48]

$$\frac{\partial}{\partial t} f_1(x,r,t) + \nabla \dot{X}(x,r,Y,t) f_1(x,r,t) + \nabla \dot{R}\,(x,r,Y,t) f_1(x,r,t) = h(X,r,Y,t) \quad [1]$$

Where x, r, t, Y and h are the internal coordinate, the external (spatial) coordinate, the time, the continuous phase vector (continuous phase quantities) and the net birth rate (change in number of particles due to discrete processes). $\dot{X}$ and $\dot{R}$ are the partial derivatives of the internal and external coordinates, respectively, while the divergence terms represent convective transport along the external and internal coordinates. The changes in each class are affected through an appropriate coalescence kernel formed from known relations and /or empirical functions. However, the coalescence kernels are often empirical functions and need a number of fitting parameters, casting doubts over their ability to model dynamic mesoscale processes. PBMs are often coupled with DEM or CFD or both for optimal process understanding. Recent DEM-PBM coupled efforts have been used to model milling,[49] film coating;[50] and wet granulation.[51-56]

1.3.4 Finite Element Method

Finite Element Method (FEM) is another popular technique for analyzing problems at the continuum scale, and is closely related in principle to the Finite Volume Method used in most CFD codes. As explained by Sinka et al.[57] who modeled density distributions during compaction of convex tablets, overall solution in FEM is expressed in terms of number of a discreet number of values (degrees of freedom (DOF)) at corners of control volumes (nodes). DOFs are displacements of nodes which can be tracked from stress-strain relationships. FEM solves the

DOFs of the problem by converting the governing differential equations in each element into a large discrete set of algebraic equations for the nodal values. Accuracy is increased by increasing the approximation order within elements. As FEM is conceptually non conservative, it is not used typically for discontinuous processes. FEM has been quite popular for modeling compaction of powders in combination with DEM, where high deformation cannot be tackled by conventional DEM approaches.[57-63]

2. Particle-Fluid Forces

2.1 Origin

Particle fluid interactions refer to exchange of mass, momentum and energy between phases and form the basis of coupling. These may result from transport of droplet vapor to or from the droplet surface, or phase change at the surface during evaporation or condensation. Droplets are subject to body (*weight and buoyancy*) forces and interfacial forces of drag and lift. These interfacial forces arise due to disequilibrium of pressure forces exerted by molecules of a medium when an object moves through it, and act parallel (drag) or perpendicular (lift) to the flow direction. In general, drag forces represent fluid resistance to motion of a particle, and can be classified into *form drag* (due to particle shape), *interference drag* (when two competing airflows must pass through a restricted area) and *skin drag* (due to friction of fluid and object skin). Physical effects which modify drag on the particle are: (a) *Virtual mass effect* which modifies the form drag as the induced fluid acceleration by particle motion which amounts to additional work done (b) *Bassett force* accounts for the viscous effects due to the temporal delay in boundary layer development as the relative velocity changes with time , (c) *Faxen correction* c the curvature of the velocity profile in the conveying flow field, while (d) *Magnus effect*

accounts for changes in drag and lift forces due to spinning of a particle. Virtual mass, Bassett and Magnus forces can be neglected when the density of particles is much greater than the surrounding fluid [64,65] which is the case for most pharmaceutical applications with air as the surrounding medium.

2.2 Factors affecting Drag

1) **Reynolds Number (*Re*) & Mach Number (*Ma*):** Drag coefficient varies inversely with Reynolds number in the Stokes flow regime (*Re* <1) when the viscous forces are important while inertial forces can be neglected. Due to viscosity, a pressure gradient (higher at forward stagnation point and lower at the rear) develops and contributes to form drag. The other contribution to drag forces comes from shear forces (shear drag). Several formalisms are used to model the steady state drag force in Stokes flow regime can be expressed as in Eq.2:

$$F_d = C * 0.5\rho_f \frac{\pi}{4} {d_p}^2 \left(v_p - v_f\right)^2 \qquad [2]$$

As Re increases then the inertial forces become more important, flow begins to separate forming vortices behind the sphere which reduces the pressure in the wake thereby increasing form drag and decreasing the shear drag. However, at critical Reynolds number (Re_{cr}) when the boundary layer becomes turbulent, the separation point moves rearward and reduces the form drag and decreases the drag coefficient. At high *Ma*, formation of shock waves increases the drag coefficient. Al low *Re*, drag coefficient decreases with increasing *Ma*, due to rarefied flow effects. For particles with Knudsen numbers (*Kn*) of the order of unity, *Kn* being the ratio of molecular free path to that of a representative physical length scale, the shock wave engulfs the particle of comparable size to the wave thickness. Figure 9 plots the variation of drag coefficient of a sphere with respect to *Re* and *Ma.*

2) **Turbulence**: Instantaneous drag on a particle can be affected by the many length scales of turbulent flows. According to Bagchi & Balachandar[66], there are two competing mechanisms : (a) increased turbulence intensity decreases the mean settling velocity and the resulting mean drag , this effect decreases with *Re* ,and (b) particles sample regions of downwash more preferentially than regions of upwash, so that the mean settling velocity is higher. Additional complexities are present in particle laden flows where particle interactions can induce local turbulence. Di Felice [67] provided a correlation which accounted for variation in Stokesian drag (Re <<1) with volume fraction as the particles undergo hindered settling. Several researchers have pointed an increase in drag coefficient at moderate *Re* [68-70] while several others have reported a decrease[71] while some concluded insignificant effect.[72-74] Increasing the turbulence intensity (I_r) was found to decrease the critical Reynolds number [75] and a decrease in drag coefficient at Re_{cr}.[76]

3) **Particle morphology**: The effect of size in intuitive from Eq. 2, as the drag force increases with increased particle size. However, as particle size decreases to the mean free molecular path in the medium; Cunningham's correction factor is used to account for the drag force as non-continuum effects reduce the drag force and produce a larger settling velocity. Particle shape significantly affects the form drag by affecting the projected area to the fluid. The effect of shape on drag is not as straightforward and is difficult to formalize.[24,77] There have been empirical drag laws based on the generalized C_d vs *Re* correlations for non-spherical particles.[78,79] Hölzer and Sommerfeld[80] proposed a drag law which utilized regular sphericity, crosswise sphericity and lengthwise sphericity while taking correction factors from experimental data. They found excellent agreement (<15%) with observations for a variety of isometric and non-isometric particle shapes. The aerodynamic advantage of an elongated

particle is frequently exploited for designing carrier particles for DPI formulations. The ratio of aerodynamic diameter to physical diameter of a particle is increases with the aspect ratio and plateaus off at a value of 2-2.5 when the aspect ratio >=15-20.[81] High fine particle fraction (FPF, defined as fraction of particles with an MMAD < 5μm), of the drug have been observed with carrier particles with a high aspect ratio.[81-84] Some popular drag law formalisms showing modeling variation of drag with different parameters have been listed in Table 2.

2.3 Measurement of Drag Force

For pharmaceutical applications, the determination of aerodynamic diameter is often used, which essentially represents the size of a sphere with the same terminal velocity, hence the same drag force, in a fluid. The aerodynamic diameter represents the size of a sphere having the same Stokesian drag as the particle under consideration. The Andersen Cascade Impactor (ACI) is compendially specified for determination of aerodynamic sizes of aerosols. It works on the principle of inertial separation of particles in ultra-Stokesian flow. A fixed volume of air is drawn through the valve by a pump downstream at a critical flow rate so that the actual inhalation from a DPI is simulated without matching the flowrate-time profiles. Time of flight instruments offer a non-invasive method in which the particle is accelerated to point where the velocity temporarily lags behind that of the flow, at which point the time to pass between two light beams is measured. The flow regime can be ultra-Stokesian or Stokesian, the former being more sensitive to particle shape and density. Particle acceleration introduces droplet distortion which can reduce the aerodynamic diameter and underpredict sizes.[85,86] Mitchell and Nagel (2004)[87] provide a comprehensive summary of these two methods, in addition to other methods used for particle sizing.

2.4 Applications & Numerical Modeling

CFD has been arguably the most popular technique to model a wide range of pharmaceutical processes involving multiphase flow. One of the most common applications of CFD is to investigate hydrodynamics in a dissolution apparatus, which have been known to give variable performance and unpredictable profiles[88-90] pointing out a need for optimizing design and process features. In silico evaluations have indeed confirmed variable hydrodynamics of the system as identified by local inhomogenities in fluid flow patterns.[91-93] McCarthy et al.[92] conducted a parametric study to highlight changes in fluid flow structures spatially and temporally as function of different rotation speeds. Hydrodynamics of USP Dissolution apparatus 3 have highlighted periodic flow structures and the performance being impacted significantly by the dip rate.[94] They revealed local vortices and recirculation domains specific to the upstroke and downstroke in addition to local stagnation zones. CFD modeling of hydrodynamics in UPS type 4 dissolution apparatus have also revealed concentration gradient differences at the upper and lower edges of the contact,[95] and noticeable differences in tablet shear stress distribution when flow is pulsating due to separation in velocity boundary layer around the tablet.[96] Koganti et al.[97] modeled scale up of dissolution from a 21 L lab scale vessel to a 4000 L commercial scale vessel using CFD using dimensionless variables. These studies used the 2 equation RANS models to model turbulence.

Another particularly important problem in the dilute flow regime is one of design of Volume Holding Chambers (VHC's) or spacers for improving therapeutic efficacy of pressurized metered dose inhalers (pMDIs), which allow grater droplet evaporation time and reduce aerosol velocity to decrease the Stokes number (*St*, ratio of aerodynamic response time to the characteristic flow time) which in turn reduces mouth-throat deposition.[64] The performance of

spacer-pMDI interactions is rather unpredictable and variable[98-100] necessitating studies to investigate role of role features for optimizing performance. CFD has been used to model post-nozzle flow and aerosol deposition from pMDIs into human airways with variable degree of success. Most of these studies have focused on an idealized single component (solid API) plume initiated at an arbitrary speed (much lower than that observed experimentally) to account for speed dampening by the propellant vapor, while considering spherical drag force to be the most important force acting on the particles. Kleinstreuer et al.[101] modeled droplet deposition behavior in a hypothetical spacer and predicted significant decrease of particle deposition in the oral cavity, which contrasted with experimental findings suggesting scope of improvement in the modeling efforts.[102] Oliveira et al.[103] modeled flow behavior in an effort to computationally optimize design of the Volumatic ® spacer by studying air flow patterns in different cases. Recently, Remmelgas et al.[104] using CFD-DEM coupled model to simulate the flow of cohesive particles out of large and particles out of a model DPI inhaler to demonstrate that small particles leave faster than the larger particles which can become trapped in the recirculation zone.

Granular fluidization for drying, coating and granulation are examples of contact dominated flows. Fluidized bed dryers, coaters and granulators are very popular as the fluidized bed operations ensure maximum fluid-particle contact surface to enable maximum mass and heat transfer. CFD-DEM coupled investigating fluidization of cohesive particles has been extensively studied to study the interaction of cohesive force and particle weight and friction influencing the bubbling tendency.[105-107] Wang et al.[108] and Jang et al.[109] have modeled the performance batch fluidized dryer as a function of process parameters by considering TFM model, while experimentally validated Eulerian –Eulerian simulations on drying [110] and coating [111] have been published which promise rational process optimization. Moisture transfer in gas and solid phases

are described using species balance equations for each phase. CFD models have been developed to study coating in a Wurster coater [112] while coupled DEM-CFD model was developed to study the gas and particle dynamics in a fluidized bed granulator.[113] Recently, hybrid multi-scale model has been developed for a continuous fluid bed wet granulation process by dynamically CFD with a DEM and population balance model (PBM).[51] Experimentally validated CFD process modeling of a pharmaceutical freeze dryer was done[114] in which Navier Stokes equations were used under continuum conditions while the rarefied flow solutions were obtained by direct simulation Monte Carlo method for the Boltzmann equation.

Effect of processing on the density and stress distribution inside a tablet or compact is popularly studied using FEM. Density distribution changes in the compact by wall lubrication,[57] compaction process,[61] and wall friction;[62] tablet capping [63] have been investigated using FEM. Coupled CFD-DEM systems have been used to model dilute flows of non-spherical particles, by either considering a collection of spheres to model cylindrical particles in a fluidized bed;[115] spouted bed[116] or a non-spherical geometry with a drag law for non-spherical particles.[117] Ren's study demonstrated that due to the higher drag on corn shaped particles, the spouts carries them farther than the central axis of the bed while Oschmann found that cylindrical particles mix faster than spheres in a fluidized bed owing to larger surface area of the cylinders.

3. Van der Waals (VDW) Force

3.1 Origin

Cohesive forces are simply the result of electromagnetic forces acting between electrons and protons of individual molecules making up the particles. These forces arise due to the induced or permanent polarities created in molecules and are categorized into dipole-dipole

(Keesom), dipole-induced dipole (Debye), or induced dipole-induced dipole (London) interactions. London dispersion are considered long range and attractive and scale inversely with 6th power of the separation distance till the distance of closest approach (≈ 0.4 nm) is reached. The attractive VDW forces decline even more quickly at larger separations than the sixth powder dependence due to retardation effects, which is due to the finite time it takes for electromagnetic signals to travel between molecules and hence a lag before a molecule feels a dipole and responds to it.[118] Ideally the Schrödinger equation needs to be solved to map the exact profile of VDW forces, but these are overwhelming and cannot be solved for bulk systems. A simplification to solve this problem was provided by Feynman, [119] who concluded that the classical electrodynamics equations predictions were close enough to full quantum mechanical treatment of energies of two atoms at different configurations. Feynman's landmark paper also outlined a procedure to compute molecular forces, instead of evaluating energies alone. Israelachvili[120] evaluated the integrated effects of interaction energies between different macroscopic surfaces with simple geometries. The VDW force (F_{vdw}) between two bodies with a radii r_1 and r_2 separated by a distance s is given by $F_{VDW} = \frac{-A}{6s^2} . \frac{r_1 r_2}{r_1 + r_2}$, where A is the Hamaker's constant and is given by $A = -12 w_p \pi s^2$, w_p is the surface energy per unit area.

3.2 Factors influencing VDW forces

a) **Particle Size:** Give a particle of radius *r*, body forces being proportional to r^3 fall off rapidly with decreasing size followed by surface forces (drag) which are proportional to r^2. VDW scale proportionally with *r* and are important for fine particle (Figure 5). The VDW forces fall off rapidly with increasing separation distance *s* (decline in proportion to s^7 at a molecular level) and are only relevant for particles in contact.

b) **Particle Morphology**: Contact between real particles would indeed be at asperities and so a simple approximation would be to consider an effective asperity diameter as opposed to particle diameter. This would reduce the attractive forces at the contacting point but a large number of asperities, expected in case of rough particles, would tend to counterbalance this effect. Adhesive force measurements off irregularly shaped toner particles are much smaller than that predicted for smooth particles of the same size.[121] Finlay points out that the adhesive force between two particles would be exquisitely determined by region near the contact making shape a critical aspect of consideration.[64] Considering that no two particles have the same shape or roughness, it appears to be a rather daunting task to resolve the three dimensional microstructure of particulate contacts to correctly predict attractive VDW forces at these contacts, by iteratively solving equations governing adhesion and deformation (as they affect each other) over this contact domain. Different α-lactose monohydrate grades with differing shapes and roughness were shown to have markedly different surface energies.[122]

c) **Environmental Conditions:** The London dispersion forces are always between molecules of a neighboring medium. In addition to London force, polar interactions may also manifest themselves and modify the net VDW .Strictly speaking VDW forces are unaffected by moisture; but if the cohesion decreases on increasing moisture, the primary cohesion is electrostatic in nature. On the contrary any increase in cohesion on increasing RH is attributed to increasing capillary forces.[123]

3.3 Estimating VDW forces: Material Characterization

There are a few material properties, like *Hamaker's constant* and *surface energy* which convey direct information about the strength of VDW forces for a given material. Walton[123]

argues for an intimate relationship between the surface energy per unit area of the contacting materials, and cohesive force at a sphere-plane contact despite significant plastic deformation; the cohesive force can be evaluated at contact point from the energy displacement derivative and the actual molecular contact area using the Hamaker's constant (H) . The determination of H is based on Hamaker's theory of pairwise summation of forces constituent of atoms of a macroscopic body under the assumption that each interaction can be treated independently, which is too simplistic for complicated pharmaceutical systems. An alternative parameter for use is surface energy, which implicitly includes the effects of an adsorbed layer and elastic deformation.[64] The cohesive force between two particles can be captured using Atomic Force Microscopy (AFM). In AFM, one particle is attached to the cantilever of the AFM while another is attached to a piezo crystal. The position when the particles are contacted for the first time is registered on a computer. The cantilever is registered from the test particle and adhesion forces between the particles are measured as deflection of the cantilever. Li et al. used this technique to correlate VDW forces with powder flowability and compactibility for a number of powders.[124] AFM is advantageous in directly yielding a quantitative measurement of the cohesive force between two particles, but suffers from the drawback of very high resolution so that bulk systems made of non-ideal polydisperse particles may not be adequately represented. Particles with large surface discontinuities may not be measured at all with AFM while the true contact area between the probe and substrate surface cannot be precisely determined.[125] Variation of surface energies with lactose preparation technique and size fraction have been reported,[126] and milling was found to increase the dispersive energy by formation of amorphous domains. Techniques like Inverse Gas Chromatography (IGC), which measure the residence time a probe molecule spends with a substrate, yield a distribution of surface energies over the whole powder bed. Cline and Dalby [127]

report a direct correlation of surface energy interaction between the carrier and drug and the FPF. A direct correlation was found between the cohesive index,[128] and FPF for a number of formulations. Carrier interaction forces as measured by AFM are not predictive of surface energy differences.[125] Contact angle measurements can also be used for dispersive energy, but these frequently yield lower values than IGC as the latter samples the highest energy sites on powder surface.

Characterization of the general cohesivity of powders (sum of VDW, capillary and electrostatic forces) is of utmost importance to determine their flow behavior under different stress conditions for design of storage equipment (hoppers and silos) and processes. As described earlier, powder flow depends upon the stress and thus relevant characterization of flow can only be done at appropriate stress levels. Testing under packed bed conditions under high stress can be used to predict flow out of a bin or hopper. Shear cell testing is routinely done, wherein a powder is compacted with normal loading stress after which tensile stresses are applied till the compact fails. Parameters like *cohesion strength* and *flow function*,[129] ratio of major principal stress to the unconfined yield strength may be obtained. Free surface tests, like bulk density, tapped density, angle of repose, compactibility, Carr's index (CI) and Hausner's ratio (HR) are indicators of non- consolidated flow under the influence of gravity e.g. flow into a die in a tablet press. These measures are indicators of particle-particle friction in a dynamic mass of bed. HR and compactibility reflect volume reduction and any decrease in these values correlate with a decrease in cohesion. Dynamic testing conditions, as in a powder rheometer involves movement of blade through a powder bed along a helical path to determine the flow energy , which is defined as the energy needed in moving a blade from the top of the powder bed through to the bottom. Additionally, normalized basic flow energy (NBFE) is defined as the energy needed to

displace a conditioned powder sample during downwards movement of the blade while specific energy reflects the energy needed per gram as the blade during its upwards traverse in the unconfined powder. Avalanching behavior of cohesive powders, measured in an AeroFlow apparatus by monitoring bed height and time between avalanching in a rotating drum photoelectrically, can be used to characterize flowability. Flow under aerated conditions are determined by monitoring the pressure drop as the powder is aerated or fluidized in a column with different impinging air velocities. These tests are suitable for designing applications in a fluidized bed. Thalberg et al.[130] investigated the applicability of these tests for inhalation grade powders and found HR have the widest working range and the highest discriminating power , while uniaxial compression was suited for more cohesive powders in contrast to the AeroFlow which worked well for powders with low cohesivity. Leturia et al.[131] investigated a diverse group of powders using these techniques and found the HR to be best suited for low stress flows and highly correlated with Normalized Basic NBFE.

Other methods which measure adhesive force between particles are detachment of particles under the influence of a centrifugal force, [132] electric field [133] or aerodynamic stress when a gas stream is used.[134] Recently, Zafar et al (2014)[122] developed a drop test, in which the test particles that are adhered to a substrate are mounted on and are subjected to a tensile force by impacting the stub against a stopper ring by dropping from a set height.

3.4 Numerical Modeling in Pharmaceutical applications

Pharmaceutical unit operations often involve multiphase and multicomponent systems. The role of cohesion in affecting particle fluidization behavior has been described earlier in Section (1.2). The role of VDW forces in dense flows is often critical to most solid state unit operations, where a typical mixture may contain very fine and cohesive API along with a free

flowing excipient leading to segregation and content uniformity issues. In DEM simulations, incorporation of cohesive forces can be done in the following ways: (a) a constant force can be directly added which can be computed from the product of cohesive energy density and the contact area of the particle[135] (b) using proportionality constant ,the Bond number (*Bo*), relating the particle weight to the cohesive forces the ratio of cohesive forces to particle weight when the particles are a critical distance apart, has been used for modeling flows in a hopper;[136,137] bed dilation and avalanching flow in a rotating cylinder; [138] segregation in a tote blender,[139] identifying flow regimes in a screw feeder,[140] (c) using the Hamaker's constant to calculate the cohesive force, as studied by Yang et al. (2008)[141] to study force structures in packed beds of coarse and fine particles, (d) and to add a spring constant[142] to model cohesive interactions. More complicated DEM models have been presented using several parameters to account for non-linear elastic and plastic effects, plastic energy dissipation, adhesion.[143-145] Walton & Johnson[146] include parameters to account for torsion and bending strength that may exist between adhesive particles. Cohesive flows were associated with significant bed dilation and avalanching,[138] widening of shear bands,[147] while total normal forces were found to have tensile greater component than compressive.[141] Yang et al. [141] also concluded that with the same cohesion, decreasing particle size transformed the force structure from being vertically aligned to a more symmetric distribution, as the cohesion between particles increases although they have smaller magnitudes. Figure 10 demonstrates some effects of particle cohesion.

4. Capillary Forces

4.1 Origin

Capillary condensation of atmospheric moisture is an important effect to be considered in determining overall adhesion between particles, especially considering the fine particle size and ambient humidity encountered with most pharmaceutical operations. The origin of the capillary forces can be attributed to a Laplace pressure difference (ΔP) across a curved surface. A model capillary bridge is shown in Figure 11.

The static capillary force has 2 components; the first is a hydrostatic force due to the Laplace pressure differential, and a surface tension force which acts axially along the three phase contact line. The capillary force is given addition, a dissipative viscous force due to particle lubrication is present which resists particle motion and can be significant during dynamic processing especially for viscous binders.[148] Due to the discrete nature of the liquid and the combined effects of several components, force associated with a capillary bridge is difficult to evaluate especially when it is intended to application in a dynamic system.

In general, the capillary force of a liquid bridge is given by a solution of the Young-Laplace equation, but unfortunately it cannot be analytically solved. Several analytical solutions with restrictive assumptions and numerical solutions have been presented which relate the interfacial tension of the bridging liquid, volume of the bridge and the interparticle separation distance. For a toroidal liquid bridge, the solutions strongly depend on the curvature of the liquid bridge (H) which in turns depends on the so called half filling angle (φ_i).Mazzone et al.[149] found the capillary force between two steel particles for different binder liquids to be a strong function of separation distance but a weak function of the fill angle which prompted them to use a constant fill angle approximation. Lian[150] assumed a toroidal liquid bridge approximation for estimation of the capillary force. Toroidal bridges do not have a constant mean surface curvature and thus the surface tension and capillary forces can be evaluated at the mid-point of the bridge

("gorge method") or at contact line with one of the spheres ("boundary method"). The boundary method is supported from experimental and numerical results by Hotta et al.[151] while the results of Lian et al.[150] support the gorge method. A toroidal liquid bridge was formed when the separation distance of two particles is less than a critical value S_c which was determined from the half filling angle. The separation was modified by Pitois et al.[152] who used a circular approximation of the bridge profile and made it a function of particle velocity. Rabinovich et al.[153] hypothesized the capillary force between two particles as a derivative of the energy of the bridge and proposed a differential equation to determine the filling angle with respect to the separation distance. Mikami et al[154] provided a solution Young-Laplace equation by varying a number of dimensionless variables to find a dependence on the filling angle for two equal sized spheres, while Soulie` et al[155] proposed a solution for unequal spheres. Table 3 lists some numerical formalism which has been used to capture capillary forces.

For the viscous dissipative force expressions can be derived from solution of the Naviers-Stokes equation. This expression is however hyperbolic with respect to the separation distance so that a point of singularity is observed, a problem which is bypassed by assuming a finite minimum separation distance which is physically related to rough surfaces.[156] The approximate closed form solution obtained is used to model the normal component of the viscous force of the liquid bridge between two spheres where the normal component is given by Fisher[157] as $F_{vn} = 6\pi\eta R^* v_n \frac{R^*}{S}$, where η is the viscosity, v_n is the relative normal velocity between two spheres, S is the separation distance and R^* is the reduced radius. There is no rigorous analytical solution for the tangential component of the viscous force but Goldman et al.[158] derived the following asymptotic solution, valid under limiting conditions, for the viscous force for sufficiently small

separation distances: $F_{vt} = (\frac{8}{15} ln\frac{R}{S} + 0.9588)\ 6\pi\eta R^{*} v_t$ where, v_t is the relative normal velocity between two particles and R is the radius of the sphere.

4.2 Factors influencing Capillary forces

(a) Particle Size: The Kelvin effect (Eqn. 3) clearly predicts capillary condensation at lower partial pressures with decreased particle size or increased curvature. This equation can be used to predict the radius of liquid capillary bridge (r_{lb}) between the particle and a wall at a given RH when assuming that $r_{lb} << r_p$.

$$r_{lb} = \frac{-2\gamma_{LV} M_l}{R_u \rho_l T ln(RH)} \quad [3]$$

The effect of particle size is readily determined from equation which clearly predicts increased capillary condensation with lower particle sizes.

(b) Particle Morphology: As with the previous cases, extrapolating smooth particle theories to real non-spherical and rough particles can be rather tricky. The asperity diameter can be substituted in place of the particle diameter if it is much greater than the meniscus radii. When the condensed liquid fills the regions between asperities which may be case at higher humidities or small asperities, particle diameter is suitable from a qualitative view-point.[64] The cohesive strength between granules increases sharply for small volumes of liquid for rough particles [159,160] after which there is no increase. The morphology of the bound liquid inside a pile was revealed using X ray microtomography for spherical glass beads & irregular sand particles.[161] They found that the pressure inside the liquid levels off when the liquid occupies more than 2.5% of the pile volume and a half filling angle of 30 degrees. Addition of more liquid to the pile does not increase the cohesive force as the projected area over which the pressure acts on the particle is unchanged. They do not observe any difference

between the liquid morphology between the smooth spheres and irregular sand particle particles. The static mechanical strength for saturated capillaries is regarded to be independent of the liquid content volume over a wide range [162,163] as the increase in bridge size is balanced by a decrease in curvature.

4.3 Measurement of Capillary Force

AFM provides a generic test to measure the cohesive force between the particles, of which one of the components is the capillary force. It was shown by AFM studies that the energy needed to separate a drug from the carrier surface increased with increasing RH.[164] Static strength of capillary forces is determined by direct tensile tests or uniaxial compression tests where the compact is assumed to fail due to tensile stress. Quasi static side crushing was used to measure the strength in batch [165,166] and recently in continuous granulators.[167] One of the more economical and widely used techniques is the power consumption by the main motor.[168,169] This technique correlates well with the granule growth and mean granule size. However, this technique reflects load on the motor rather than on the impeller and is strongly dependent of motor efficiency; which is in turn influenced by losses due to cooling fan and air drag, friction in bearings ad eddy current losses. Impeller torque consumption by a torque rheometer does not suffer from these drawbacks and is an excellent indictor of the rheological properties and strength of the wet mass.

4.4 Applications & Numerical Modeling in Pharmaceutical Systems

Capillary forces hold particles together in pharmaceutical systems. Breaking these capillary bonds is needed for drying while forming them with suitable binding liquid is needed for wet granulation. The discrete nature of capillary bridges and the ability of DEM to model dynamic processing conditions make it an attractive choice to model drying and wet granulation.

DEM offers the ability to model the dynamic interplay of capillary, viscous and friction forces which eventually dictate the process performance. However, several assumptions with respect to binder distribution between particles which may or may not be of equal size, surface wetting and the amount of liquid from each bridge taking part in bond formation[24] and variation of material properties as function of increasing binder content. Inclusion of advanced models is also hindered by a huge computational cost.

Some DEM based efforts have thus modeled motion of wet particles, without explicit inclusion of capillary forces.[170,171] Talu et al[172] included capillary forces to model agglomeration in a 2D system while Lian et al[173] used a 3D box containing few particles to develop a preliminary understanding of particle agglomeration processes. Most often, even distribution of binder is considered with constant layer of thickness around each particle[100,174-176] while some studies have considered binder distribution based on size ratio[137] and different substrate contact angle.[177] Capillary forces were found to decrease mixing in a rotating drum though an optimum fill level was identified Liu et al,[174] Alexander et al.[138] and Sahni and Chaudhuri[178] used the force model proposed by Lian et al.[173] to simulate contact drying. However, classical DEM has two drawbacks for modeling capillary force based applications; the first one is that it's being computationally very demanding and the other being the neglect of the fluid forces. These have necessitated development of other approaches, where DEM is coupled with another technique. Recently, Balakin et al.[179] proposed an inexpensive computationally model for agglomeration of solid particles covered with a liquid flocculant based on analytical equations and implemented these in a computational code using a Eulerian-Lagrangian approach for a set of particles in a shear flow system. A microscale DNS model CFD (DNS) -DEM model was proposed by Washinto et al.[180] in which they modeled droplet penetration in a static bed and droplet

imprigement on a dynamic bed. They used a continuum surface model[181] to model the effect of surface tension force on the fluid phases, while the capillary force was captured from the Continuum Capillary Force (CCF) model, in which the capillary force exerted on the particle is given by the line integral of surface tension along the three phase contact line. The authors obtained good agreement with experiments done by Chouk et al.[182]

Population balance models (PBM) are widely used too to model agglomeration.[52-56] PBMs rely on development of coalescence kernels which are based on ideal binary collisions and incorporate a number of empirical fitting parameters,[47] casting a doubt on their ability to model dynamic processes. Coupled DEM-PBM models have been developed to model wet granulation [183] in which DEM was used to provide a mechanistic rate kernel, while Sen et al.[51] & Barrasso et al.[52] implemented bidirectional PBM-DEM coupling to evaluate collision frequencies and liquid distribution in a drum granulator and twin screw granulator respectively while Sen et al.[51] presented a coupled CFD-DEM-PBM approach to model fluidized bed granulation. The multi-scale coupling approach is presented in Figure 12.

5. Electrostatic Forces

5.1 Origin

Electrostatic forces between particles arise due to presence of electrostatic charges on particles. Electrostatic charges arise on particles due to transfer or segregation of charged species under one or a combination of the following conditions: (a) mechanical contact between two particles (*triboelectrification*), (b) application of mechanical stress (*piezoelectrification*), (c) application of heat (*pyroelectrification*), (d) influence of electric field from a charged body in proximity (*electrostatic induction*). Electrostatics forces between two particles are given by the

well-known Coloumb's inverse square law which makes the electrostatic forces long range, which is unlike other contact forces discussed previously. Pharmaceutical applications allow for frequent contact between relatively non polar particles so that triboelectrification is assumed to be the most important cause of static electrification of pharmaceutical powders.

Triboelectrification of powders has been studied since the 6th century BC when the ancient Greeks discovered rubbed amber attracting small objects. Static electrification has been studied extensively since then across a range of industries for charged powders offer a number of applications. Contact electrification of metals is widely accepted to be due to transfer of electrons between contacting bodies under the influence of a contact potential difference (V_c) which arises due to a difference in work function (ϕ) of the contacting bodies.[184] Work function is defined as the minimum energy required for removing an electron from Fermi level to free space. The Fermi level is canonically given as the center of the HOMO (Highest Occupied Molecular Orbital)-LUMO (Lowest Unoccupied Molecular Orbital) gap[185] and represents the chemical potential for electrons. It is conventionally understood that charge transfer (Δq) between two contacting bodies takes place till the Fermi levels are aligned.

$$\Delta q = C_o V_c = -\frac{C_o(\emptyset_1 - \emptyset_2)}{e} \qquad [4]$$

In sharp contrast with that of metal triboelectrification, there is considerable debate in the academic community over the nature of charge transfer species involving insulators. However, fortunately or unfortunately, that is where the pharmaceutical industry's interests lie.

The electron transfer hypothesis is often criticized on grounds that the energy requirements for electron transfer are much higher (few eV) than what might be gained from ambient thermal energy (kT ≈ 0.025 eV at 298K).[186] The alternate mechanism proposed is that of ion transfer. In a study with functionalized polymer with mobile counter-ion, the sign of charge

of ion containing polymers was found to be same as the sign of the covalently bound polymer and the charge increased in magnitude on increasing the ion concentration to demonstrate ion transfer.[187] Law et al[188] also demonstrated ion transfer by showing a linear correlation between toner charge and amount of cesium transferred, cesium being used as a negative charge control agent. Similar studies by Diaz conducted to study charge transfer for toner charging [189,190] advocate ion transfer as the possible mechanism.

The argument frequently presented against Harper's conjecture that either insulators or electrons take part in tribocharging is that there are no ideal insulators in real systems. It was hypothesized surface energy states, *intrinsic* where electrons can be present from molecule /solid chemistry in the forbidden gap, or *extrinsic* where exchangeable electrons were present on the surface from adsorption or contamination.[191] Indeed, surface and chemical defects along with entanglement of polymer chains can produce trapped electron states.[192,193] Presence of high energy electrons have been demonstrated on insulator surfaces.[194] Rowley[195] found tribocharging of α-lactose monohydrate in a cyclone charger, made of either polyvinyl chloride or stainless steel, to be in agreement with the work function differential of the contacting species. Liu and Bard[196] also gave strong evidence of electrons taking part in tribocharging of insulators by identifying electrons and not ions as the charge carrier species when Teflon (polytetrafluroethylene) was rubbed against Lucite (polymethylmethacrylate). Other notable studies which correlate work function difference with tribocharging for relevant systems[197-203] and hence electrons to be fundamental carriers which was proposed from earlier theoretical models.[204,205] Linear correlations between charge density of polymers and metal work functions also support electron exchange hypothesis.[206,207] A semi quantitative triboelectric series was formulated[208] which listed a wide variety of materials according to their effective work functions

incorporating results of charging with metals or similar materials. Work function of materials has been used to select materials for storage, packaging and device components for DPI formulations.[195,209-211]

Adsorbed impurities, like moisture and adventitious ions, on the surface can also play a significant role in tribocharging of matter. Creux et al.[212]observed preferential hydroxide adsorption at aqueous interfaces which was demonstrated computationally from MD simulations by Zangi and Engberts.[213] Contact electrification of functionalized polymers was postulated to involve adsorbed hydroxide ions determined by zeta potential measurements.[186] Adsorbed material also was found to alter the work function of materials.[214] Theories of contact electrification have been comprehensively reviewed.[215-218] Figure 13 represents a schematic illustration of different theories put forward to explain tribocharging.

5.2 Factors Influencing Electrostatic Force

a) **Particle Morphology (Shape & Size):** Ireland[219] concluded that particles with irregular geometry accumulate more charge during sliding than rolling due to the greater average contact area for sliding contact. Kramer and Urbanetz[215] postulated increased thermal activation of electrons due to greater frictional heat on sliding contact. Kwek et al.[220] demonstrated higher charging of rough mannitol particles produced by spray drying as compared to smooth ones due to a greater surface potential. Ireland's study also concluded that continuous contact transfers more charge than bouncing contact due to greater average contact time, and greater discharging of airborne particles. Rolling particles were also concluded to have a greater charge accumulation capacity as they present a fresh surface every rotation. Sarkar et. al. [200] showed decreased charge accumulation for irregular shaped glass beads relative to spheres on discharging from a PVC based hopper-chute assembly. A

number of studies [195,200,219] demonstrated greater charge on the finer particle due to greater contact surface area and more number of particle–wall contacts.[195,200,219] Supuk et al. demonstrated significantly higher charging of APIs.[221]

b) **Relative humidity:** Several studies have shown a decrease in magnitude of net charge with increasing humidity.[222-224] This is believed to be due to dampening of charge at higher RH as the surface conductivity of contacting bodies is enhanced by increased adsorbed water. At thickness of water layer greater than 2nm, the water layer can be considered to be bulk water which offers a great grounding path. Surface conductivity of the moist air is also higher which further promotes gas discharge.[225]

c) **Crystal structure:** The role of crystal structure has not been investigated in great detail. Lactose powder with higher amorphous content was found to record a greater charge on actuation from a DPI than more crystalline powder.[226] Amorphous content can influence the surface work function and make the surface softer and amenable to more deformation. Higher surface moisture levels can also impact tribocharging by influencing dissipation and distribution of charge, as opposed to crystals where charges can be localized at sharp facets.

d) **Process Parameters:** Processes with increased intensity yield greater net charges as greater impact velocity results in greater impact charge.[227,228] Increasing the process intensity was reported to decrease the time to saturation charge, but not the charge magnitude itself.[203] This was believed to be due to a greater frequency of particle-wall contacts and decrease in charge relaxation due to decreased time between collisions.

5.3 Determination of Relevant Material properties

5.3.1 Work Function: Work Function of a material can be determined by Photoemission spectroscopy (PES) and Kevin-probe microscopy. The former method utilizes the principles of

photoelectron effect whereby the kinetic energy of an electron emitted from a surface upon irradiation with light of appropriate wavelength, typically UV (UPS) & X-Ray (XPS) is measured. UPS treats surface electrons while XPS has a greater surface penetration and is used to determine orbital energies. On the contrary, Kelvin probe microscopy utilizes an AFM set up to quantify the electrostatic force between the substrate and cantilever tip, and the tip is usually calibrated against a material of known work function e.g. gold. Most commonly, a voltage consisting of a DC bias, V_{DC}, and an AC voltage, $V_{AC,}$ (set at frequency ω corresponding to the resonance frequency of the cantilever tip) are applied. V_{DC} is varied during the scan so that the value at which the response i.e. the electrostatic forces become 0, corresponds to the contact potential difference. If work function of the tip is known, work function of the sample can be determined trivially.

Computational methods have also been utilized to measure work function of material. Density Functional theory is frequently used for materials routinely used for the electronic industry,[229] while semi empirical methods have been used to determine work function of insulators.[185,200,230]

5.3.2 Particle Charge: One of the simplest and most popular devices for measurement of powder charge is the Faraday's cup. It basically consists of two concentric metal cups separated by an insulator like expanded polyethylene or Teflon. The outer cup is electrically grounded while the inner cup is connected to an electrometer and is electrically insulated. When a charged powder is placed in the inner cup, an equal and opposite charge is induced in the conducting material of the cup. The powder charge is measured between the inner cup and ground using an electrometer with a known capacitance. However, Faraday cup measurements are known to be sensitive to external environmental disturbances.[218] Electrical Low Pressure impactor (ELPI) is

another method which is frequently used as it can classify charge on particle size fractions.[211] It is essentially a cascade impactor which measures electrical current resulting from dissipation of particle charges upon deposition. Unlike the average charge for a given mass of particles that is determined by ELPI, an ESPART (Electrical –single particle aerodynamic relaxation time) device obtains measures individual particle charges. ESPART measures the particle's response to an oscillating electric field which gives information about the particle's aerodynamic diameter as well as its charge to mass ratio as used by Saini et al.[231] to demonstrate polar charging using from DPI actuations.

5.4 Applications and Numerical Modeling

Within the context of pharmaceutical industry, powder triboelectrification is traditionally considered undesirable as it often leads to poor flow and agglomeration resulting in segregation [232],poor flow[233] and increased adhesion to the wall and dispersal in manifesting in poor pulmonary delivery from DPIs [234] along with storage and handling problems.[235] The tribocharged powders are a major safety hazard as well, especially in presence of flammable gases, solvent fumes and dust found easily in chemical and pharmaceutical factories.[236] Significant effort has to be spent to control tribocharging through approaches like static eliminators[237] or flow additives.[238] As pointed out by few studies, electrostatic forces between particles can be potentially utilized within the pharmaceutical industry to form ordered mixtures[239] and dry powder coating of tablets.[240]

Computational efforts in characterizing static electrification of granular media have been attempted through continuum approaches**,** [241-243] but these fail to link granular flow kinematics with tribocharging. Probability based particle dynamics models have been used to electrostatics behavior of particles of different sizes, but did not account for real work function values.[244]

Watano [245,246] used a 3D DEM based studies to model triboelectrification of powders such that the charge transfer after each collision was a function of charge density and the contact area using Hertzian contact mechanics.[247] presented a CFD-DEM coupled model, similar to that by Watano [245] for modeling tribocharging of pneumatically conveyed powders model. They found that beyond a critical mean charge, the image charge on the pie walls becomes very important and cannot be neglected. These studies do not explicitly consider work functions and the effects of screening. Tribocharging modeling including the effect of screening was done by Hogue et al.,[248] though they used empirical functions for charging and discharging. Pei et al.[249] used a DEM-CFD coupled model to study contact electrification during fluidization. They used a condenser model so that charge transfer takes place in accordance with the work function difference, but they did not incorporate long range electrostatic forces. They demonstrated increased charge density at regions near the wall and faster charge accumulation with higher gas velocity. Recently, Naik et al.[230] have published process parametric studies from a DEM based model which considers reduction of contact potential of particles with each successive collision, with the charge transfer taking place in accordance with the work function difference at the time of maximum particle deformation. They considered long range electrostatic forces and the screening effect of particles.

6. Conclusions

Contemporary pharmaceutical industry is under increasing economic pressure to deliver and manufacture drug formulations which underscores the need for better process and material understanding. In an increasingly multidisciplinary research outlook, importing tools and techniques from allied industries which have technological commonalities is rapidly gaining

momentum. Process modeling techniques are an example, wherein advances in modeling methodologies and computation power have helped us explore old and newer processes in much greater depth than which would be possible by experiments alone. Process modeling using one or a combination of approaches, coupled validated against experiments provides a fundamental approach to iteratively increase our understanding giving us scope for efficient optimization and scaling of both known and novel processes.

The current article outlines the different process modeling techniques available to us and discusses some applications. At the heart of these simulation approaches, is the incorporation of fundamental forces which also have been discussed in terms of their origin, affecting variables characterization, numerical formalisms and incorporation in process models. While it can be claimed that we have moved significantly since the time Coulomb started exploring granular mechanics for civil engineering applications, there remains substantial work that needs to be done. Coupling of solid contact and interstitial fluid forces is still a challenging area, and is restricted by significant computation requirements. VDW forces have been modeled using various techniques, but most are simple approaches for spherical particles. Shape and size distribution effects need to be carefully assessed to map the effects of VDW forces over a complicated 3D microstructure. In addition, a combination of contact forces is also exceedingly hard to model; owing to the huge demand of computation of forces in dense particle flows. The origin of electrostatic forces is widely debated, and its implementation in codes is cumbersome owing to both the contact and long range effects. There is significant work to be done for inclusion of capillary forces as well, where numerical formalisms are simplistic in their assumptions of dynamic capillary and viscous forces. In addition, the alteration of material properties upon moisture incorporation is still not accounted leaving the models seriously

compromised in their ability to model reality. Despite these shortcomings, there is undoubtedly a bright future for process modeling techniques as the engineering disciplines explore more efficient algorithms and increases in computation power to increase our scope into complex problems.

7. References

1. Bridgwater J. 2003. The dynamics of granular materials–towards grasping the fundamentals. *Granular Matter* **4**(4):175-181.
2. Muzzio FJ, Shinbrot T, Glasser BJ. 2002. Powder technology in the pharmaceutical industry: the need to catch up fast. *Powder Technology* **124**(1):1-7.
3. Scannell JW, Blanckley A, Boldon H, Warrington B. 2012. Diagnosing the decline in pharmaceutical R&D efficiency. *Nature Reviews Drug discovery* **11**(3):191-200.
4. Paul SM, Mytelka DS, Dunwiddie CT, Persinger CC, Munos BH, Lindborg SR, Schacht AL. 2010. How to improve R&D productivity: the pharmaceutical industry's grand challenge. *Nature Reviews Drug Discovery* **9**(3):203-214.
5. Basu P, Joglekar G, Rai S, Suresh P, Vernon J. 2008. Analysis of manufacturing costs in pharmaceutical companies. *Journal of Pharmaceutical Innovation* **3**(1):30-40.
6. Suresh P, Basu PK. 2008. Improving pharmaceutical product development and manufacturing: impact on cost of drug development and cost of goods sold of pharmaceuticals. *Journal of Pharmaceutical Innovation* **3**(3):175-187.
7. FDA. 2004. Guidance for industry: PAT—A framework for innovative pharmaceutical development, manufacturing, and quality assurance. ed., DHHS, Rockville, MD.
8. FDA. 2006. Guidance for industry: Q8 pharmaceutical development. ed., Rockville, MD.
9. Federsel H. 2003. Searching for scalable processes: addressing the challenges in times of increasing complexity. *Current opinion in drug discovery & development* **6**(6):838-847.
10. Gernaey KV, Cervera-Padrell AE, Woodley JM. 2012. A perspective on PSE in pharmaceutical process development and innovation. *Computers & Chemical Engineering* **42**:15-29.
11. Crowe CT, Schwarzkopf JD, Sommerfeld M, Tsuji Y. 2011. Multiphase flows with droplets and particles. ed.: CRC press.
12. Coulomb CA. 1773. Essai sur une application des règles de maximis & minimis à quelques problèmes de statique, relatifs à l'architecture. ,Mem. Math. Phys. Acad. R. Sci.,Paris **7** : 323-382

13. Bagnold RA. 1954. Proceedings of the Royal Society of London A: Mathematical, Physical and Engineering Sciences, 49-63.

14. Geldart D. 1973. Types of gas fluidization. *Powder technology* **7**(5):285-292.

15. Yang W-C. 2007. Modification and re-interpretation of Geldart's classification of powders. *Powder Technology* **171**(2):69-74.

16. Castellanos A, Valverde JM, Pérez AT, Ramos A, Watson PK. 1999. Flow regimes in fine cohesive powders. *Physical Review Letters* **82**(6):1156.

17. Campbell CS. 2006. Granular material flows–an overview. *Powder Technology* **162**(3):208-229.

18. Howell D, Behringer R, Veje C. 1999. Stress fluctuations in a 2D granular Couette experiment: a continuous transition. *Physical Review Letters* **82**(26):5241.

19. Mueth DM, Jaeger HM, Nagel SR. 1998. Force distribution in a granular medium. *Physical Review E* **57**(3):3164.

20. Campbell CS. 2011. Elastic granular flows of ellipsoidal particles. *Physics of Fluids* (1994-present) **23**(1):013306.

21. Hilton J, Cleary P. 2011. The influence of particle shape on flow modes in pneumatic conveying. *Chemical Engineering Science* **66**(3):231-240.

22. Guo Y, Wassgren C, Ketterhagen W, Hancock B, James B, Curtis J. 2012. A numerical study of granular shear flows of rod-like particles using the discrete element method. *Journal of Fluid Mechanics* **713**:1-26.

23. Guo Y, Wassgren C, Hancock B, Ketterhagen W, Curtis J. 2013. Granular shear flows of flat disks and elongated rods without and with friction. *Physics of Fluids* (1994-present) **25**(6):063304.

24. Guo Y, Curtis JS. 2015. Discrete Element Method Simulations for Complex Granular Flows. *Annual Review of Fluid Mechanics* **47**:21-46.

25. Rogers A, Ierapetritou M. 2014. Proceedings of the 8th International Conference on Foundations of Computer-Aided Process Design, 144.

26. Kremer D, Hancock B. 2006. Process simulation in the pharmaceutical industry: a review of some basic physical models. *Journal of Pharmaceutical Sciences* **95**(3):517-529.

27. Wilcox DC. 1998. Turbulence modeling for CFD. ed.: DCW industries La Canada, CA.

28. Weber MW, Hrenya CM. 2006. Square-well model for cohesion in fluidized beds. *Chemical Engineering Science* **61**(14):4511-4527.

29. Chiesa M, Mathiesen V, Melheim JA, Halvorsen B. 2005. Numerical simulation of particulate flow by the Eulerian–Lagrangian and the Eulerian–Eulerian approach with application to a fluidized bed. *Computers & Chemical Engineering* **29**(2):291-304.

30. Kosinski P, Hoffmann AC. 2007. An Eulerian–Lagrangian model for dense particle clouds. *Computers & Fluids* **36**(4):714-723.

31. Hertz H. 1882. Über die Berührung fester elastischer Körper.

32. Mindlin R, Deresiewicz H. 1953. Elastic spheres in contact under varying oblique forces. *Journal of Applied Mechanics*, **20** : 327-344

33. Johnson K, Kendall K, Roberts A. 1971. Proceedings of the Royal Society of London A: Mathematical, Physical and Engineering Sciences,301-313.

34. Derjaguin BV, Muller VM, Toporov YP. 1975. Effect of contact deformations on the adhesion of particles. *Journal of Colloid and Interface Science* **53**(2):314-326.

35. Cundall PA, Strack OD. 1979. A discrete numerical model for granular assemblies. *Geotechnique* **29**(1):47-65.

36. Walton OR, Braun RL. 1986. Viscosity, granular-temperature, and stress calculations for shearing assemblies of inelastic, frictional disks. *Journal of Rheology* (1978-present) **30**(5):949-980.

37. Thornton C, Yin K. 1991. Impact of elastic spheres with and without adhesion. *Powder Technology* **65**(1):153-166.

38. Lu G, Third J, Müller C. 2015. Discrete element models for non-spherical particle systems: From theoretical developments to applications. *Chemical Engineering Science* **127**:425-465.

39. Malone KF, Xu BH. 2008. Determination of contact parameters for discrete element method simulations of granular systems. *Particuology* **6**(6):521-528.

40. Mishra B. 2003. A review of computer simulation of tumbling mills by the discrete element method: part I—contact mechanics. *International Journal of Mineral Processing* **71**(1):73-93.

41. Williams JR, O'Connor R. 1999. Discrete element simulation and the contact problem. Archives of *Computational Methods in Engineering* **6**(4):279-304.

42. Zhu H, Zhou Z, Yang R, Yu A. 2007. Discrete particle simulation of particulate systems: theoretical developments. *Chemical Engineering Science* **62**(13):3378-3396.

43. Zhu H, Zhou Z, Yang R, Yu A. 2008. Discrete particle simulation of particulate systems: a review of major applications and findings. *Chemical Engineering Science* **63**(23):5728-5770.

44. Ketterhagen WR, am Ende MT, Hancock BC. 2009. Process modeling in the pharmaceutical industry using the discrete element method. *Journal of Pharmaceutical Sciences* **98**(2):442-470.

45. Feng Y, Yu A. 2004. Assessment of model formulations in the discrete particle simulation of gas-solid flow. *Industrial & Engineering Chemistry Research* **43**(26):8378-8390.

46. Ramkrishna D. 2000. Population balances: Theory and applications to particulate systems in engineering. ed.: Academic press.

47. Cameron I, Wang F, Immanuel C, Stepanek F. 2005. Process systems modelling and applications in granulation: A review. *Chemical Engineering Science* **60**(14):3723-3750.

48. Mortier STF, De Beer T, Gernaey KV, Remon JP, Vervaet C, Nopens I. 2011. Mechanistic modelling of fluidized bed drying processes of wet porous granules: a review. *European journal of Pharmaceutics and Biopharmaceutics* **79**(2):205-225.

49. Capece M, Davé R, Bilgili E. 2015. On the origin of non-linear breakage kinetics in dry milling. *Powder Technology* **272**:189-203.

50. Kumar R, Freireich B, Wassgren C. 2015. DEM–compartment–population balance model for particle coating in a horizontal rotating drum. *Chemical Engineering Science* **125**:144-157.

51. Sen M, Barrasso D, Singh R, Ramachandran R. 2014. A multi-scale hybrid CFD-DEM-PBM description of a fluid-bed granulation process. *Processes* **2**(1):89-111.

52. Barrasso D, Eppinger T, Pereira FE, Aglave R, Debus K, Bermingham SK, Ramachandran R. 2015. A multi-scale, mechanistic model of a wet granulation process using a novel bi-directional PBM–DEM coupling algorithm. *Chemical Engineering Science* **123**:500-513.

53. Adetayo A, Litster J, Pratsinis S, Ennis B. 1995. Population balance modelling of drum granulation of materials with wide size distribution. *Powder technology* **82**(1):37-49.

54. Chaudhury A, Wu H, Khan M, Ramachandran R. 2014. A mechanistic population balance model for granulation processes: effect of process and formulation parameters. *Chemical Engineering Science* **107**:76-92.

55. Liu L, Litster J. 2002. Population balance modelling of granulation with a physically based coalescence kernel. *Chemical Engineering Science* **57**(12):2183-2191.

56. Ramachandran R, Barton PI. 2010. Effective parameter estimation within a multi-dimensional population balance model framework. *Chemical Engineering Science* **65**(16):4884-4893.

57. Sinka I, Cunningham J, Zavaliangos A. 2004. Analysis of tablet compaction. II. Finite element analysis of density distributions in convex tablets. *Journal of Pharmaceutical Sciences* **93**(8):2040-2053.

58. Muliadi AR, Litster JD, Wassgren CR. 2012. Modeling the powder roll compaction process: Comparison of 2-D finite element method and the rolling theory for granular solids (Johanson's model). *Powder Technology* **221**:90-100.

59. Ransing R, Gethin D, Khoei A, Mosbah P, Lewis R. 2000. Powder compaction modelling via the discrete and finite element method. *Materials & Design* **21**(4):263-269.

60. Zavaliangost A, Procopio AT. 2005. Understanding strength of powder compacts using a detailed multi-scale simulation. *Advances in Powder Metallurgy & Particulate Materials*, 52-61.

61. Khoei AR, Azami A, Azizi S. 2007. Computational modeling of 3D powder compaction processes. *Journal of Materials Processing Technology* **185**(1):166-172.

62. Michrafy A, Dodds J, Kadiri M. 2004. Wall friction in the compaction of pharmaceutical powders: measurement and effect on the density distribution. *Powder Technology* **148**(1):53-55.

63. Wu C-Y, Hancock B, Mills A, Bentham A, Best S, Elliott J. 2008. Numerical and experimental investigation of capping mechanisms during pharmaceutical tablet compaction. *Powder Technology* **181**(2):121-129.

64. Finlay WH. 2001. The mechanics of inhaled pharmaceutical aerosols: an introduction. ed.: Academic Press.

65. Hjelmfelt Jr A, Mockros L. 1966. Motion of discrete particles in a turbulent fluid. *Applied Scientific Research* **16**(1):149-161.

66. Bagchi P, Balachandar S. 2003. Effect of turbulence on the drag and lift of a particle. *Physics of Fluids* **15**(11):3496-3513.

67. Di Felice R. 1994. The voidage function for fluid-particle interaction systems. *International Journal of Multiphase Flow* **20**(1):153-159.

68. ZARIN NA, ARTHUR NICHOLLS J. 1971. Sphere drag in solid rockets—non-continuum and turbulence effects. *Combustion Science and Technology* **3**(6):273-285.

69. Brucato A, Grisafi F, Montante G. 1998. Particle drag coefficients in turbulent fluids. *Chemical Engineering Science* **53**(18):3295-3314.

70. JM Y. 1996. Interaction of massive particles with turbulence. Department of Mechanical and Aerospace Engineering, ed.: Cornell University.

71. Rudoff RC, Bachalo, W. D. 1988. Measurements of droplet drag coefficients in a polydispersed turbulent flow field. AIAA, Aerospace Sciences Meeting, 26th, ed., Reno, NV.

72. Warnica W, Renksizbulut M, Strong A. 1995. Drag coefficients of spherical liquid droplets Part 2: Turbulent gaseous fields. *Experiments in fluids* **18**(4):265-276.

73. Wu J-S, Faeth G. 1994. Sphere wakes at moderate Reynolds numbers in a turbulent environment. *AIAA journal* **32**(3):535-541.

74. Wu J-S, Faeth G. 1995. Effect of ambient turbulence intensity on sphere wakes at intermediate Reynolds number. *AIAA Journal* **33**(1):171-173.

75. Torobin L, Gauvin W. 1961. The drag coefficients of single spheres moving in steady and accelerated motion in a turbulent fluid. *AIChE Journal* **7**(4):615-619.

76. Clamen A, Gauvin W. 1969. Effects of turbulence on the drag coefficients of spheres in a supercritical flow Ŕegime. *AIChE Journal* **15**(2):184-189.

77. Mandø M, Yin C, Sørensen H, Rosendahl L. 2007. 6th International Conference on Multiphase Flow, ICMF,9-13.

78. Ganser GH. 1993. A rational approach to drag prediction of spherical and nonspherical particles. *Powder Technology* **77**(2):143-152.

79. Haider A, Levenspiel O. 1989. Drag coefficient and terminal velocity of spherical and nonspherical particles. *Powder Technology* **58**(1):63-70.

80. Hölzer A, Sommerfeld M. 2008. New simple correlation formula for the drag coefficient of non-spherical particles. *Powder Technology* **184**(3):361-365.

81. Gonda I, Abd El Khalik A. 1985. On the calculation of aerodynamic diameters of fibers. *Aerosol Science and Technology* **4**(2):233-238.

82. Larhrib H, Martin GP, Marriott C, Prime D. 2003. The influence of carrier and drug morphology on drug delivery from dry powder formulations. *International Journal of Pharmaceutics* **257**(1):283-296.

83. Ikegami KK, Yoshiaki; Takeuchi, Hirofumi; Yamamoto, Hiromitsu; Isshiki, Nobuyuki; Momose, Den Ichi. 2002. Improved inhalation behavior of steroid KSR-592 in vitro with Jethaler(R) by polymorphic transformation to needle-like crystals (beta-Form). *Pharmaceutical Research* **19** (10):1439 - 1445.

84. Chan HK, Gonda I. 1989. Respirable form of crystals of cromoglycic acid. *Journal of Pharmaceutical Sciences* **78**(2):176-180.

85. Cheng Y, Barr E, Marshall I, Mitchell J. 1993. Calibration and performance of an API aerosizer. *Journal of Aerosol Science* **24**(4):501-514.

86. Marshall I, Mitchell J, Griffiths W. 1991. The behaviour of regular-shaped non-spherical particles in a TSI aerodynamic particle sizer. *Journal of Aerosol Science* **22**(1):73-89.

87. Mitchell J, Nagel M. 2004. Particle size analysis of aerosols from medicinal inhalers. *KONA Powder and Particle Journal* **22**(0):32-65.

88. Cox DC, Wells CE, Furman WB, Savage TS, King AC. 1982. Systematic error associated with apparatus 2 of the USP dissolution test II: effects of deviations in vessel curvature from that of a sphere. *Journal of Pharmaceutical Sciences* **71**(4):395-399.

89. McCormick T. 1995. Industry perspective on dissolution apparatus calibration. *Dissolution Technologies* **2**:12-15.

90. Qureshi SA, McGilveray IJ. 1999. Typical variability in drug dissolution testing: study with USP and FDA calibrator tablets and a marketed drug (glibenclamide) product. *European Journal of Pharmaceutical Sciences* **7**(3):249-258.

91. Kukura J, Arratia PE, Szalai ES, Muzzio FJ. 2003. Engineering tools for understanding the hydrodynamics of dissolution tests. *Drug Development and Industrial Pharmacy* **29**(2):231-239.

92. McCarthy LG, Kosiol C, Healy AM, Bradley G, Sexton JC, Corrigan OI. 2003. Simulating the hydrodynamic conditions in the United States Pharmacopeia paddle dissolution apparatus. *AAPS PharmSciTech* **4**(2):83-98.

93. Baxter JL, Kukura J, Muzzio FJ. 2005. Hydrodynamics-induced variability in the USP apparatus II dissolution test. *International Journal of Pharmaceutics* **292**(1):17-28.

94. Perivilli S, Kakhi M, Stippler E. 2014. Computational Fluid Dynamics Simulation of Hydrodynamics in USP Apparatus 3—The Influence of Dip Rate. Pharmaceutical research:1-12.

95. D'Arcy DM, Liu B, Bradley G, Healy AM, Corrigan OI. 2010. Hydrodynamic and species transfer simulations in the USP 4 dissolution apparatus: Considerations for dissolution in a low velocity pulsing flow. *Pharmaceutical research* **27**(2):246-258.

96. Kakhi M. 2009. Mathematical modeling of the fluid dynamics in the flow-through cell. *International Journal of Pharmaceutics* **376**(1):22-40.

97. Koganti V, Carroll F, Ferraina R, Falk R, Waghmare Y, Berry M, Liu Y, Norris K, Leasure R, Gaudio J. 2010. Application of modeling to scale-up dissolution in pharmaceutical manufacturing. *AAPS PharmSciTech* **11**(4):1541-1548.

98. Barry PW, O'Callaghan C. 1996. Inhalational drug delivery from seven different spacer devices. *Thorax* **51**(8):835-840.

99. Berg E, Madsen J, Bisgaard H. 1998. In vitro performance of three combinations of spacers and pressurized metered dose inhalers for treatment in children. *European Respiratory Journal* **12**(2):472-476.

100. Liu P, Yang R, Yu A. 2011. Dynamics of wet particles in rotating drums: effect of liquid surface tension. *Physics of Fluids* **23**(1):013304.

101. Kleinstreuer C, Shi H, Zhang Z. 2007. Computational analyses of a pressurized metered dose inhaler and a new drug-aerosol targeting methodology. *Journal of Aerosol Medicine* **20**(3):294-309.

102. Ruzycki CA, Javaheri E, Finlay WH. 2013. The use of computational fluid dynamics in inhaler design. *Expert Opinion on Drug Delivery* **10**(3):307-323.

103. Oliveira RF, Teixeira SF, Silva LF, Teixeira JC, Antunes H. 2012. Development of new spacer device geometry: a CFD study (part I). *Computer Methods in Biomechanics and Biomedical Engineering* **15**(8):825-833.

104. Remmelgas J, Thalberg K, Björn IN, van Wachem B. 2015. Simulation of the Flow of Cohesive Particles in a Model Inhaler Using a CFD/DEM Model. *Procedia Engineering* **102**:1526-1530.

105. Yu AB, Xu BH. 2003. Particle-scale modelling of gas–solid flow in fluidisation. *Journal of Chemical Technology and Biotechnology* **78**(2-3):111-121.

106. Ye M, Van der Hoef M, Kuipers J. 2004. A numerical study of fluidization behavior of Geldart A particles using a discrete particle model. *Powder technology* **139**(2):129-139.

107. Pandit JK, Wang X, Rhodes M. 2005. Study of Geldart's Group A behaviour using the discrete element method simulation. *Powder technology* **160**(1):7-14.

108. Wang H, Yang W, Senior P, Raghavan R, Duncan S. 2008. Investigation of batch fluidized-bed drying by mathematical modeling, CFD simulation and ECT measurement. *AIChE journal* **54**(2):427-444.

109. Jang J, Rosa C, Arastoopour H. 2010. CFD simulation of pharmaceutical particle drying in a bubbling fluidized bed reactor. Refereed Proceedings.The 13th International Conference on Fluidization - New Paradigm in Fluidization Engineering.

110. Jang J, Arastoopour H. 2014. CFD simulation of a pharmaceutical bubbling bed drying process at three different scales. *Powder Technology* **263**:14-25.

111. Duangkhamchan W, Ronsse F, Dewettinck K, Pieters J. 2011. CFD study of solids concentration in a fluidised-bed coater with variation of atomisation air pressure. *Powder Technology* **212**(1):103-114.

112. Karlsson S, Rasmuson A, van Wachem B, Björn IN. 2009. CFD modeling of the Wurster bed coater. *AIChE journal* **55**(10):2578-2590.

113. Fries L, Antonyuk S, Heinrich S, Palzer S 2011. DEM–CFD modeling of a fluidized bed spray granulator. *Chemical Engineering Science* **66**(11):2340-2355.

114. Alexeenko AA, Ganguly A, Nail SL. 2009. Computational analysis of fluid dynamics in pharmaceutical freeze-drying. *Journal of Pharmaceutical Sciences* **98**(9):3483-3494.

115. Zhong WQ, Zhang Y, Jin BS, Zhang MY. 2009. Discrete Element Method Simulation of Cylinder-Shaped Particle Flow in a Gas-Solid Fluidized Bed. *Chemical Engineering & Technology* **32**(3):386-391.

116. Ren B, Zhong W, Jin B, Shao Y, Yuan Z. 2013. Numerical simulation on the mixing behavior of corn-shaped particles in a spouted bed. *Powder Technology* **234**:58-66.

117. Oschmann T, Vollmari K, Kruggel-Emden H, Wirtz S. 2015. Numerical Investigation of the Mixing of Non-spherical Particles in Fluidized Beds and during Pneumatic Conveying. *Procedia Engineering* **102**:976-985.

118. Lifshitz E. 1956. The theory of molecular attractive forces between solids.

119. Feynman RP. 1939. Forces in molecules. *Physical Review* **56**(4):340.

120. Israelachvili JN. 1991. Intermolecular and surface forces: second edition. ed.: Academic press.

121. Hays DA. 1995. Toner adhesion. *The Journal of Adhesion* **51**(1-4):41-48.

122. Zafar U, Hare C, Hassanpour A, Ghadiri M. 2014. Drop test: A new method to measure the particle adhesion force. *Powder Technology* **264**:236-241.

123. Walton OR. 2008. Review of adhesion fundamentals for micron-scale particles. *KONA Powder and Particle Journal* **26**:129-141.

124. Li Q, Rudolph V, Weigl B, Earl A. 2004. Interparticle van der Waals force in powder flowability and compactibility. *International Journal of Pharmaceutics* **280**(1):77-93.

125. De Boer A, Chan H, Price R. 2012. A critical view on lactose-based drug formulation and device studies for dry powder inhalation: which are relevant and what interactions to expect? *Advanced Drug Delivery Reviews* **64**(3):257-274.

126. Sethuraman VV, Hickey AJ. 2002. Powder properties and their influence on dry powder inhaler delivery of an antitubercular drug. *AAPS PharmSciTech* **3**(4):7-16.

127. Cline D, Dalby R. 2002. Predicting the quality of powders for inhalation from surface energy and area. *Pharmaceutical Research* **19**(9):1274-1277.

128. Apte S. 2012. Excipient-API interactions in dry powder inhalers. *Journal of Excipients and Food Chemicals* **3**(4):129-142.

129. Jenike A. 1961. Gravity Flow of Bulk Solids. University of Utah Engineering Experiment Station. Bulletin 108.

130. Thalberg K, Lindholm D, Axelsson A. 2004. Comparison of different flowability tests for powders for inhalation. *Powder Technology* **146**(3):206-213.

131. Leturia M, Benali M, Lagarde S, Ronga I, Saleh K. 2014. Characterization of flow properties of cohesive powders: A comparative study of traditional and new testing methods. *Powder Technology* **253**:406-423.

132. Salazar-Banda G, Felicetti M, Goncalves J, Coury J, Aguiar M. 2007. Determination of the adhesion force between particles and a flat surface, using the centrifuge technique. *Powder Technology* **173**(2):107-117.

133. Takeuchi M. 2006. Adhesion forces of charged particles. *Chemical Engineering Science* **61**(7):2279-2289.

134. Shukla N, Henthorn KH. 2009. Effect of relative particle size on large particle detachment from a microchannel. *Microfluidics and Nanofluidics* **6**(4):521-527.

135. Grima AP, Wypych PW. 2011. Development and validation of calibration methods for discrete element modelling. *Granular Matter* **13**(2):127-132.

136. Faqih AN, Chaudhuri B, Mehrotra A, Tomassone MS, Muzzio F. 2010. Constitutive model to predict flow of cohesive powders in bench scale hoppers. *Chemical Engineering Science* **65**(10):3341-3351.

137. Anand A, Curtis JS, Wassgren CR, Hancock BC, Ketterhagen WR. 2010. Segregation of cohesive granular materials during discharge from a rectangular hopper. *Granular Matter* **12**(2):193-200.

138. Alexander AW, Chaudhuri B, Faqih A, Muzzio FJ, Davies C, Tomassone MS. 2006. Avalanching flow of cohesive powders. *Powder Technology* **164**(1):13-21.

139. Sudah O, Arratia P, Alexander A, Muzzio F. 2005. Simulation and experiments of mixing and segregation in a tote blender. *AIChE Journal* **51**(3):836-844.

140. Hou Q, Dong K, Yu A. 2014. DEM study of the flow of cohesive particles in a screw feeder. *Powder Technology* **256:**529-539.

141. Yang R, Zou R, Yu A, Choi S. 2008. Characterization of interparticle forces in the packing of cohesive fine particles. *Physical Review E* **78**(3):031302.

142. Luding S. 2005. Shear flow modeling of cohesive and frictional fine powder. *Powder Technology* **158**(1):45-50.

143. Tomas J. 2007. Adhesion of ultrafine particles—a micromechanical approach. *Chemical Engineering Science* **62**(7):1997-2010.

144. Tomas J. 2007. Adhesion of ultrafine particles—energy absorption at contact. *Chemical Engineering Science* **62**(21):5925-5939.

145. Luding S. 2008. Cohesive, frictional powders: contact models for tension. *Granular Matter* **10**(4):235-246.

146. Walton OR, Johnson SM. Powders and Grains. 2009: Proceedings of the 6th International Conference on Micromechanics of Granular Media ,897-900.

147. Hu N, Molinari J. 2004. Shear bands in dense metallic granular materials. *Journal of the Mechanics and Physics of Solids* **52**(3):499-531.

148. Iveson SM, Litster JD, Hapgood K, Ennis BJ. 2001. Nucleation, growth and breakage phenomena in agitated wet granulation processes: a review. *Powder Technology* **117**(1):3-39.

149. Mazzone D, Tardos G, Pfeffer R. 1987. The behavior of liquid bridges between two relatively moving particles. *Powder Technology* **51**(1):71-83.

150. Lian G, Thornton C, Adams MJ. 1993. A theoretical study of the liquid bridge forces between two rigid spherical bodies. *Journal of Colloid and Interface Science* **161**(1):138-147.

151. Hotta K, Takeda K, Iinoya K. 1974. The capillary binding force of a liquid bridge. *Powder Technology* **10**(4):231-242.

152. Pitois O, Moucheront P, Chateau X. 2001. Rupture energy of a pendular liquid bridge. *The European Physical Journal B-Condensed Matter and Complex Systems* **23**(1):79-86.

153. Rabinovich YI, Esayanur MS, Moudgil BM. 2005. Capillary forces between two spheres with a fixed volume liquid bridge: theory and experiment. *Langmuir* **21**(24):10992-10997.

154. Mikami T, Kamiya H, Horio M. 1998. Numerical simulation of cohesive powder behavior in a fluidized bed. *Chemical Engineering Science* **53**(10):1927-1940.

155. Soulie F, Cherblanc F, El Youssoufi MS, Saix C. 2006. Influence of liquid bridges on the mechanical behaviour of polydisperse granular materials. *International Journal for Numerical and Analytical Methods in Geomechanics* **30**(3):213-228.

156. Balakin BV, Alyaev S, Hoffmann AC, Kosinski P. 2013. Micromechanics of agglomeration forced by the capillary bridge: The restitution of momentum. *AIChE Journal* **59**(11):4045-4057.

157. Fisher R. 1926. On the capillary forces in an ideal soil; correction of formulae given by WB Haines. *The Journal of Agricultural Science* **16**(03):492-505.

158. Goldman A, Cox RG, Brenner H. 1967. Slow viscous motion of a sphere parallel to a plane wall—I Motion through a quiescent fluid. *Chemical Engineering Science* **22**(4):637-651.

159. Mason G, Clark W. 1965. Liquid bridges between spheres. *Chemical Engineering Science* **20**(10):859-866.

160. Halsey TC, Levine AJ. 1998. How sandcastles fall. *Physical Review Letters* **80**(14):3141.

161. Herminghaus S. 2005. Dynamics of wet granular matter. *Advances in Physics* **54**(3):221-261.

162. Hornbaker D, Albert R, Albert I, Barabási A-L, Schiffer P. 1997. What keeps sandcastles standing? *Nature* **387**(6635):765-765.

163. Kudrolli A. 2008. Granular matter: Sticky sand. *Nature materials* **7**(3):174-175.

164. Price R, Young P, Edge S, Staniforth J. 2002. The influence of relative humidity on particulate interactions in carrier-based dry powder inhaler formulations. *International Journal of Pharmaceutics* **246**(1):47-59.

165. Rahmanian N, Ghadiri M, Jia X. 2011. Seeded granulation. *Powder Technology* **206**(1):53-62.

166. Rahmanian N, Ghadiri M, Jia X, Stepanek F. 2009. Characterisation of granule structure and strength made in a high shear granulator. *Powder Technology* **192**(2):184-194.

167. Rahmanian N, Ghadiri M. 2013. Strength and structure of granules produced in continuous granulators. *Powder Technology* **233**:227-233.

168. Holm P, Schaefer T, Larsen C. 2001. End-point detection in a wet granulation process. *Pharmaceutical Development and Technology* **6**(2):181-192.

169. Leuenberger H. 1982. Granulation, new techniques. *Pharmaceutica Acta Helvetiae* **57**(3):72.

170. Gantt JA, Gatzke EP. 2005. High-shear granulation modeling using a discrete element simulation approach. *Powder Technology* **156**(2):195-212.

171. Mishra B, Thornton C, Bhimji D. 2002. A preliminary numerical investigation of agglomeration in a rotary drum. *Minerals Engineering* **15**(1):27-33.

172. Talu I, Tardos GI, Khan MI. 2000. Computer simulation of wet granulation. *Powder Technology* **110**(1):59-75.

173. Lian G, Thornton C, Adams MJ. 1998. Discrete particle simulation of agglomerate impact coalescence. *Chemical Engineering Science* **53**(19):3381-3391.

174. Liu P, Yang R, Yu A. 2013. DEM study of the transverse mixing of wet particles in rotating drums. *Chemical Engineering Science* **86**:99-107.

175. Muguruma Y, Tanaka T, Tsuji Y. 2000. Numerical simulation of particulate flow with liquid bridge between particles (simulation of centrifugal tumbling granulator). *Powder Technology* **109**(1):49-57.

176. Yang R, Zou R, Yu A. 2003. Numerical study of the packing of wet coarse uniform spheres. *AIChE journal* **49**(7):1656-1666.

177. Shi D, McCarthy JJ. 2008. Numerical simulation of liquid transfer between particles. *Powder Technology* **184**(1):64-75.

178. Sahni E, Chaudhuri B. 2011. Experiments and numerical modeling to estimate the coating variability in a pan coater. *International Journal of Pharmaceutics* **418**(2):286-296.

179. Balakin BV, Shamsutdinova G, Kosinski P. 2015. Agglomeration of solid particles by liquid bridge flocculants: Pragmatic modelling. *Chemical Engineering Science* **122**:173-181.

180. Washino K, Tan H, Hounslow M, Salman A. 2013. A new capillary force model implemented in micro-scale CFD–DEM coupling for wet granulation. *Chemical Engineering Science* **93**:197-205.

181. Brackbill J, Kothe DB, Zemach C. 1992. A continuum method for modeling surface tension. *Journal of Computational Physics* **100**(2):335-354.

182. Chouk V, Reynolds G, Hounslow M, Salman A. 2009. Single drop behaviour in a high shear granulator. *Powder Technology* **189**(2):357-364.

183. Reinhold A, Briesen H. 2012. Numerical behavior of a multiscale aggregation model—coupling population balances and discrete element models. *Chemical Engineering Science* **70**:165-175.

184. Harper WR. 1998. Contact and frictional electrification. ed.: Laplacian Press Morgan Hill, CA.

185. Trigwell S, Grable N, Yurteri CU, Sharma R, Mazumder MK. 2003. Effects of surface properties on the tribocharging characteristics of polymer powder as applied to industrial processes. IEEE Transactions on Industry Applications **39**(1):79-86.

186. McCarty LS, Whitesides GM. 2008. Electrostatic charging due to separation of ions at interfaces: contact electrification of ionic electrets. *Angewandte Chemie International Edition* **47**(12):2188-2207.

187. Diaz A. 1998. Contact electrification of materials: The chemistry of ions on polymer surfaces. The *Journal of Adhesion* **67**(1-4):111-122.

188. Law K-Y, Tarnawskyj IW, Salamida D, Debies T. 1995. Investigation of the contact charging mechanism between an organic salt doped polymer surface and polymer-coated metal beads. *Chemistry of Materials* **7**(11):2090-2095.

189. Diaz AF, Guay J. 1993. Contact charging of organic materials: Ion vs. electron transfer. IBM *Journal of Research and Development* **37**(2):249-260.

190. Diaz A, Fenzel-Alexander D. 1993. An ion transfer model for contact charging. *Langmuir* **9**(4):1009-1015.

191. Lowell J. 1977. Surface states and the contact electrification of polymers. *Journal of Physics D: Applied Physics* **10**(1):65.

192. Wang D, Klaassen AA, Janssen GE, de Boer E, Meier RJ. 1995. The detection of radicals in strained, high-modulus polyethylene fibres. *Polymer* **36**(22):4193-4196.

193. Saitta AM, Soper PD, Wasserman E, Klein ML. 1999. Influence of a knot on the strength of a polymer strand. *Nature* **399**(6731):46-48.

194. Kron A, Reitberger T, Stenberg B. 1997. Luminescence from γ-and β-irradiated HDPE and LLDPE. *Polymer International* **42**(2):131-137.

195. Rowley G. 2001. Quantifying electrostatic interactions in pharmaceutical solid systems. *International Journal of Pharmaceutics* **227**(1):47-55.

196. Liu C, Bard AJ. 2008. Electrostatic electrochemistry at insulators. *Nature materials* **7**(6):505-509.

197. Chowdry A, Westgate C. 1974. The role of bulk traps in metal-insulator contact charging. *Journal of Physics D: Applied Physics* **7**(5):713.

198. Duke C, Fabish T. 1978. Contact electrification of polymers: A quantitative model. *Journal of Applied Physics* **49**(1):315-321.

199. Elajnaf A, Carter P, Rowley G. 2006. Electrostatic characterisation of inhaled powders: effect of contact surface and relative humidity. *European Journal of Pharmaceutical Sciences* **29**(5):375-384.

200. Sarkar S, Cho J, Chaudhuri B. 2012. Mechanisms of electrostatic charge reduction of granular media with additives on different surfaces. *Chemical Engineering and Processing: Process Intensification* **62**:168-175.

201. Carter P, Cassidy O, Rowley G, Merrifield D. 1998. Triboelectrification of Fractionated Crystalline and Spray-dried Lactose. *Pharmacy and Pharmacology Communications* **4**(2):111-115.

202. Carter P, Rowley G, Fletcher E, Hill E. 1992. An experimental investigation of triboelectrification in cohesive and non-cohesive pharmaceutical powders. *Drug Development and Industrial Pharmacy* **18**(14):1505-1526.

203. Šupuk E, Seiler C, Ghadiri M. 2009. Analysis of a Simple Test Device for Tribo-Electric Charging of Bulk Powders. *Particle & Particle Systems Characterization* **26**(1-2):7-16.

204. Lowell J, Rose-Innes A. 1980. *Contact electrification. Advances in Physics* **29**(6):947-1023.

205. Gallo C, Lama W. 1976. Some charge exchange phenomena explained by a classical model of the work function. *Journal of Electrostatics* **2**(2):145-150.

206. Davies D. 1969. Charge generation on dielectric surfaces. *Journal of Physics D: Applied Physics* **2**(11):1533.

207. Lowell J. 1976. The electrification of polymers by metals. *Journal of Physics D: Applied Physics* **9**(11):1571.

208. Diaz A, Felix-Navarro R. 2004. A semi-quantitative tribo-electric series for polymeric materials: the influence of chemical structure and properties. *Journal of Electrostatics* **62**(4):277-290.

209. Staniforth J, Rees JE. 1981. Powder mixing by triboelectrification. *Powder Technology* **30**(2):255-256.

210. Byron PR, Peart J, Staniforth JN. 1997. Aerosol electrostatics I: properties of fine powders before and after aerosolization by dry powder inhalers. *Pharmaceutical Research* **14**(6):698-705.

211. Telko MJ, Kujanpää J, Hickey AJ. 2007. Investigation of triboelectric charging in dry powder inhalers using electrical low pressure impactor (ELPI™). *International Journal of Pharmaceutics* **336**(2):352-360.

212. Creux P, Lachaise J, Graciaa A, Beattie JK, Djerdjev AM. 2009. Strong specific hydroxide ion binding at the pristine oil/water and air/water interfaces. *The Journal of Physical Chemistry B* **113**(43):14146-14150.

213. Zangi R, Engberts JB. 2005. Physisorption of hydroxide ions from aqueous solution to a hydrophobic surface. *Journal of the American Chemical Society* **127**(7):2272-2276.

214. Bagus PS, Käfer D, Witte G, Wöll C. 2008. Work Function Changes Induced by Charged Adsorbates: Origin of the Polarity Asymmetry. *Physical Review Letters* **100**(12):126101.

215. Karner S, Urbanetz NA. 2011. The impact of electrostatic charge in pharmaceutical powders with specific focus on inhalation-powders. *Journal of Aerosol Science* **42**(6):428-445.

216. Matsusaka S, Maruyama H, Matsuyama T, Ghadiri M 2010. Triboelectric charging of powders: A review. *Chemical Engineering Science* **65**(22):5781-5807.

217. Matsusaka S, Masuda H. 2003. Electrostatics of particles. *Advanced Powder Technology* **14**(2):143-166.

218. Wong J, Kwok PCL, Chan H-K. 2015. Electrostatics in pharmaceutical solids. *Chemical Engineering Science* **125**:225-237.

219. Ireland PM 2010. Triboelectrification of particulate flows on surfaces: Part I—Experiments. *Powder Technology* **198**(2):189-198.

220. Kwek J, Heng D, Lee S, Ng W, Chan H-K, Adi S, Heng J, Tan RB. 2013. High speed imaging with electrostatic charge monitoring to track powder deagglomeration upon impact. *Journal of Aerosol Science* **65**:77-87.

221. Šupuk E, Zarrebini A, Reddy JP, Hughes H, Leane MM, Tobyn MJ, Timmins P, Ghadiri M. 2012. Tribo-electrification of active pharmaceutical ingredients and excipients. *Powder Technology* **217**:427-434.

222. Rowley G, Mackin L. 2003. The effect of moisture sorption on electrostatic charging of selected pharmaceutical excipient powders. *Powder Technology* **135**:50-58.

223. Kwok PCL, Noakes T, Chan H-K. 2008. Effect of moisture on the electrostatic charge properties of metered dose inhaler aerosols. *Journal of Aerosol Science* **39**(3):211-226.

224. Zhu K, Tan RB, Ng WK, Shen S, Zhou Q, Heng PW. 2008. Analysis of the influence of relative humidity on the moisture sorption of particles and the aerosolization process in a dry powder inhaler. *Journal of Aerosol Science* **39**(6):510-524.

225. Kuo I-FW, Mundy CJ. 2004. An ab initio molecular dynamics study of the aqueous liquid-vapor interface. *Science* **303**(5658):658-660.

226. Murtomaa M, Savolainen M, Christiansen L, Rantanen J, Laine E, Yliruusi J. 2004. Static electrification of powders during spray drying. *Journal of Electrostatics* **62**(1):63-72.

227. Matsusaka S, Ghadiri M, Masuda H. 2000. Electrification of an elastic sphere by repeated impacts on a metal plate. *Journal of Physics D: Applied Physics* **33**(18):2311.

228. Watanabe H, Ghadiri M, Matsuyama T, Ding YL, Pitt KG, Maruyama H, Matsusaka S, Masuda H 2007. Triboelectrification of pharmaceutical powders by particle impact. *International Pournal of Pharmaceutics* **334**(1):149-155.

229. Zhu H, Ramprasad R. 2011. Effective work function of metals interfaced with dielectrics: A first-principles study of the Pt-HfO 2 interface. *Physical Review B* **83**(8):081416.

230. Naik S, Sarkar S, Gupta V, Hancock BC, Abramov Y, Yu W, Chaudhuri B. 2015. A combined experimental and numerical approach to explore tribocharging of pharmaceutical excipients in a hopper chute assembly. *International journal of Pharmaceutics* **491**(1):58-68.

231. Saini D, Trigwell S, Srirama P, Sims R, Sharma R, Biris A, Mazumder M. 2008. Portable free-fall electrostatic separator for beneficiation of charged particulate materials. *Particulate Science and Technology* **26**(4):349-360.

232. Šupuk E, Hassanpour A, Ahmadian H, Ghadiri M, Matsuyama T. 2011. Tribo-electrification and associated segregation of pharmaceutical bulk powders. *KONA Powder and Particle Journal* **29**(0):208-223.

233. Pingali KC, Shinbrot T, Hammond SV, Muzzio FJ. 2009. An observed correlation between flow and electrical properties of pharmaceutical blends. *Powder Technology* **192**(2):157-165.

234. Noakes T. 2004. Electrostatics: the next issue for inhaled medications. Drug Deliv Technol 4:1-5.

235. Bailey A. 1993. Charging of solids and powders. *Journal of Electrostatics* **30**:167-180.

236. Hearn G. 1998. Static electricity: concern in the pharmaceutical industry? *Pharmaceutical Science & Technology Today* **1**(7):286-287.

237. Pingali KC, Hammond SV, Muzzio FJ, Shinbrot T. 2009. Use of a static eliminator to improve powder flow. *International Journal of Pharmaceutics* **369**(1):2-4.

238. Orband JL, Geldart D. 1995. The use of an antistatic agent to improve powder flowability. *Particle & particle systems characterization* **12**(4):204-206.

239. Wirth KE, Linsenbühler M. 2004. Electrostatically supported mixing of fine grained particles. *Chemical Engineering & Technology* **27**(7):729-732.

240. Luo Y, Zhu J, Ma Y, Zhang H. 2008. Dry coating, a novel coating technology for solid pharmaceutical dosage forms. *International Journal of Pharmaceutics* **358**(1):16-22.

241. Al-Adel MF, Saville DA, Sundaresan S. 2002. The effect of static electrification on gas-solid flows in vertical risers. *Industrial & Engineering Chemistry Research* **41**(25):6224-6234.

242. Böttner C-U, Sommerfeld M. 2002. Numerical calculation of electrostatic powder painting using the Euler/Lagrange approach. *Powder technology* **125**(2):206-216.

243. Klinzing G. 1986. Clustering under the influence of electrostatic forces. *International Journal of Multiphase Flow* **12**(5):853-857.

244. Duff N, Lacks DJ. 2008. Particle dynamics simulations of triboelectric charging in granular insulator systems. *Journal of Electrostatics* **66**(1):51-57.

245. Watano S. 2006. Mechanism and control of electrification in pneumatic conveying of powders. *Chemical Engineering Science* **61**(7):2271-2278.

246. Watano S, Saito S, Suzuki T. 2003. Numerical simulation of electrostatic charge in powder pneumatic conveying process. *Powder Technology* **135**:112-117.

247. Korevaar M, Padding J, Van der Hoef M, Kuipers J. 2014. Integrated DEM–CFD modeling of the contact charging of pneumatically conveyed powders. *Powder Technology* **258**:144-156.

248. Hogue MD, Calle CI, Weitzman PS, Curry DR. 2008. Calculating the trajectories of triboelectrically charged particles using Discrete Element Modeling (DEM). *Journal of Electrostatics* **66**(1):32-38.

249. Pei C, Wu C-Y, England D, Byard S, Berchtold H, Adams M. 2013. Numerical analysis of contact electrification using DEM–CFD. *Powder Technology* **248**:34-43.

250. Ristow GH. 1997. Outflow rate and wall stress for two-dimensional hoppers. *Physica A: Statistical Mechanics and its Applications* **235**(3):319-326.

251. Langston P, Tüzün U, Heyes D. 1994. Continuous potential discrete particle simulations of stress and velocity fields in hoppers: transition from fluid to granular flow. *Chemical Engineering Science* **49**(8):1259-1275.

252. Langston P, Tüzün U, Heyes D. 1995. Discrete element simulation of granular flow in 2D and 3D hoppers: dependence of discharge rate and wall stress on particle interactions. *Chemical Engineering Science* **50**(6):967-987.

253. Ketterhagen WR, Curtis JS, Wassgren CR, Hancock BC. 2008. Modeling granular segregation in flow from quasi-three-dimensional, wedge-shaped hoppers. *Powder Technology* **179**(3):126-143.

254. Ketterhagen WR, Curtis JS, Wassgren CR, Kong A, Narayan PJ, Hancock BC. 2007. Granular segregation in discharging cylindrical hoppers: a discrete element and experimental study. *Chemical Engineering Science* **62**(22):6423-6439.

255. Masson S, Martinez J. 2000. Effect of particle mechanical properties on silo flow and stresses from distinct element simulations. *Powder Technology* **109**(1):164-178.

256. Hirshfeld D, Rapaport D. 2001. Granular flow from a silo: discrete-particle simulations in three dimensions. *The European Physical Journal E* **4**(2):193-199.

257. Langston P, Tüzün U, Heyes D. 1995. Discrete element simulation of internal stress and flow fields in funnel flow hoppers. *Powder Technology* **85**(2):153-169.

258. Zhu H, Yu A. 2005. Micromechanic modeling and analysis of unsteady-state granular flow in a cylindrical hopper.*Journal of Engineering Mathematics* **52 :** 307-320

259. Cleary PW, Sawley ML. 2002. DEM modelling of industrial granular flows: 3D case studies and the effect of particle shape on hopper discharge. *Applied Mathematical Modelling* **26**(2):89-111.

260. Hidalgo RC, Zuriguel I, Maza D, Pagonabarraga I. 2009. Role of particle shape on the stress propagation in granular packings. *Physical review letters* **103**(11):118001.

261. Hidalgo RC, Zuriguel I, Maza D, Pagonabarraga I. 2010. Granular packings of elongated faceted particles deposited under gravity. *Journal of Statistical Mechanics: Theory and Experiment* **2010**(06):P06025.

262. Mack S, Langston P, Webb C, York T. 2011. Experimental validation of polyhedral discrete element model. *Powder Technology* **214**(3):431-442.

263. Li J, Langston PA, Webb C, Dyakowski T. 2004. Flow of sphero-disc particles in rectangular hoppers—a DEM and experimental comparison in 3D. *Chemical Engineering Science* **59**(24):5917-5929.

264. Favier J, Abbaspour-Fard M, Kremmer M. 2001. Modeling nonspherical particles using multisphere discrete elements. *Journal of Engineering Mechanics* **127**(10):971-977.

265. Moakher M, Shinbrot T, Muzzio FJ. 2000. Experimentally validated computations of flow, mixing and segregation of non-cohesive grains in 3D tumbling blenders. *Powder Technology* **109**(1):58-71.

266. Manickam S, Shah R, Tomei J, Bergman T, Chaudhuri B. 2010. Investigating mixing in a multi-dimensional rotary mixer: Experiments and simulations. *Powder Technology* **201**(1):83-92.

267. Lemieux M, Bertrand F, Chaouki J, Gosselin P. 2007. Comparative study of the mixing of free-flowing particles in a V-blender and a bin-blender. *Chemical Engineering Science* **62**(6):1783-1802.

268. Lemieux M, Léonard G, Doucet J, Leclaire L-A, Viens F, Chaouki J, Bertrand F. 2008. Large-scale numerical investigation of solids mixing in a V-blender using the discrete element method. *Powder Technology* **181**(2):205-216.

269. Yamane K. 2004. Discrete-element method application to mixing and segregation model in industrial blending system. *Journal of Materials Research* **19**(02):623-627.

270. Terashita K, Nishimura T, Natsuyama S. 2002. Optimization of operating conditions in a high-shear mixer using dem model: determination of optimal fill level. *Chemical and Pharmaceutical Bulletin* **50**(12):1550-1557.

271. Terashita K, Nishimura T, Natsuyama S, Satoh M. 2002. DEM Simulation of Mixing and Segregation in High-Shear Mixer. *Journal of the Japan Society of Powder and Powder Metallurgy* **49**(7):638-645.

272. Kuo H, Knight P, Parker D, Adams M, Seville J. 2004. Discrete element simulations of a high-shear mixer. *Advanced Powder Technology* **15**(3):297-309.

273. Nakamura H, Fujii H, Watano S. 2013. Scale-up of high shear mixer-granulator based on discrete element analysis. *Powder Technology* **236**:149-156.

274. Chan EL, Washino K, Ahmadian H, Bayly A, Alam Z, Hounslow MJ, Salman AD. 2015. Dem investigation of horizontal high shear mixer flow behaviour and implications for scale-up. *Powder Technology* **270**:561-568.

275. Kaneko Y, Shiojima T, Horio M. 2000. Numerical analysis of particle mixing characteristics in a single helical ribbon agitator using DEM simulation. *Powder Technology* **108**(1):55-64.

276. Muzzio FJ, Llusa M, Goodridge CL, Duong N-H, Shen E. 2008. Evaluating the mixing performance of a ribbon blender. *Powder Technology* **186**(3):247-254.

277. Cleary PW. 2013. Particulate mixing in a plough share mixer using DEM with realistic shaped particles. *Powder Technology* **248**:103-120.

278. Alian M, Ein-Mozaffari F, Upreti SR. 2015. Analysis of the mixing of solid particles in a plowshare mixer via discrete element method (DEM). *Powder Technology* **274**:77-87.

279. Feng Y, Yu A. 2007. Microdynamic modelling and analysis of the mixing and segregation of binary mixtures of particles in gas fluidization. *Chemical Engineering Science* **62**(1):256-268.

280. Cleary PW. 2002. Metcalfe G. 2002.Quantitative comparison of mixing rates between DEM and experiment in a slowly rotating cylinder.Proceedings of the 4th World Congress Particle Technology,Sydney,Australia

281. Pereira G, Tran N, Cleary P. 2014. Segregation of combined size and density varying binary granular mixtures in a slowly rotating tumbler. *Granular Matter* **16**(5):711-732.

282. Wachs A, Girolami L, Vinay G, Ferrer G. 2012. Grains3D, a flexible DEM approach for particles of arbitrary convex shape—Part I: Numerical model and validations. *Powder Technology* **224**:374-389.

283. Mishra B, Rajamani RK. 1992. The discrete element method for the simulation of ball mills. *Applied Mathematical Modelling* **16**(11):598-604.

284. Mishra B, Rajamani RK. 1994. Simulation of charge motion in ball mills. Part 1: experimental verifications. *International Journal of Mineral Processing* **40**(3):171-186.

285. Concas A, Lai N, Pisu M, Cao G. 2006. Modelling of comminution processes in Spex Mixer/Mill. *Chemical Engineering Science* **61**(11):3746-3760.

286. Capece M, Bilgili E, Davé RN. 2014. Formulation of a physically motivated specific breakage rate parameter for ball milling via the discrete element method. *AIChE Journal* **60**(7):2404-2415.

287. Ning Z, Boerefijn R, Ghadiri M, Thornton C. 1997. Distinct element simulation of impact breakage of lactose agglomerates. *Advanced Powder Technology* **8**(1):15-37.

288. Naik S, Malla R, Shaw M, Chaudhuri B. 2013. Investigation of comminution in a Wiley Mill: Experiments and DEM Simulations. *Powder Technology* **237**:338-354.

289. Jayasundara C, Yang R, Yu A, Curry D. 2006. Discrete particle simulation of particle flow in the IsaMill process. *Industrial & Engineering Chemistry Research* **45**(18):6349-6359.

290. Cleary P, Sinnott M, Morrison R. 2008. DEM prediction of particle flows in grinding processes. *International Journal for Numerical Methods in Fluids* **58**(3):319-353.

291. da Cunha ER, de Carvalho RM, Tavares LM. 2013. Simulation of solids flow and energy transfer in a vertical shaft impact crusher using DEM. *Minerals Engineering* **43**:85-90.

292. Morrison RD, Cleary PW, Sinnott MD. 2009. Using DEM to compare the energy efficiency of pilot scale ball and tower mills. *Minerals Engineering* **22**(7):665-672.

293. Li J, Mason D. 2000. A computational investigation of transient heat transfer in pneumatic transport of granular particles. *Powder Technology* **112**(3):273-282.

294. Li J, Campbell GM, Mujumdar A. 2003. Discrete modeling and suggested measurement of heat transfer in gas–solids flows. *Drying technology* **21**(6):979-994.

295. Li J, Mason DJ, Mujumdar AS. 2003. A numerical study of heat transfer mechanisms in gas–solids flows through pipes using a coupled CFD and DEM model. *Drying Technology* **21**(9):1839-1866.

296. Sahni E, Hallisey J, Morgan B, Strong J, Chaudhuri B. 2012. Quantifying drying performance of a filter dryer: Experiments and simulations. *Advanced Powder Technology* **23**(2):239-249.

297. Sahni EK, Chaudhuri B. 2013. Numerical simulations of contact drying in agitated filter-dryer. *Chemical Engineering Science* **97**:34-49.

298. Chaudhuri B, Muzzio FJ, Tomassone MS. 2010. Experimentally validated computations of heat transfer in granular materials in rotary calciners. *Powder Technology* **198**(1):6-15.

299. Vargas WL, McCarthy J. 2002. Conductivity of granular media with stagnant interstitial fluids via thermal particle dynamics simulation. *International Journal of Heat and Mass Transfer* **45**(24):4847-4856.

300. Vargas WL, McCarthy J. 2001. Heat conduction in granular materials. *AIChE Journal* **47**(5):1052-1059.

301. Vargas WL, McCarthy J. 2002. Stress effects on the conductivity of particulate beds. *Chemical Engineering Science* **57**(15):3119-3131.

302. Yamane K, Sato T, Tanaka T, Tsuji Y. 1995. Computer simulation of tablet motion in coating drum. *Pharmaceutical Research* **12**(9):1264-1268.

303. Kalbag A, Wassgren C, Penumetcha SS, Pérez-Ramos JD. 2008. Inter-tablet coating variability: residence times in a horizontal pan coater. *Chemical Engineering Science* **63**(11):2881-2894.

304. Ketterhagen WR. 2011. Modeling the motion and orientation of various pharmaceutical tablet shapes in a film coating pan using DEM. *International journal of pharmaceutics* **409**(1):137-149.

305. Nakamura H, Iwasaki T, Watano S. 2006. Numerical simulation of film coating process in a novel rotating fluidized bed. *Chemical and Pharmaceutical Bulletin* **54**(6):839-846.

306. Freireich B, Ketterhagen WR, Wassgren C. 2011. Intra-tablet coating variability for several pharmaceutical tablet shapes. *Chemical Engineering Science* **66**(12):2535-2544.

307. Goldschmidt MJV, Weijers GGC, Boerefijn R, Kuipers JAM. 2003. Discrete element modelling of fluidised bed spray granulation. *Powder Technology* **138**(1):39-45.

308. Wu C-Y, Cocks AC. 2006. Numerical and experimental investigations of the flow of powder into a confined space. *Mechanics of Materials* **38**(4):304-324.

309. Siiriä S, Yliruusi J. 2007. Particle packing simulations based on Newtonian mechanics. *Powder Technology* **174**(3):82-92.

310. Mehrotra A, Chaudhuri B, Faqih A, Tomassone M, Muzzio F. 2009. A modeling approach for understanding effects of powder flow properties on tablet weight variability. *Powder Technology* **188**(3):295-300.

311. Nwose EN, Pei C, Wu C-Y. 2012. Modelling die filling with charged particles using DEM/CFD. *Particuology* **10**(2):229-235.

312. Harthong B, Jérier J-F, Dorémus P, Imbault D, Donzé F-V. 2009. Modeling of high-density compaction of granular materials by the discrete element method. *International Journal of Solids and Structures* **46**(18):3357-3364.

313. Couroyer C, Ning Z, Ghadiri M. 2000. Distinct element analysis of bulk crushing: effect of particle properties and loading rate. *Powder Technology* **109**(1):241-254.

314. Ezaoui A, Lecompte T, Di Benedetto H, Garcia E. 2011. Effects of various loading stress paths on the stress-strain properties and on crushability of an industrial soft granular material. *Granular Matter* **13**(4):283-301.

315. Martin C. 2003. Unloading of powder compacts and their resulting tensile strength. *Acta Materialia* **51**(15):4589-4602.

316. Shoaib M, Kari L, Azhdar B. 2012. Simulation of high-velocity compaction process with relaxation assists using the discrete element method. *Powder Technology* **217**:394-400.

317. Sweeney S, Martin C. 2003. Pore size distributions calculated from 3-D images of DEM-simulated powder compacts. *Acta Materialia* **51**(12):3635-3649.

318. Millikan RA. 1923. The general law of fall of a small spherical body through a gas, and its bearing upon the nature of molecular reflection from surfaces. *Physical Review* **22**(1):1.

319. Putnam A. 1961. Integrable form of droplet drag coefficient. *American Rocket Society Journal* **31**:1467-1468.

320. Clift R, Gauvin WH.1970. The motion of particles in turbulent gas streams.*Proc. Chemeca*,**1**:14

321. Chien SF. 1994. Settling velocity of irregularly shaped particles. *SPE Drilling & Completion* **9**(04):281-289.

322. Willett CD, Adams MJ, Johnson SA, Seville JP. 2000. Capillary bridges between two spherical bodies. *Langmuir* **16**(24):9396-9405.

List of Tables

Unit Operation	Study Focus	Reference Number
Hopper flow	Discharge rate	250-252
	Segregation	253-254,137
	Stress Distribution	255-258
	Effect of shape	259-264
Mixing	Blender Type	Double Cone blender : 265-266 V Blender:267,268 Drum blender :269 High Shear Mixer : 270-274 Ribbon blender : 275,276 Tote blender :139 Ploughshare :277,278 Fluidized beds: 279
	Effect of shape	280-282
Milling	Ball charge motion	283,284
	Breakage Rate	285,286
	Feed rate & speed	287,288
	Flow structure	289,290
	Energy Consumption	291,292
Drying	Dryer Type	Air (Pneumatic) Dryer : 293-295 Filter Dryer : 296,297

		Drum : 298
	Interstitial Fluid	299
	Stress Chains	300,301
Film Coating	Coater Type	Drum: 302 Pan Coater : 297,303,304 Fluidized Bed : 305
	Effect of shape	306
Granulation	Granulator Type	Drum: 171-72 Tumbling : 175 Fluidized Bed: 307
Compression	Die filling	308-311
	Compaction	312
	Loading Rate	313,314
	Relaxation/unloading	315,316
	Rearrangement	315
	Pore size Distribution	317

Table 1: Some common pharmaceutical processes investigated using Discrete Element Modeling

Drag Coefficient	Comments
Effect of Reynolds Number(Re)	
$\frac{24}{Re}$	Re << 1, Stokes Flow
$\frac{24}{Re} * \frac{1}{C_c}$ Where, $C_c = 1 + 2.52\lambda/d$	C_c is the Cunnigham's correction factor and corrects for particle diameter approaching the mean free of molecules in the fluid
$\frac{24}{Re}(\frac{1}{1+\ Kn[2.49 + 0.84e^{-1.74/Kn}]})$	0.6 < Ma <1 ,*Kn* represents the Knudsen number Ref : 318
$\frac{24}{Re}(\frac{1+\frac{2}{3}\mu_b}{1+\mu_b})$	Applicable for droplets with viscosity μ_b in which shear stress on particle induces internal motion
$\frac{24}{Re}(1 + 0.15Re^{0.687})$	Re < 800,<5% deviation from standard drag curve
$\frac{24}{Re}(1 + \frac{Re^{2/3}}{6})$ } ; Re <1000 $\frac{24}{Re} * 0.0183$; 1000 $\leq$ Re < 3 $\times 10^5$	Discontinuous at Re =1000 Ref : 319
$\frac{24}{Re}((1 + Re^{0.687} + 0.0175(1 + 4.25 \times 10^4\ Re^{-1.16})^{-1})$	Re< Re_{cr} , Experimental validity demonstrated within $\pm$6% over the entire subcritical Re number Ref : 320
Effect of Turbulence	
$3990Re^{-6.10} - 4.47\ \times 10^5 Ir^{-0.97} Re^{-1.8}$	Re_M < Re < 3 X 10^4 , Ir>0.7[76]

$\frac{24}{Re} * \frac{1}{\beta}$ Where, $\beta = 3.7 - 0.65\exp[\frac{1.5-logRe)^2}{2}]$	Where α is the volume fraction of fluid Ref : 67
Effect of shape	
$\frac{24}{Re}[1 + exp(2.3288 - 6.4581\emptyset + 2.4486\emptyset^2)]Re^{(0.0964+0.5565\emptyset)} + \frac{73.69Re\ exp(-5.0748\emptyset)}{Re + 5.378\exp(6.2122\emptyset)}$	<7% deviation from experimental data for spheres and isometric particles; poor for cuboids & cylinders, disks and plates esp at high Re Ref : 79
$\frac{24}{ReK_1K_2}[1 + 0.1118(ReK_1K_2)^{0.65657}] + \frac{0.4305}{1 + \frac{3305}{ReK_1K_2}}$	K_1 and K_2 are shape factors in Stokes and Newton flow regimes. Performs similarly to the earlier correlation above, slightly worse for spheres but better for cuboids, cylinders, disks and plates Ref : 78
$\frac{30}{Re}$ + 67.289exp(-5.03$\emptyset$)	0.2<$\emptyset < 1$, Re <1000, poor for cylinders even for low aspect ratios,simple to implement Ref : 321
$\frac{8}{Re}\frac{1}{\sqrt{\emptyset_\parallel}} + \frac{16}{Re}\frac{1}{\sqrt{\emptyset}} + \frac{3}{\sqrt{Re}}\frac{1}{\emptyset^{\frac{3}{4}}} + 0.4210^{0.4(-\log\emptyset)^{0.2}}\frac{1}{\emptyset_\perp}$ Where, $\emptyset_\parallel = {A_{vs}}/{A_{pp}}$ $\emptyset_\perp = {A_{vs}}/{0.5A - A_{pp}}$	$\emptyset_\parallel$ and $\emptyset_\perp$represent lengthwise and crosswise sphericities respectively, where A_{vs} is the area of a volume equivalent sphere. Considers particle orientation and performs much better for cuboids & cylinders, disks and plates Ref: 80

Table 2: Modification of particle drag as a function of various factors

Numerical formalism of Capillary Force	Reference	Analytical solution
$F = \pi \Delta P_{cap} {r_2}^2 + 2\pi r_2 \gamma_{LV}$ Where, $\Delta P_{cap} = \gamma_{LV}\left(\frac{1}{r_1} - \frac{1}{r_2}\right)$	157	Gorge method, surface tension and capillary pressure are evaluated at the mid-point of the bridge
$F_{cap} = \pi \Delta P r^2 sin^2 \emptyset + 2\pi \operatorname{asin}(\emptyset) + \sin(\theta + \emptyset)$	279	Boundary method, Capillary force and surface tension are evaluated at the contact line with one of the spheres
$F_{cap} = 2\pi\gamma\rho_2(1 + H\rho_2)$ Where, $H = \frac{\rho_2 - \rho_1}{2\rho_1\rho_2}$ $\rho_1 = \frac{S_i + r_i(1 - cos\varphi_i)}{\cos(\varphi_i + \theta)}$ $\rho_2 = r_i \sin\varphi_i - \rho_1(1 - \sin(\varphi_i + \theta)$	150	
$F_{cap} = \frac{2\pi r \gamma_{LV} cos\theta}{1 + \frac{x}{2S_c}} - 2\pi r sin\alpha \sin(\theta + \alpha)$ $S_c = \frac{x}{2}(-1 + \sqrt{1 + V_{lb}/(\pi r x^2)})$	153	
$F_{cap} = \frac{2\pi r cos\theta}{1 + 10\left(\frac{h^2 r}{V_{lb}}\right) + 2.1(\frac{h^2 r}{V_{lb}})^{\frac{1}{2}}}$	322	Empirical Equation,

		applicable when $\frac{V_{lb}}{a^3} <$ 0.001
$F_{cap} = \pi\sqrt{r_1 r_2}\gamma_{LV}[\exp\left(\frac{Ah}{R_2} + B\right) + C]$ $A = -1.1(\frac{V}{{R_2}^3})^{0.53}$ $B = (-0.148ln(\frac{V}{{R_2}^3})^{0.53}\beta^2 - 0.0082ln(\frac{V}{{R_2}^3})^{0.53}$ $+ 0.48$ $C = 0.0018ln(\frac{V}{{R_2}^3})^{0.53} + 0.078$	155	

Table 3: Table showing different capillary force models used in numerical studies

List of Figures

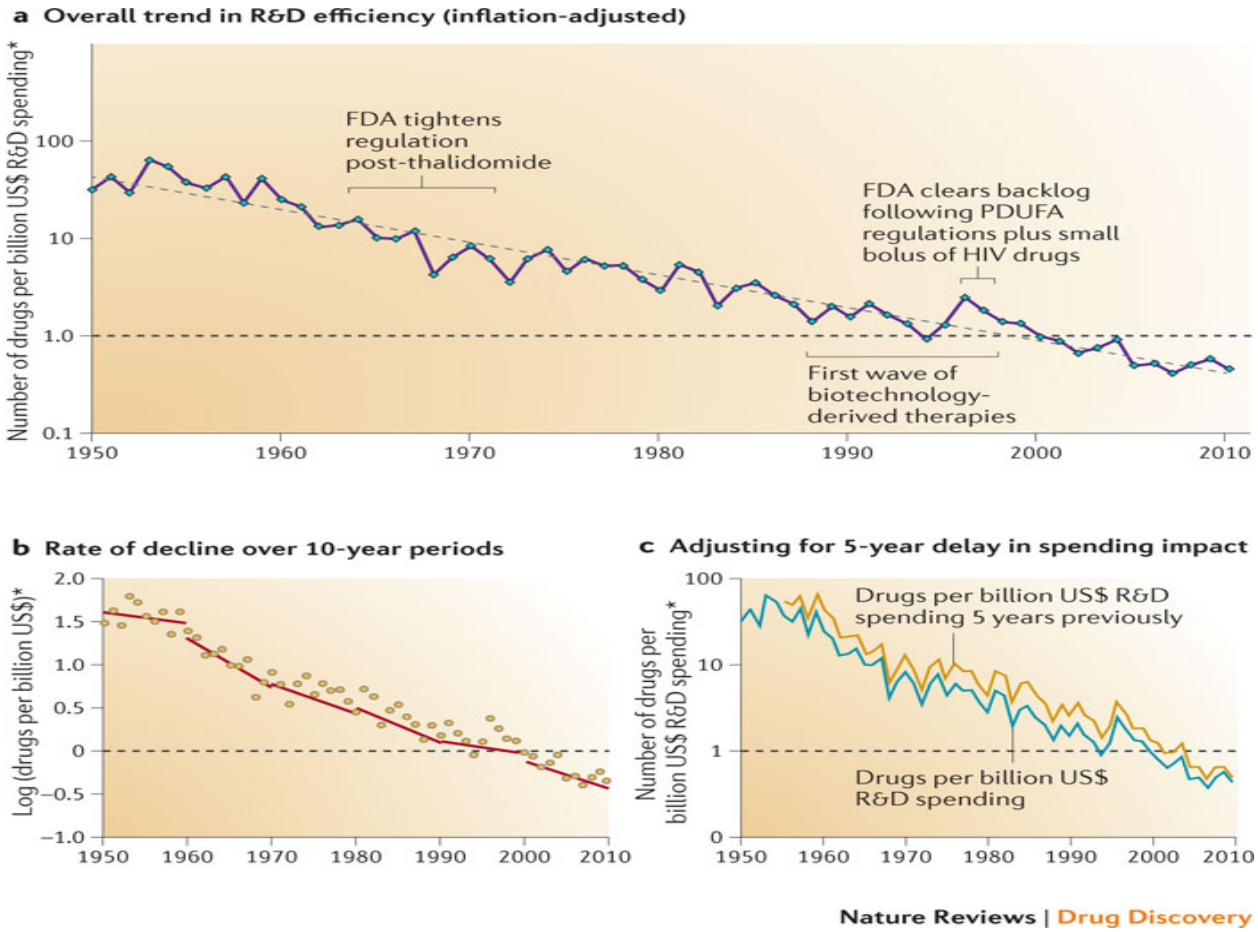

Figure 1. Declining productivity of the pharmaceutical industry (Scannell et al.[3])

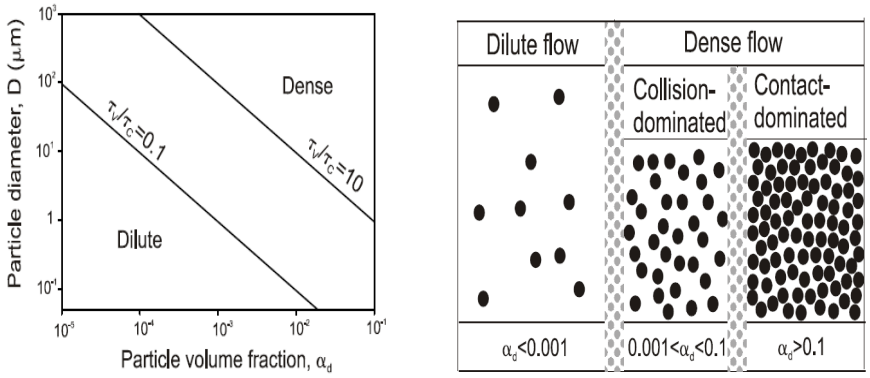

Figure 2. Multiphase flow regimes depending upon the volume fraction of the dispersed phase (Crowe et al.[11])

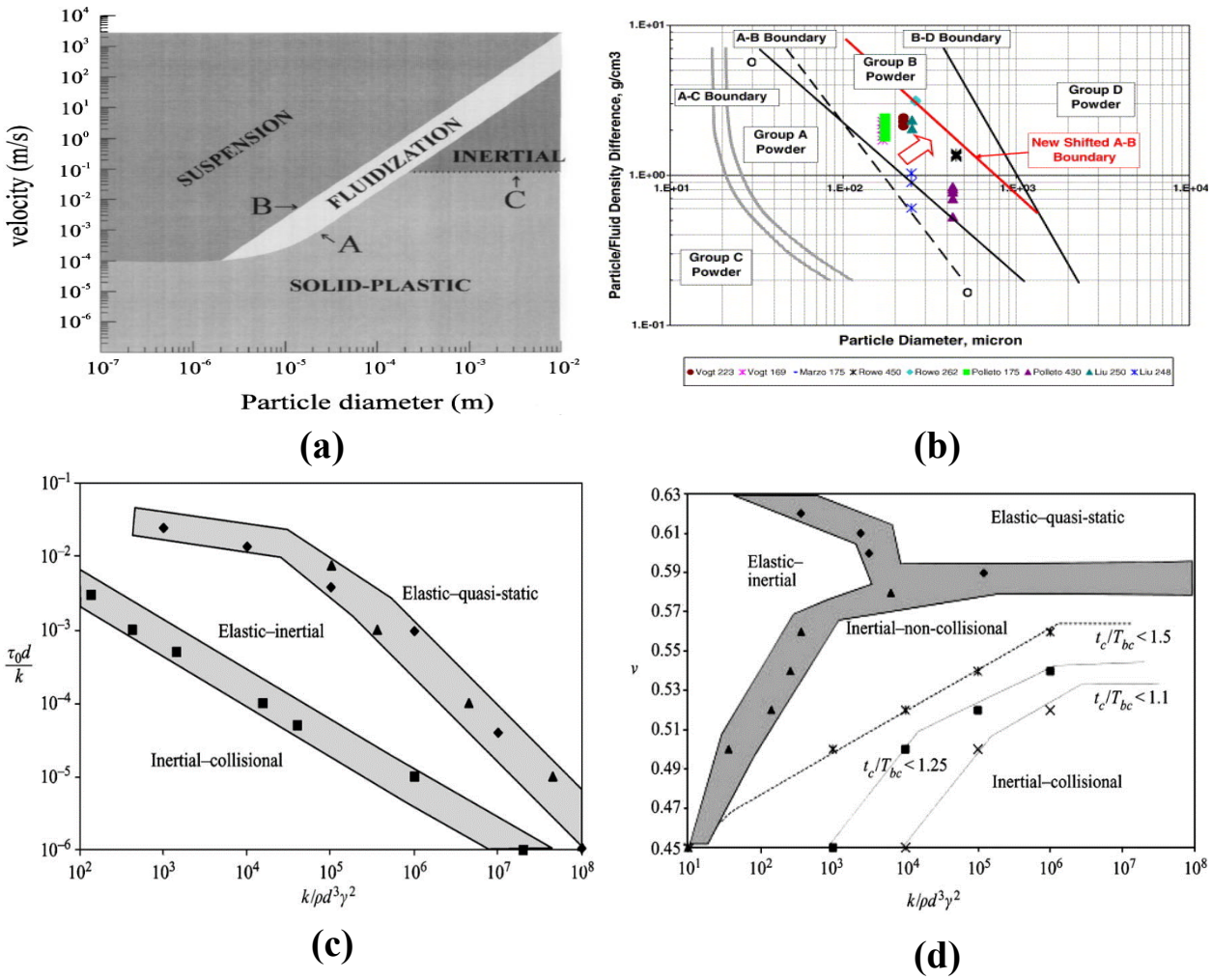

Figure 3. Powder flow regimes: (a) Phase diagram determining transitioning of cohesive powder between different flow regimes as a function of particle diameter (Castellanos et al[16]) and (b) Original and modified Geldart's powder classification based on fluidization behavior (Yang[15]) (c) A flow map of controlled stress granular flows with constant coefficient of restitution and friction (Campbell[17]) and (d) granular flow maps as a function of granular concentration (Campbell[17])

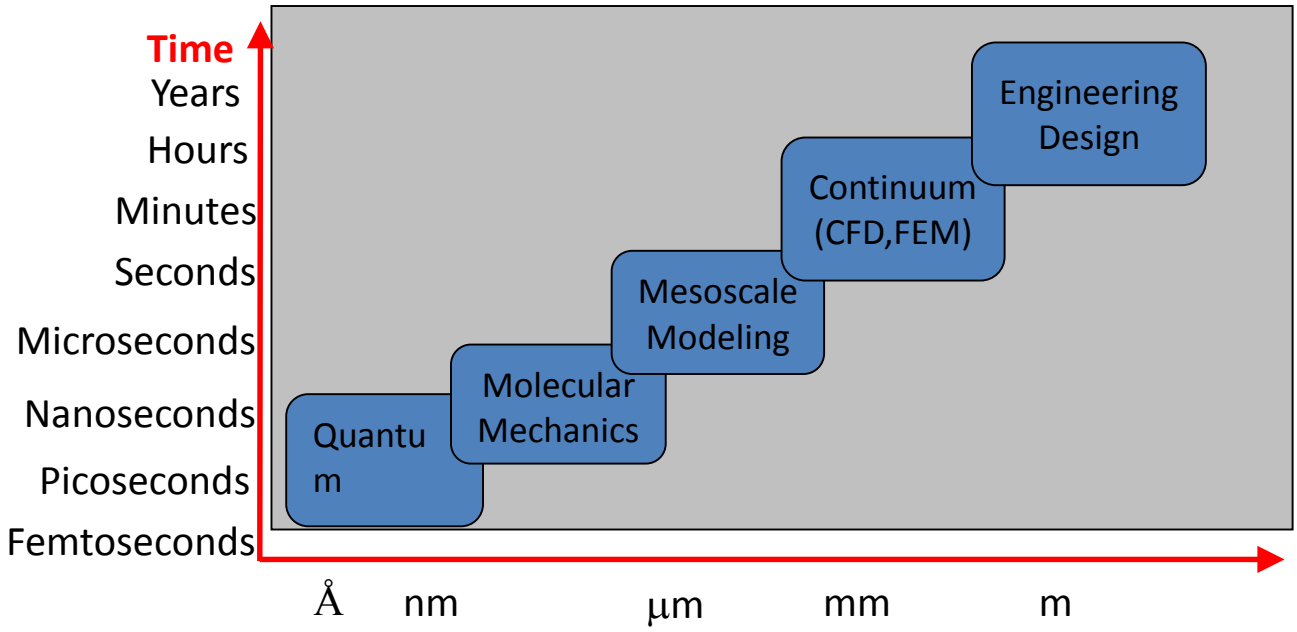

Figure 4. Computational Material Sciences at different length and time scales

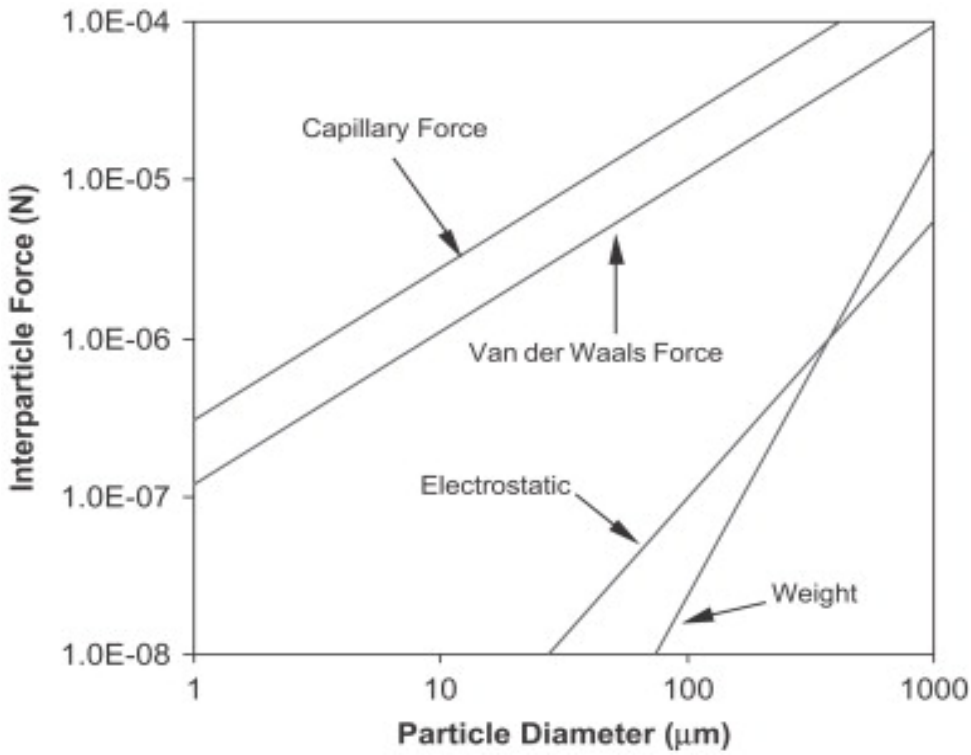

Figure 5. Importance of interparticulate forces as a function of particle diameter (Zhu et al.[42])

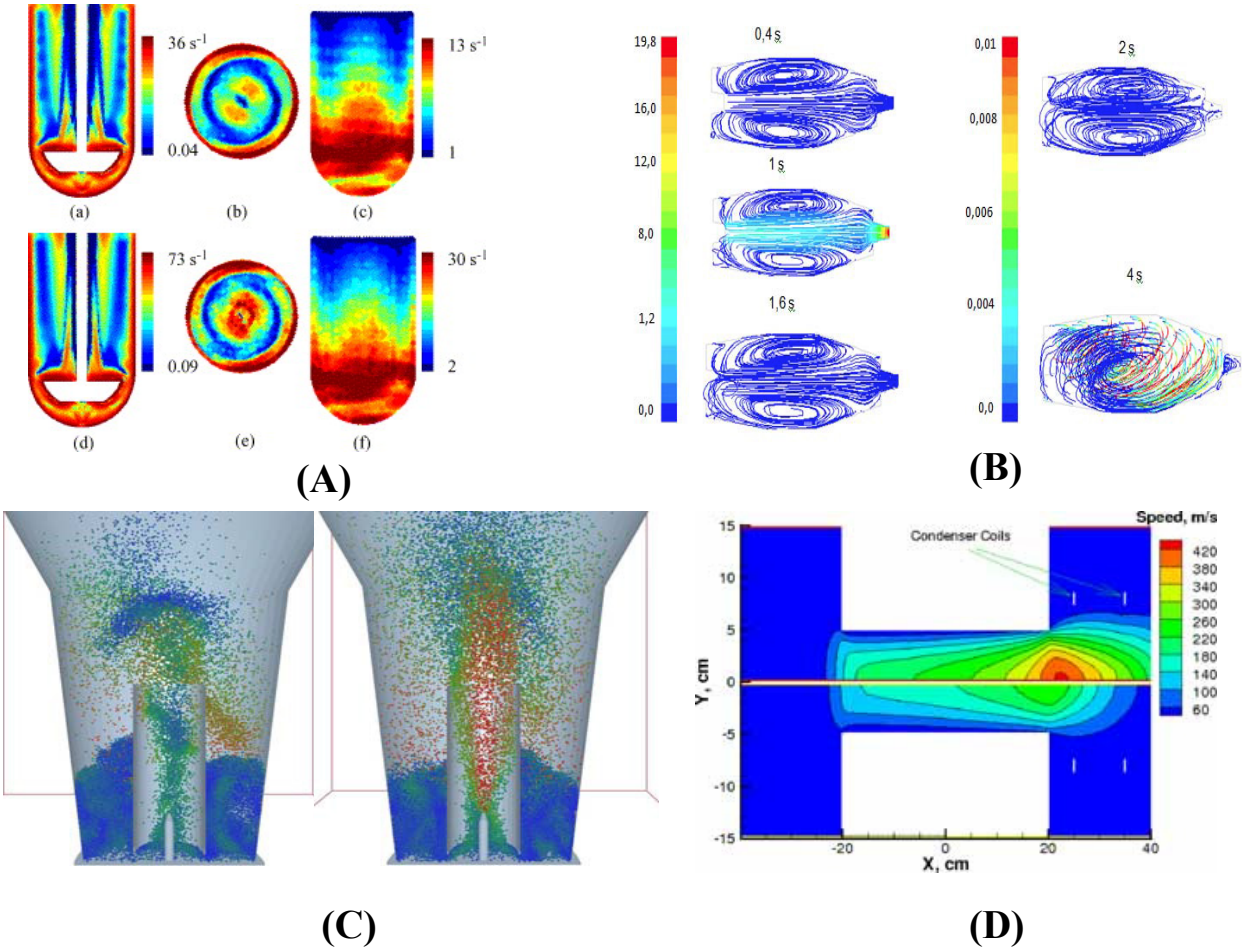

Figure 6.Some applications of CFD in pharmaceutical systems. (a) Modeling strain rate variability in USP Type 2 apparatus at different Reynolds numbers (Baxter et al.[93]) (b) Air flow patterns in Volumatic™ spacer (Oliveira et al.[103]) (c) Fluidized bed granulation in a Wurster tube with increasing spout velocity (Fries et al.[113]) (d) Flow speed in a lab scale dryer for two different chamber pressures: 50 mTorr (top) and 30 mTorr (bottom) (Alexeenko et al.[114])

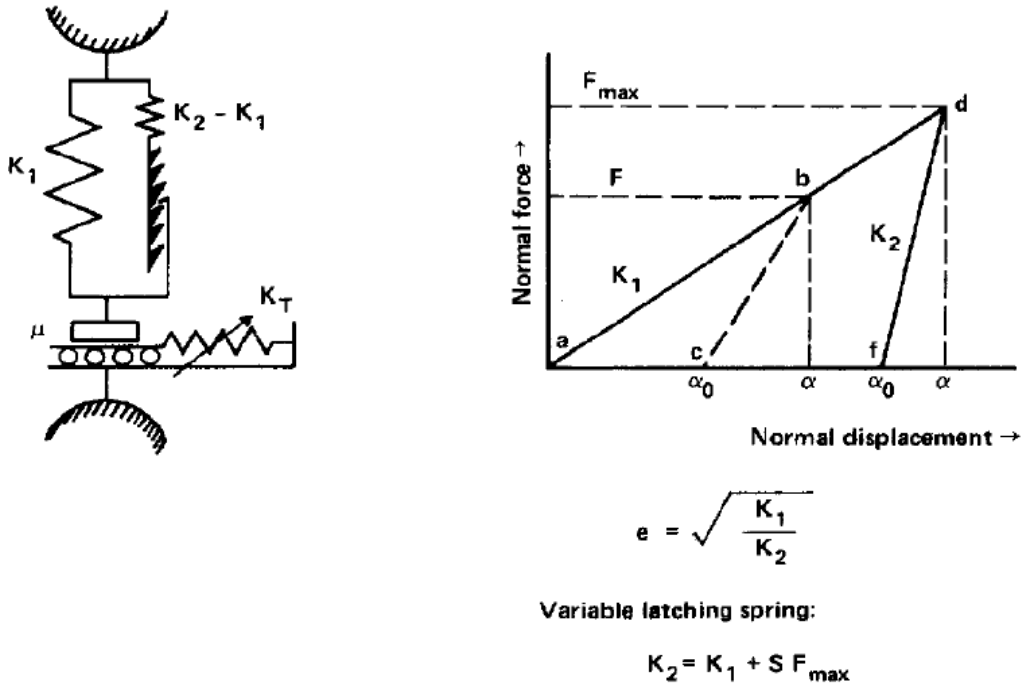

Figure 7. Schematic of partially latching spring model and the corresponding force deflection curve used to describe inelastic normal direction forces acting between two colliding disks.K_1 and K_2 are the loading and unloading spring stiffnesses (Walton & Braun[36])

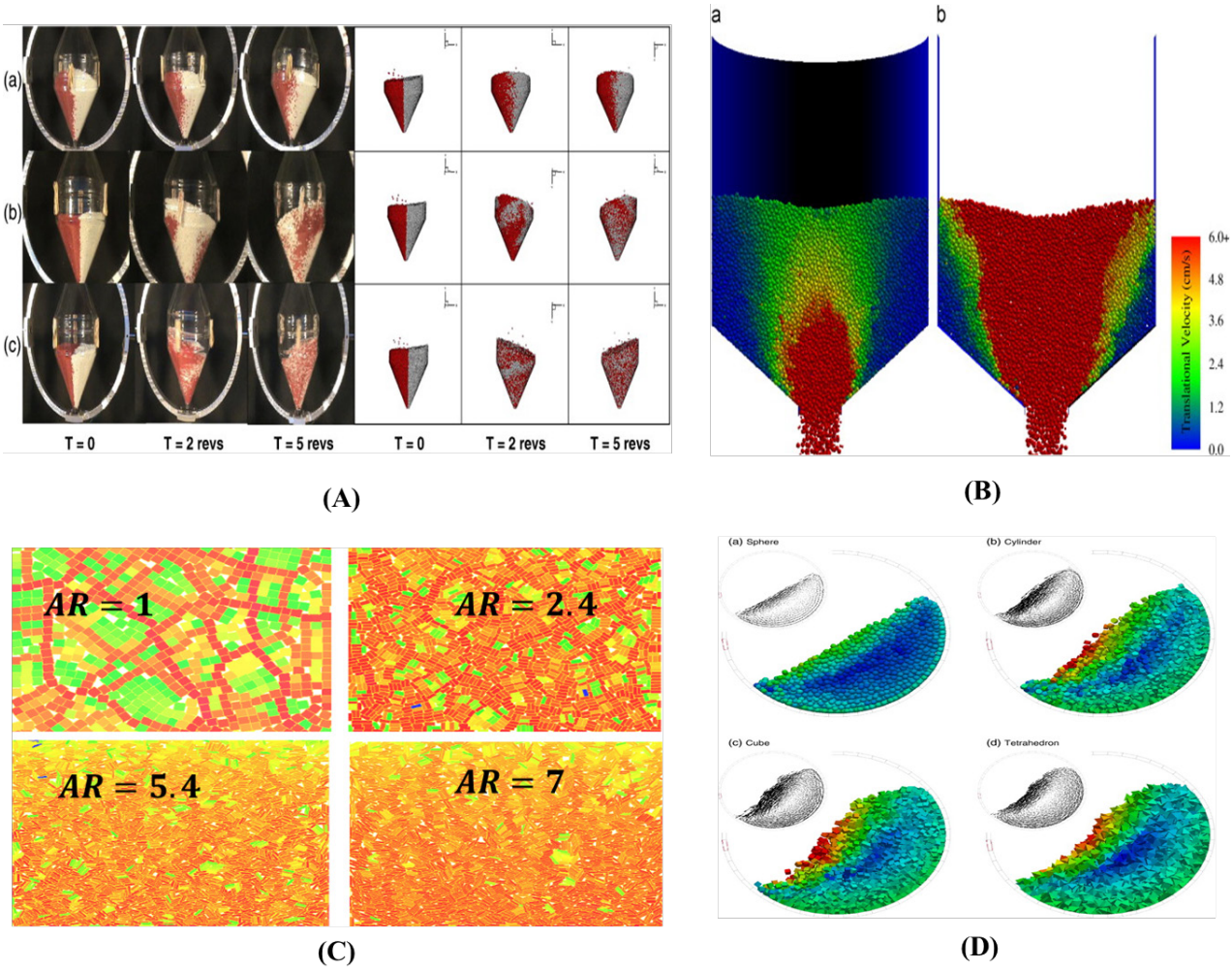

Figure 8.Some applications of DEM in pharmaceutical systems. (a) Mixing progression in a bin and V blender correlated with experiments (Manickam et al.[266]) (b) Discharge from cylindrical and wedge shaped hoppers (Anand et al.[137]) (c) Change is stress distribution in a packing with increasing aspect ratio (AR) of particles as viewed on a log-scale color map measuring contact forces normalized with respect to mean force (Hidalgo et al.[261]) (d) Velocity distribution in a rotating drum with change in particle shape (Wachs et al[282])

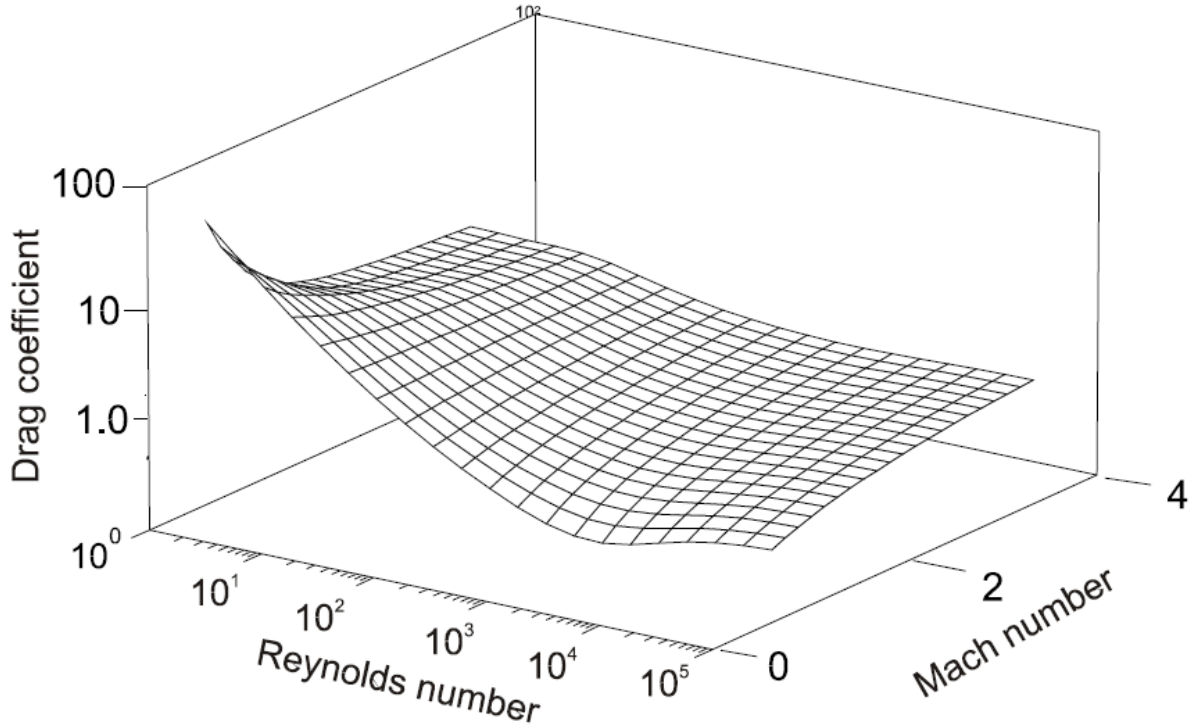

Figure 9.Variation of drag coefficient of a sphere as a function of Reynolds number and Mach number (Crowe et al[11])

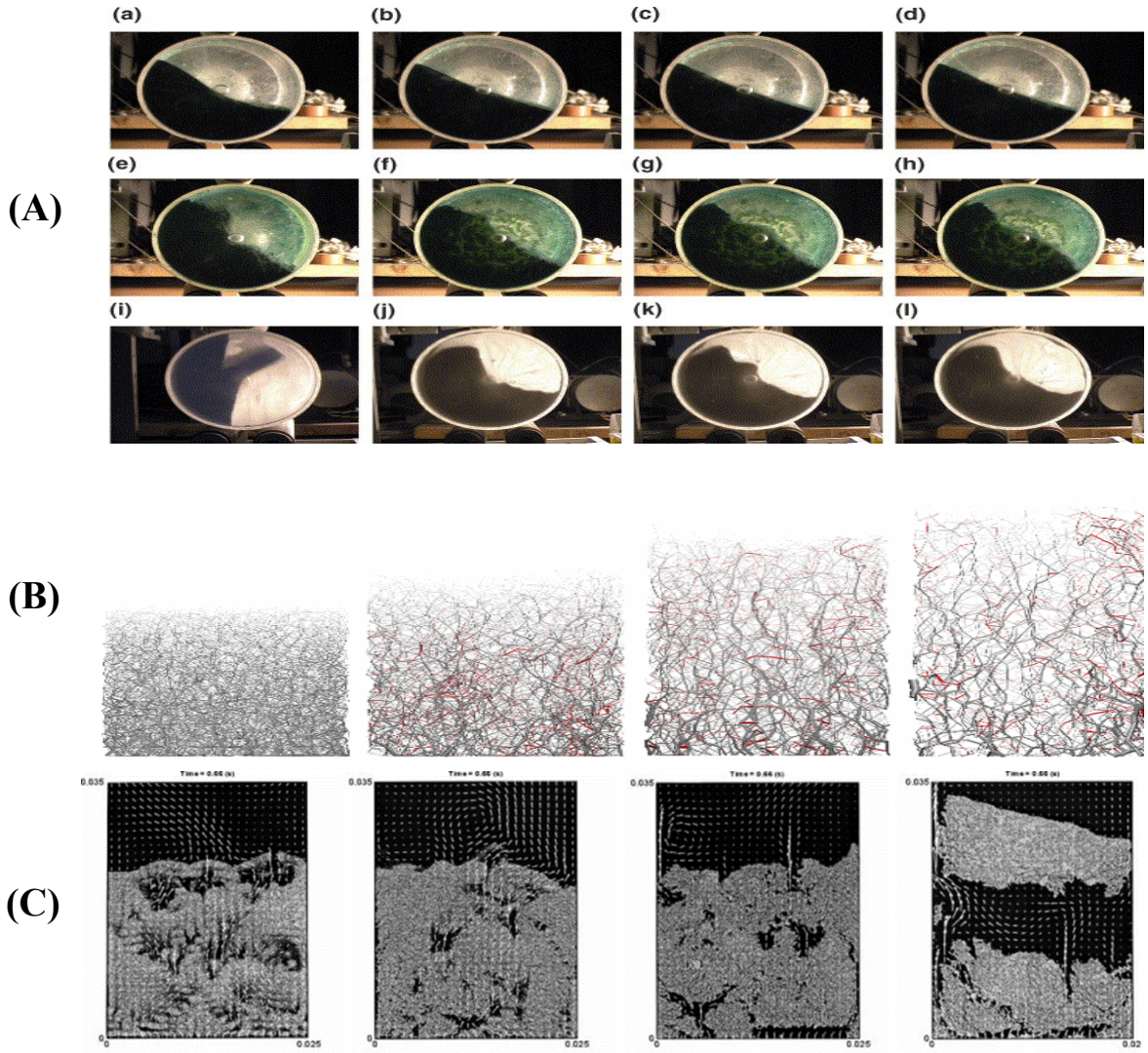

Figure 10. Effect of cohesion in granular flows: (A) Bed dilation in a drum blender for dry glass beads (a-d), wet glass beads (e-h) and Avicel PH102 (Alexander et al.[138]) (b) Variation of normal forces (gray: compressive, red: tensile) in the packing of particles of different sizes. Size decreases from left to right Yang et al.[141]) (d) Fluidization of cohesive particles as particles increase in cohesivity from left to right (Yu and Xu[105])

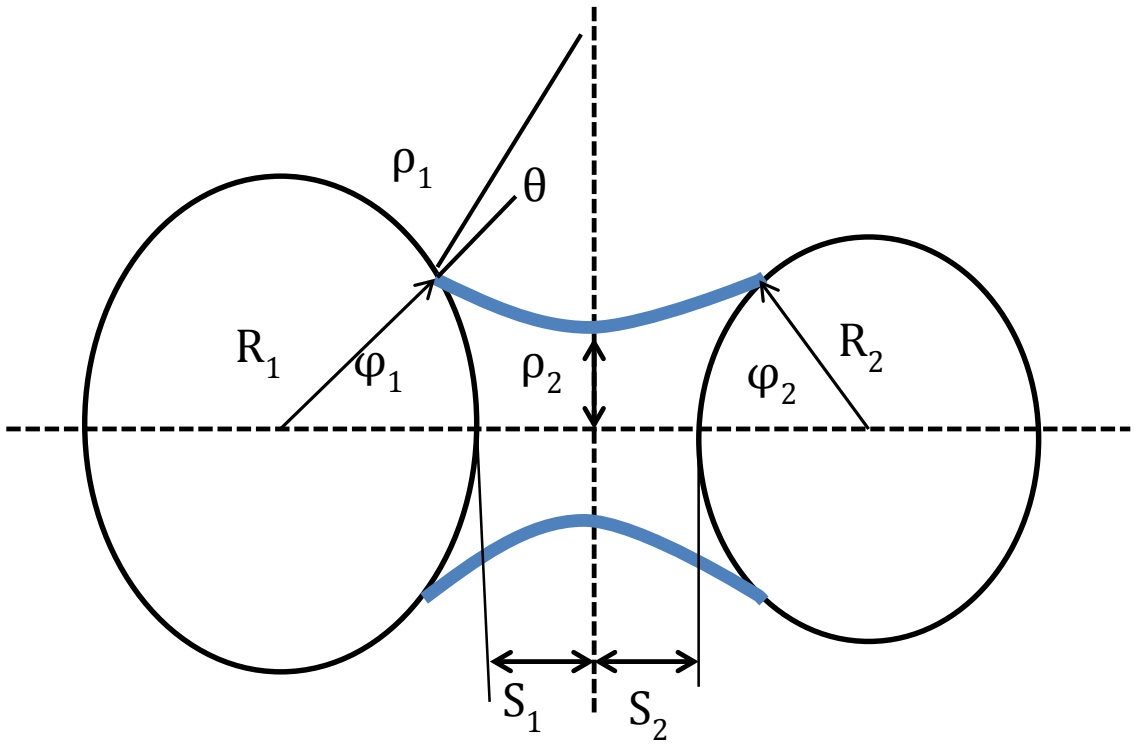

Figure 11. Schematic Representation of a capillary bridge (Iveson et al.[148])

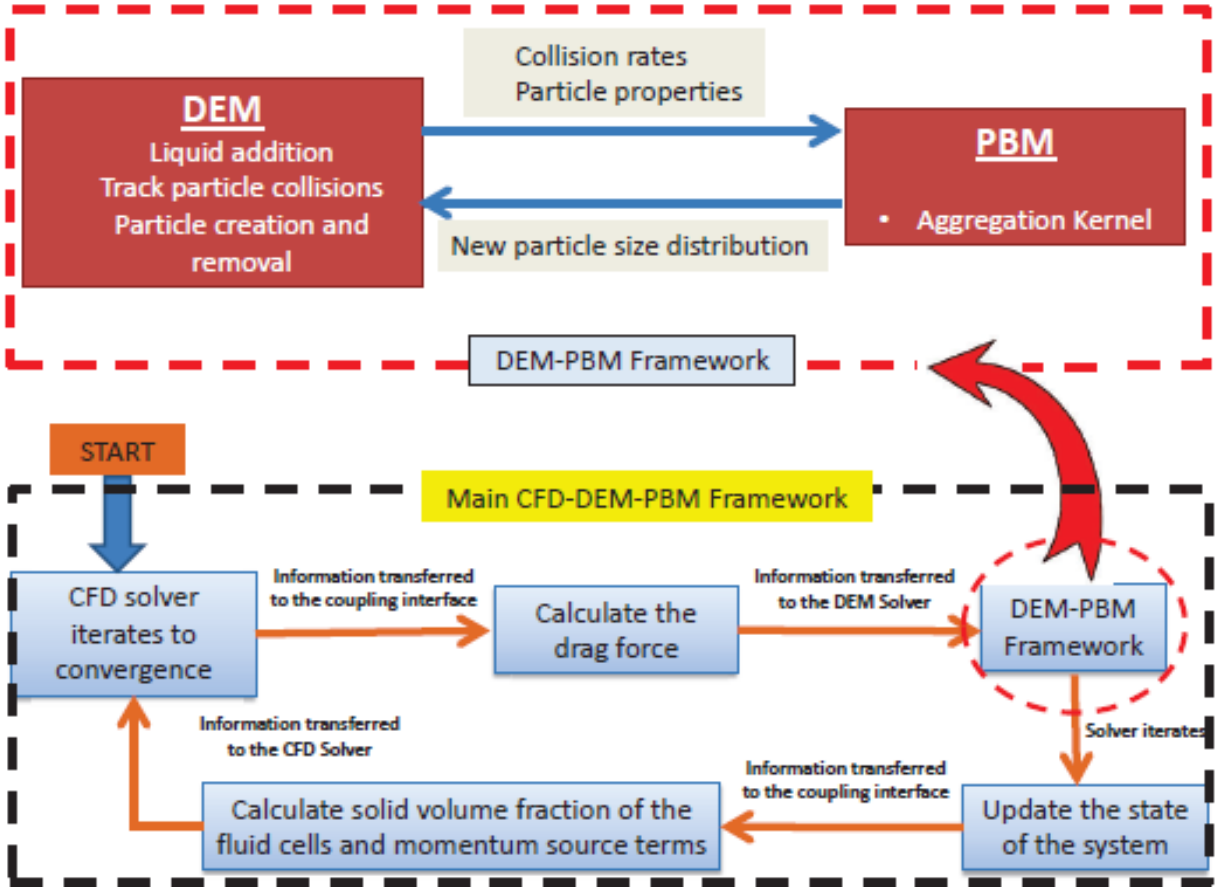

Figure 12. Schematic representation of a coupled CFD-DEM-PBM approach to model fluidized bed granulation process (Sen et al.[51])

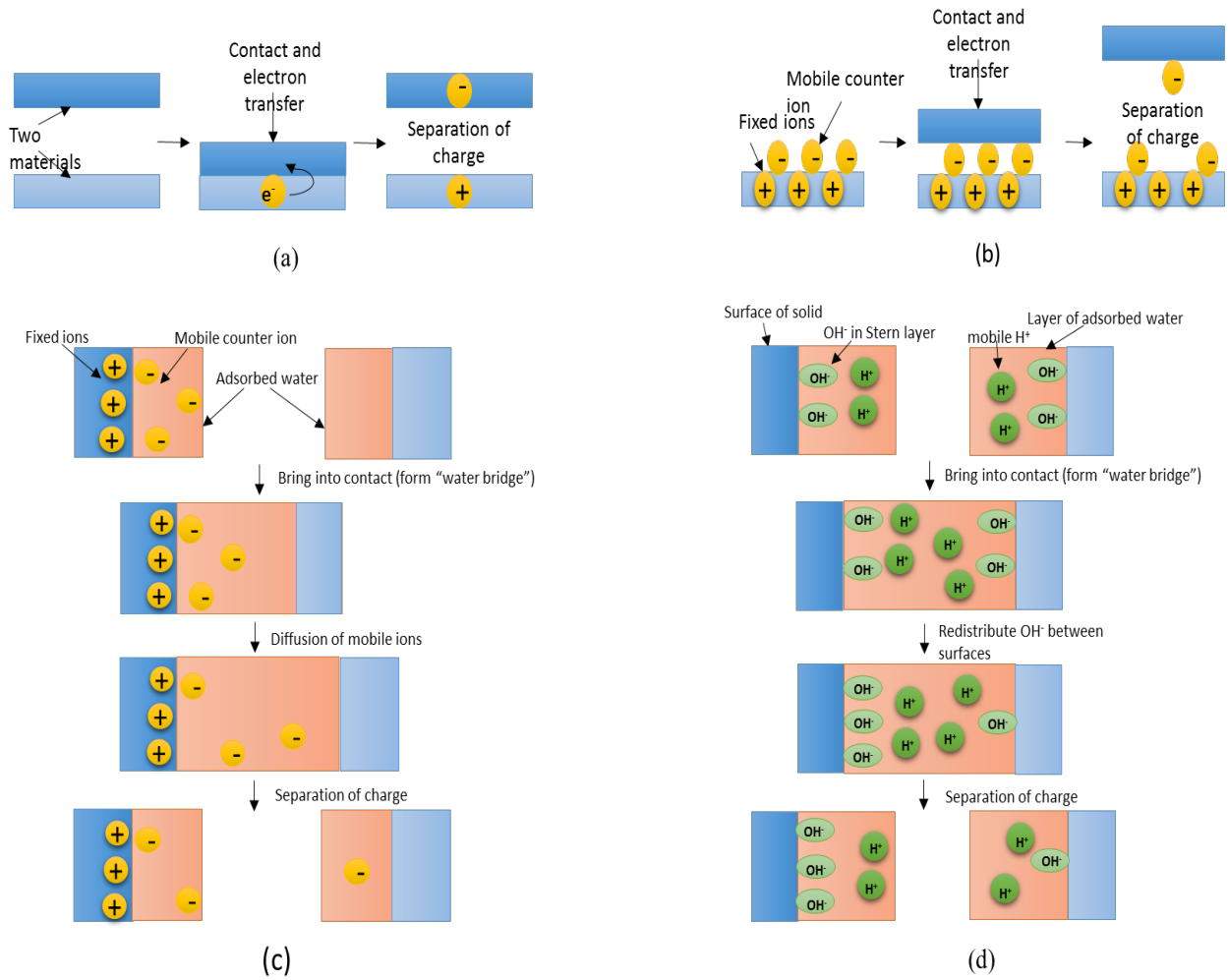

Figure 13. Triboelectrification mechanisms (McCarty & Whitesides[186]): (a) Electron Transfer (b) Ion Transfer, and role of adsorbed moisture when (c) substrate has mobile ions and (d) substrate does not have mobile ions

Chapter 3

Investigation of Multiphase Multicomponent Aerosol Flow Dictating pMDI-spacer Interactions

Abstract

The use of Pressurized metered dose inhalers (pMDI's) for the treatment of asthma and other chronic obstructive pulmonary diseases is frequently associated with breath–actuation synchronization problems and poor pulmonary delivery, particularly amongst the pediatric and geriatric population groups. Spacers, or Valved Holding Chambers (VHC's), are frequently used to address these problems. However, the performance of spacers with different pMDIs is also highly variable and needs to be investigated. The purpose of the current study is to develop a CFD model which can characterize multiphase multicomponent aerosol flow issuing from a commercial suspension- based pMDI into a spacer. The CFD model was initially calibrated against published experimental measurements in order to correctly model the spray characteristics. This model was used to examine several combinations of inhaler-spacer- USP Throat geometries to investigate the effect of discharge rate of coflow air and spacer geometry. The CFD model predictions compared favorably with experimental measurements. In particular, the predictions show, in accordance with experimental determinations, a decrease of drug retained by the spacers with increasing coflow air. The recirculation observed near the obstructions in axial path of the spray within either spacer is considered to be central for increasing spray retention and drug deposition behavior. Fluid flow patterns within the spacers were correlated with drug deposition behavior through a dimensionless variable, the Recirculation index (RCI). Bigger particles were found to be selectively retained within the spacer.

Keywords: Pressurized metered dose inhalers, spacers, Computational Fluid Dynamics, recirculation, fine particle fraction, drug deposition

1. Introduction

Pulmonary delivery to the lungs is an attractive choice to the pharmaceutical industry, owing to (a) more efficient treatment of respiratory ailments, and, (b) delivery of low bioavailability drugs to the lungs which have high surface area. However, pulmonary delivery is limited to fine active pharmaceutical ingredients (API) with a mass median aerodynamic diameter (MMAD) typically less than 5μm.[1,2] The use of pMDIs has been the primary choice for the therapeutic management in the treatment of asthma for the past 50 years, a disease which affects about 300 million people annually.[3] Despite their widespread use, these devices are associated with breath–actuation synchronization problems particularly amongst the pediatric and geriatric population groups resulting in variable pulmonary delivery of the API.[4,5] Dose delivery efficiency, defined as the fraction of drug from each actuation delivered to the lungs, for commercial pMDIs are between 10-20% for adults and lower for children.[6] Spacers, or Valved Holding Chambers (VHCs), are frequently used to address these problems. Spacers serve two purposes: (a) they allow droplets more time to evaporate before being inhaled, yielding smaller inhaled particle sizes and less mouth-throat deposition, and (b) reduction of aerosol momentum (and consequently inertia) which in turn reduces mouth-throat deposition.[1] However, the performance of spacers with different pMDIs is also highly variable;[7-9] largely because of the poorly understood pMDI-spacer interactions.

One reason attributed to a poor understanding of pMDI-spacer interactions is that the mechanics governing aerosol generation from a pMDI is exceedingly complicated. It involves a compressible, locally sonic (150-225 m/s) [10,11] and turbulent ($Re \approx 10^4 - 10^5$)[11] flow near the near the nozzle as the propellant undergoes flash evaporation on actuation. Basic mechanics governing aerosol generation remains poorly understood and considerable work is needed in this

area. Experimental characterization of atomization within the spray nozzle, including identifying the physical form of the emergent aerosol, is difficult mainly because of the small time and length scales involved. Recently, Stein et al.[12] have hypothesized 'multiplet' form of the aerosol, where a droplet (propellant and additive) contains several drug particles. In this study, the distribution of drug particles into the liquid droplets dictating the initial size distribution was computed according to the Poisson's distribution.

Despite these limitations, CFD has been used to model post-nozzle flow and aerosol deposition from pMDIs into human airways[10,11,13,14] with variable degree of success. Most of these studies have focused on an idealized single component (solid API) plume initiated at a speed (much lower than that observed experimentally) in order to account for rapid retardation experienced by the propellant vapor ,while considering drag force to be the most important force acting on the particles. Experimentally validated CFD studies which resolve multicomponent aerosol flow combining spacer and oral cavity geometries have been surprisingly few. Kleinstruer et al.[10] modeled droplet deposition behavior in a hypothetical spacer and predicted significant decrease of particle deposition in the oral cavity, which contrasted with experimental findings.[15] Oliviera et al.[3] modeled flow behavior in an effort to computationally to optimize the design of the Volumatic ® spacer by studying air flow patterns in different cases. However, the particle initialization parameters were arbitrary and the simulation results were not experimentally validated.

The CFD model predictions made in the current study were compared against experimental results from the literature. From a product development perspective it is envisaged that, through the increased process insight gained using such CFD modeling, fewer experimental prototypes would be required, thus shortening the overall design-to-prototype lead times.

Furthermore, a predictive tool which considers the variability of the inhalation process in targeted patient populations would ultimately inform on the development of guidelines for pMDI-spacer labeling in order to reduce waste and enhance therapeutic efficacy.

The overall goals of the project were realized with the following methodology:

(a) Calibrate the spray model using experimental data from pMDI (Proventil HFA) spray in 'unconfined surrounds', which represents aerosol actuation into quiescent air with the presence of a mouthpiece and spacer. Measured particle size and velocity data were compared with CFD predictions at different locations in the open air phase. Various two equation Reynolds averaged Navier Stokes (RANS) turbulence models were investigated.

(b) The CFD model which was developed for open air was extended to inhaler-spacer and inhaler-spacer – USP Throat systems and parameters of interest were evaluated.

2. Materials and Methods

Modeling the mechanistic details of aerosol generation upon actuation within the pMDI canister up to the nozzle was not considered in this work. Consequently, the CFD model development required the characterization of a spray model defined at the nozzle outlet which could accurately predict particle size and velocity observations from a Proventil HFA inhaler. For this purpose, published phase Doppler anemometry (PDA) measurements of Proventil HFA inhaler actuations in unconfined surrounds were used to calibrate the spray model.[16] Subsequently this spray model was used in inhaler-spacer and inhaler-spacer – USP Throat configurations and several parameters of interest (geometry and co-flow rate) were investigated.

2.1 Geometry

The Proventil inhaler, and the Aerochamber Plus and Optichamber Advantage spacers were procured from UConn Pharmacy, Monaghan Medical Corp. and Philips Respironics respectively. The precise dimensions of these geometries were obtained using a commercial mold, Reprosil, which is a hydrophilic vinyl polysiloxane impression material. The dimensions of the USP Throat were taken from Longest et al.[11] Geometry and creation and mesh generation for the respective inhaler, spacer and USP Throat configuration were carried out using ANSYS Workbench Tools 14.0 (ANSYS Inc., Canonsburg, PA). The inhaler nozzle dimensions are shown below in Figures 1a and 1b. A cylindrical computational domain representing the unconfined surrounds is extended beyond the mouthpiece wall (Figure 2) with two sampling points 3 and 6 cm away from the mouthpiece in order to match the measurement locations described in the reference experimental study.[16] To model the inhaler-spacer systems, computational geometries of either spacer was combined with the inhaler geometry in a way such that the inhaler mouthpiece was inserted half an inch into either spacer (Figures 3a and 3b), while the USP Throat was attached to the spacer outlet in an end-to-end arrangement.[9] Table 1 lists the parameters under investigation to model the inhaler-spacer and inhaler-spacer-throat combinations, and coaxial air flow rate.Following geometrical systems are investigated –(a)PA: Proventil-Aerochamber Plus,(b) PO: Proventil-Optichamber Advantage,(c)PT: Proventil-USP Throat,(d)PAT: Proventil-Aerochamber plus-USP Throat, and (e)POT: Proventil-Optichamber Advantage-USP Throat.

The geometries were meshed using ANSYS Meshing ™ which consisted of mostly tetrahedral elements for the inhaler-spacer systems and hexahedral elements for the unconfined

surrounds. Grid convergence was tested for various levels of refinement and results for grid independent meshes are reported below. Table 2 lists the mesh attributes for various systems under study. Maximum skewness <0.95 and minimum orthogonal quality >0.18 are set as criteria for acceptable mesh quality.

2.2 Simulation Set Up

The Euler-Lagrange approach of ANSYS Fluent 14.0 was used to model the multiphase flow, taking into account local turbulence and droplet evaporation. Model set up and boundary conditions along with the major assumptions are described in the next sections.

2.2.1 Assumptions

The CFD model was based on the following assumptions:

(a) The discrete phase occupies less than 10% of the overall simulation volume, which corresponds to a dilute multiphase flow and thus particle-particle or particle wall collision dynamics are not considered. Walls are set to a "trap" boundary condition, implying that the particle's trajectory is terminated when it collides with a wall and is considered to be deposited on the wall.

(b) The spray is modeled as three distinct non interacting streams of droplets/particles composed of the individual components i.e. the drug (albuterol sulfate), the propellant (HFA 134a) and the additive (ethanol). This assumption follows Steyn and Myrdal that for dilute suspension based pMDIs with an MMAD > 2 μm, most of the droplets are not loaded with the drug particles. Zou et al.[17] report the formulation composition of a close analogue of the Proventil HFA inhaler which differs marginally in the amount of ethanol used, and has a drug concentration of approximately 0.3%w/w and an MMAD of 2.65μm.

(c) Consistent with the approach used in other studies[10,11], non-cavitating choked flow is assumed at the pMDI nozzle

(d) Considering the high turbulence around the injection nozzle, through mixing and kinematic equilibrium between the phases is assumed so that all the phases are initiated at the same speed.

(e) Drag force is considered to be the most important force acting on particle. Magnus, lift, buoyancy, Faxen corrections etc. can be excluded because of the large difference between the density of the particles and the surrounding medium.[1]

(f) At distances corresponding to the sampling planes in the open air case or the spacer outlet, the fluid velocity is considerably less than the speed of sound ($Ma << 0.3$). This allows us to assume incompressible flow of the fluid at these locations.[1]

(g) The experimental results in the spacer were obtained according to a protocol involving a minimum delay of 55 seconds between consecutive spray actuations.[9] This delay ensured that the aerosol content from a particular actuation cleared the spacer region before the next one was performed. Consequently, computational results were calculated for one spray actuation.

2.2.2 Solver Settings & Boundary Conditions

The k-ω turbulence turbulence model was used to model the dynamics of the continuous phase and its interaction with the discrete phase issuing from the inhaler nozzle, as used in other studies.[13,14] Physical models to incorporate the effects of drag through the Stokes-Cunningham drag law (Chapter 2, Eq. 2), cooling due to propellant evaporation (inert heating model), droplet break up near the nozzle and Brownian motion were included for realistic simulation results. The physical models and solver settings used for the studies are listed in Table 3. The governing equations for the CFD model are described in Appendix Section A1.

A coaxial air flow with was generated through suction via a pump attached downstream of the pMDI-spacer configuration. This was modeled by prescribing a velocity inlet boundary condition at the 'outlet' for all cases to maintain a constant volumetric flow rate. The 'air inlet' surface shown in Figures 3a and 3b was set to a pressure inlet boundary condition and initialized with atmospheric pressure. Both the coaxial air flow and the injection were started simultaneously at time t = 0 (in accordance with the experimental protocol) with and the time of injection (corresponding to the duration of an actuation) was specified as 0.1 seconds (as described in section 1.1). Convergence of simulation was evaluated by monitoring the static pressure and volumetric flow rate at the outlet and the reduction in residuals to a threshold value of 10^{-4} associated with the solution of the governing transport equations.

2.2.3 Model Input Parameters

Characterization of the spray requires specification of cone angle, duration of actuation, and mass flow rate, initial particle/droplet size distribution and injection velocity for each injection stream. The determination of these parameters is described below:

1) Spray Duration & Cone Angle

These parameters were determined experimentally by visual analysis using high speed video imaging using a Casio EX-FH25 operating at 420 frames per second. The cone angle was determined to be 16.0° $\pm$ 6.25% from 6 independent measurements, while the spray duration was estimated to be 0.1s $\pm$ 4% based on 8 independent measurements. The number of frames was counted from the moment the aerosol appeared beyond the mouthpiece until stoppage of new material coming out of mouthpiece.

2) *Discrete Phase*

(a) **Mass flow rate**: Mass flow rates were calculated based on the experimentally determined spray duration, as described above. The formulation composition for the Proventil inhaler was taken from Zou et al.[18] Accordingly, the average mass flow rates ($\dot{m}$) were computed in the following manner, where 0.1 sec is the experimentally determined duration of spray injection.

$$\dot{m} = \frac{m_i}{t_s} \quad [1]$$

Table 4 lists the amount of drug and excipient released per actuation to be used in the computational study.

(b) **Nozzle injection velocity**: As discussed above, choked flow out of an inhaler nozzle is assumed. This limits the magnitude of the average nozzle exit velocity (v) of the aerosol to the local speed of sound.

$$v = \sqrt{kRT} \quad [2]$$

Here, k is the ratio of specific heat capacities. Considering kinetic equilibrium due to the high turbulence near the injection nozzle as discussed above, each injection stream was initiated with the same velocity, which was computed to be 185 m/s.

(c) **Particle Size Distribution**: Rosin-Rammler distribution was assumed for the drug in the size range from 1 μm to 10 μm with an MMAD of 2.65μm based on formulation composition reported by Zou et al.[18] In accordance with a published article by Steyn and Myrdal [14] on size distribution for dilute suspension based pMDIs, HFA 134a and ethanol were given a MMAD of 10 μm with size distribution ranging from 0.1-20 μm.

The Rosin-Rammler distribution is defined as:

$$Q = exp(-\frac{D}{X})^q \quad [3]$$

Where Q is fraction of total mass contained in particles of diameter greater than D, X is the mean particle diameter and q is the 'spread parameter' which is an index measure of the polydispersity of the spray. It is reported that the spray from a pMDI polydisperse, with a geometric standard deviation (GSD) the size distribution around 1.6-1.8.[12] The value for q for the drug was taken as 1.5, while that for the propellant and ethanol was taken as 2 after fitting so that the GSD and median particle size for the species were matched.

3. Results & Discussion

3.1 Spray in Unconfined Surrounds

Injection into unconfined, stagnant surrounds was investigated to set up and calibrate the underlying continuous and discrete phase models and their associated parameters. The results were compared against experimental measurements,[16] which reported number averaged and volume averaged data from Phase Doppler Anemometry (PDA) and Laser Light Scattering (LLS) respectively. Table 5 compares the results of various two-equation RANS turbulence models with the experimental results. The predictions compare well with experimental findings .There predictions of the three RANS two equation turbulence models are not significantly different, with Standard k- ω providing results closest to experimental determinations.

3.2 Case Studies involving Spacer & USP Throat Systems

3.2.1 Fluid Phase

The Standard two equation k-ω turbulence model was used to approximate the eddy viscosity. Figure 4 plots the temporal evolution of axial velocity at different locations for both the spacers at both flow rates. During the actuation (t <=0.1 s), the centerline velocity is the

strongest as the aerosol plume moves through it. However, negative velocities near the spacer and the obstructive bodies: “Diaphragm” and “Hemisphere” for PA and “Baffle-wall” and “Baffle Surface” for PO; indicate recirculation behavior. Recirculation is critical to spacer performance as it enables retention of the particulate contents for a longer time as their Stokes number is decreased. The recirculation behavior is highlighted in Figure 5, which plots the temporal evolution of fluid streamlines in the spacer at both the flow rates at 0.1 s the recirculation field is the strongest. The flow appears to be obstructed inducing strong recirculation which decays with time and emptying of the spacer contents. The recirculation field is the strongest at t=0.1s, where the extent of recirculation bubble corresponds to the region of maximum plume velocity along the centerline. Vector plots around the obstructive bodies in both the spacers highlight the role of these bodies in inducing recirculation (Figure 6). Figure 6 demonstrates that the interaction of the continuous phase is markedly different for both the spacers. The flow must pass through the spokes of the baffle wall in PO, while it has to navigate around the hemisphere and the diaphragm. In addition to inducing recirculation, Figure 7 demonstrates that the flow obstruction also produces some turbulence as seen from the turbulence kinetic energy (TKE) plots. The geometric design features of the spacers are thus critical to inducing fluid flow patterns and impacting drug deposition, especially as the particles have lost their initial momentum after 0.1 s (end of injection/actuation) and they are subsequently transported by the dynamics of the continuous phase. This is highlighted in Figure 8, which plots the particle momentum source (DPM Z momentum) such that a low value implies that the particle is conveyed with the fluid.

3.2.2 Discrete Phase

The classification of drug distribution over time into spacer deposition, transported and escaped fraction in terms of mass (percentage of injected mass) and size (MMAD) is plotted in Figure 9 a-e. When the co-flow air discharge is increased, drug deposition on all surfaces decreases (Figure 9a) while the escaping drug fraction increases (Figure 9b). PO has greater drug deposition and lesser drug escape in comparison to PA. Figure 9c indicates that drug clearance, which represents the loss of transported drug due to either deposition within or escape from either spacer, increases with increasing flow rate and decreased spacer size (PA). The deposited drug has a higher MMAD than the escaped drug (Figure 9d) which confirms that the bigger particles are preferentially deposited within the spacer (Figure 9e). In contrast, the escaped drug fraction consists of the smallest particles from both the spacers. The increase in MMAD at a higher air co-flow is explained by deposition of the largest particles; while at a lower flow rate deposition of relatively smaller particles reduces the MMAD. The collective results related to particle deposition on spacer surfaces wall in terms of mass and size (MMAD) on different surfaces in the inhaler-spacer- USP Throat systems are presented with histograms in Figure 10. It is observed that there is preferential retention of the biggest particles on the obstructive bodies in both the spacers, which is corroborated by vector plots (Figure 6) which demonstrate the flow obstruction and recirculation around these bodies. The presence of the spacer significantly reduces the amount of drug impacting the USP-Throat wall, which is one of the motivations for using spacers especially for drugs which have adverse effects on the throat wall.

3.2.3 Model Validation

The CFD model was compared with experimental predictions. Figure 11 shows that there is excellent agreement in the drug deposition predictions with experimental observations. There

is a slight offset for data for fine particle fraction (Group 3) and MMAD, but the trends are still well predicted by the CFD model.

3.2.4 Correlating Continuous & Discrete Phase

The above sections highlight the importance of recirculation in the spacers in affecting their performance. The recirculation behavior needs to be quantified, and is done so in the article by evaluating the Recirculation Index (RCI). The RCI is a dimensionless variable which represents the ratio of the intensity of recirculation, quantified by the difference in maximum and minimum velocities corresponding to the centerline and near wall regions, to the volumetric flow rate. Thus the RCI represents a particle's tendency to be recirculated relative to its tendency to be escaped along with the coflow air. Since the recirculation is induced by the obstructive bodies in the confined spacers, the RCI is evaluated on mid-plane contours (X=0) near these bodies i.e. beginning from the obstructive bodies to the maximum centerline velocity, a region denoted by the recirculation domain (RCD)

$$RCI = \frac{Maximum\ velocity_{RCD} - Minimum\ velocity_{RCD}}{Mean\ velocity_{RCD}} \quad [4]$$

A high RCI indicates that there is a high tendency of flow recirculation which increases the probability of drug deposition within the spacer. RCI increased with increasing the spacer size and decreasing the co-flow rate as seen in Figure 12 RCI was well correlated with the drug deposition, with PO at 11 LPM and PA at 28.3 LPM manifesting maximum and minimum deposition respectively.

4. Conclusions

A CFD model was developed for suspension based Proventil pMDI whose predictions compared favorably with experimental results in open air and in geometric systems having different spacer-Throat combinations. This CFD model was calibrated against experimental results in open air to test for accuracy of boundary conditions. The fraction of drug retained within the spacer decreased with increasing the volumetric flow rates for both spacers in both experiments and simulations. Particle size distribution emerging out of the smaller spacer (PA) was bigger compared to the PO system.

Recirculation behavior within the spacer is determined to be critically important for retention of drug particles and influence deposition within the spacer. Recirculation was quantified by the Recirculation Index (RCI), which measures the tendency of the particles to recirculate relative to their tendency to be transported with the co-flow air. RCI was directly correlated with the deposition within the spacer. RCI was found to increase with decreasing co-flow rate and increasing spacer size.

Particle metrics for the systems where Throat was included paralleled the deposition and size data when Throat was not included. There was significant reduction of Throat-wall deposition when a spacer was used. Selective retention of larger particles was found within both spacers at both volumetric flow rates of coaxially flowing air. Out of the fraction of drug that leaves the spacer, there is greater entrapment of bigger particles on the USP Throat wall while the smaller ones preferentially escape through the Throat outlet.

5. Acknowledgments

We thank NIPTE/USFDA for financial support for this project. We are grateful to Philips Respironics and Monaghan Medical Corp for providing us with samples of Optichamber Advantage and Aerochamber Plus respectively. We thank the technicians of the Department of Mechanical Technology at University of Connecticut for assisting us with measuring the dimensions of the two spacers and the Proventil Inhaler. Prof Kurt Schwenk is especially thanked for assisting with high speed video imaging studies. We express our gratitude to ANSYS for providing technical support throughout the course of the project. We also would like to thank undergraduate students Cindy Sounthenavat, Hania Zaman, and Mike Saito for assisting with data analysis for this project.

6. References

1. Finlay WH. 2001. The mechanics of inhaled pharmaceutical aerosols: an introduction. ed.: Academic Press.

2. Newman SP. 2005. Principles of metered-dose inhaler design. *Respiratory Care* **50**(9):1177-1190.

3. Oliveira RF, Teixeira SF, Silva LF, Teixeira JC, Antunes H. 2012. Development of new spacer device geometry: a CFD study (part I). *Computer Methods in Biomechanics and Biomedical Engineering* **15**(8):825-833.

4. Guidry G, Brown W, Stogner S, George R. 1992. Incorrect use of metered dose inhalers by medical personnel. *CHEST Journal* **101**(1):31-33.

5. Melani AS, Zanchetta D, Barbato N, Sestini P, Cinti C, Canessa PA, Aiolfi S, Neri M. 2004. Inhalation technique and variables associated with misuse of conventional metered-dose inhalers and newer dry powder inhalers in experienced adults. *Annals of Allergy, Asthma & Immunology* **93**(5):439-446.

6. Labiris NR, Dolovich MB. 2003. Pulmonary drug delivery. Part II: the role of inhalant delivery devices and drug formulations in therapeutic effectiveness of aerosolized medications. *British Journal of Clinical Pharmacology* **56**(6):600-612.

7. Barry PW, O'Callaghan C. 1996. Inhalational drug delivery from seven different spacer devices. *Thorax* **51**(8):835-840.

8. Berg E, Madsen J, Bisgaard H. 1998. In vitro performance of three combinations of spacers and pressurized metered dose inhalers for treatment in children. *European Respiratory Journal* **12**(2):472-476.

9. Liu X, Guo C, Doub W, Ngo D, Chowdhury B, Starke P, Limb S, Peri P, Lostritto R,Schroeder A. 2011. Assessment of effects of VHCs on in vitro MDI perfoprmance characteristics usong the Andersen Cascade Impactor, Annual Meeting of AAPS, Washington, DC.

10. Kleinstreuer C, Shi H, Zhang Z. 2007. Computational analyses of a pressurized metered dose inhaler and a new drug-aerosol targeting methodology. *Journal of Aerosol Medicine* **20**(3):294-309.

11. Longest PW, Hindle M, Choudhuri SD, Byron PR. 2007. Numerical simulations of capillary aerosol generation: CFD model development and comparisons with experimental data. *Aerosol Science and Technology* **41**(10):952-973.

12. Stein SW, Sheth P,Myrdal PB. 2012. A model for predicting size distributions delivered from pMDIs with supspended drug. *International Journal of Pharmaceutics* **422**:101-115.

13. Oliveira RF, Teixeira S, Silva LF, Teixeira JC, Antunes H. 2010. Proceedings of the World Congress on Engineering.

14. Zhang Z, Kleinstreuer C. 2004. Airflow structures and nano-particle deposition in a human upper airway model. *Journal of Computational Physics* **198**(1):178-210.

15. Ruzycki CA, Javaheri E, Finlay WH. 2013. The use of computational fluid dynamics in inhaler design. *Expert opinion on drug delivery* **10**(3):307-323.

16. Liu X, Doub WH, Guo C. 2012. Evaluation of metered dose inhaler spray velocities using Phase Doppler Anemometry (PDA). *International Journal of Pharmaceutics* **423**(2):235-239.

17. Tzou TZ, Pachuta RR, Coy RB, Schultz RK. 1997. Drug form selection in albuterol containing metered dose inhaler formulations and its impact on chemical and physical stability. *Journal of Pharmaceutical Sciences* **86**(12):1352-1357.

List of Tables

Parameter	
Geometry	PA,PO,PT,PAT,POT
Coaxial flow rate (LPM)	11 , 28.3

Table 1: Parametric study for different variables under investigation.

	PT	PA	PAT	PO	POT
Elements	1183545	2295902	3746435	2533109	4028766
Max. Skewness	0.90	0.9	0.92	0.89	0.90
Min.Orthogonal quality	0.13	0.13	0.13	0.21	0.13

Table 2: Attributes of different meshes used for different systems under consideration

Parameters	
Turbulence Model	Standard k-ω
Physical models	2 way coupling, Brownian motion, Break up-Law(TAB),Pressure dependent boiling, Inert heating, Ideal Gas, Species Transport (Diffusion)
Solution Method	SIMPLE
Drag Law	Stokes-Cunningham
Injection time (ms)	100
Fluid Time Step (ms)	5

Table 3: Parameters used for simulation for the spacers systems under study

Ingredient	Mass (g)	Mass flow rate (kg/s)
Albuterol Sulfate	0.0108	$1.08 * 10^{-6}$
Ethanol	0.58	$5.13 * 10^{-5}$
HFA 134a	5.22	$5.91 * 10^{-4}$

Table 4: Formulation of a Proventil HFA inhaler

	Diameter at 3 cm (µm)		**z Velocity at 3cm (m/s)**		**Diameter at 6 cm (µm)**		**z Velocity at 6cm (m/s)**	
	Mass Avg	No. Avg	Mass Avg	No. Avg	Mass Avg	No. Avg	Mass Avg	No. Avg
Experimental	**4.2**	**4.8**	**-**	**6.5**	**4.0**	**4.6**	**-**	**6.3**
Realizable k-ε	4.40	4.46	5.47	7.07	4.68	4.48	4.76	6.72
Standard k-ε	4.36	4.49	5.99	7.09	4.43	4.50	5.21	6.67
Standard k-ω	4.26	4.48	5.51	6.80	4.63	4.51	4.15	6.63

Table 5: Comparison of experimental results with various two-equations RANS models

List of Figures

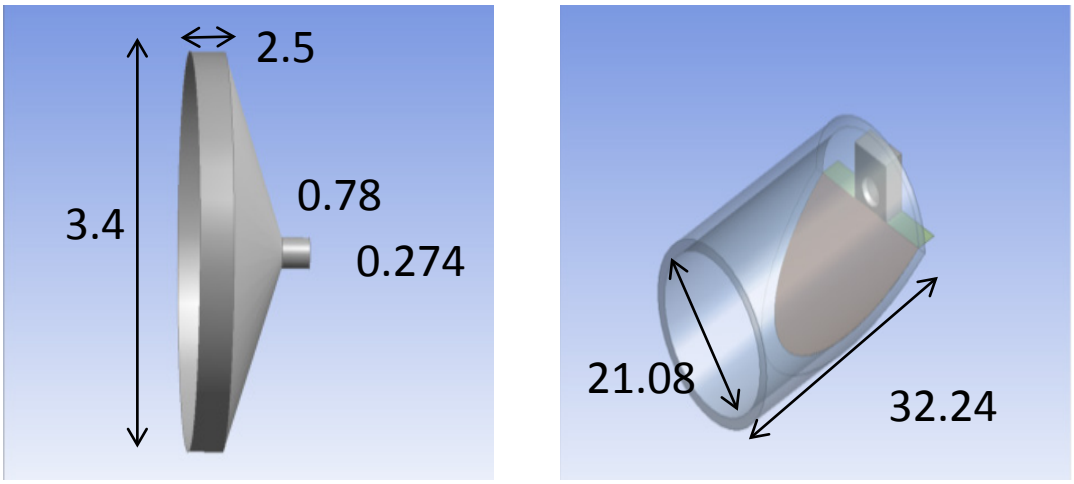

Figure 1. Dimensions of Proventil inhaler mouthpiece: (a) Nozzle (b) Mouthpiece. All dimensions are in mm

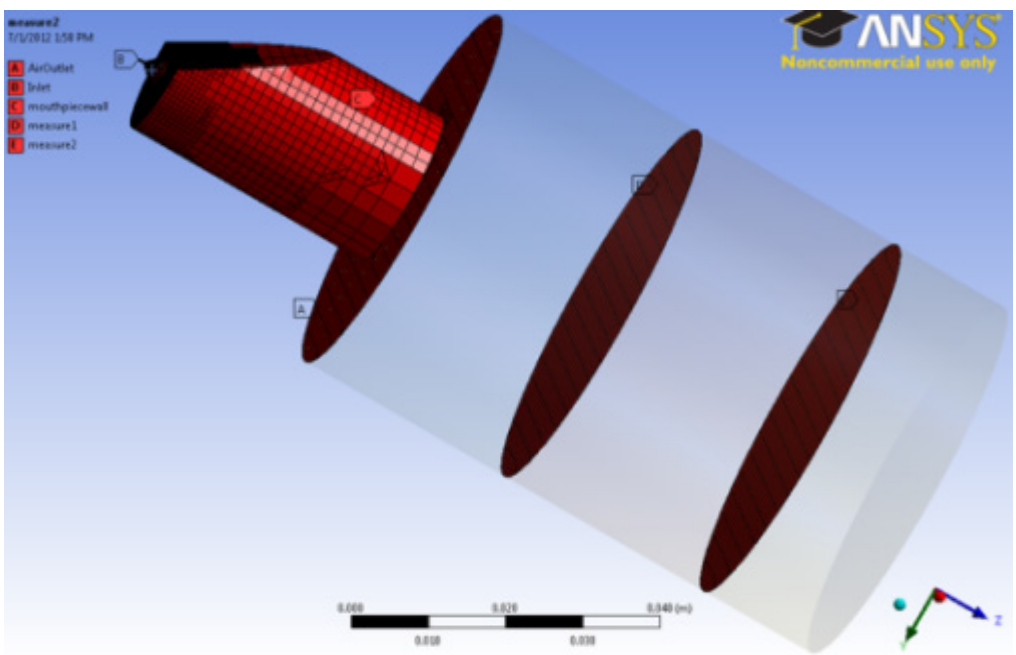

Figure 2. Case set up for Unconfined surrounds case. The outer cylinder (air) is modeled as a pressure outlet .2 measurement locations, 3 and 6 cm away from the plane of the mouthpiece are also highlighted

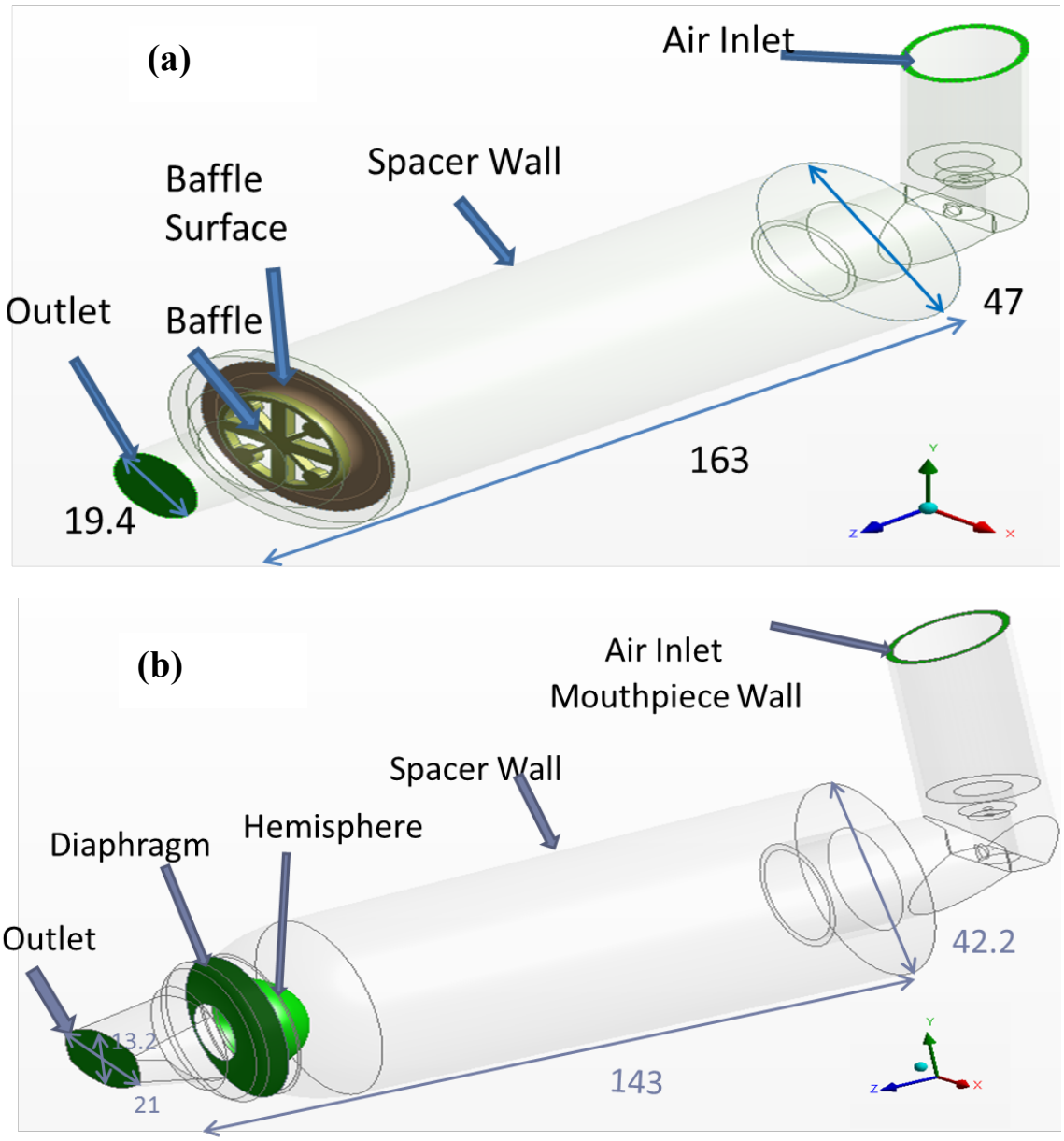

Figure 3. Dimensions of spacers under investigation (a) Optichamber Advantage (PO) (b) Aerochamber Plus (PA). All dimensions are in mm

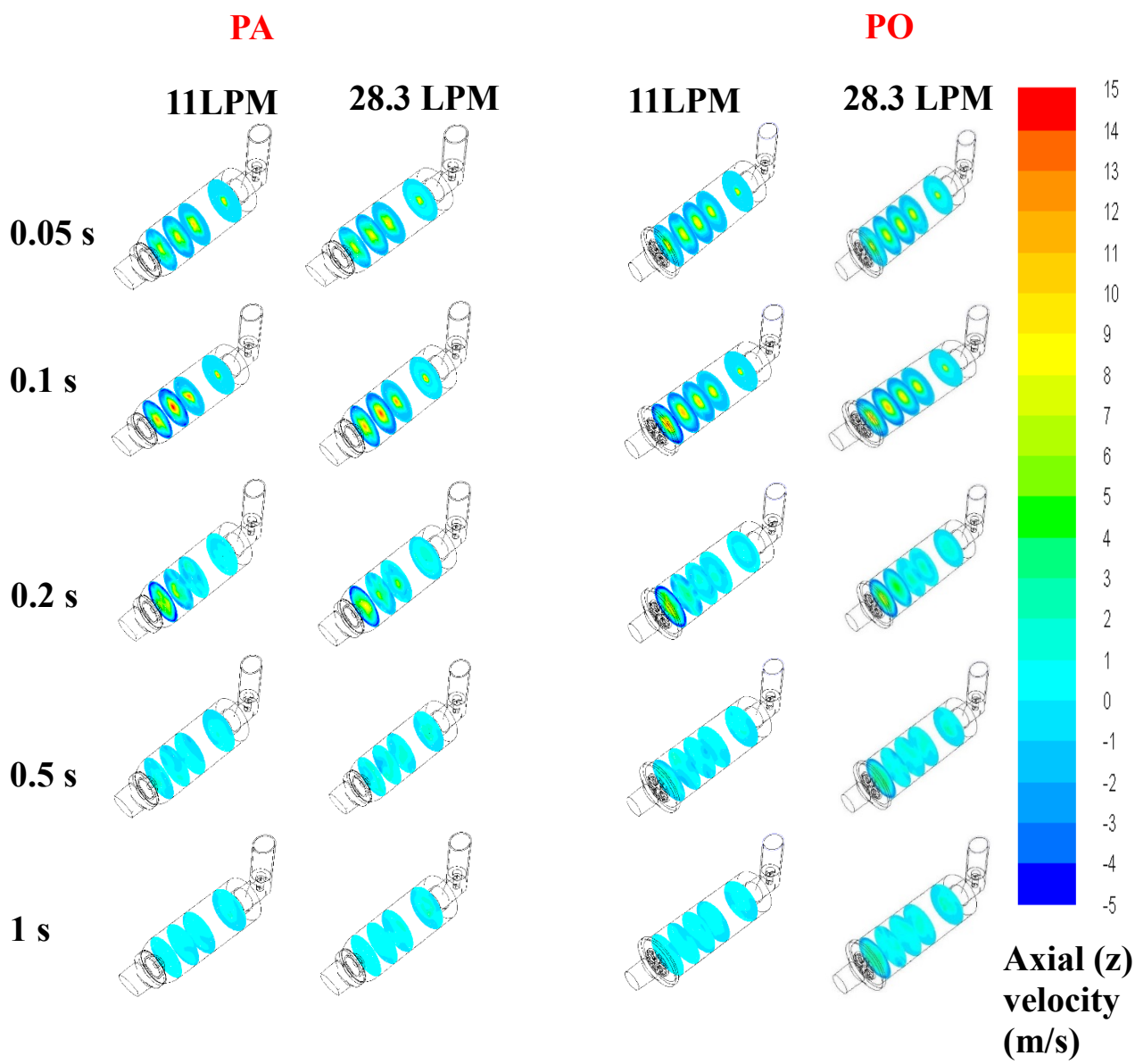

Figure 4. Longitudinal cross sections showing variation of axial (Z) velocity at different axial locations within both the spacers at different co-flow air rates

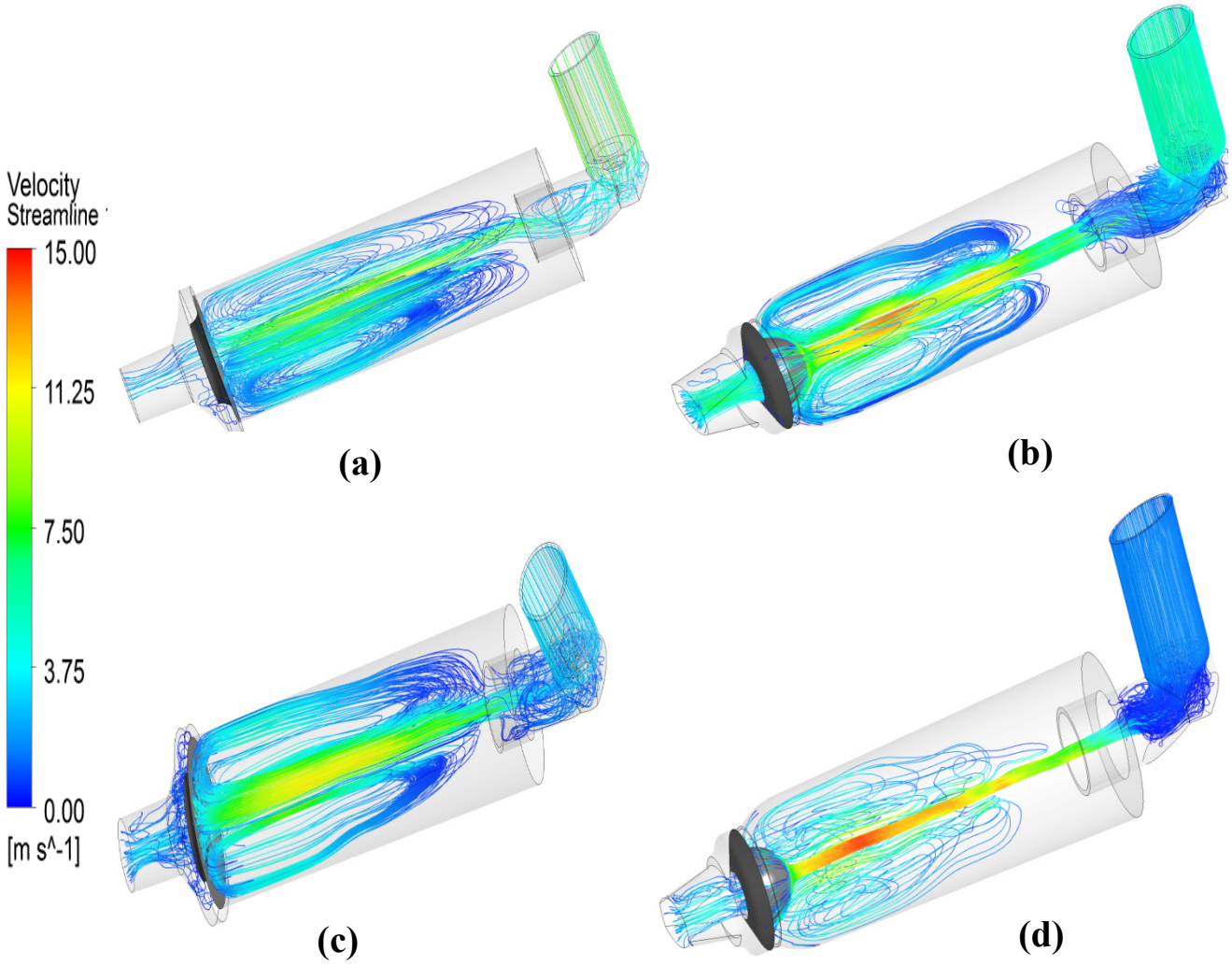

Figure 5. Velocity streamlines in the spacers at 0.1 s demonstration recirculation: (a) P0,28.3 LPM (b) PA,28.3 LPM (c) PO,11 LPM (d) PA ,11 LPM

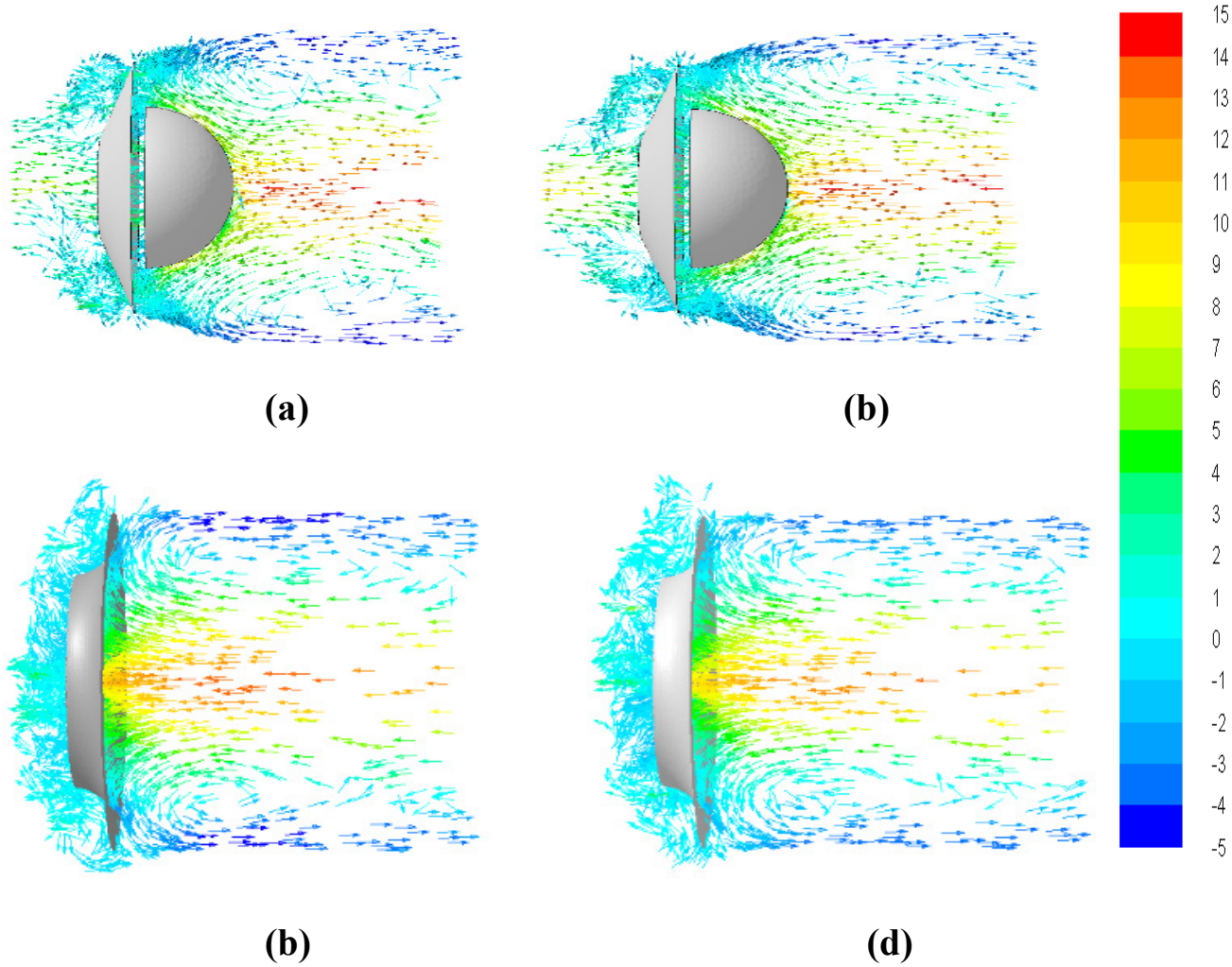

Figure 6.In plane vector plots showing evolution of flow recirculation near the obstructive bodies within the spacers at different co-flow air rates at 0.1 sec. (a) PA, 11LPM (b) PA, 28.3 LPM, (c) PO, 11 LPM, (d) PO, 28.3 LPM

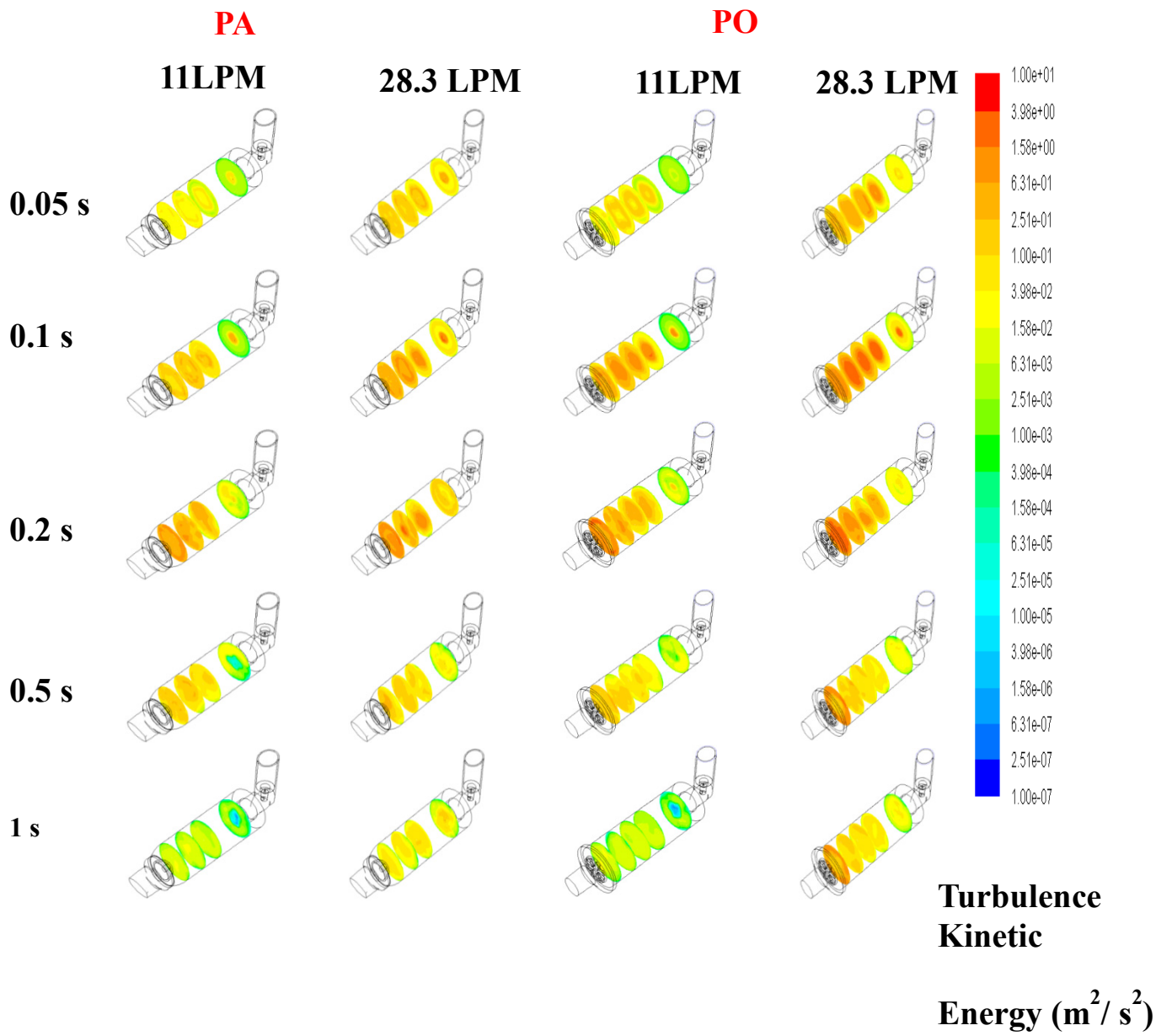

Figure 7. Longitudinal cross sections showing variation of Turbulence Kinetic Energy (TKE) at different axial locations within both the spacers at different co-flow air rates

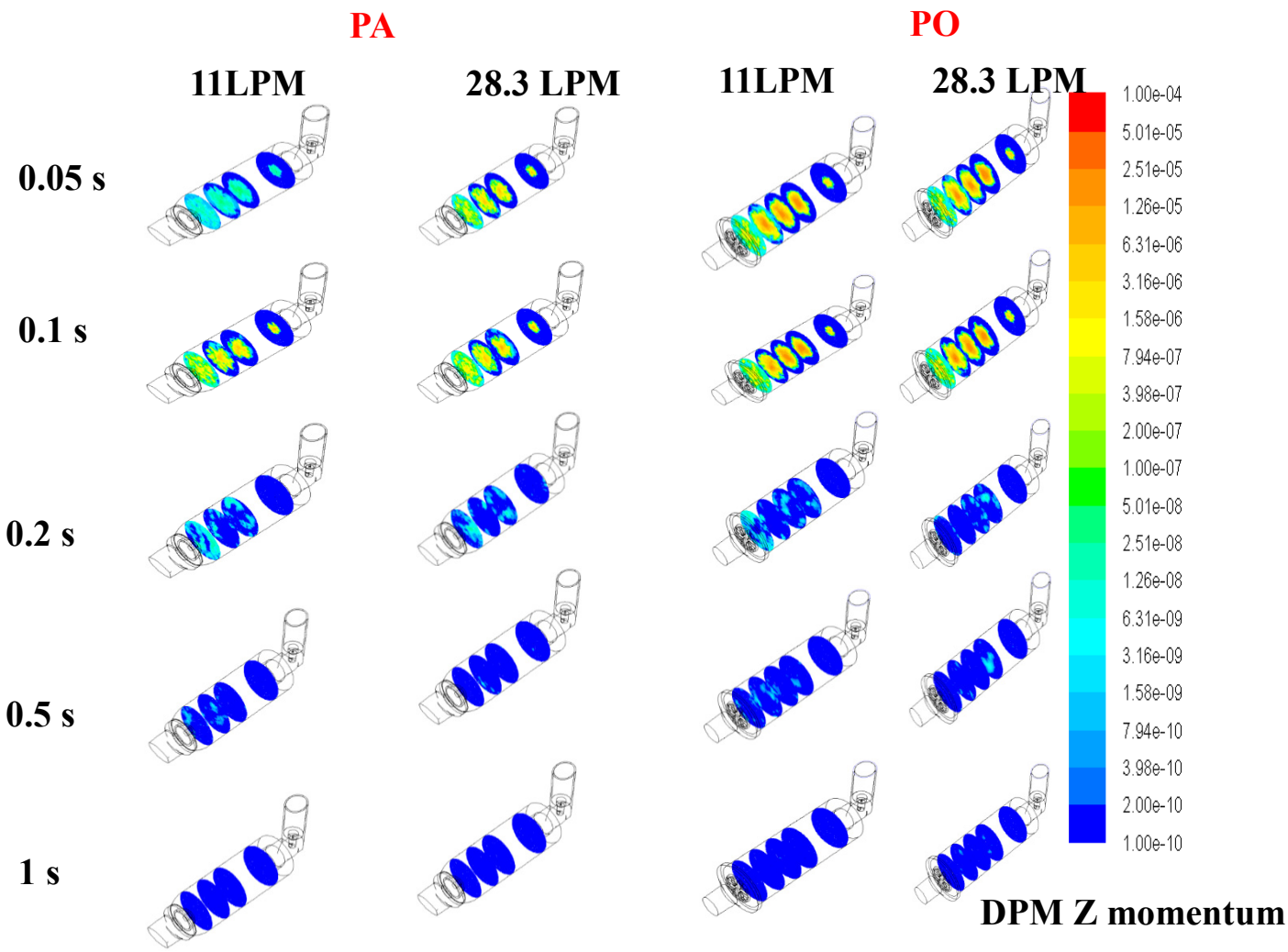

Figure 8. Longitudinal cross sections showing variation of DPM Z momentum at different axial locations within both the spacers at different co-flow air rates

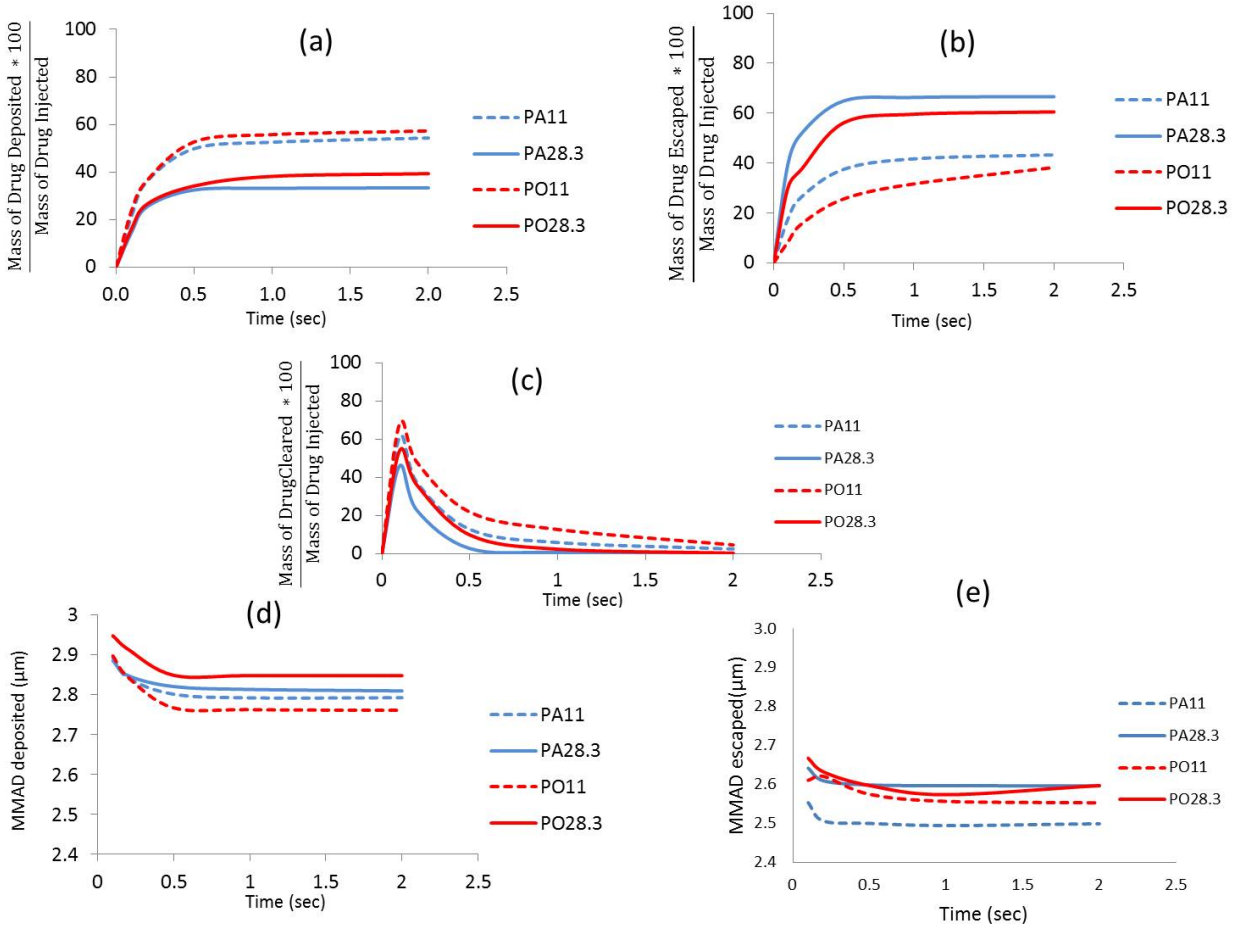

Figure 9. Particle phase transient behavior as a function of spacer and volumetric co-flow rate.(a) Drug Deposition within the spacer (b) Drug fraction escaping from the spacer (c) Clearance of drug from the spacer representing the combined effect of drug deposition and escape (d) Size (MMAD) of the deposited drug fraction (e) Size (MMAD)of the escaped drug fraction)

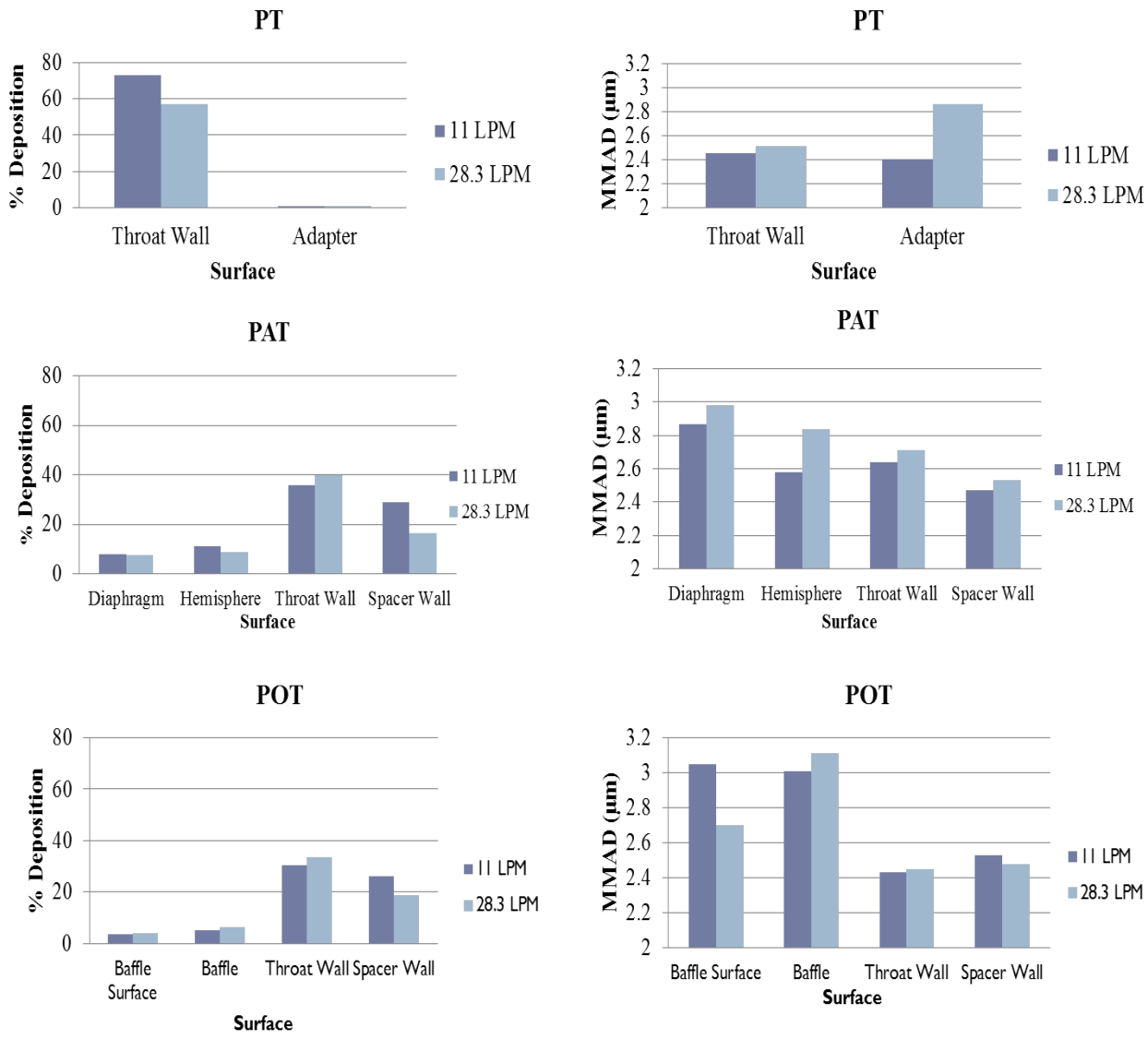

Figure 10. Drug deposition on the various solid surfaces within the spacer and USP Throat at different volumetric co-flow rates

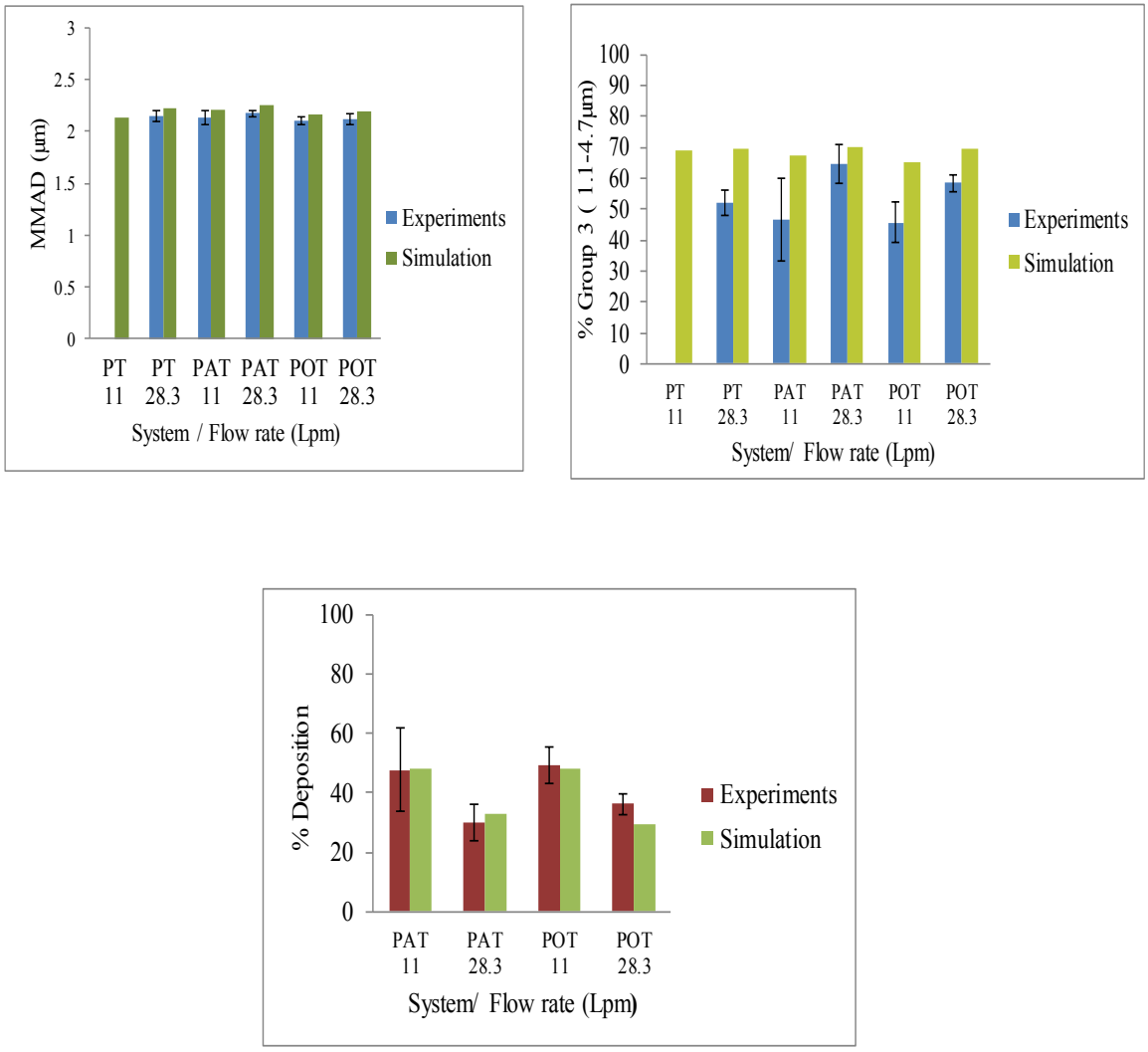

Figure 11. Comparison of model predictions with experimental data (a) MMAD at the end of USP Throat (b) Group 3 (fraction of drug between 1.1 & 4.7µm) at the end of the USP Throat (c) Drug deposition within the spacer

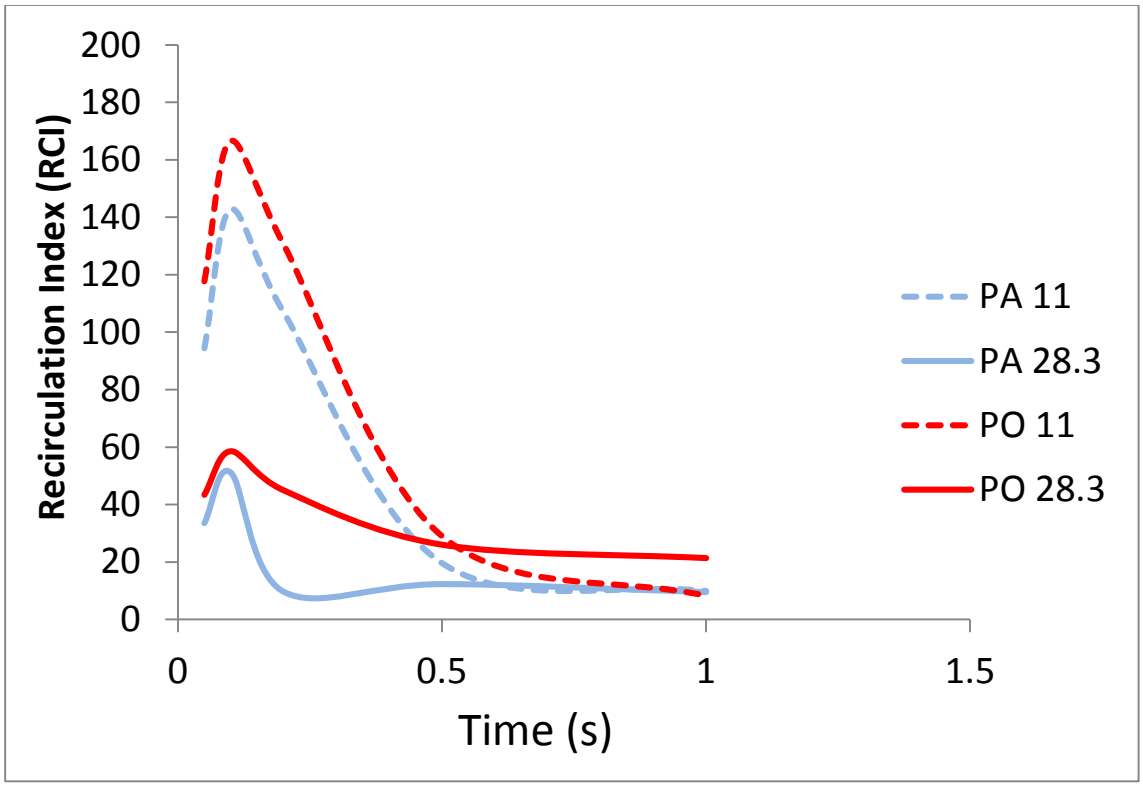

Figure 12. Variation of the Recirculation Index (RCI) within the spacers at different co-flow rates

Chapter 4

Investigation of Mixing & Segregation of Ordered Mixtures for DPI formulations

Abstract

The purpose of the current study is to explore the guidelines towards rationally choosing blenders and processing conditions based on relevant criteria to make robust and high performing ordered mixtures for Dry Powder Inhalers (DPIs), and to develop quantitative experimental and numerical approaches for optimizing the process. Mixing patterns of carrier (LH100) and fine (AZFL) lactose in high shear (HSM) and low shear DoubleCone (DCN) blenders were systematically investigated as function of process parameters. Quantitative and quantitative differences were observed between the blenders with respect to the mixing time, press-on forces, static charging and abrasion of carrier fines. Mixing was observed to be quicker in HSM but was associated with greater loss of fines and abrasion of fines. However, press on forces and segregation from hopper for the ordered mixtures were observed to be independent of the blender used. Discrete element method (DEM) based simulations correlated well with experimental data and revealed mechanistic differences between the blenders, resulting in different impact of process and material variables towards ordered mixture formation. However, DCN was predictive to be more sensitive to increasing adhesion force between the carrier and fines relative to HSM.

Keywords: Ordered mixtures, mixing, adhesion, cohesion, segregation, discrete element method, press-on forces.

1. Introduction

The concept of adhesive or ordered mixtures, wherein fine particles coat the surface of a coarse particle and are held together by adhesive and electrostatic forces,[1] has been used to produce homogenous pharmaceutical formulations containing potent drugs.[2] Ordered mixtures are frequently used for DPI formulations and this is the focus of the current article , but they can also be used to improve flow and reduce segregation,[3] improve the dissolution of drugs.[4-6] The fundamental difference between an ordered and a random mixture is the nature of forces which limit the freedom of migration for the fine constituent particles.[7] Ordered mixtures are frequently employed for Dry Powder Inhaler (DPI) formulations owing to two distinct advantages: (a) pulmonary delivery of fine API is made possible as the cohesive forces are balanced by carrier-API adhesive force to ensure API dispersion ideally to the primary particle size , and (b) improving the powder flow and the formulation so it is able to scale up, handle and fill the formulation into the dry powder inhaler devices.[8]

Formation of ordered mixtures is dependent upon the magnitude of cohesive and adhesive forces between particles in conjunction with the mechanical energy input for mixing. Figure 1 shows the schematic representation of an ordered mixture formation and involves 4 distinct but kinetically competing mechanisms:[9] (a) random mixing of fine particle aggregates (FPA) with carrier particles;(b) breakage of aggregates; (c) adhesion of fines on the carrier surface;(d) redistribution of fines, and eventual release of fines upon patient inspiration. The idea is to achieve a balance of cohesive and adhesive forces to yield an acceptable fine particle fraction (FPF) for an ordered mixture. To this end, contrary requirements must be met: the adhesive forces must be of a magnitude greater than the cohesive interactions to facilitate uniform dispersion, but weak enough to be broken when entrained in air and release an

acceptable FPF. However, a balance of adhesive forces is not easy to achieve as the performance of ordered mixtures is affected by a number of factors, some of which cannot be independently varied.

The performance of ordered mixtures in a DPI formulation is judged by the pulmonary delivery of active fines as quantified by the Fine Particle Fraction (FPF) which is defined as the fraction of particles under 5 μm .FPF is dictated by the distribution of fines over the carrier surface, which is in turn impacted by the surface and bulk properties of both the carrier and the fines, the mixing process, device design and the inhalation process itself. A rough understanding of the knowledge map is available, but considering the poor drug delivery efficacy of most DPIs ranging around 10-30%[10] there is clearly scope for significant improvement.[11,12] A number of experimental studies have focused on the role of material properties of the carrier and surface properties with respect to size and size distribution,[13,14] shape and morphology,[15-17] surface energy,[18-20] humidity,[21] triboelectrification,[22] polymorphic form;[15] process variables like energy input,[23] mixing order,[24] drug loading,[25] and device design.[26] Despite these studies, the role of mixing and dispersions mechanisms remains rather poorly understood and needs to be investigated in greater detail.[27]

The aim of the current study is to systematically investigate the flow behavior and mixing patterns of a binary mixture of powders (model drug and carrier lactose) in a laboratory scale high shear and low shear blenders, and segregation in bench scale hoppers using systematic experiments and simulations. The mixing and segregation patterns are estimated as a function of different material (adhesive force), process and formulation parameters (rotational speed, fill and initial loading, drug loading, drug to carrier ratio) to improve our understanding of the mixing process. Finally, the impact of the mixing process and blender with respect to the press-on

forces, tribocharging and abrasion of fines would be elucidated to rationally guide in choosing the blender and process parameters.

2. Materials & Methods

2.1 Materials

Fine lactose (AZFL, d_{50} = 3μm) was provided by AstraZeneca Inc. which has physical characteristics of a representative API. Lactohale 100 (LH100, d_{50} = 164μm) provided from DFE Pharma is used as the carrier lactose. The physical characteristics of the fines and lactose are listed in Table 1. It can be seen that the AZFL, referred as "drug" for the purposes of this article is distinctly finer and more cohesive than the carrier.

2.2 Experimental Procedure

2.2.1 Analytical Method Development

In the absence of any chemical or crystallographic difference between the drug and the carrier fines, particle size difference between the carrier and fines was exploited to (a) characterize the mixing and segregation (from the hoppers) (b) characterize the adhesion force between the carrier and the drug from pressure-titration studies, (c) the estimate press-on forces in the ordered mixtures and (d) determine the tendency for abrasion of fines of a particular process. *Fine Particle Content* (FPC), defined as the fraction of particles under 10 μm determined from the volume weighted PSD, was monitored by laser diffraction in a Malvern Mastersizer ™ 2000 E instrument equipped with the dry Scirocco dispersion unit which has a range of 0-4 bars. The cut off size for FPC determination was chosen as a best compromise to maximize the carrier and fines' distinction, while operating at the maximum signal to noise ratio.

Linearity and sensitivity of the analytical method was established. Different aliquots were taken to determine the linear response in the concentration region of interest (0- 5%w/w of fines). Figure 2 demonstrates the linear response and sensitivity of the analytical method. The regression equation demonstrates the presence of carrier fines (1.7%), and the sensitivity of the analytical method to the changes in drug concentration. Carrier fines serve to passivate the active sites on the carrier surface, so that the drug binding is largely reversible.

2.2.2 Mixing Experiments

A 1 L high shear mixer, HSM, (KG5 Model, Key Intl, NJ) and a biaxial 2.5 L low shear Double Cone blender (DCN),[28] fabricated at University of Connecticut Department of mechanical Technology were used to form the ordered mixtures. The blenders used in the study are depicted in the Figure 3. AZFL and LH100 were loaded in the blenders at a given fill, drug: carrier ratio and loading configuration and rotated at a given speed. Top loading (TL) and central loading (CL) refer to the initial configurations where AZFL is loaded on top of LH100 or when AZFL is sandwiched in layers of the LH100. A complete 2 factorial statistical design was followed in which all the trials were done in triplicate under standard laboratory conditions (Temperature: 20 $\pm$ 5 °C, RH: 25 $\pm$ 5 %). Approximately 100 mg of the sample were taken from the mixing vessels from 6 locations at pre-defined time intervals and measured at 4 bar pressure, which ensured dispersion of the blend to the primary particle size. The Relative Standard Deviation (RSD) which was computed as the ratio of the standard deviation and average of the FPC of the 6 samples, was used to track the mixing progress as function of time. Mixing was assumed to be completed when the RSD fell below 1.5%, and was verified by SEM imaging.

2.2.3 Experiments of Segregation due to Hopper Discharge

Two different hoppers were fabricated out of plexiglass, each for mass (45°) and funnel flow (75°) regimes, in order to study the segregation of ordered mixtures, each having the base and outlet diameters of 6 cm and 1.2 cm. All studies were done at standard laboratory conditions as described above. The flow was aided by a fixed vibration of the hopper maintained at 24 Hz. The ordered mixtures were loaded in the hopper and discharged on an in-house conveyor belt. Figure 4 shows the experimental set up used for the hopper studies. The total emptying time during the discharge of the ordered mixture from the hopper was measured. The discharged mass was sampled, divided into even bins based on the length of pile and analysed in the Malvern Mastersizer at 4 bar pressure. FPC was determined at different time points, and was divided by the FPC of the ordered mixture to compute the Segregation Index (SGI). Segregation of the mixture is detected by departure of SGI from unity indicating drug rich or drug deficient temporal zones. Table 2 lists the process variables under investigation during formation and segregation of ordered mixtures in the mixers and hoppers respectively.

2.3 Characterization of Quality Attributes

2.3.1 Cohesive /Adhesive Force Estimation

Pressure titration studies done in the Malvern Mastersizer 2000 E, in which different hand-mixed blends were subjected to a range of pressures, were used to estimate the cohesive force difference between the carrier and the drug; while the same procedure was used for ordered mixtures to characterize the press-on forces. Figure 5 shows the steep slope for the pressure titration curve for the drug which exists primarily as agglomerates at low dispersion pressures and breaks up into primary particle size only at pressures of 2 bars or above. In contrast to the

steep curve, the carrier exists largely as a free flowing powder and breaks down to the primary particle size as low pressures.

2.3.2 Press –On Forces

The press on forces, which indicate the force with which the fines are held to the carrier surface, is an integral part governing the mechanical stability of the ordered mixtures. In order to evaluate these forces, the ordered mixtures were subjected to different pressures (0-4 bar) within the particle sizer. The FPC evaluated for each pressure was divided with the value obtained at 4 bar pressure to compute the normalized FPC. The procedure assumes complete dispersion of the aggregates into their primary particle size at 4 bar pressure. Mixtures from both the blenders, formulated at different drug concentrations are evaluated using this procedure.

2.3.3 Abrasion of carrier fines

The propensity of the process to cause abrasion of carrier fines needs to be evaluated for its possibility in influencing the pulmonary delivery of fine particles. Higher abrasion can result in less shielding of high energy sites which can be accessed by the drug fines resulting in irreversible binding. However; it was hard to characterize this phenomenon, given that the carrier and the drug cannot be separated as the upper limit volume based particle size distribution (10µm) particles as the upper limit for fines includes both carrier and drug components. Considering these challenges, the number distribution PSD plots, which demonstrated a clear difference in the carrier and drug fines (Figure 6) were used to distinguish between the carrier and drug. The question of which fines' species, either the drug or carrier, is sheared off the carrier surface to cause de-mixing is addressed by plotting the change in the normalized FPC at different time points, which is essentially the AUC of fines under 10 µm size determined from

the number weighed PSD. The reference time point was chosen as the first sampling time point in order to bypass the effects of loading configuration.

2.3.4 Static Charging of Blends

The static charge of the blends was determined by discharging the blender contents into a Faraday Cup (1.19 L, Monroe Electronics), while the charge was read off from a calibrated nano-Coloumbmeter (Model 284, Monroe Electronics) as primarily done by our group previously.[29,30]

2.4 Statistical Analysis

Statistical analysis of data was performed using Minitab 17.0 using the generalized linear model[31] set to a 95% confidence limit. The model assumes normally distributed error, which was established from the residual plots. The time, speed, loading configuration and fill were treated as categorical variables and statistical significance of the slope is tested. In accordance with the Akike Information Criterion (AIC) guidelines, [32] the model which explains the maximum variability with the fewest parameters was selected for comparison.

3. Discrete Element Method (DEM)

DEM is a process modeling methodology in which the trajectory of a particulate system is computed by summing up all the contact normal and tangential forces acting on the particle and numerically integrating them to obtain updated velocity and position of each particle. The normal forces (F_N) and the tangential forces (F_T) in inter-particle or particle–wall collision are calculated with the "latching spring model" and "incrementally slipping model" respectively, developed by Walton and Braun.[33] Details of the DEM algorithm are given in Appendix Sec A2.

In addition to normal and tangential forces, cohesive forces are included in the DEM model to predict the formation and segregation of ordered mixtures. The short range cohesive interactions would be included when the separation of the two particles is less than *2r*, *r* being the particle radius.[34,35] In order to compare simulations considering differently sized particles, the magnitude of cohesive forces is represented in terms of the dimensionless Bond number (K), which is a measure of cohesiveness that is independent of particle size such that K = F/w, where w is the weight of the small particle and F is the cohesive force.[36] This approach has been used successfully before to simulate cohesive flows of granular material. For the binary mixture of particles of different sizes, the forces between "like" and "unlike" particles are independently specified. F_{ss} , F_{bb} , F_{bs} the represent the cohesive forces to be incorporated through respective bond numbers such that between small-small, big-big and big-small particles such that K_{ss} = F_{ss}/w, K_{bb} = F_{bb}/w , K_{bs} = F_{bs}/w. The value of K_{bb} was chosen to match the flow pattern of coarse carrier between experiments and simulations. The ratio of the bond numbers were calculated to match the ratio of cohesive forces between the coarse and fine particles matches the ratio of slopes of the pure components (Figure 4). The major computational tasks of DEM in each time step are to add/delete contact between particles thus updating neighbor lists and compute all contact forces from acting on the particles and sum them up to update their position by integrating Newton's laws of motion. A central difference scheme, Verlet's Leap Frog method, is used for integration of force and torque balance equations. Bearing in the mind the limitations of DEM to handle both small particle sizes and large size ratio of particles; the size of the coarse and fine particles are chosen to be 3 and 1 mm respectively. The number of particles chosen for the study satisfies the constraints of volumetric fill and the mass ratio of surrogate API to the coarse carrier. The formation of ordered mixtures within the blending equipment is

monitored through the coordination number (CRN), defined as the number of particles attached to a particle of different size. This reflects the number of particles which are a part of an ordered mixture. The state of mixing within the blending equipment is characterized by comparing experimentally obtained RSD plots to those obtained with simulations. The blenders are divided into different radial sectors in which the number and weight of small and big particles are counted. RSD is computed from the weight fractions of fines in the different sectors. This allows us to predict trend-lines for parametric studies within the design space, as opposed to a 1:1 correlation between experimental and numerical data and henceforth lead to advancement in our understanding of formation of ordered mixtures. For the hopper studies, ordered mixtures were deposited in the hopper by random deposition and applying the respective Bond numbers used during mixing studies till the RSDs of the ordered mixture in the blender and hopper were matched. Table 3 lists the parameters used for the DEM study.

4. Results & Discussion

4.1 Formation of Ordered mixtures

4.1.1 Effect of Process Parameters on Content Homogeneity

The progress of mixing, as tracked by the temporal evolution of % Relative Standard Deviation (RSD), revealed the distinctive features versus performance of the both the blenders. In principle, the mechanical energy input from the blenders must compensate for the cohesive forces between the drug particles. The de-agglomerated fines are spread over the surface and are held by adhesive forces. In this light, the blender must contribute in two ways: (a) impart enough shear (b) produce sufficient mixing of particles to enable redistribution of fines. Both the mixers however differ in their mechanistic production of shear. While HSM uses the shear forces from

the rotating impellers, there is failure of the slip planes in the DCN along the biaxial curves which results in shear enabling better mixing. Statistical analysis of the data revealed that the speed and drug to carrier ratio were the significant variables ($P < 0.0001$) affecting RSD in the HSM, while speed was the only significant factor influencing mixing in the DCN. Table 4 lists the P values of the best linear regression model explaining the variability in RSD. Within the HSM, increased speed led to much faster mixing which is rather intuitive. However, there was a statistically significant demixing peak obtained at higher drug ratio which is also indicated from the %RSD variation. However, volume weighed and number weighed plots may not be necessarily correlated, given that the volume weighed PSD plots are influenced significantly by the coarsest particles while the number weighed plots account for particles only less than 10µm. The best mixing was obtained in the DCN when both axes were rotated at a different speed, X30Y10, where the blender was rotated about the horizontal and vertical axes at 30 rpm and 10 rpm respectively and the worst performance was obtained at X10Y10. These results are in agreement with previously published results.[28] Figure 7 plots the variation of RSD with time for both the blenders at a 30% fill loaded in the CL configuration. The interaction of different process variables for HSM is displayed in Figure 8.It can be seen that while HSM formed the ordered mixtures significantly faster in contrast to DCN. However, both blenders took approximately the same number of rotations. Visual observation of the ordered mixtures was done from SEM imaging at different resolutions as shown in Figure 9. The particles are distributed in the surface discontinuities and crevices where they are shielded from shear forces, and certainly by adhesive forces.

Qualitatively similar trend-lines are obtained for both experimental and computational DEM studies (Figure 10). A measure of the shear forces generated with the blenders can be

reached gathered from the particle velocities reached, as seen from snapshots from vector animations in Figure 11. The vectors are colored according to their magnitudes, while the alignment of the vector is in direction of the net velocity. It can be seen that while HSM reaches velocities of approximately 1.5m/s , the vector lines are in phase which indicate chaos in the system are poor which manifests in low redistribution of fines. The converse is true for DCN where the maximum velocity reached is much lower (<1 m/s) where vector lines are seen to intersect at much higher speeds. Figure 12 shows vector snapshots at the same conformation for X10Y10 and X30Y10. At low speeds, this can translate to more agglomeration as the API contacts are increased and stabilized by higher physical affinity. When the speed around both axes is the same for DCN, the system enters a phase and mixing is compromised. Figure 13 shows better performance at X30Y10 and X10Y30 while X30Y30 and X10Y10 show greater fines segregation to the wall. These trends are observed experimentally as well. Figure 14 depicts the spatial variation in CRN in both the blenders at the best and worst performing speeds. HSM demonstrates greater more ordered units in the snapshot in comparison to DCN. At 500 rpm, there is considerable bed dilation and wall adhesion of fines relative to that observed at 100 rpm. Homogeneity throughout the bed is determined by the Saturation Index which is defined as the instantaneous ratio of number averaged CRN for coarse particles in the mixture (CRN_{av}) to that which would be expected in the ideal random mixture (CRN_i) i.e. $Saturation\ Index = \frac{CRN_{n,av}}{CRN_i}$. The variation of SI in both DCN and HSM are depicted in Figure 15 a and b respectively. It is interesting to observe that DCN and HSM differ in their approach towards the ideal Saturation Index limit (i.e. Saturation Index = 100%). HSM approaches it quickly while DCN does not approach the limit. A higher SI value for HSM at 100 rpm indicates aggregates containing both carrier and fine particles. The best mixing performance is represented by a combination of SI and

RSD which are obtained at 500 rpm. This condition also provides the maximum shear forces and high chaos. The rationale behind using high shear mixers to create ordered mixtures is clearer.

4.1.2 Effect of Material Properties

The study of material properties in isolation without affecting other attributes is not readily possible experimentally. However, this can be done *in silico* by DEM based studies. DEM simulations were done to assess the performance of the blenders for materials with different adhesive properties. High shear mixers are a popular choice to formulate ordered mixtures [23], but these mixers have some undesirable effects which can restrict their use. Shear sensitive drugs cannot be formulated for the risk of amorphization or a polymorphic transformation, and additional high energy spots on the carrier surface can be created, and loss of drug fines to the wall. Low shear blenders can be considered as an alternative, but the mechanical energy input, as seen in the preceding subsection; is low and may not lead to optimum mixing. The pertinent question of the choice of blender needs to be addressed by the formulator, and it is dependent upon the material properties of the mixture components. The variation of the Saturation Index in both the blenders also reveals the same information (Figure 16). It can be concluded that the low shear DCN is markedly dependent upon compensation by adhesive forces or triboelectric forces which can facilitate formation of ordered mixtures.

4.1.3 Quality Attributes for Ordered mixtures

(a) *Press on Forces*

Press on forces holding the fines and the coarse carrier particles are indeed critical to performance of the formulation blend. Figure 17 shows the normalized FPF for HSM and DCN respectively and reveal that higher drug concentrations indeed yield greater fine particle

fractions. This relates to a lower press-on force at higher drug concentrations which can explain a greater tendency to demix at higher drug concentrations, but release a greater FPF upon patient inspiration to have a therapeutic impact. This is very interesting to observe that the quality of the ordered mixtures, with respect to the press on forces, do not differ from both the blenders and thus the adhesive interactions for an ordered mixture are independent of the blender it was generated from. At higher drug load, surface coverage is envisaged to be multilayered so that the average compressive press-on forces decrease as outer layers are sampled.

(b) *Wall adhesion/Sticking*

Loss of cohesive fines to the equipment wall is undesirable, but often unavoidable. Increasing the speed in both the blenders increased the wall adhesion which is quantitatively monitored from the decline in average FPC with time from the bulk in both the blenders and visual observation. Quantitative estimation of wall adhesion is achieved by monitoring the change in the average FPC over time. Figures 18a and b graphically and visually show the sticking of fines to the vessel wall in the HSM respectively at various time instants. The same is shown for DCN in Figures 18c and d correspondingly. It is very interesting to observe the differing temporal evolution of wall adhesion in both the blenders; in DCN it decreases with time while HSM provides an opposite trend. HSM provides a much stronger velocity gradient, especially considering the fact that it is a smaller vessel and stronger impact of particles on the wall. High wall adhesion at 500 rpm in the HSM can also be understood from the DEM snapshots (Figure 14b). On the other hand, DCN provides weaker velocity field but biaxial rotations aid in provided necessary torques to dislodge the particles from the wall and bringing them back to the bulk.

(c) *Static Charging of Ordered mixtures*

Even though the quality of ordered mixtures cannot be discriminated, based on the pressure titration studies described earlier; the choice of equipment does impact the static charge on the final blend. Static charging for DPI powders has been recognized to impact the performance of mixtures significantly.[25] The histogram in Figure 19 demonstrates the variation of static charge with blenders and parameters (drug: carrier ratio and speed). Ten trials were done in each blender but no statistically valid inference could be drawn. The measurement procedure is coarse and merits a separate controlled study. However, it can be seen that the average charge is low (≈ 0.2 -0.5 nC/g) which suggests that that the magnitude of electrostatic force for this case is very small (<< 1%) relative to the overall adhesive force.[8] This could be the case because there is no work function differential between the carrier and the drug to drive electron transfer, which are both α-lactose monohydrate. However, there can be local charge patches which can arise due to impurities, surface defects and processing. Another reason for low charge observation is enhanced charge dissipation kinetics in the HSM which is fabricated out of stainless steel, in DCN the process intensity is low and a significant delay takes place in opening up the blender for analysis. Given the low charging, there is significant variation induced as the detection limit for the nano-Colombmeter is approached.

(d) *Abrasion of Carrier Fines*

Abrasion of carrier fines in HSM was found to be significantly higher than in DCN. High abrasion of carrier fines can decrease the shielding of active carrier sites and increase fine particle agglomeration as well and thereby impact FPF. Statistical analysis revealed that this phenomenon is most strongly influenced by speed ($P < 0.0001$), as highlighted in Figure 20a-d. The abrasion of carrier fines is observed as the % Change shifts increases from the previous time

points so as to indicate shearing off of the fines. In DCN, the % Change is always negative implying that more fines are incorporated within ordered units with time .In contrast, abrasion is observed in HSM especially at 500 rpm beginning at 120 sec while at 100 rpm, this effect is observed at 480 sec. The % Change for the size range < 1 μm i.e. the drug particles (Figure 5) is negligible as it is covered loosely and always aerosolized so that average FPC is recovered (Figure 18a and b) It is very interesting to observe that the smallest carrier fines do not significantly change implying that they adhere to the coarser particles, speculated to be due to small amorphous domains created during the high shear process while the bigger carrier fines tend to be sheared off the surface.

4.2 Segregation of Ordered mixtures from Hoppers

The ordered mixtures were formulated in the HSM at 100 rpm and characterized for RSD and FPC. The flow of ordered mixtures from the hopper was quantified and characterized as a function of drug load and fill volume. Positive control studies on a segregated mixture were performed which demonstrated the ability of the procedure to detect segregation. Except for the 2% mixture in the 75 ° hopper, none of the mixtures flowed readily , even after opening the outlet diameter, and so a fixed vibration source (24 Hz) was used to aid the flow . There was no observed segregation from the SGI vs time plots (Figure 21 a-d). This indicates the physical stability of the ordered mixtures. Figure 22 shows a DEM snapshot of the velocity field of the discharging of 100 mL of the 2% mixtures at different time points from the unvibrated 75° hopper. Hydrostatic pressure distribution, characteristic of a mass flow regime are observed. The flow in the 75° hopper was quicker than the 45° hopper which is expected. The hopper emptying time also compared very well with the experimental results, being approximately equal to 10 sec.

Increasing the drug load and the fill volume increased the discharge time, however there was no segregation of the blends observed.

5. Conclusions

Comprehensive experimental and computational DEM models were developed to map the dynamic interplay of material and process variables dictating formation of ordered mixtures for DPI formulations. Table 5 provides a summary of both the blenders with respect to different parameters which might influence choice of the formulator. The formation of ordered mixtures was studied in low shear double cone (DCN) and high shear mixers (HSM). The impact of process variables on mixing studied and it was determined that rotation speed, and drug ratio were very important in dictating the mixing in the HSM while the speed was the single most factor important in DCN. The effect of fill could not be determined with the range of fill levels used. Increased rotation speed and a central loading configuration were associated with the fastest mixing (but increased speed was also associated with a greater abrasion of carrier fines and wall adhesion of API. Ordered mixtures from DCN were formed after a much longer time, but had a lower carrier fines' abrasion. Press-on forces of the blend from both the blenders were not differentiable, but were found to be inversely related to the fines' loading which can lead to both processing difficulty but therapeutic efficacy. There was no observed segregation of the ordered mixtures from the hopper. DEM simulations revealed HSM achieved greater velocities but produced lower chaos, while the inverse was true for DCN. DCN was predicted to form ordered mixtures quickly given the adhesion between the drug and carrier was strong. The effect of material adhesion was not pronounced for HSM. HSM was also predicted to approach the theoretical limit of ideal ordered mixture in contrast to DCN.

6. Acknowledgements

The authors would like to acknowledge NSF-CPPR for funding the research. DFE Pharma is also thanked for providing the LH100 samples. Mark Drobney at University of Connecticut Dept. of Mechanical Technology is thanked for fabricating the hoppers. We acknowledge our gratitude to Dr Prabhakar Singh for assisting us with SEM imaging .Shariq Mohammed at the Dept. of Statistics is acknowledged for useful discussions on the setting up the statistical model. We are also grateful to several undergraduate students who have helped us with the experimentation: Mark Basile II, Aki Yamamoto, Blerta Mulla, Connor Walker and Madhumita Das.

7. References

1. Staniforth JN. 1987. British pharmaceutical conference science award lecture 1986: order out of chaos. *Journal of Pharmacy and Pharmacology* **39**(5):329-334.

2. Saharan VA, Kukkar V, Kataria M, Kharb V, Choudhury P. 2008. Ordered mixing: mechanism, process and applications in pharmaceutical formulations. *Asian Journal of Pharmaceutical Sciences* **3**:240-259.

3. Linsenbühler M, Wirth K-E. 2005. An innovative dry powder coating process in non-polar liquids producing tailor-made micro-particles. *Powder Technology* **158**(1):3-20.

4. Charnay C, Bégu S, Tourné-Péteilh C, Nicole L, Lerner D, Devoisselle J-M. 2004. Inclusion of ibuprofen in mesoporous templated silica: drug loading and release property. *European Journal of Pharmaceutics and Biopharmaceutics* **57**(3):533-540.

5. Mellaerts R, Mols R, Jammaer JA, Aerts CA, Annaert P, Van Humbeeck J, Van den Mooter G, Augustijns P, Martens JA. 2008. Increasing the oral bioavailability of the poorly water soluble drug itraconazole with ordered mesoporous silica. *European Journal of Pharmaceutics and Biopharmaceutics* **69**(1):223-230.

6. Nyström C, Westerberg M. 1986. The use of ordered mixtures for improving the dissolution rate of low solubility compounds. *Journal of Pharmacy and Pharmacology* **38**(3):161-165.

7. Thalberg K, Berg E, Fransson M. 2012. Modeling dispersion of dry powders for inhalation. The concepts of total fines, cohesive energy and interaction parameters. *International Journal of Pharmaceutics* **427**(2):224-233.

8. Finlay WH. 2001. The mechanics of inhaled pharmaceutical aerosols: an introduction. ed.: Academic Press.

9. Nguyen D, Rasmuson A, Björn IN, Thalberg K. 2015. Mechanistic time scales in adhesive mixing investigated by dry particle sizing. *European Journal of Pharmaceutical Sciences* **69**:19-25.

10. Labiris NR, Dolovich MB. 2003. Pulmonary drug delivery. Part II: the role of inhalant delivery devices and drug formulations in therapeutic effectiveness of aerosolized medications. *British Journal of Clinical Pharmacology* **56**(6):600-612.

11. Apte S. 2012. Excipient-API interactions in dry powder inhalers. *Journal of Excipients and Food Chemicals* **3**(4):129-142.

12. Marriott C, Frijlink HW. 2012. Lactose as a carrier for inhalation products: breathing new life into an old carrier. *Advanced Drug Delivery Reviews* **64**(3):217-219.

13. Guenette E, Barrett A, Kraus D, Brody R, Harding L, Magee G. 2009. Understanding the effect of lactose particle size on the properties of DPI formulations using experimental design. *International Journal of Pharmaceutics* **380**(1):80-88.

14. Sundell-Bredenberg S, Nyström C. 2001. The possibility of achieving an interactive mixture with high dose homogeneity containing an extremely low proportion of a micronised drug. *European Journal of Pharmaceutical Sciences* **12**(3):285-295.

15. Kaialy W, Nokhodchi A. 2012. Antisolvent crystallisation is a potential technique to prepare engineered lactose with promising aerosolisation properties: effect of saturation degree. *International Journal of Pharmaceutics* **437**(1):57-69.

16. Kawashima Y, Serigano T, Hino T, Yamamoto H, Takeuchi H. 1998. Effect of surface morphology of carrier lactose on dry powder inhalation property of pranlukast hydrate. *International Journal of Pharmaceutics* **172**(1):179-188.

17. Littringer EM, Mescher A, Schroettner H, Achelis L, Walzel P, Urbanetz N. 2012. Spray dried mannitol carrier particles with tailored surface properties–The influence of carrier surface roughness and shape. *European Journal of Pharmaceutics and Biopharmaceutics* **82**(1):194-204.

18. Cline D, Dalby R. 2002. Predicting the quality of powders for inhalation from surface energy and area. *Pharmaceutical Research* **19**(9):1274-1277.

19. Podczeck F. 1998. Adhesion forces in interactive powder mixtures of a micronized drug and carrier particles of various particle size distributions. *Journal of Adhesion Science and Technology* **12**(12):1323-1339.

20. Tong HH, Shekunov BY, York P, Chow AH. 2006. Predicting the aerosol performance of dry powder inhalation formulations by interparticulate interaction analysis using inverse gas chromatography. *Journal of Pharmaceutical Sciences* **95**(1):228-233.

21. Price R, Young P, Edge S, Staniforth J. 2002. The influence of relative humidity on particulate interactions in carrier-based dry powder inhaler formulations. *International Journal of Pharmaceutics* **246**(1):47-59.

22. Murtomaa M, Mellin V, Harjunen P, Lankinen T, Laine E, Lehto V-P. 2004. Effect of particle morphology on the triboelectrification in dry powder inhalers. *International Journal of Pharmaceutics* **282**(1):107-114.

23. Bridson R, Robbins P, Chen Y, Westerman D, Gillham C, Roche T, Seville J. 2007. The effects of high shear blending on α-lactose monohydrate. *International Journal of Pharmaceutics* **339**(1):84-90.

24. Zeng XM, Martin GP, Tee S-K, Ghoush AA, Marriott C. 1999. Effects of particle size and adding sequence of fine lactose on the deposition of salbutamol sulphate from a dry powder formulation. *International Journal of Pharmaceutics* **182**(2):133-144.

25. Young PM, Sung A, Traini D, Kwok P, Chiou H, Chan H-K. 2007. Influence of humidity on the electrostatic charge and aerosol performance of dry powder inhaler carrier based systems. *Pharmaceutical Research* **24**(5):963-970.

26. Coates MS, Fletcher DF, Chan HK, Raper JA. 2004. Effect of design on the performance of a dry powder inhaler using computational fluid dynamics. Part 1: grid structure and mouthpiece length. *Journal of Pharmaceutical Sciences* **93**(11):2863-2876.

27. De Boer A, Chan H, Price R. 2012. A critical view on lactose-based drug formulation and device studies for dry powder inhalation: which are relevant and what interactions to expect? *Advanced Drug Delivery Reviews* **64**(3):257-274.

28. Manickam S, Shah R, Tomei J, Bergman T, Chaudhuri B. 2010. Investigating mixing in a multi-dimensional rotary mixer: Experiments and simulations. *Powder Technology* **201**(1):83-92.

29. Naik S, Sarkar S, Gupta V, Hancock BC, Abramov Y, Yu W, Chaudhuri B. 2015. A combined experimental and numerical approach to explore tribocharging of pharmaceutical excipients in a hopper chute assembly. *International Journal of Pharmaceutics* **491**(1):58-68.

30. Sarkar S, Cho J, Chaudhuri B. 2012. Mechanisms of electrostatic charge reduction of granular media with additives on different surfaces. *Chemical Engineering and Processing: Process Intensification* **62**:168-175.

31. Nelder JA, Baker R. 1972. Generalized linear models. *Encyclopedia of Statistical Sciences*.

32. Akaike H. 1974. A new look at the statistical model identification. *Automatic Control, IEEE Transactions* **19**(6):716-723.

33. Walton OR, Braun RL. 1986. Viscosity, granular- temperature, and stress calculations for shearing assemblies of inelastic, frictional disks. *Journal of Rheology* **30**(5):949-980.

34. Chaudhuri B, Muzzio FJ, Tomassone MS. 2006. Modeling of heat transfer in granular flow in rotating vessels. *Chemical Engineering Science* **61**(19):6348-6360.

35. Faqih AN, Chaudhuri B, Mehrotra A, Tomassone MS, Muzzio F. 2010. Constitutive model to predict flow of cohesive powders in bench scale hoppers. *Chemical Engineering Science* **65**(10):3341-3351.

36. Alexander AW, Chaudhuri B, Faqih A, Muzzio FJ, Davies C, Tomassone MS. 2006. Avalanching flow of cohesive powders. *Powder Technology* **164**(1):13-21.

List of Tables

Sample	d_{10} (µm)	d_{50} (µm)	d_{90} (µm)	Tapped Density (g/cc)	Bulk Density (g/cc)	Carr's Index	Hausner's Ratio	Specific Surface Area (m^2/g)
Lactohale100 (LH100,Carrier)	64	137	215	0.84	0.69	19%	1.2	0.1
Lactose Fines (AZFL,Drug)	1	3	6	0.52	0.26	49%	2.0	4.3

Table 1: Particle size and cohesivity of powders used for the study

Formation of Ordered mixtures	
Mixer	High Shear Mixer (HSM),Double Cone Blender (DCN)
Loading Configuration	Top-bottom (TL), Central (CL)
Fill (%)	30,45
Rotational Speed (rpm)	Double Cone Blender :10,30 High Shear Mixer : 100,500
Segregation of Ordered mixtures	
Hopper Angle (°)	45 , 75
Fill Volume (mL)	50,100,150

Table 2: Parametric studies for evaluation of effect of process variables in formation and segregation of ordered mixture

DEM parameters	
Radius of coarse particle (mm)	3
Diameter of fine particles (mm)	1
Number of coarse particles	3780(DCN),1974(HSM)
Number of fine particles	5732(DCN),2804(HSM)
Cohesivity factor for coarse-coarse collisions (K_{bb})	20
Cohesivity factor for coarse-fine collisions(K_{bs})	50
Cohesivity factor fine-fine collisions(K_{ss})	70
Density of particles(kg/m^3)	1500
Coefficient of Restitution : inter-particle	0.65
Coefficient of restitution:particle-wall	0.5
Normal Stiffness : inter-particle (N/m)	6000
Normal Stiffness: particle-wall (N/m)	6000
Coefficient of Friction	0.7
Time Step (μs)	0.5

Table 3: DEM parameters used for the study.

HSM		DCN	
Time	<0.001	Time	<0.001
Speed	0.01	Speed	0.02
Ratio	0.04	Ratio	0.22
Fill	0.37	Fill	0.33
Loading Configuration	0.03	Speed*Ratio	0.38
-	-	Loading Configuration*Ratio	0.59

Table 4: Statistical significance of the process variables under study. The model explains the variability in the RSD data was chosen. The RSD was statistically different at different time points.

Parameters	HSM	DCN
Mixing Time	++	--
Press –on Forces	+	+
Wall Adhesion of Fines	--	+
Static Charging of Blends	+	+
Abrasion of carrier fines	--	++
Segregation	+	+

Table 5: Qualitative comparison of the blenders with respect to different parameters

List of Figures

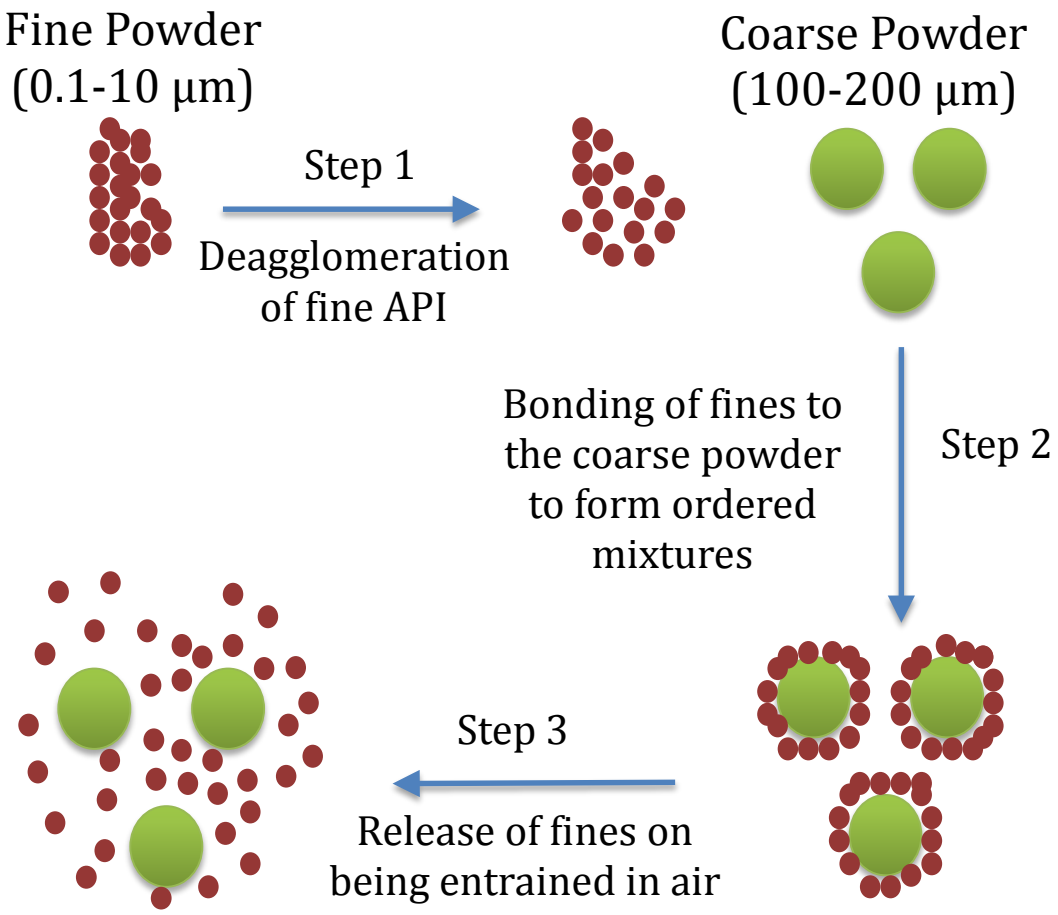

Figure 1. Schematic diagram showing processes involving formation of ordered mixtures and subsequent release of fines

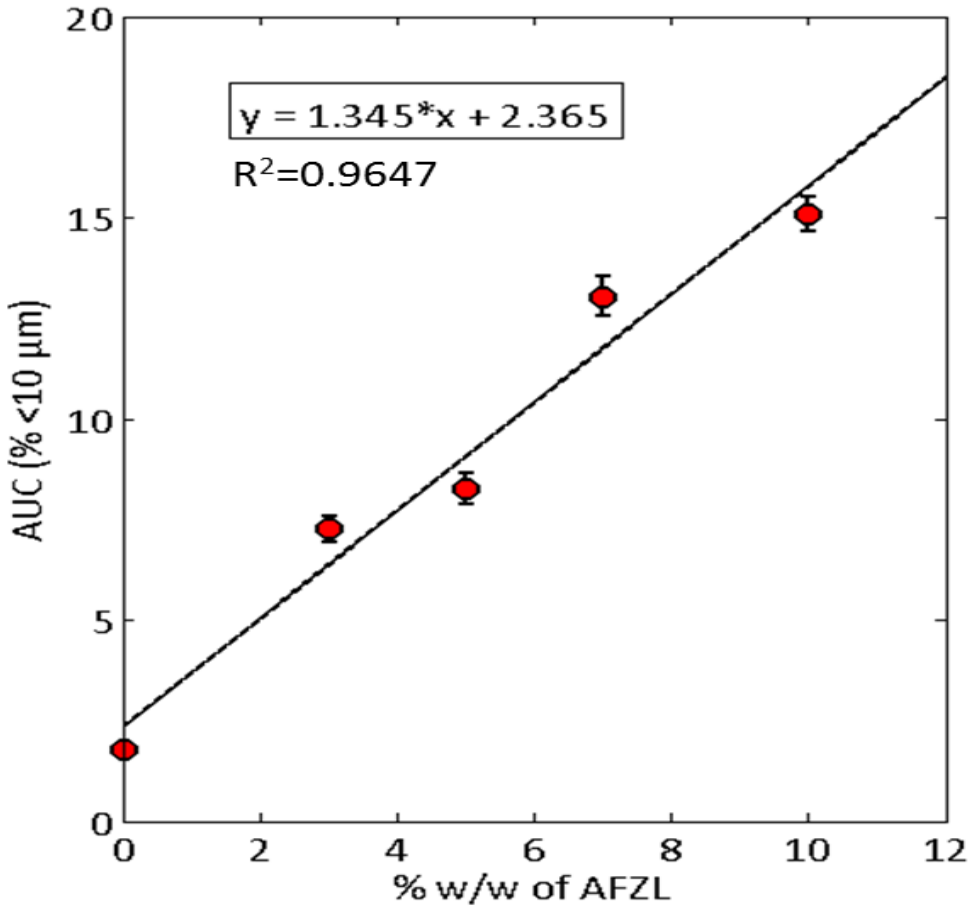

Figure 2. Linearity and Sensitivity of the Analytical Method. The intercept indicates the presence of carrier fines, while the slope indicates the sensitivity of the instrument in the concentration region of interest

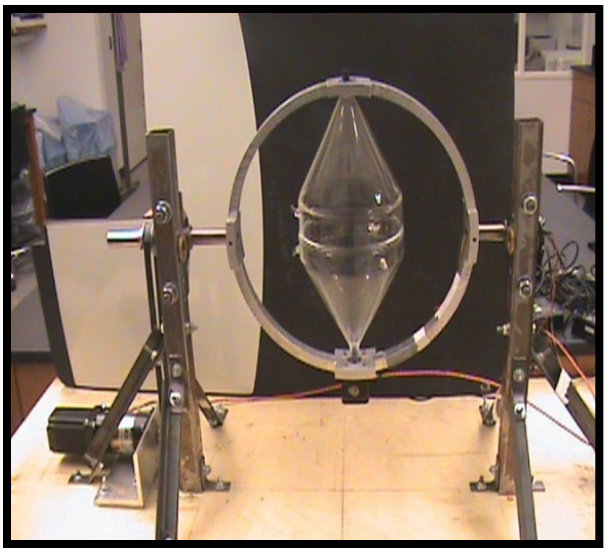

(a) **(b)**

Figure 3. Blenders used for the study : (a) Double Cone Blender (DCN) (b)High Shear Mixer (HSM). DCN is an in-house biaxial blender which can rotate up to speeds of 40 rpm about both vertical or horizontal axes. On the other hand, HSM (KG5, Key Intl.) has a 1L bowl capacity in which the impeller can reach speeds up to 750 rpm

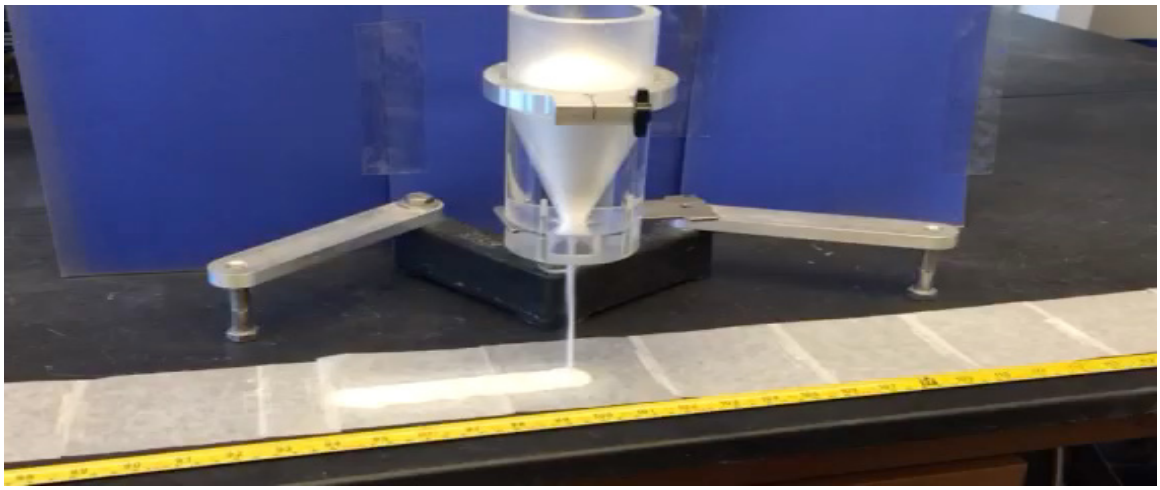

Figure 4.Experimental set up for studying segregation of ordered mixtures from a hopper. The hopper mass is discharged onto a moving belt made out of weighing paper. The time of discharge is estimated from the attached ruler, which is also used to evenly distribute the discharged mass.

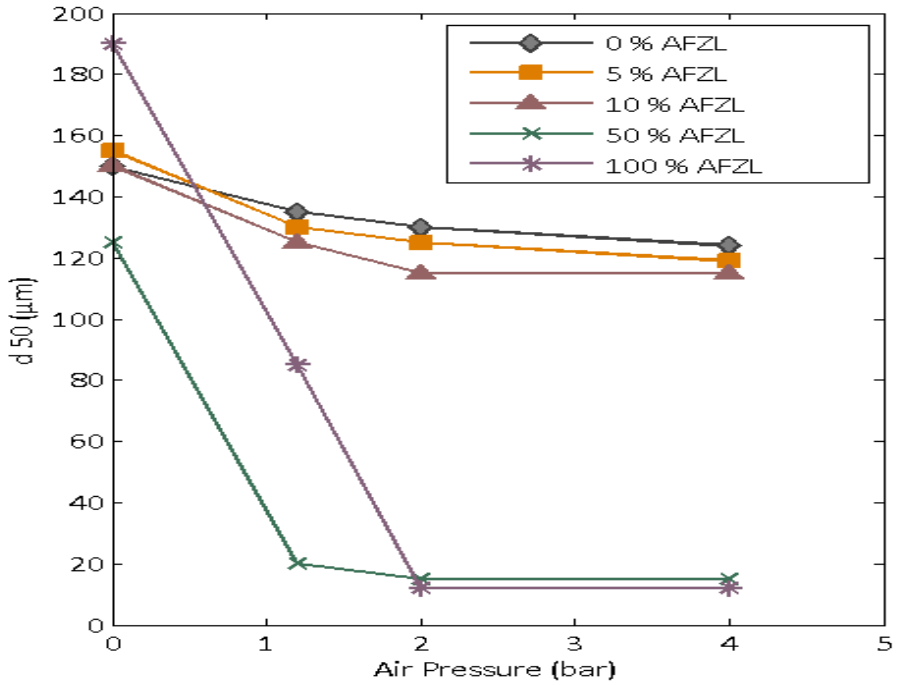

Figure 5. Pressure titration studies for different carrier-drug blends. The difference in cohesivities of the two powders can be judged from the difference in slopes.

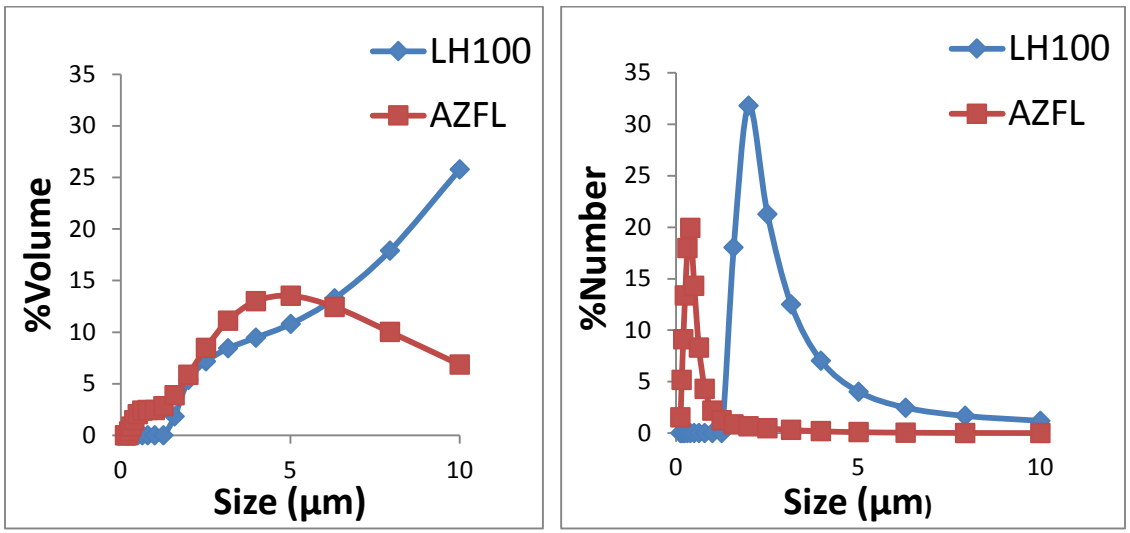

Figure 6. Particle size distribution under 10 µm for the LH100 and AZFL as determined by (a) Volume distribution and (b) Number distribution. The number distribution plot can distinguish the carrier and drug fines clearly in contrast to the volume weighed plot

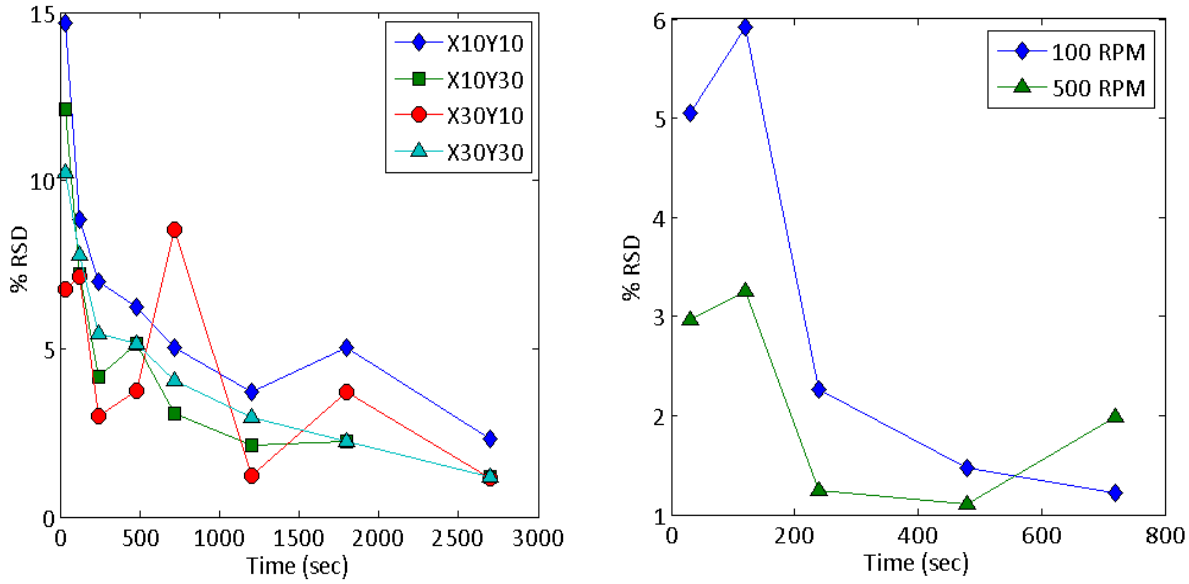

(a) **(b)**

Figure 7. Variation of % RSD as function of speed for both (a) DCN and (b) HSM. Higher speed causes demixing which is statistically significant. Mixing is much quicker in HSM.* A speed of X30Y10 denotes a rotation speed of 30 rpm and 10 rpm around the X and Y axes respectively.

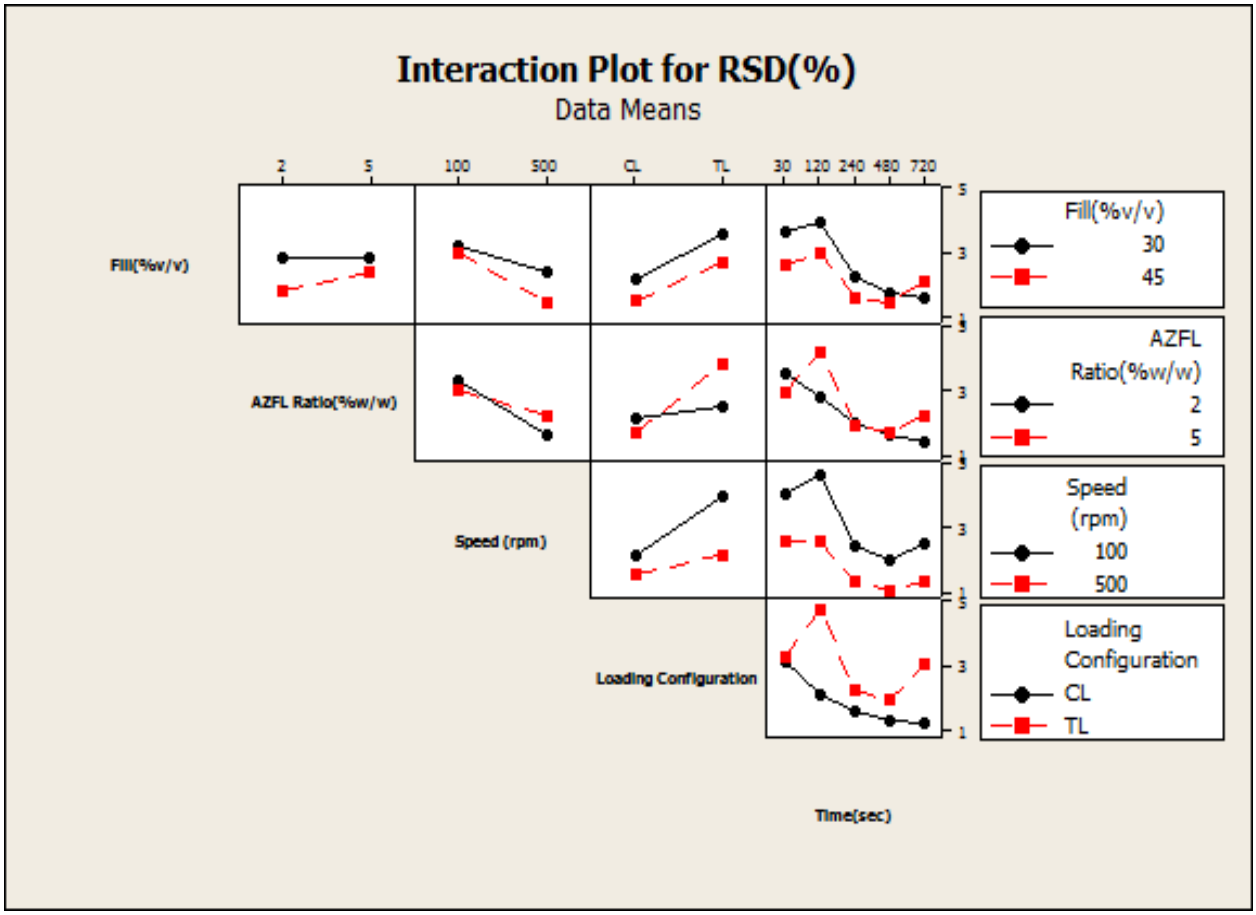

Figure 8. Interaction plot showing interaction of different variables under study for HSM generated from generated *from Minitab 17.0*

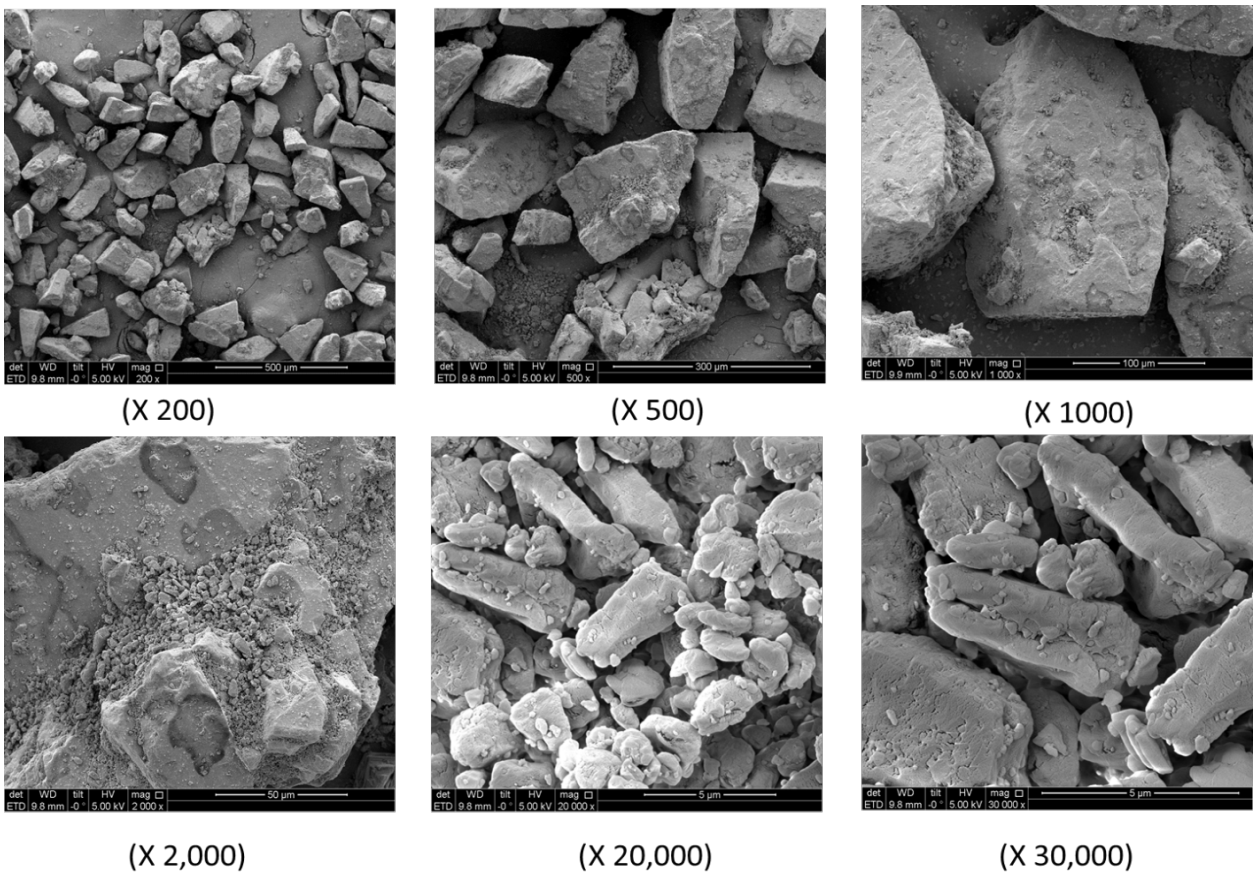

Figure 9. SEM images showing ordered mixtures at different resolutions.

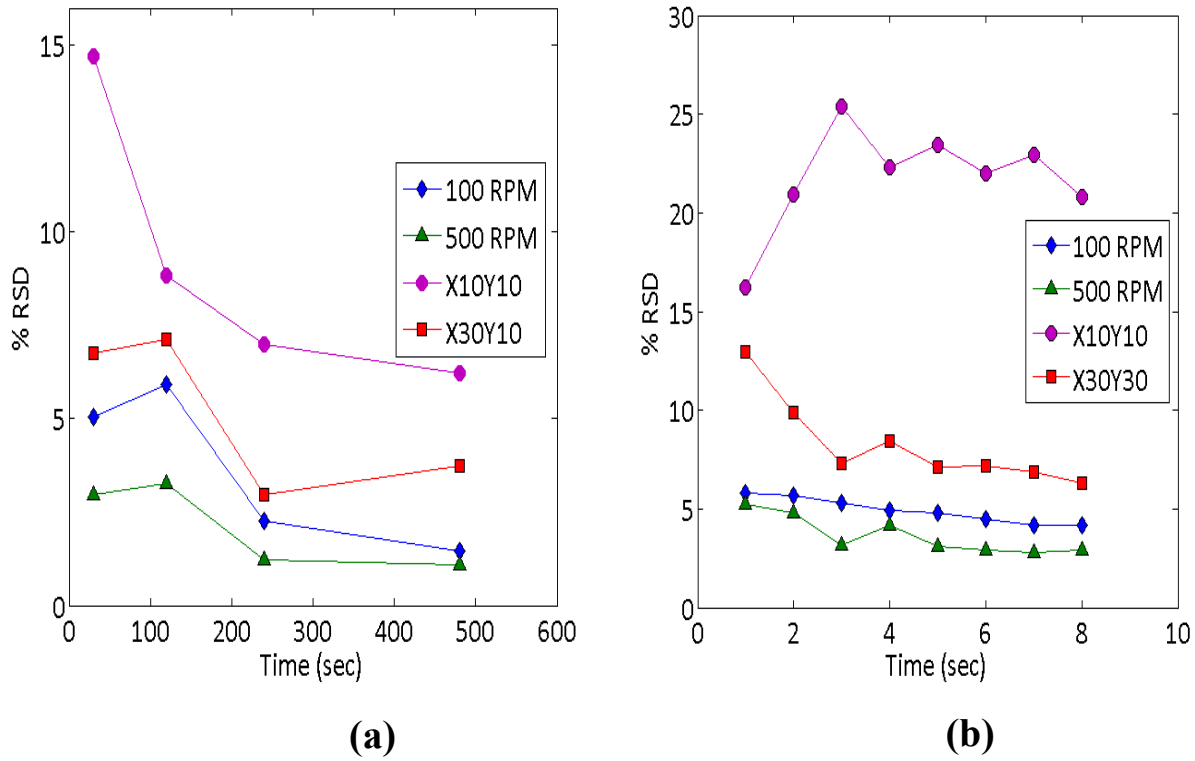

(a) **(b)**

Figure 10. Correlation between experiments and simulations for progression of mixing in the blenders.

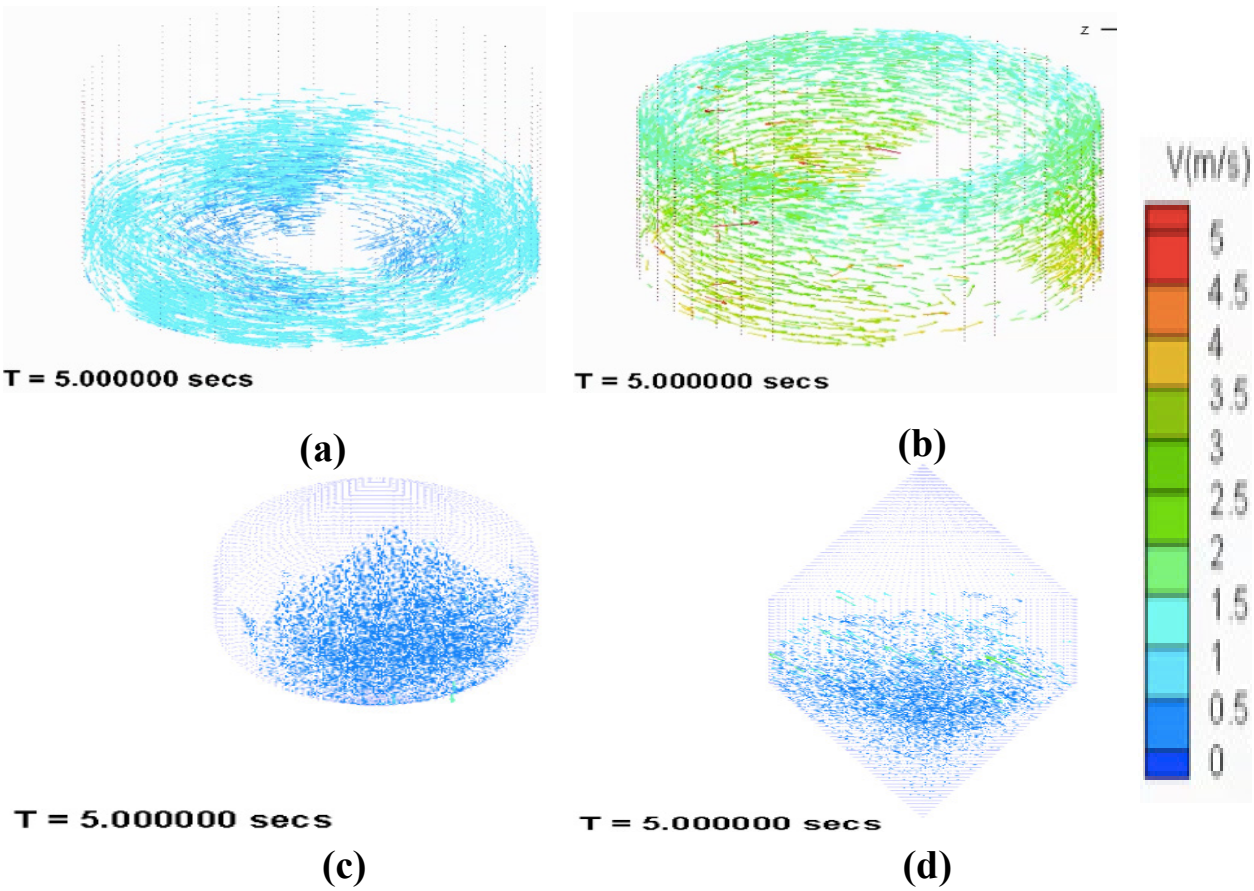

Figure 11. Snapshot showing comparison between the DCN and HSM blenders after 5 sec. In the HSM, significant amount of ordered units are formed at (a) 100 rpm and (b) 500 rpm relative to those in DCN at (c) X10Y10 and (d) X30Y10.There is pronounced segregation at X10Y10 relative to X30Y10

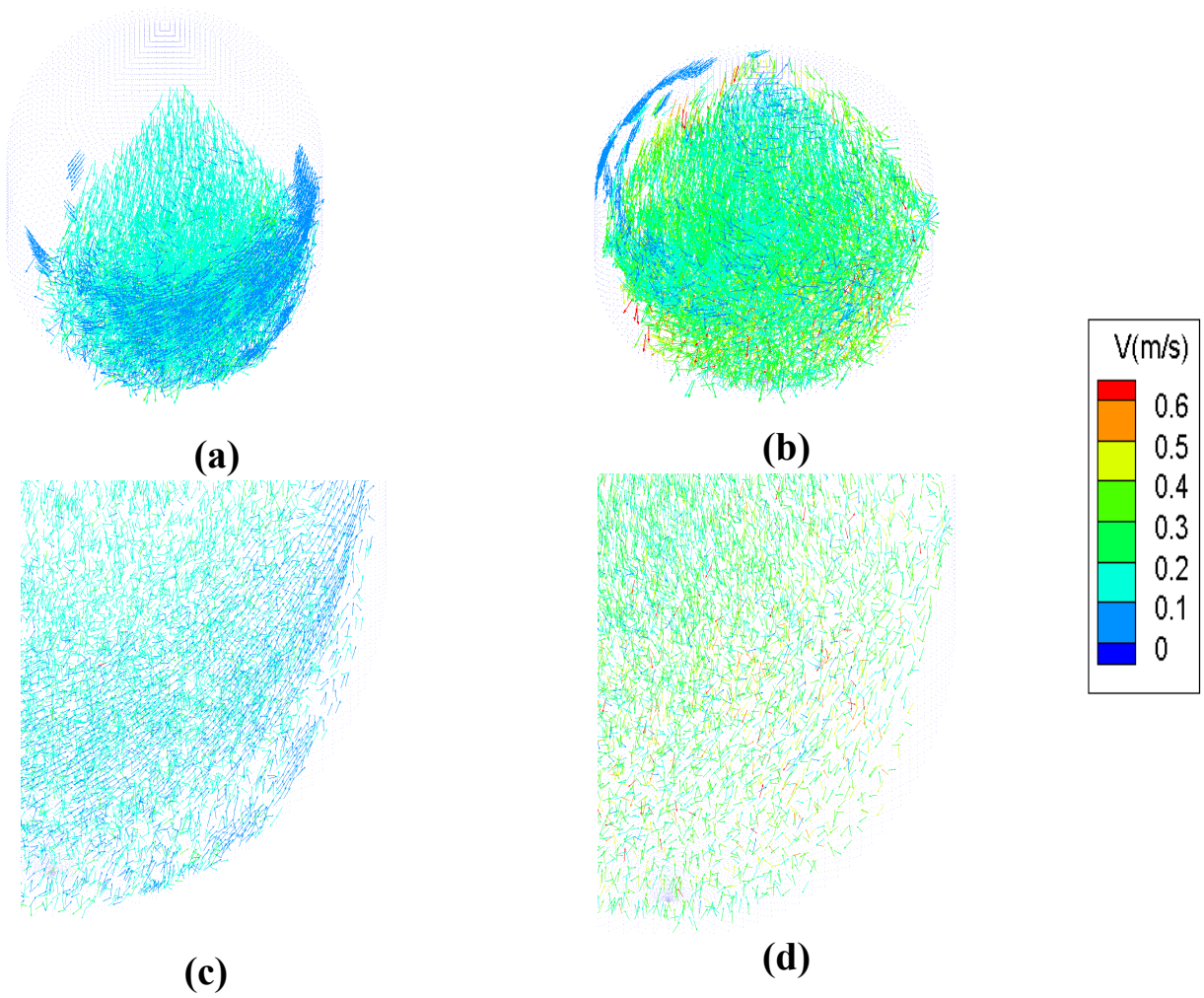

Figure 12. Velocity vectors with constant length in the DCN blender at the same tumbling position at (a,c) X10Y10 (b,d) X30Y10.The bottom images zoom around the region near the wall.

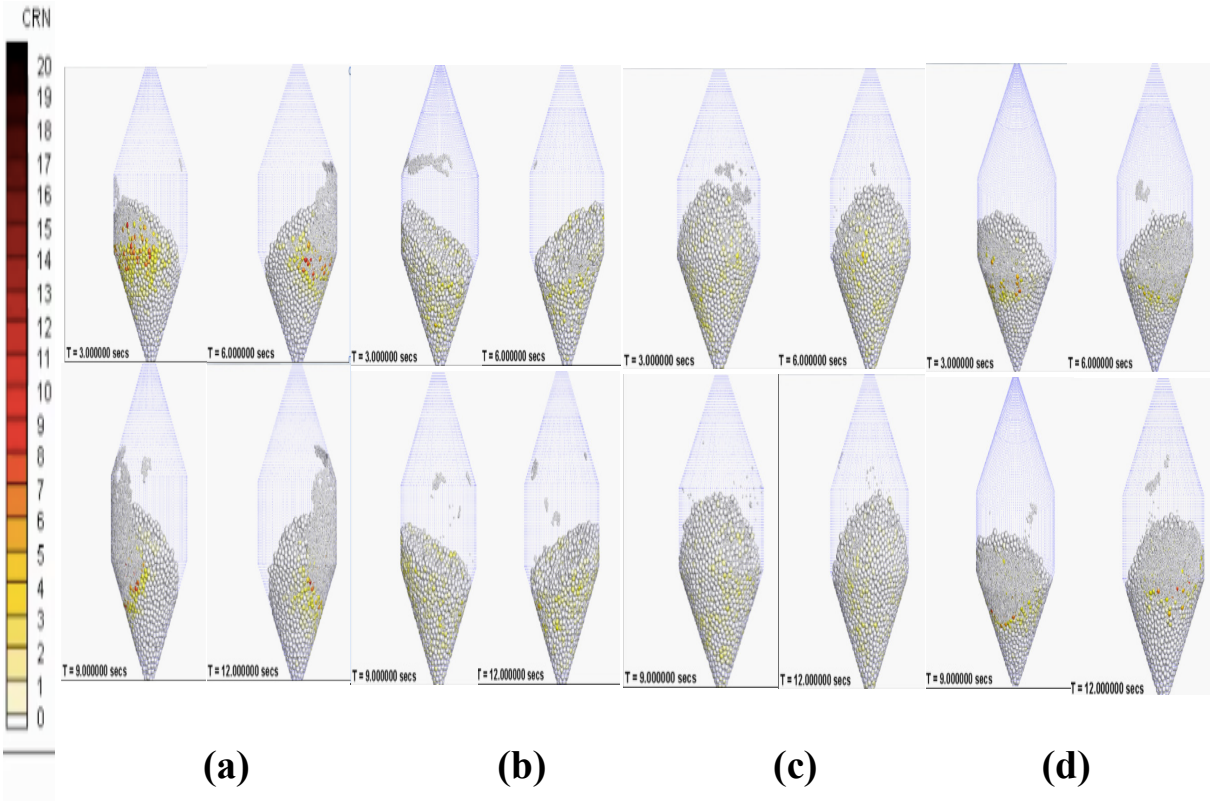

Figure 13. Snapshot showing formation of ordered mixtures in DCN colored according their CRN at fixed time instants (3s, 6s, 9s, and 12s) at different speeds (a) X10Y10 (b) X10Y30 (c) X30Y10 (d) X30Y30.It can be seen that when the speed of rotation around both the axes is the same, there is increased segregation of fines and poor ordered mixture formation

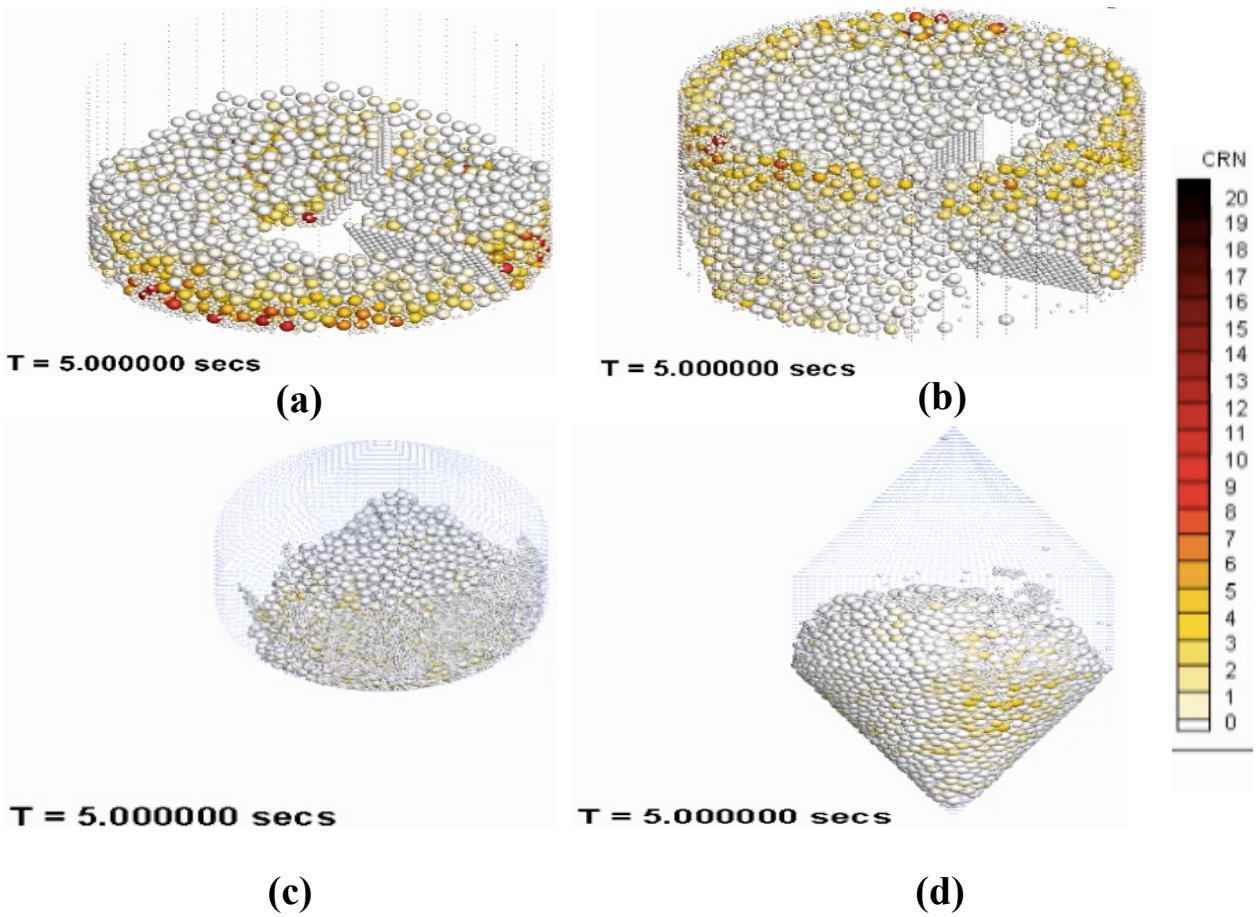

Figure 14. Snapshot showing comparison between the DCN and HSM blenders after 5 sec. In the HSM, significant amount of ordered units are formed at (a) 100 rpm and (b) 500 rpm relative to those in DCN at (c) X10Y10 and (d) X30Y10.There is pronounced segregation at X10Y10 relative to X30Y10

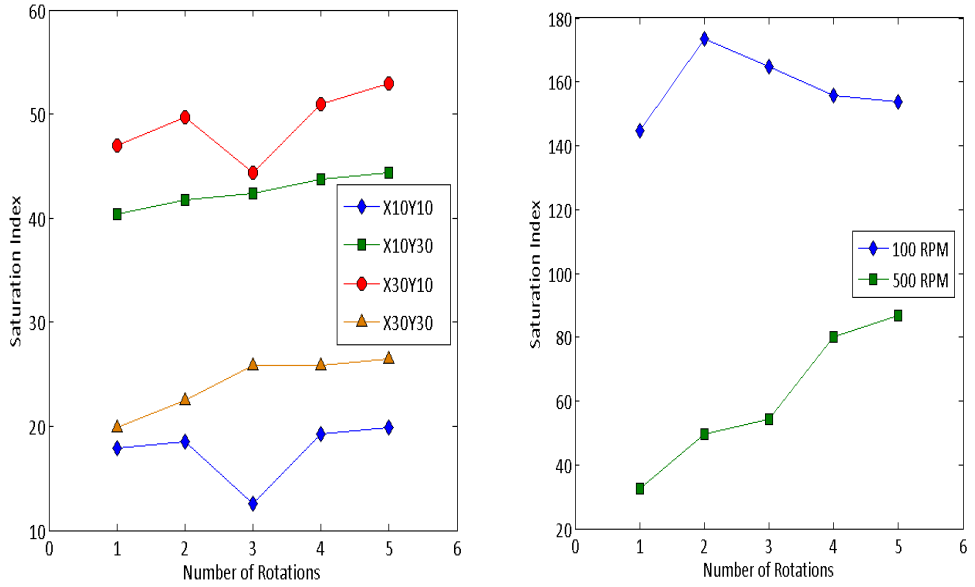

Figure 15. Effect of rotation speed in with a fixed adhesive force (Kbs =50) between fine and coarse particles in (a) DCN (b) HSM. It can be seen that for DCN, the value of 100 is never approached while HSM does approach the limit.

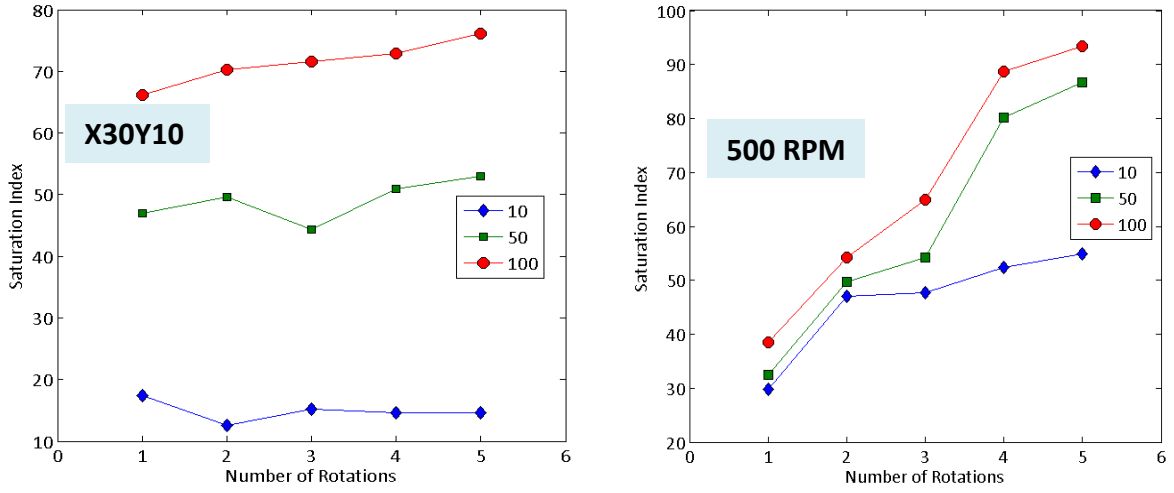

Figure 16. Effect of adhesion at given speed in (a) DCN at X30Y10, and (b) HSM at 500 rpm. It can be seen that for DCN, the value of 100 is never approached while HSM does approach the limit.

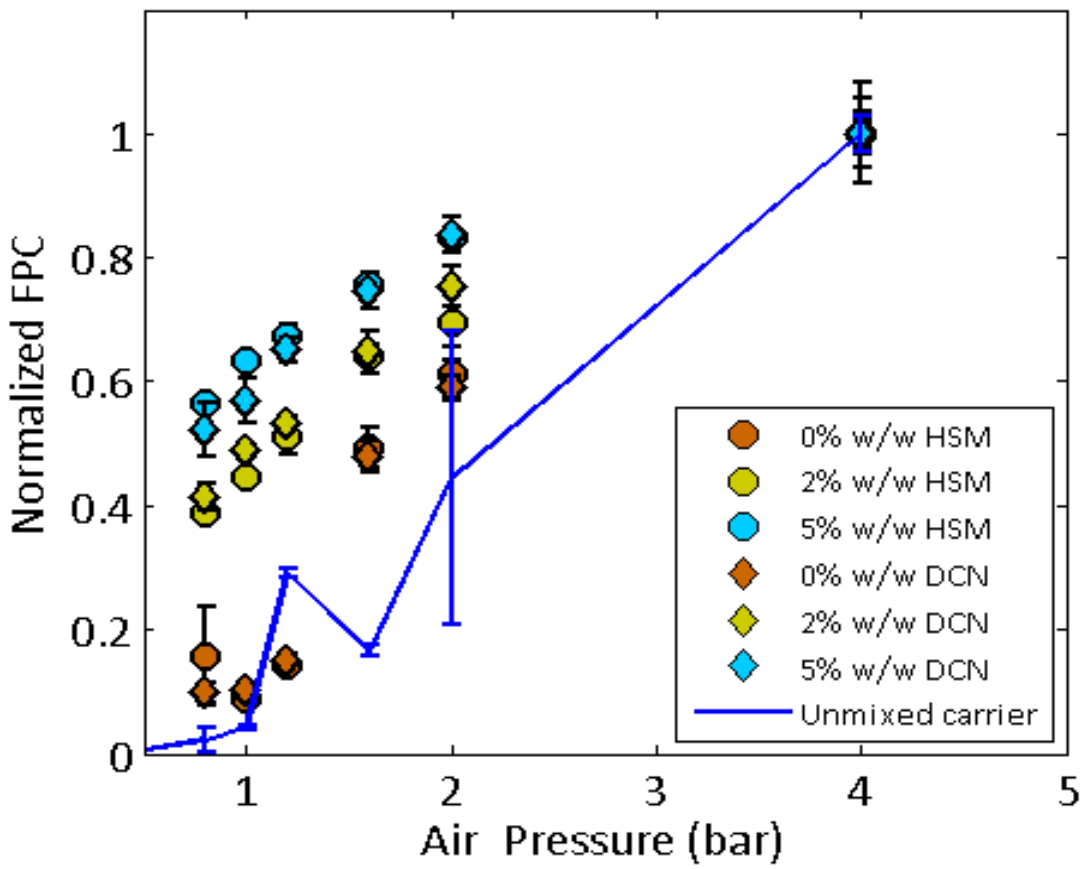

Figure 17. Press on forces within the ordered mixture, as estimated by the normalized FPC as a function of blender type and drug ratio. The press on forces decrease with increasing drug load but do not differ between blenders

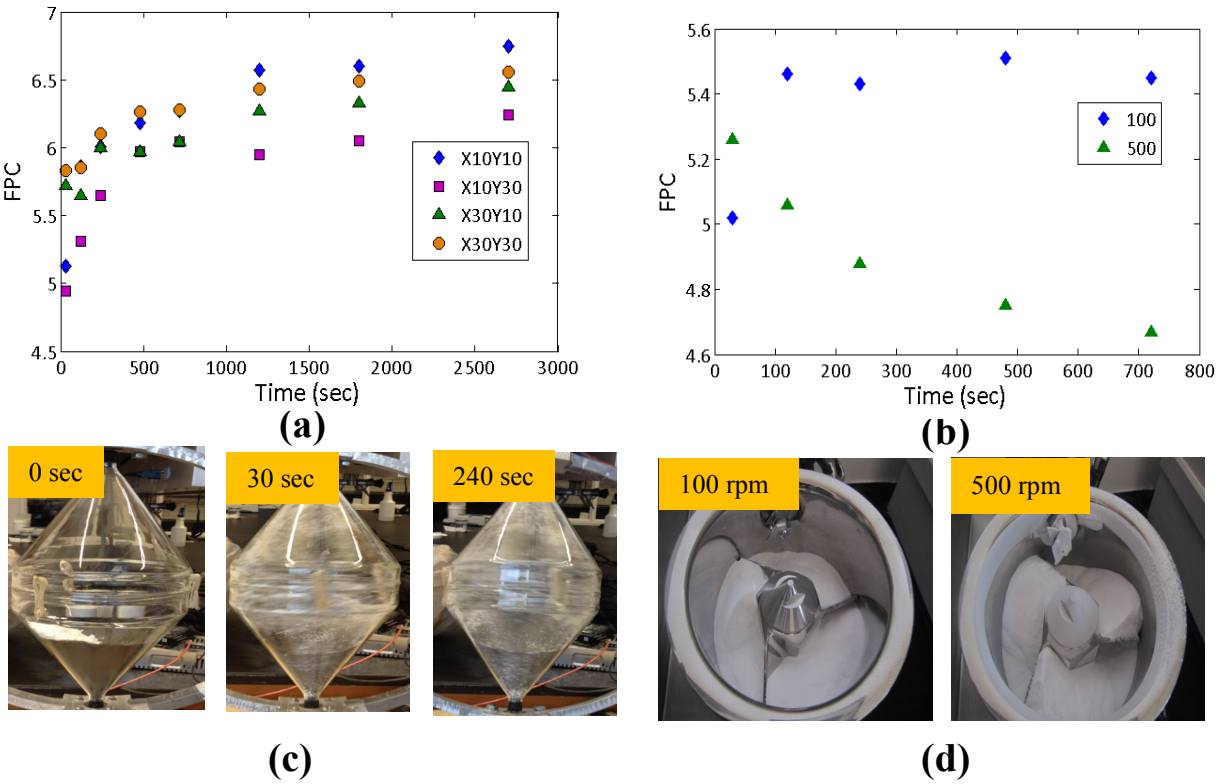

Figure 18. Wall adhesion of fines within the blenders. Temporal evolution of average FPC in (a) DCN and (b) HSM (c) Visual representation of adhesion in the DCN. As shown by mixing art sand and AZFL (for visual clarity) at X30Y10 and (d) Wall adhesion of fines in HSM at 100rpm and 500 rpm. * Art sand of the same size range as LH100 was used in the DCN snapshots for visual clarity

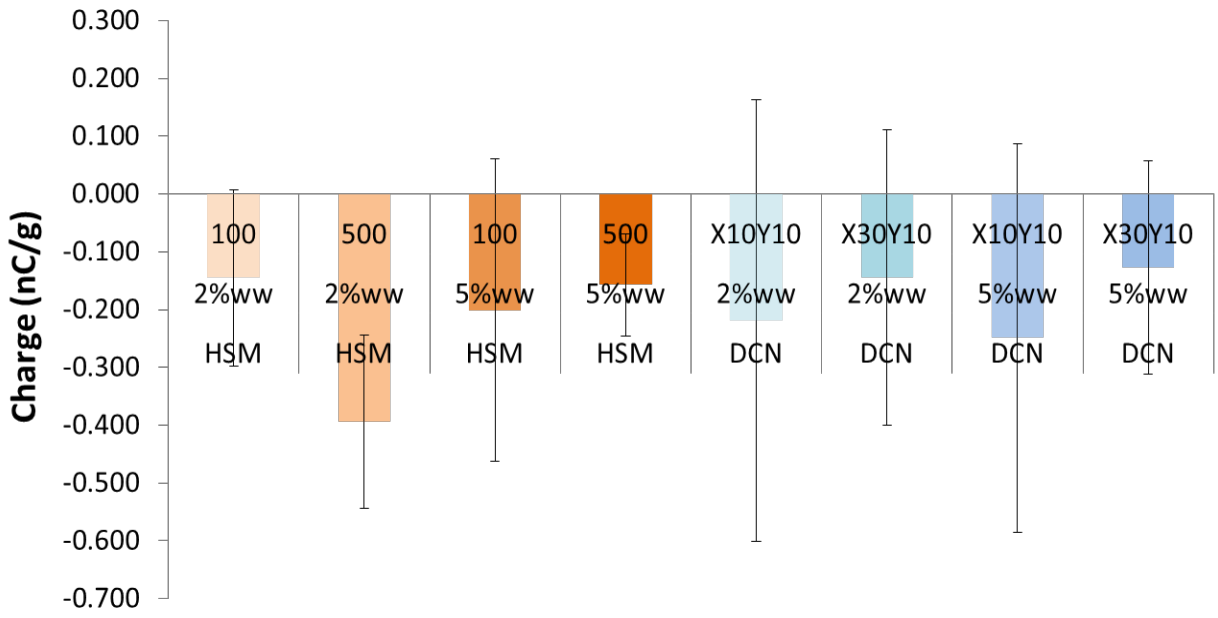

Figure 19. Static charging of the blends in DCN and HSM as a function of drug load and speed. The charging is low and there is poor reproducibility of the data

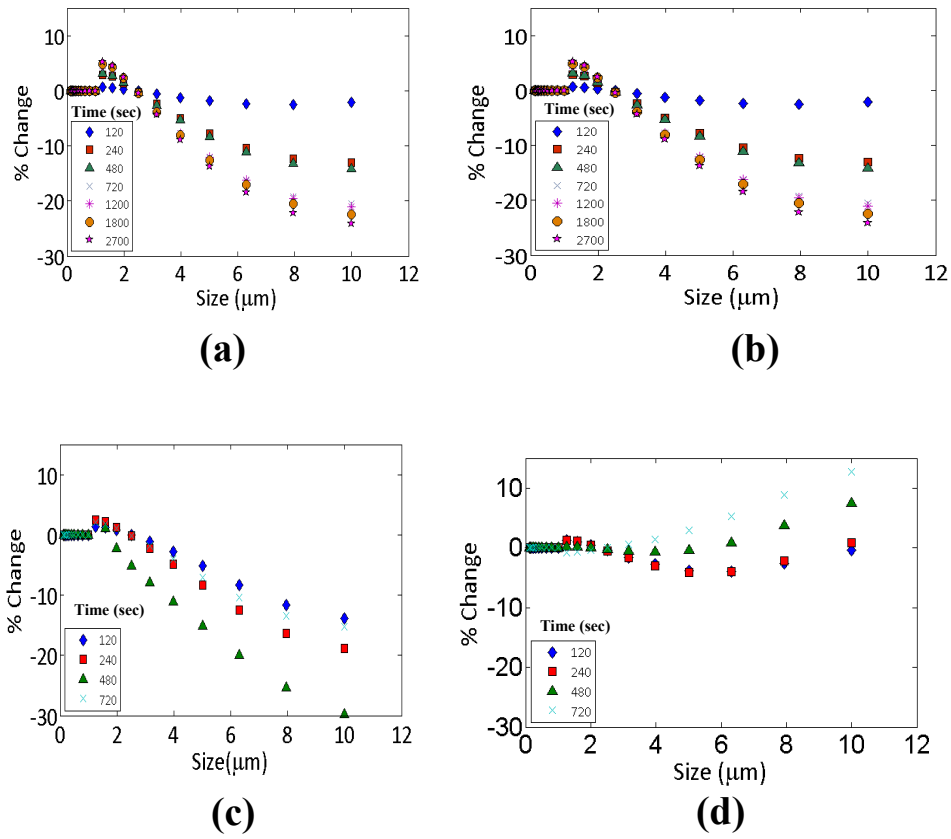

Figure 20. Change in FPC at different time points relative to 30 sec as determined from the number weighed PSD plots in DCN at (a) X10Y10 (b) X30Y10 and HSM at (c) 100 rpm (d) 500 rpm. No carrier fines' abrasion is observed in DCN while this effect is significant in the HSM at 500 rpm. Data at 30% fill and CL configuration is reported

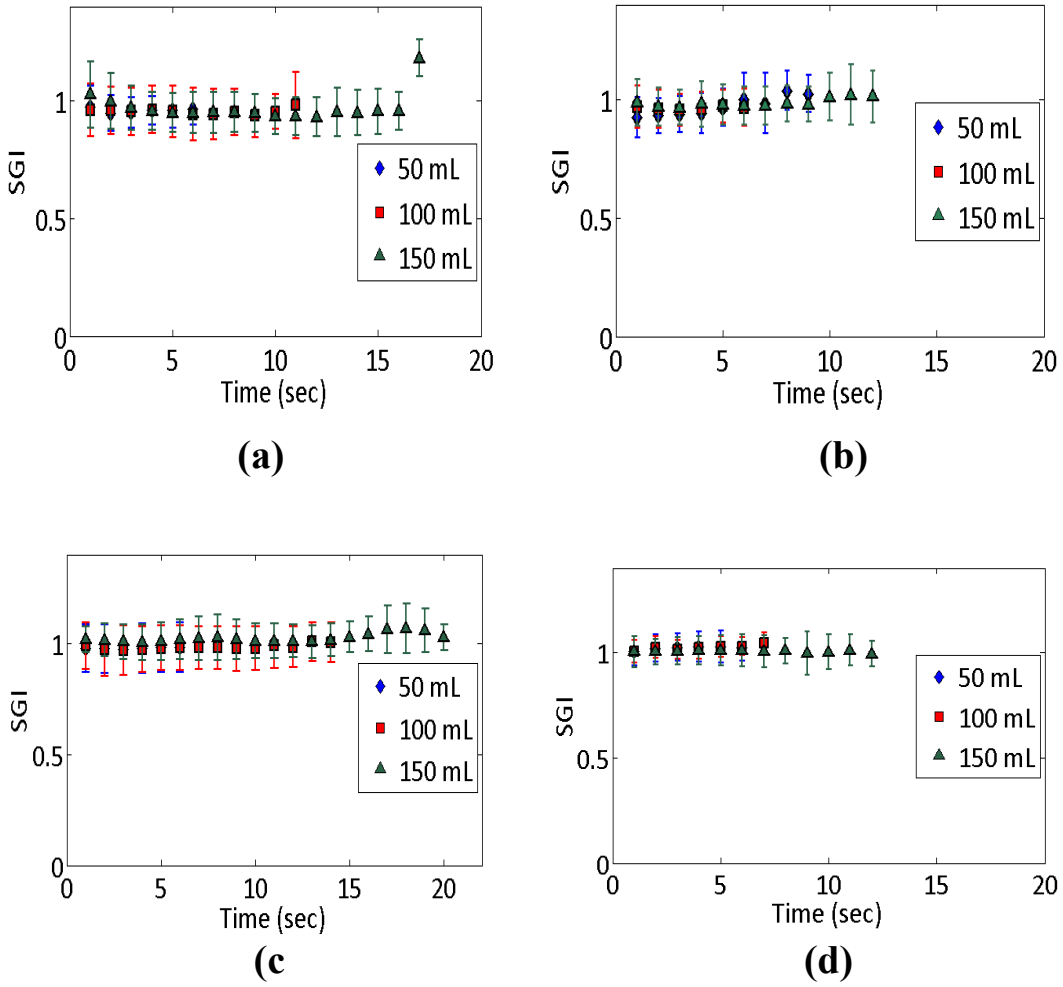

Figure 21. Variation of SGI as in the hoppers as a function of fill volume and drug load : (a) 45°hopper ,2%w/w mixture (b) 45°hopper ,5%w/w mixture (c) 45°hopper ,2%w/w mixture (d) 75°hopper ,5%w/w mixture

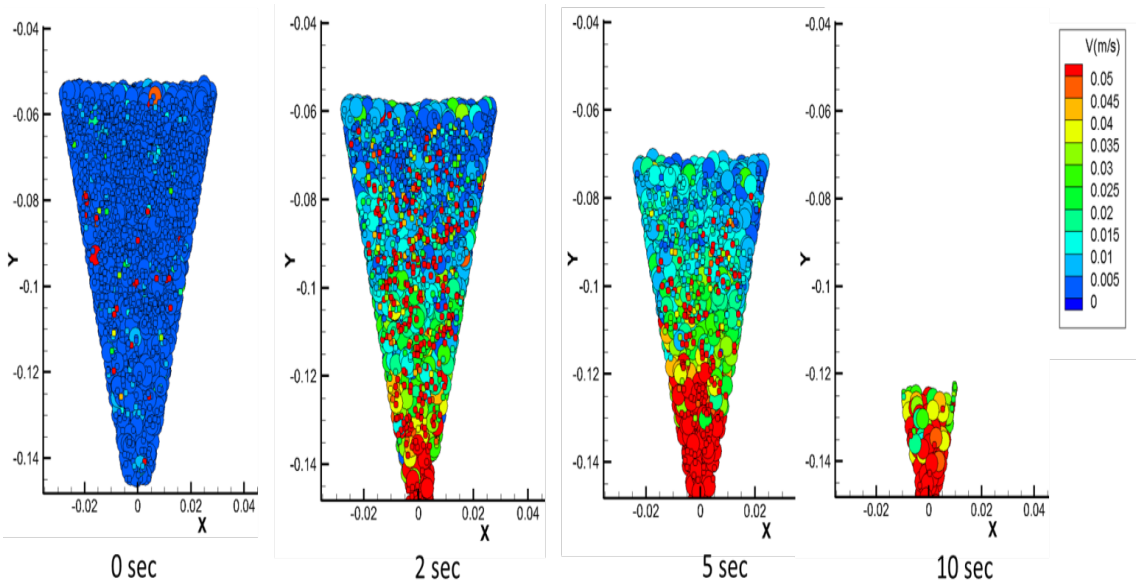

Figure 22. Variation of particle velocities with time during discharge of the 2% w/w mixture from the unvibrated 75^0 hopper. Mid plane (Z=0) contours are represented

Chapter 5

Triboelectrification of Binary Mixtures

Abstract

The study presents the results of an investigation of the role of different operational and material variables in the triboelectrification process and subsequent charge remediation by addition of different additives under typical production conditions encountered in the industry (35±5% RH, 25±2°C). Different particle types, surfaces, additives and their concentrations are considered as variables for the study. It was found that charge reduction linearly increased with increasing concentrations before plateauing off at higher concentrations for all additives. The extent of charge reduction was found to be a function of both moisture content and work function of the additives. Multiscale modeling approaches using semi empirical quantum mechanics and Discrete Element Method (DEM) based modeling was done to investigate the role of work function in determining tribocharging of mixtures. The work function difference model was found to be a good quantitative predictor of tribocharging of pure systems on a given surface, but quantitative predictions for binary mixtures involving were found to be relatively poor.

Keywords: Triboelectrification, work function, powders, molecular dynamics (MD), discrete element method (DEM), hygroscopicity

1. Introduction

Triboelectrification, defined as the static charging of materials on contact, occurs due to charge transfer or separation between the contacting materials. This phenomena was known to the early Greeks and ever since many technological applications have been built around it, however the fundamental understanding remains poor. This is cause of concern for the pharmaceutical industry, where tribocharging is largely an undesirable phenomena causing sticking of fine powder, particle jamming, flow instabilities, poor API dispersal in inhalers etc.[1-3] The main point of contention is the nature of the charge transfer species, whether it is an electron supporting the work function (defined as the minimum energy required in removing an electron from Fermi level to free space) difference theory [4-10] or an ion.[11-13] The argument behind the electron transfer theory is that electron is the fundamental charge unit and this model is widely accepted for metals. However, proponents of the alternate ion transfer mechanism criticize this theory on grounds of energy requirements as the work function difference is typically significantly greater than the ambient thermal energy; and insulators have no free electrons. However, there are no perfect insulators as demonstrated by high energy electrons from photoluminescence experiments[14] and electrons do exist in the forbidden gap. The work function of insulators has been calculated from the HOMO LUMO gap.[15] The other major theories that have been proposed are ion transfer[13,16] and selective adsorption of impurities, specifically moisture[17,18] to explain generation of static charges on powders. For typical materials encountered in the pharmaceutical industry under a production environment of about 40%RH, the thickness of adsorbed monolayer of water is much less than Debye length of aqueous solutions.[19] This implies that the particles are not independent spatially and there is possibility of ions dissolved at the surface moving to another surface in close proximity through a linked liquid

film or bridge. At the thicknesses of water layer greater than 3nm, one typically deals with the properties of bulk water which provides a great grounding path for the generated charges leading to dampening of charges. It has been documented that the moisture increases conductivity of ions linearly in a sub-monolayer regime and later exponentially after a monolayer is formed.[20] The high dielectric constant of water also decreases electrostatic interactions between particles, though the dielectric constant is much lower at the interface.[21] An empirical relation of the ionic character and the extent of water adsorption at a given RH [17] is given as follows:

$$h = \frac{M_w v \phi \Gamma}{-\rho_w \ln(0.01RH)} \qquad [1]$$

Where, h is the water layer thickness, Γ is the surface ion concentration, v is the number of ions formed by the dissolved salt, M_w is the molecular weight of water, ρ_w is the density of water, ϕ is the osmotic coefficient and RH is the relative humidity.

Given the multi-scale nature of triboelectrification which makes experimental characterization very hard; computational approaches can be used which can lend more insight that that provided by experiments alone. The computational approaches must address the charge transfer process itself at the electronic scale, and then at the particle scale accounting for the type (drug-drug, drug-additive, additive-additive, additive–wall and additive drug-wall), frequency and duration of contacts which determine the macroscopic granular charge. Computational efforts in characterizing static electrification of granular media have been attempted through continuum approaches,[22-24] but these fail to link granular flow kinematics with tribocharging. Probability based particle dynamics models have been used to study electrostatics behavior of particles of different sizes, but did not account for real work function values.[25] Particle scale modeling triboelectrification under dynamic process conditions can be by Discrete Element Method (DEM) based simulations, which account for all forces acting on a particle and

eventually determine the trajectory evolution of the granular system and have been used widely to model a range of particulate processes in the pharmaceutical industry and elucidate mesoscale phenomena.[26,27] However, a recent review painted a grim picture of electrostatic force implementation in DEM.[28] DEM based studies to model triboelectrification of powders has been attempted through empirical functions for charging and discharging.[29] Pei et al [30] used a DEM-CFD coupled model to study contact electrification during fluidization. They used a condenser model so that charge transfer takes place in accordance with the work function difference, but they did not incorporate long range electrostatic forces. Very recently, Naik et al.[31] published an article modeling tribocharging of pure powder system from a hopper-chute demonstrating correlation between work function difference and net granular charge. However, there is a need to extend multi-scale modeling approaches to mixed systems which are more representative of pharmaceutical processing.

Considering the importance of powder tribocharging in industrial operations, the current article intends to gain a deeper insight into the interaction of materials with an emphasis on their material and molecular properties under relevant conditions (35±5% RH, 25±2°C) both experimentally and numerically. In experiments, the broad methodology adopted is to (a) identify the factors influencing the tribocharging of primary glass and lactose spheres, (b) identify optimum conditions, i.e. conditions which give least statistical variability, and (c) study mitigation of charges on the whole granular assembly when different additives are added. We believe the environmental conditions chosen would represent optimum conditions for tribocharging while providing maximum difference between adsorbed moisture content for the excipients. Besides this, the size difference between the additives (about 200μm) and primary particles (1mm) would restrict the moisture adsorption under these conditions to additives only.

For simulations, the work function difference model is used. Work functions are computed from semi-empirical molecular mechanics calculations. The choice of scale for reporting charge data, either normalized to mass or area is also considered. The computational set up is set in accordance with published experimental data earlier by Trigwell[15] and Naik et al.[31]

2. Experimental Method, Materials and Characterization Techniques

2.1 Experimental Method

The primary particles were loaded onto the hopper and deionized using a benchtop air ionizer (3M ^{R} 963 E). They were then released through a dam (1cm opening) in the base of the hopper to flow over the chute into Faraday's cup connected to a nano-Coulomb-meter (Monroe Electronics, NJ, Model 284), in which the magnitude of accumulated charge was measured. The particles in the Faraday's cup were then weighed to determine the mass of particles which gave the recorded charge. The recording of time started when the dam was released and it was stopped when the last primary sphere exited the chute. The experiments were videotaped using a digital camera (Sony DCR –SR42) recording at 40 frames per second .After one experimental run, the hopper and chute assembly was thoroughly cleaned using distilled water and 70% isopropyl alcohol (Fischer Scientific, MA) followed by drying and deionization using a benchtop air ionizer. All experiments were done in triplicate at ambient temperature (25$\pm$2°C) and RH (35$\pm$5%) with the chute inclined at an angle of 30° with respect to the horizontal which represented optimum conditions (for 30g of primary particles) for surface contact and flow of particles. For charge reduction studies, the additives and particles were layered over each other to ensure optimum mixing while discharges, as shown in the schematic diagram. Ketterhagen et

al.[32] observed a homogenous discharge arising from such a layered setup within the hopper. The electrostatic charging due to flow and charge reduction effects will be examined for the following parameters:

- Primary Particle type: Lactose Non pareils (NP) and Glass Beads (GB)
- Equipment surface type: Aluminum and PVC
- Additive type: L-ascorbic acid, stearic acid, magnesium stearate
- Additive concentration (%w/w): 0, 1, 2, 5, 10 and 15

The charging in a simple granular assembly was represented as a charge to mass ratio (Q/m). It is considered that since all the particles have the same work function, the only charge exchange that occurs is through contact with a material of another type i.e. the powdered additive and the equipment. The minor variations in temperature and humidity were accommodated by plotting percentage charge reduction (%CR) against concentration of the additive for the different primary particle –surface cases.

$$\%CR = \frac{\left(\frac{Q}{m}\right)_{c=0} - \left(\frac{Q}{m}\right)_{c=c_a}}{\left(\frac{Q}{m}\right)_{c=0}} * 100 \qquad [2]$$

The %CR reflects the reduction in charge to mass ratio of the entire granular assembly when the experiments were conducted with an additive at concentration C_a and without an additive (C = 0).

2.2 Materials

The experimental assembly similar to the set up used by Ireland [34] and Hogue et al.,[29] as shown in Figure 1, was fabricated at the University of Connecticut machine shop and consists of a hopper mounted on an inclined plane (36 inches in length and 5 inches in width) with the

support base made of acrylic, are both made of either aluminum or polyvinyl chloride (PVC). The electrostatic charges generated on particles were measured using a Faraday's cup attached to a nano-Coulomb-meter (Monroe Electronics, Model 284). Glass beads and lactose non pareils (1mm in diameter) were used as the primary particles. Pure samples of stearic acid, magnesium stearate and L -ascorbic acid purchased from Fischer Scientific were used as additives to reduce the tribocharging.

2.3 Characterization of Materials

The purity of the additive samples was determined using XPS (ESCALAB MKII) with a focused monochromatic Al K α source (hν = 1486.4 eV) at a background pressure of 10^{-9} mbar and a pass energy of 100eV. Table 1 lists the relative elemental composition for the different additives considered in this study. Characterization of specific surface area of materials was done using BET methodology in a NOVA Quantachrome 1000 analyzer with 5 point determination. The specific surface area accounts for both the size and density of the additive particles. The moisture content of these materials was determined using TGA (TA Q500) after equilibrating at 35% RH at 25°C. Table 2 represents the summary of the additive properties obtained experimentally.

3. Multi-Scale Modeling

3.1 Atomistic Scale: Work Function Determination based on Semi-Emperical Quantum Mechanics

In silico computations for work function of the additives were done using MOPAC2009 from structures generated with AVOGADRO 1.0.3 with Restricted Hartree Fock (RHF) PM3

methodology. This method was adopted from the work done by Mazumder et al, [15] who computed the work function as

$$\Phi = \chi - \tfrac{1}{2} E_g \qquad [3]$$

Where Φ, χ and E_g represent the work function, ionization potential and the band gap (energy gap between HOMO-LUMO orbitals) respectively. The calculated work functions are tabulated in the Table 3. The work functions of the aluminum and glass are reported as 4.53 and 5.32 eV respectively while the same of lactose was determined to be 5.85 eV. PVC has the highest work function in the series.[35] The values compared favorably with all materials except for PVC which was over predicted. The reason for this discrepancy is the limited number of monomeric units which could be incorporated in the computation. It is well known that an increase in chain length decreases the band gap of materials.[36] However, considering the fact that PVC has the highest work function amongst all the materials studied, the over-predicted values should not affect our qualitative understanding of the tribocharging phenomenon.

3.2 Particle Scale: Discrete Element Method

The charge transfer mediated by continuous particle-particle and particle-wall collision was modeled in order to understand the electrostatic behavior of the particles and its impact on particle dynamics due to the changes in the net forces acting on the particle. The charge transfer between the particle i and the particle j during a single collision is given by Δq,

$$\Delta q = \frac{\varepsilon_o S}{z q_e}\left[\phi_i - \phi_j\right] \qquad [4]$$

Where, ε_o is the permittivity of free space (8.854×10^{-12} F m^{-1}), s represents the contact area, z is the cutoff distance for charge transfer considered to be 250 nm, q_e is the charge of an electron (1.602×10^{-19} C). The charge transfer takes place only when $\phi_i \neq \phi_j$ and at the time step

with maximum impact forces between the particles. The final charge (q_{final}) has been calculated as,

$$q_{final} = q_{initial} + \Delta q \qquad [5]$$

The charge transfer between the wall and the impacting particle has been modeled similarly, and the net charge on any particle at any time step has been assumed to be distributed homogenously. Since the Aluminum is a conductor, contact potential difference reduction with accumulation of charge on the surface is expected to be negligible and is ignored.

The introduction of electrostatic charge into the DEM algorithm requires addition of electrostatic forces that works in conjunction with the existing contact mechanics models. The Columbic force (F_c) acting on a particle with charge q_i due to the presence of another particle with charge q_j, is given by,

$$F_c = \frac{q_i q_j}{4\pi\varepsilon_o r^2} \qquad [6]$$

Where r is the distance between the particles. In order to predict the exact transformation in particle dynamics due to the non-homogenous charge density and spatial resistance across the system, an effective Screened Columbic (F_{sc}) force has also been computed based on the approach by Naik et al.[31] A Screened Coulomb force (F_{sc}) will be experienced by each particle with charge q_i separated by distance r from another particle q_j for the presence of other charged particles in closer vicinity.

$$F_{sc,i} = \frac{q_i q_j}{4\pi\varepsilon_o}\left(\frac{\tau}{r} + \frac{1}{r^2}\right) e^{-\tau r} \qquad [7]$$

Where, τ is expressed as,

$$\tau = q_e\sqrt{\left(\frac{1}{K_B T \varepsilon\varepsilon_0}\sum_i n_i z_i^2\right)} \qquad [8]$$

Where, ε is the relative permittivity of the medium, T is the temperature in Kelvin, K_B is the Boltzmann's constant (1.38×10^{-23} JK^{-1}), and n_i is the number of particles with charge z_i within the screening distance. The net force acting on each particle is,

$$\sum F_i = m_i g + F_n + F_n + F_{sc,i} \quad [9]$$

Where Fn and Ft are normal and tangential forces acting on the particle. Electrostatic charge on the particles within the cup was reported either as charge per unit mass, charge per unit area or charge/particle. The overall charge on the granular assembly was identified as the net charge and classified further between that of the big particles on Aluminum surfaces and small (additive) particles, represented as GB Charge and Additive Charge respectively, for various combinations. Table 4 lists the DEM parameters used for the simulations.

At the start of the simulation, the particles are loaded on top of each other as in the experiments so that the smaller particles sift through to achieve a random mixture just prior to being released over the chute. The static charge on the particles over the chute and in the Faraday cup was extracted from the Faraday cup using a post processing script and visualized using Teclpot ™.

4. Results & Discussion

4.1 Electrostatic charging of Primary Spherical Particles

The initial experiments were conducted in triplicate with a view to study the factors affecting electrostatic charging for our experimental assembly and arriving at conditions which reduced statistical variability in the charge/mass values for the different particle-surface combinations. The loading mass, chute angle and particle size were varied in this regard. When the glass beads and lactose non pareils were allowed to flow over the aluminum and PVC

equipment surfaces, we observed that the magnitude of generated charge decreased with increasing the angle of inclination of the chute which is shown in Figure 2. This can be predicted intuitively as greater normal contact through the decreased chute angle would allow greater transfer of charged species between the contacting surfaces. Decreased particle size also has a similar effect which is depicted graphically in Figure 3. There was no clear trend observed with the mass flow of glass beads. At lower mass loadings, most of the particles are in contact with the chute and flow down the chute by sliding, rolling or bouncing. At greater mass flows, there are expected stable interlocking arrangements that reduce the number of conformations a particle can take,[34] manifesting decrease in the standard deviation of the charge generated. At higher mass flows, the normal force on the particles contacting the bed is greater due to the weight exerted by the overlying bed which leads to greater tribocharging. The overall charge to mass ratio is dictated by greater normal force on particles contacting the chute and particles which do not contact the chute. The latter fraction has a much decreased charge to mass ratio due to lack of collision with the chute. Another aspect worth consideration is that the charges generated at high mass flows are near the upper end of the detection limit of the nano-Coulomb meter. These effects help us explain why a distinct trend of charge generation with mass flow was not observed (Figure 3). The least statistical variability in charge to mass ratio for the granular assembly was observed when 30g of material (1mm in size) flowed over an inclined chute kept at 30° with respect to the horizontal. The difference of the initial charge/mass values for the different set ups was evaluated using paired t tests and were found to be statistically significant.

The data obtained on tribocharging of model spheres through our experimental procedure as decribed in the previous paragraph allows us to comment on the mechanism of tribocharging. The sign and magnitude of the charge generated were found to parallel the difference in work

function of the surfaces and the primary particles. The arrangement of materials in ascending order of their apparent work functions (from Table 3) is:

Aluminum < Glass < Lactose < PVC

This explains our observation why lactose NP had a greater negative charge than glass beads on aluminum while the trend reversed on PVC surfaces where glass beads acquired greater positive charges than lactose NP.

4.2 Charge Reduction with additives

It was observed that 30g of GB/NP of 1mm size flowing over a chute inclined at 30° with respect to the horizontal gave the least statistical variability. These conditions are thus chosen to conduct our charge reduction studies. The measurement of charge to mass ratios when different additives were added showed an interesting trend and have been represented as percentage charge reduction plots.

For the analysis of the different systems under consideration, it is important to understand the basics of tribocharging. Charge transfer occurs when two surfaces come in contact and exchange some charge till the chemical potential on both surfaces are equal, either through mobile ions or through electrons. This places a key importance on determination of number of contacts between primary particles and additives, and their contact with the chute. As observed in case of primary particles, where sliding is the dominant mode of transport and hence the effective work function for contacts at other points does not change much. This approximation is also supported by the fact that our particles are dielectric in nature and local charge density at one point does not appreciably influence contacts at other points. Thus it was safely assumed that the two primary particles do not exchange charge when contacting each other at neutral points because their work function values are the same. As known from previous studies, sliding

contact transfers more charge than other modes.[34,35] So, the final charge detected is reflected by the number of charged primary glass and lactose spheres tribocharged through the contact with the chute, number of additive particles charged again by the chute,the primary spheres and additives which exchange charge by mutual contact. We also bear in mind that the additives are more cohesive in nature and do not flow well by the chute. Thus, we can approximate the final charge to be determined majorly by charge on the primary particles. The number of contacts that small particles undergo are much less than the big particles as shown in a numerical analysis [36] for equal number of big and small particles (We have much more big particles so this discrepancy in enhanced further). Let us now elucidate the following cases:

Case I : Glass Beads on PVC Surfaces :

From the tabulated values of computed work function, it can be predicted that all the additives are positively charged on PVC with the following order: ascorbic acid> glass> stearic acid> magnesium stearate. This indicates that if only work function were to be considered; magnesium stearate is least postively charged while ascorbic acid charges most positively even preferentially over glass beads. Thus, in a one to one collision between a glass bead and an ascorbic acid particle, the glass beads end up being negatively charged thereby reducing the charge. But such collisions are few owing to the less specific surface area of ascorbic acid. Following the similar rationale, magnesium stearate and stearic acid would be expected to render the glass beads more positive while becoming negative themselves in binary collisions with glass beads, however being positively charged when sliding by themseves over the PVC chute. Thus, we expect the final charge/mass values to be increased in positive charge. However, hygroscopicity of the materials plays a key role in net charge reduction of the overall granular

assembly. The glass beads are much bigger in size and do not adsorb moisture while the additives are prone to adsorption of water in accordance with their polarity and particle size. Previous research shows that the hydroxide ions tend to adsorb preferentially over surfaces,[20,37,38] especially under a positive potential. Magnesium stearate, which is most hygroscopic and ionic of the additives concerned, gives the greatest value of charge reduction which is followed by ascorbic acid and stearic acid as shown in Figure 4. This is because of the negatively charged excipient particles falling into the chute, or negative charges on additives neutralizing the positive charges on the glass beads through contact established through a liquid bridge or film (water). However, as Figure 4 shows, there is also some charge reversal associated with this case as seen from the charge reduction values going above 100%. When coupled with the pleateauing values of charge reduction at high concentrations, we can infer it to be due to moisture and specifically adsorption of negative ions which are more than likely to be hydroxide ions. Stearic acid, which is known to be a poor charge reducing agent [39] under low RH conditions also serves to reduce the strongly positive charges on the glass beads due to the little moisture adsorbed. It is however unclear the origin of the dominating moisture content in this case as opposed to the rest. It could be due to poorer drying of the surfaces concerned as we know that adsorption-desorption kinetics are much slower for thick surfaces,[40] or some other mechanism related to the adorption of atmospheric moisture.

Case II : Lactose Non-Pareils on PVC

The order of charge mitigation remains the same as in the previous case though the percentage charge reductions are much smaller (Figure 5). The same theoretical considerations apply here as well. All additives should render lactose negative in a one on one collision, with

ascorbic acid causing greatest negative charge. Just like in the the previous case, the effect of moisture adsorption clearly in the submonolayer regime is dominant. If one considers movement of ions in the liquid film to mitigate positive charges, one has to consider movement of stearates which does not seem plausible, especially under a negative potential as determined by hydroxide ion adsorption. There is no charge reversal and neither the pronounced plateauing as associated with glass beads on PVC. Clearly, there is not much adsorption which explains the relatively lower values of charge reduction in this case.

Case III: Glass Beads on Aluminum

This case presents a different order of mitigation than the others, exhibiting an order of : stearic acid > magnesium stearate > ascorbic acid (Figure 6). Based on the pure work function based arguments, a binary collision between ascorbic acid and a glass bead charges the glass bead negatively and thereby intensifying the negative charges on glass beads. Ascorbic acid is the least effective in this case, but still decreases the charge. This is attributed to be due to the strongly positively charged ascorbic acid particles which fall inside the Faraday's cup. On similar lines, stearic acid and magnesium stearate tribocharge the glass beads positively in binary collisions, magnesium stearate more than stearic acid if one were to judge solely by work function values. Magnesium stearate, otherwise strongly negatively charged on aluminium should be expected to intensify the overall negative charge, but adsorbed moisture and transfer of magnesium cation helps in mitigating charges in this case as well. Under a negative potential in submonolayer aqeous regime, positive ions have greater mobility and cause reduction of the negative charges on glass beads. Stearic acid, with similar properties is indistinguishable from

magnesium stearate till 5% concentration but proves much more effective after that because magnesium stearate plateaus off due to poor flow owing to high cohesion and water adsorption.

Case IV : Lactose Non Pareils on Aluminum

This case is represented in Figure 7 and presents the same trend in the order of charge mitigation as in the first two cases. The more negatively charged lactose particles interact with the positively charged ascorbic acid on aluminum surface while both the stearates are negatively charged. All excipients are positively charged with respect to lactose. Magnesium stearate which adsorbs maximum moisture proves most effective in this case too. The positively charged ascorbic acid comes next in the order while stearic acid, which has slight moisture, ranks a close third in the order. As some literature reports have pointed out,[19,41] the mobility and strongly positive magnesium ion in the adsorbed layer as opposed to weak surface dissolution of stearic acid to generate a mobile hydronium ion is the most likely reason for the difference between the two species.

4.3 Computational Results

4.3.1 Influence of Work Function Difference

The importance of work function difference can be gauged from Figure 8 at 3 different additive concentrations, which plots the charge per unit mass on GB, additives and the net charge on the granular assembly as a function of the work function difference ($\Delta\phi$) between the additive and the GB particles, i.e $\Delta\phi = \phi_{GB} - \phi_{additive,}$ at different additive concentrations. Both the additive charge and the GB charge are directly correlated with the work function differential, while the GB charges oppositely to the additives. However, there is weak correlation with the net charge. From the slopes for the plots in Figure 8, the order of sensitivity of $\Delta\phi$ as a predictor in

determining the static charge in the following order: Additive (small)>> GB (big)> Net. An important observation is the overwhelming importance of the particle interactions (additive-GB) relative to corresponding particle-wall interactions, such that $\Delta\phi$ approaches 0, the net charge on the system also diminishes. This provides a suitable criteria for choosing anti-static additives, especially for dry powder systems.

4.3.2 Effect of Additive Concentration

The effect of additive concentration is demonstrated in Figure 9. There is a sharp increase in tribocharging when the additives are introduced in going from 0-2% as smaller particle charge strongly, but further increase leads to a decrease in charge on the additives and an increase in charge on GB. This is further evidence of the interparticle collisions dominating over particle-wall collisions in dictating charge on the individual species. Increasing the additive concentration increases the GB-additive collisions so that GB acquires electrons from the additives and becomes more negatively charged when the additive work function is lower than that of the surface and loses electron to the additive when the additive work function is higher than that of the surface.

4.3.3 Effect of Normalization variable

Figure 9 is replotted in terms of average charge/area in Figure 10. The 2 order of magnitude difference between big and small particles as observed when plotting charge per unit mass is not observed when plotting charge per unit area. This clearly indicates that area is the more fundamental normalization variable, which is intuitive as tribocharging is in effect a surface contact phenomena. The average charge per particle shows comparable magnitudes for GB and additives (Figure 11), which is due to the fact that in a binary collision, the charge is shared equally between the particles. At 5% concentration, where the number of big and small

particles is approximately equal; the average charge per particle for GB and all the additives are almost identically opposite. Figure 12 demonstrates the effect of normalization variable for 2 additives from simulation snapshots (zoomed on the chute) for AA and SS at 2 sec. It can be seen that even though average measurements are useful, there are local charge variations in reality. While the big GB particles appear strongly charged towards the end of the chute, the charge on the additives is high towards the top.

4.3.4 Comparison with Experiments

Figure 13 plots the percentage charge reduction obtained *in silico* and are compared with those obtained experimentally in Figure 6.There is a moderate degree of qualitative correlation, however the quantitative correlation may be significantly improved. However, this may be understood given that effects of particle cohesion, density and shape variation in component materials, polydispersity and hygroscopicity were not considered. The experimental section demonstrated that charge reduction was better correlated with the moisture content that work function differential. Moisture adsorption is known to impact work function. The relatively poor correlation also demonstrates the gap between a pure work function difference driven model considering mono-disperse and freely flowing particles and real experiments.

5. Conclusions

It was found that the tribocharging and charge reduction on the lactose and glass particles is a complex function of many variables. It was observed that the tribocharging of the model spheres was in accordance with the work function difference and related to the contact between the equipment surface and particles as evidenced by increasing charge/mass values with decreasing particle size and increasing chute angle. The order of charge reduction of these

spheres was explained through a complex interplay of hygroscopicity, work function, flowability and contact area of the additives for a given particle-surface system. Except for the glass beads on aluminum surface, the order of charge mitigation is magnesium stearate > ascorbic acid > stearic acid while stearic acid proves to be most effective on the weakly charged system of glass beads on aluminum surface followed by magnesium stearate and ascorbic acid. One surprising result of our studies is that we do not observe charge increase in any case and all cases reduce electrostatic charges, or at worse reverse it. Thermodynamically speaking, excess energy is required to maintain a charge separation between two neighboring particles and this is resolved through a surface interaction based on charge / dipole interactions or adsorption of atmospheric water, which itself is a strong dipole with much more degrees of freedom compared against the additives in the solid state. Thus hygroscopic additives which can be used in low concentrations so that there is charge reduction but no corresponding clumping associated with moisture. We can predict the hygroscopicity of the materials through Equation (1) and in general determine the best possible additive under moderate RH conditions. From the results of our experimental studies and computational studies, we can conclude that it is naive to predict tribocharging of materials in a typical processing plant from values of work function which are calculated or generated in vacuum. Even when the work function difference model was used for a binary mixture; it was found that the net charge was weakly correlated to the system work function differential. It was found that while the charge on the additives and the primary particle was dictated by the work function difference between them rather than between the particles and the wall. Increased additive concentration effectively decreased the charging of the additives while increasing the GB charge. Reporting of charge normalized per unit area was found to be more fundamental relative to normalization by mass. We believe that determination or computation of

work functions of materials after adsorbing a monolayer of water would be more relevant to predict tribocharging and charge mitigation under different conditions.

6. Acknowledgements

The authors wish to thank Dr Heng Zhang, Prof. Leon Shaw and Prof. Michael Pikal who helped with the measurements on XPS, BET and TGA. The undergraduate students: Kyeunhung Lee, Dien Nguyen, Annie King, Jin Lee and Holly Grota for tirelessly performing the experiments. We express our gratitude to University of Connecticut Research Foundation for funding this research.

7. References

1. Bailey A. 1984. Electrostatic phenomena during powder handling. *Powder Technology* **37**(1):71-85.
2. Palmer KN. 1973. Dust explosions and fires. ed.: Chapman and Hall London.
3. Pingali KC, Shinbrot T, Hammond SV, Muzzio FJ. 2009. An observed correlation between flow and electrical properties of pharmaceutical blends. *Powder Technology* **192**(2):157-165.
4. Chowdry A, Westgate C 1974. The role of bulk traps in metal-insulator contact charging. *Journal of Physics D: Applied Physics* **7**(5):713.
5. Duke C, Fabish T. 1978. Contact electrification of polymers: A quantitative model. *Journal of Applied Physics* **49**(1):315-321.
6. Elajnaf A, Carter P, Rowley G. 2006. Electrostatic characterisation of inhaled powders: effect of contact surface and relative humidity. *European Journal of Pharmaceutical Sciences* **29**(5):375-384.
7. Gallo C, Lama W. 1976. Some charge exchange phenomena explained by a classical model of the work function. *Journal of Electrostatics* **2**(2):145-150.
8. Liu C, Bard AJ. 2008. Electrostatic electrochemistry at insulators. *Nature materials* **7**(6):505-509.
9. Lowell J, Rose-Innes A. 1980. Contact electrification. *Advances in Physics* **29**(6):947-1023.

10. Sarkar S, Cho J, Chaudhuri B. 2012. Mechanisms of electrostatic charge reduction of granular media with additives on different surfaces. *Chemical Engineering and Processing: Process Intensification* **62**:168-175.

11. Diaz A. 1998. Contact electrification of materials: The chemistry of ions on polymer surfaces. *The Journal of Adhesion* **67**(1-4):111-122.

12. Diaz A, Fenzel-Alexander D. 1993. An ion transfer model for contact charging. *Langmuir* **9**(4):1009-1015.

13. Diaz AF, Guay J. 1993. Contact charging of organic materials: Ion vs. electron transfer. *IBM Journal of Research and Development* **37**(2):249-260.

14. Kron A, Reitberger T, Stenberg B. 1997. Luminescence from γ-and β-irradiated HDPE and LLDPE. *Polymer International* **42**(2):131-137.

15. Trigwell S, Grable N, Yurteri CU, Sharma R, Mazumder MK. 2003. Effects of surface properties on the tribocharging characteristics of polymer powder as applied to industrial processes. *IEEE Transactions on Industry Applications* **39**(1):79-86.

16. Diaz A, Wollmann D, Dreblow D. 1991. Contact electrification: ion transfer to metals and polymers. *Chemistry of Materials* **3**(6):997-999.

17. Pence S, Novotny V, Diaz A. 1994. Effect of surface moisture on contact charge of polymers containing ions. *Langmuir* **10**(2):592-596.

18. Anderson J. 2005. Humidity dependence of tribocharging of electrophotographic carriers coated with poly (vinylidene fluoride)-poly (methyl methacrylate) blends. *Journal of Electrostatics* **63**(1):59-67.

19. McCarty L, Whitesides G. 2007. Electrostatic charging due to separation of ions at interfaces: contact electrification of ionic electrets. *Angewandte Chemie (International ed in English)* **47**(12):2188-2207.

20. de Lima Burgo TA, Rezende CA, Bertazzo S, Galembeck A, Galembeck F. 2011. Electric potential decay on polyethylene: Role of atmospheric water on electric charge build-up and dissipation. *Journal of Electrostatics* **69**(4):401-409.

21. Vold RD, Vold MJ. 1983. Colloid and interface chemistry. ed.: Addison-Wesley.

22. Al-Adel MF, Saville DA, Sundaresan S. 2002. The effect of static electrification on gas-solid flows in vertical risers. *Industrial & Engineering Chemistry Research* **41**(25):6224-6234.

23. Böttner C-U, Sommerfeld M. 2002. Numerical calculation of electrostatic powder painting using the Euler/Lagrange approach. *Powder technology* **125**(2):206-216.

24. Klinzing G. 1986. Clustering under the influence of electrostatic forces. *International Journal of Multiphase Flow* **12**(5):853-857.

25. Duff N, Lacks DJ. 2008. Particle dynamics simulations of triboelectric charging in granulator insulator systems.*Journal of Electrostatics* **66** : 51-57

26. Ketterhagen WR, am Ende MT, Hancock BC. 2009. Process modeling in the pharmaceutical industry using the discrete element method. *Journal of Pharmaceutical Sciences* **98**(2):442-470.

27. Zhu H, Zhou Z, Yang R, Yu A. 2008. Discrete particle simulation of particulate systems: a review of major applications and findings. *Chemical Engineering Science* **63**(23):5728-5770.

28. Guo Y, Curtis JS. 2015. Discrete element method simulations for complex granular flows. *Annual Review of Fluid Mechanics* **47**:21-46.

29. Hogue MD, Calle CI, Weitzman PS, Curry DR. 2008. Calculating the trajectories of triboelectrically charged particles using Discrete Element Modeling (DEM). *Journal of Electrostatics* **66**(1):32-38.

30. Pei C, Wu C-Y, England D, Byard S, Berchtold H, Adams M. 2013. Numerical analysis of contact electrification using DEM–CFD. *Powder Technology* **248**:34-43.

31. Naik S, Sarkar S, Gupta V, Hancock BC, Abramov Y, Yu W, Chaudhuri B. 2015. A combined experimental and numerical approach to explore tribocharging of pharmaceutical excipients in a hopper chute assembly. *International Journal of Pharmaceutics* **491**(1):58-68.

32. Ketterhagen WR, Curtis JS, Wassgren CR, Hancock BC. 2009. Predicting the flow mode from hoppers using the discrete element method. *Powder Technology* **195**(1):1-10.

33. Draper NR, Smith H, Pownell E. 1966. Applied regression analysis. ed.: Wiley New York.

34. Ireland PM. 2010. Triboelectrification of particulate flows on surfaces: Part I—Experiments. *Powder Technology* **198**(2):189-198.

35. Bailey A. 1993. Charging of solids and powders. *Journal of Electrostatics* **30**:167-180.

36. Lacks DJ, Levandovsky A. 2007. Effect of particle size distribution on the polarity of triboelectric charging in granular insulator systems. *Journal of Electrostatics* **65**(2):107-112.

37. Bagus PS, Käfer D, Witte G, Wöll C. 2008. Work Function Changes Induced by Charged Adsorbates: Origin of the Polarity Asymmetry. *Physical Review Letters* **100**(12):126101.

38. Jungwirth P, Finlayson-Pitts BJ, Tobias DJ. 2006. Introduction: structure and chemistry at aqueous interfaces. *Chemical Reviews* **106**(4):1137-1139.

39. Gold G, Palermo BT. 1965. Hopper flow electrostatics of tableting material I. Instrumentation and acetaminophen formulations. *Journal of Pharmaceutical Sciences* **54**(2):310-312.

40. Blacker RS, Birley AW. 1991. Electrostatic charge occurrence, significance and measurement. *Polymer Testing* **10**(4):241-262.

41. Harper WR. 1998. Contact and frictional electrification. ed.: Laplacian Press Morgan Hill, CA.

List of Tables

Additive	C	O	Na	Others
Ascorbic Acid	47.95	52.05	-	-
Stearic Acid	86.83	13.17	-	-
Magnesium Stearate	86.69	9.87	3.44	-

Table 1: XPS data showing normalized elemental percentage compositions used for the different additives under consideration

Additive	Specific Surface Area (m^2/g)	Moisture Content at 35% RH at 25° C (% w/w)	Particle Size	Flowability	
			d_{50} (µm)	Angle of Repose (°)	Hausner's Ratio
Stearic Acid	3.26	0.06	211.63	20.54	1.32
Magnesium Stearate	3.01	1.2	166.72	20.24	1.26
Ascorbic Acid	1.20	0.0	199.48	25.23	1.20

Table 2: Experimentally determined properties of different additives used for studying charge reduction on different particle-surface systems

Material	Calculated work Function (eV)
Sodium Stearate (SS)	4.22
Ascorbic Acid (AA)	4.40
Sodium Bicarbonate (SB)	4.46
Aluminum (Al)	4.53
Glass Beads (GB)	5.32
Stearic Acid (SA)	5.50
Magnesium Stearate(MS)	5.67
Lactose non-Pareils (NP)	5.85
Polyvinyl Chloride (PVC)	7.36

Table 3: Work function of the additives were determined using MOPAC2009 from structures generated with AVOGADRO 1.0.3 with Restricted Hartree Fock (RHF) PM3 methodology. The unit of Work Function is Electron volts (eV).

DEM parameters	Values
Glass Bead radius (mm)	1
Additive radius (mm)	0.5
Glass Bead density (kg/m^3)	2500
Additive density (kg/m^3)	1020
Number of GB particles	2865
Concentration of additive particles (%w/w)	2, 5, 10
Chute angle (^{O})	30
Coefficient of restitution: particle-particle	0.6
Coefficient of restitution: particle-wall	0.3
Friction coefficient: particle/particle	0.5
Friction coefficient: particle/wall	0.5
Time step (s)	5 e-06

Table 4: DEM simulations used to investigate tribocharging of binary mixtures in a hopper-chute assembly.

List of Figures

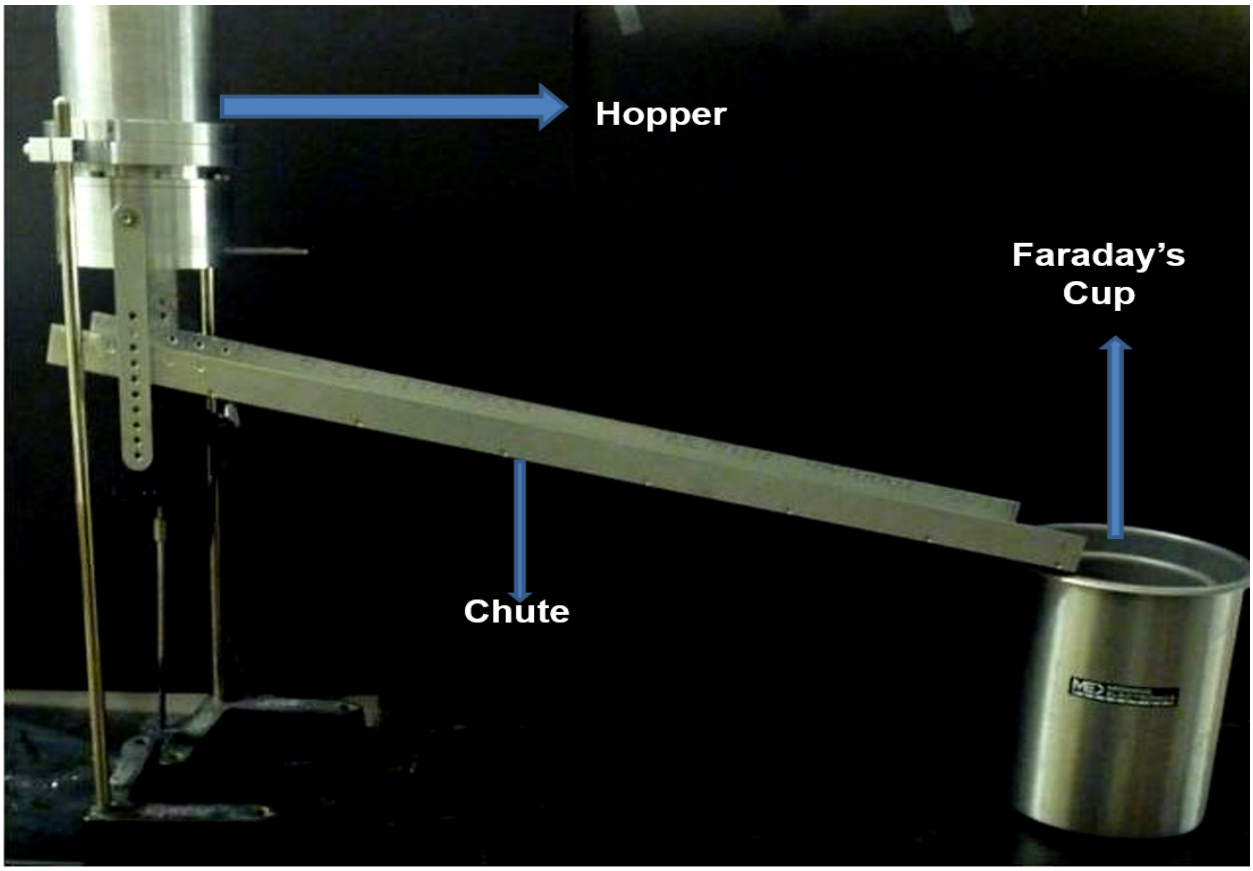

Figure 1. Experimental hopper and chute assembly over which granular material flows into a Faraday's cup where charges are detected

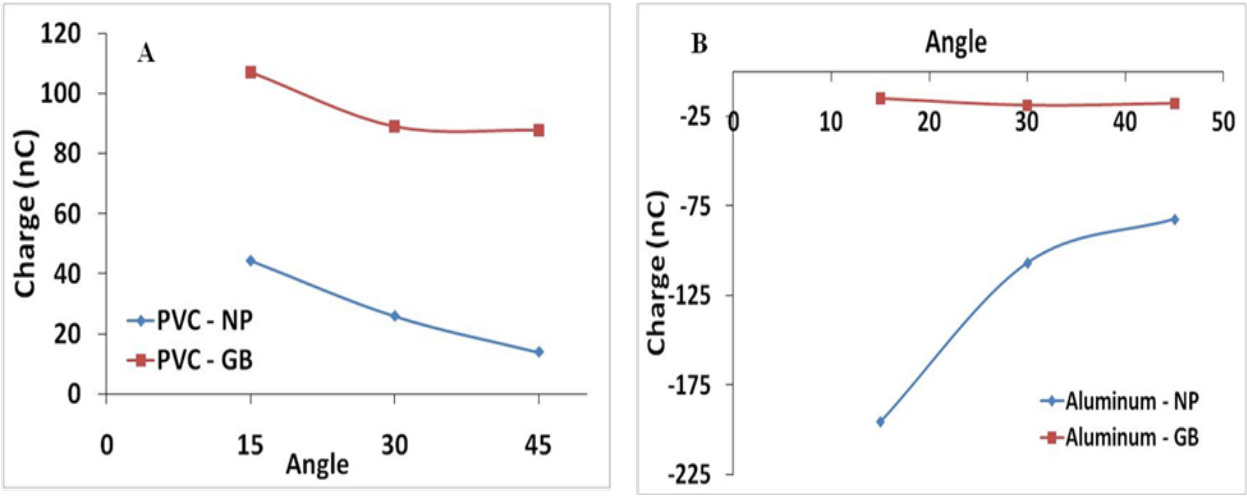

Figure 2. Variation in tribocharging with chute angle for different materials for 30g of glass beads and lactose non-pareils 1 mm in diameter on A) PVC surface B) Aluminum Surface

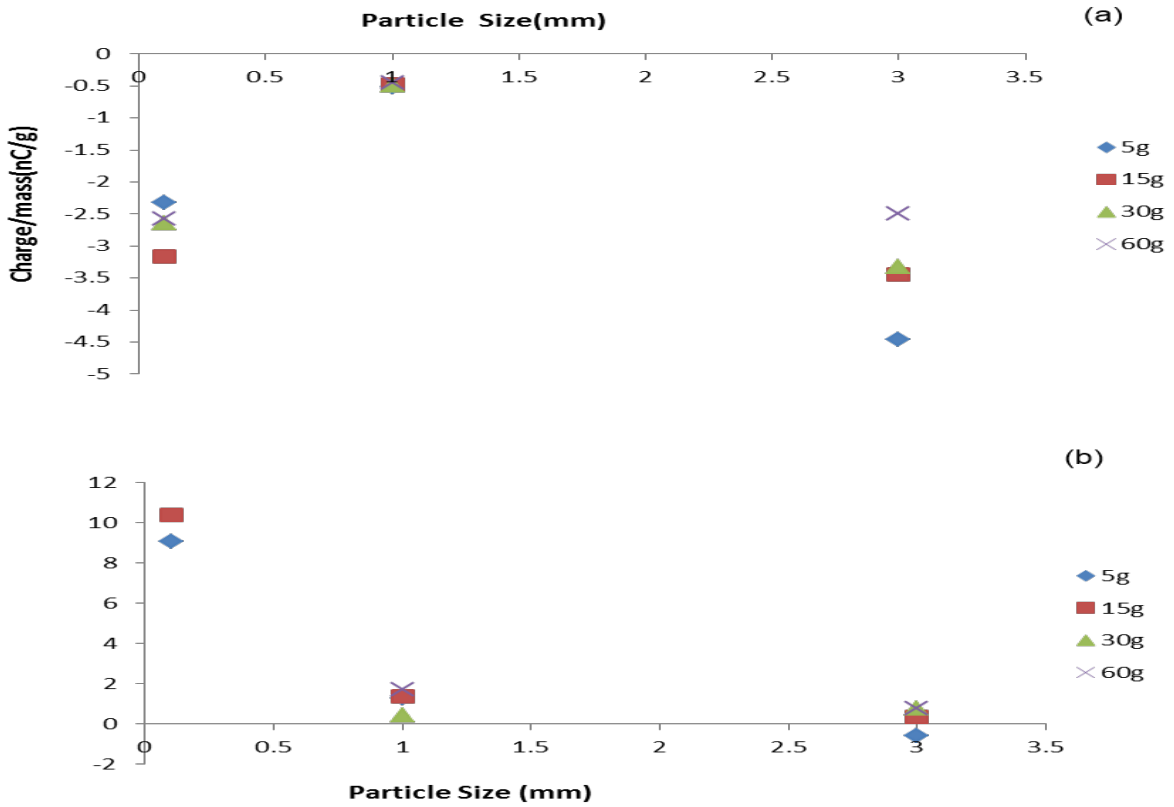

Figure 3. Variation in charge accumulated per unit mass for different sizes of glass beads on (a) Aluminum Surface, and (b) PVC surface

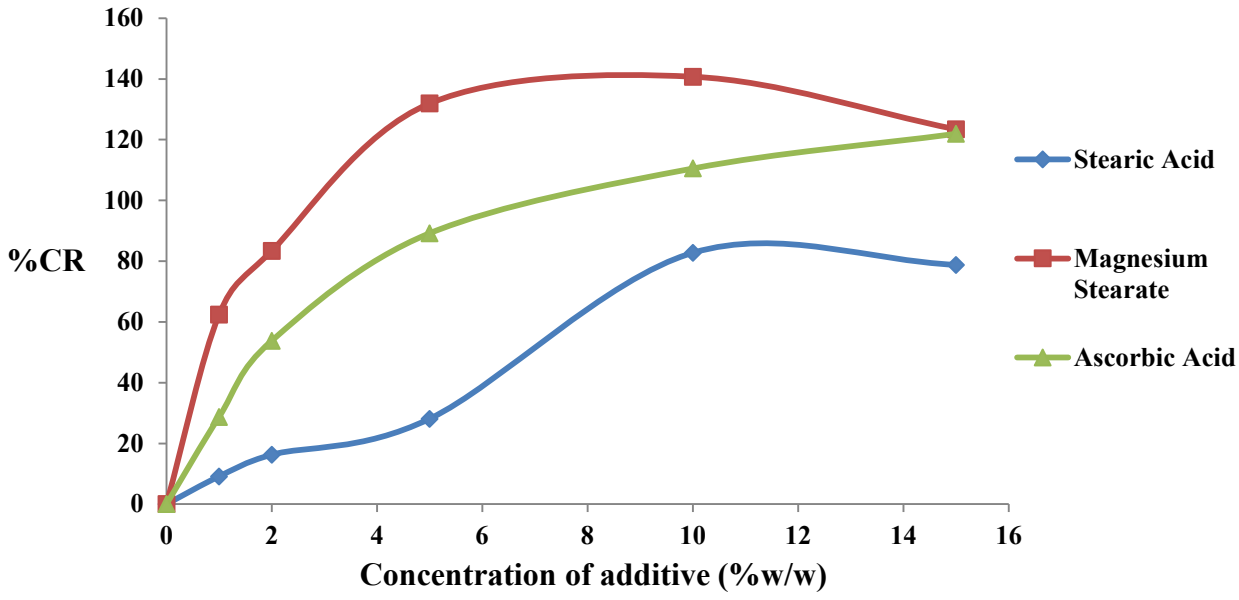

Figure 4. Plot of percentage charge reduction versus additive concentration for different additives used to mitigate charges on glass beads flowing over PVC surface

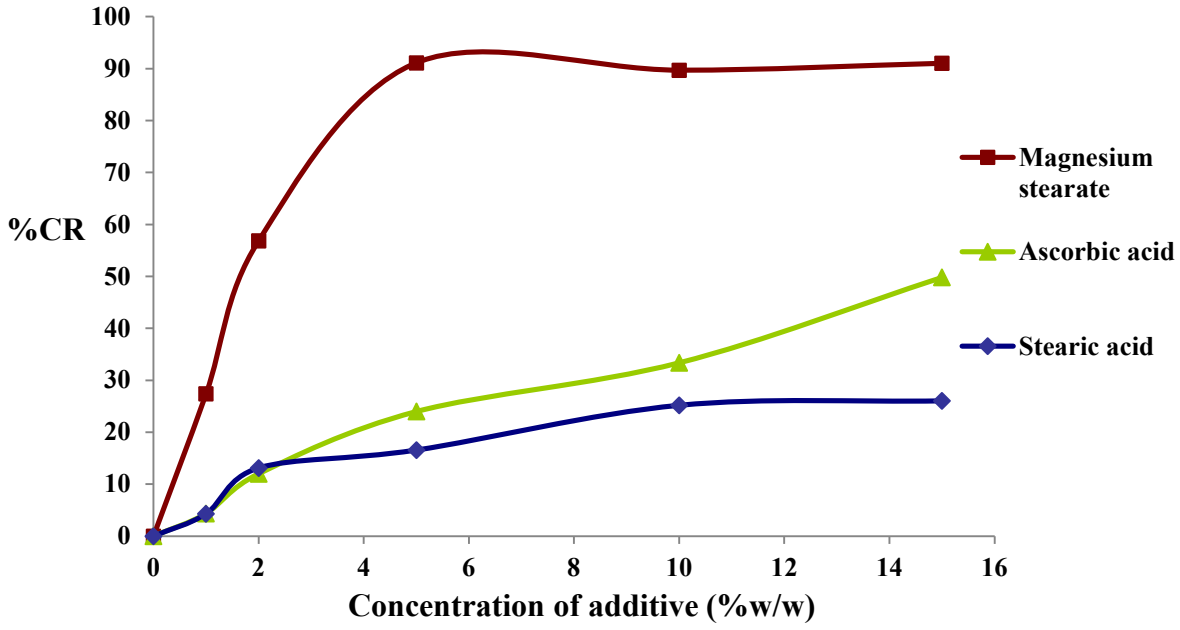

Figure 5. Plot of percentage charge reduction versus additive concentration for different additives used to mitigate charges on lactose non pareils flowing over PVC surface

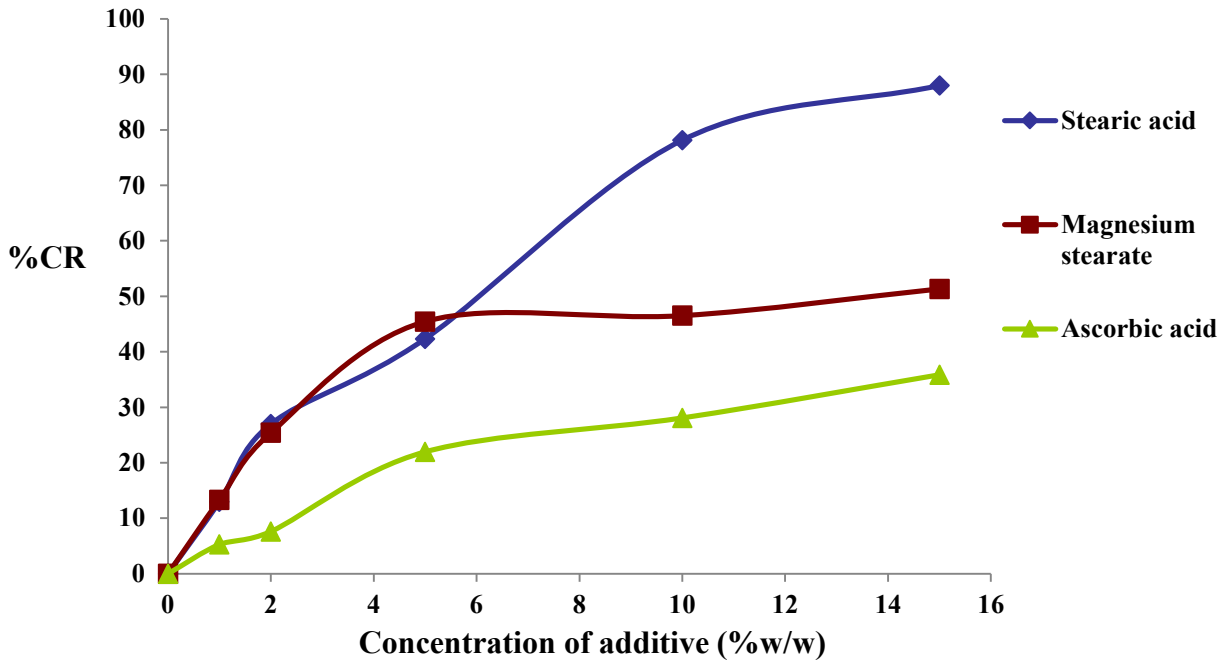

Figure 6. Plot of percentage charge reduction versus additive concentration for different additives used to mitigate charges on glass beads flowing over aluminum surface

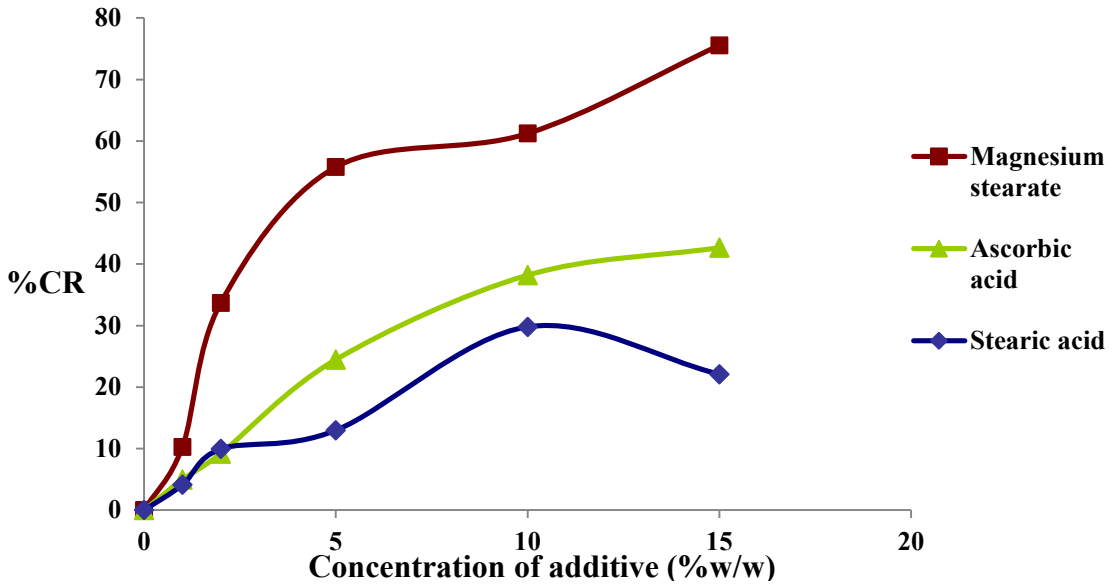

Figure 7. Plot of percentage charge reduction versus additive concentration for different additives used to mitigate charges on lactose non pareils flowing over aluminum surface

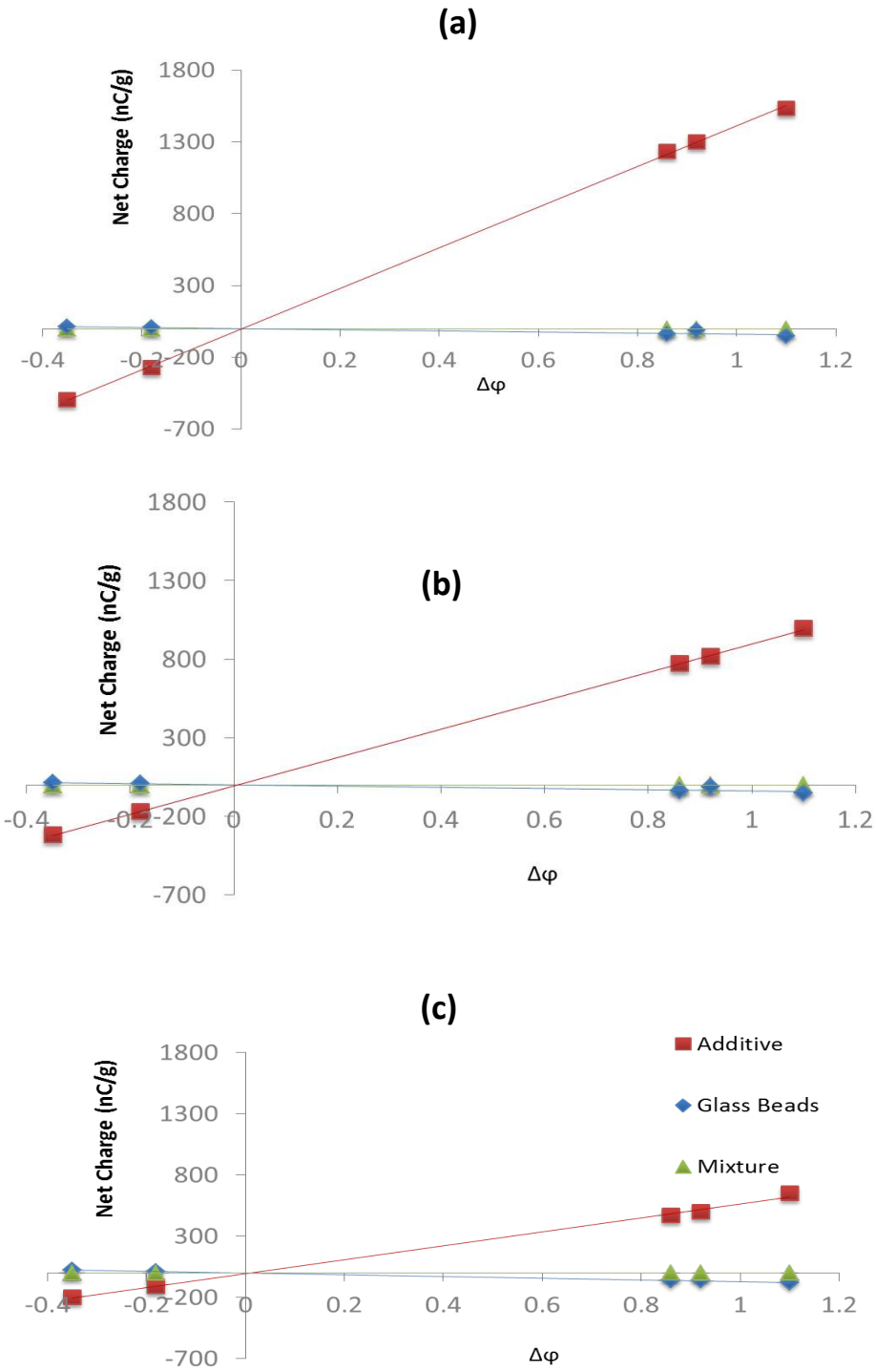

Figure 8. Charge per unit mass on additives, GB, and the overall granular assembly as a function of the work function difference ($\Delta\phi$) between the additive and the glass beads at different additive concentrations (a) 2% (b) 5% and (c) 10%

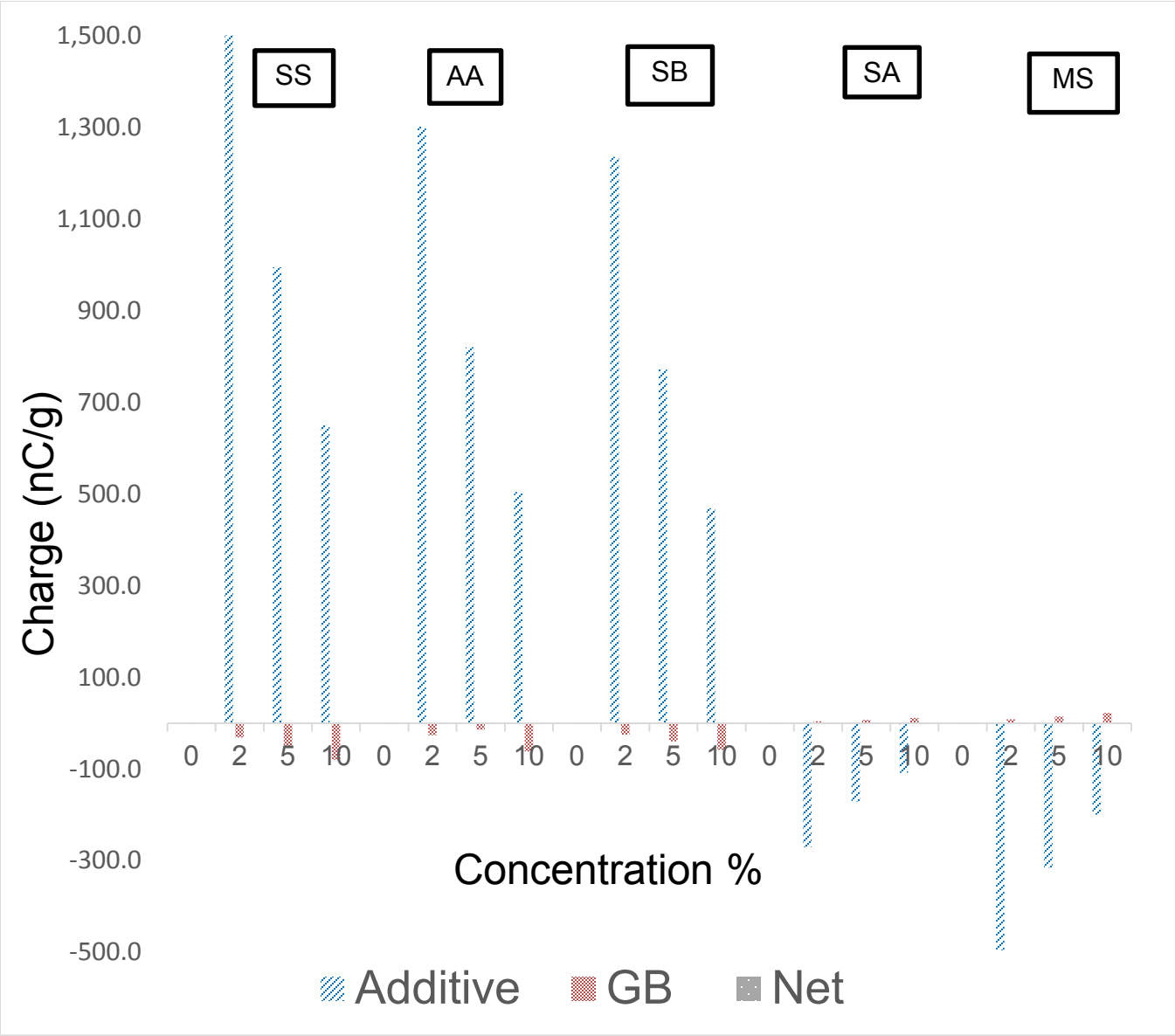

Figure 9. Charge per unit mass on additives, GB, and the overall granular assembly as a function of the additive concentration

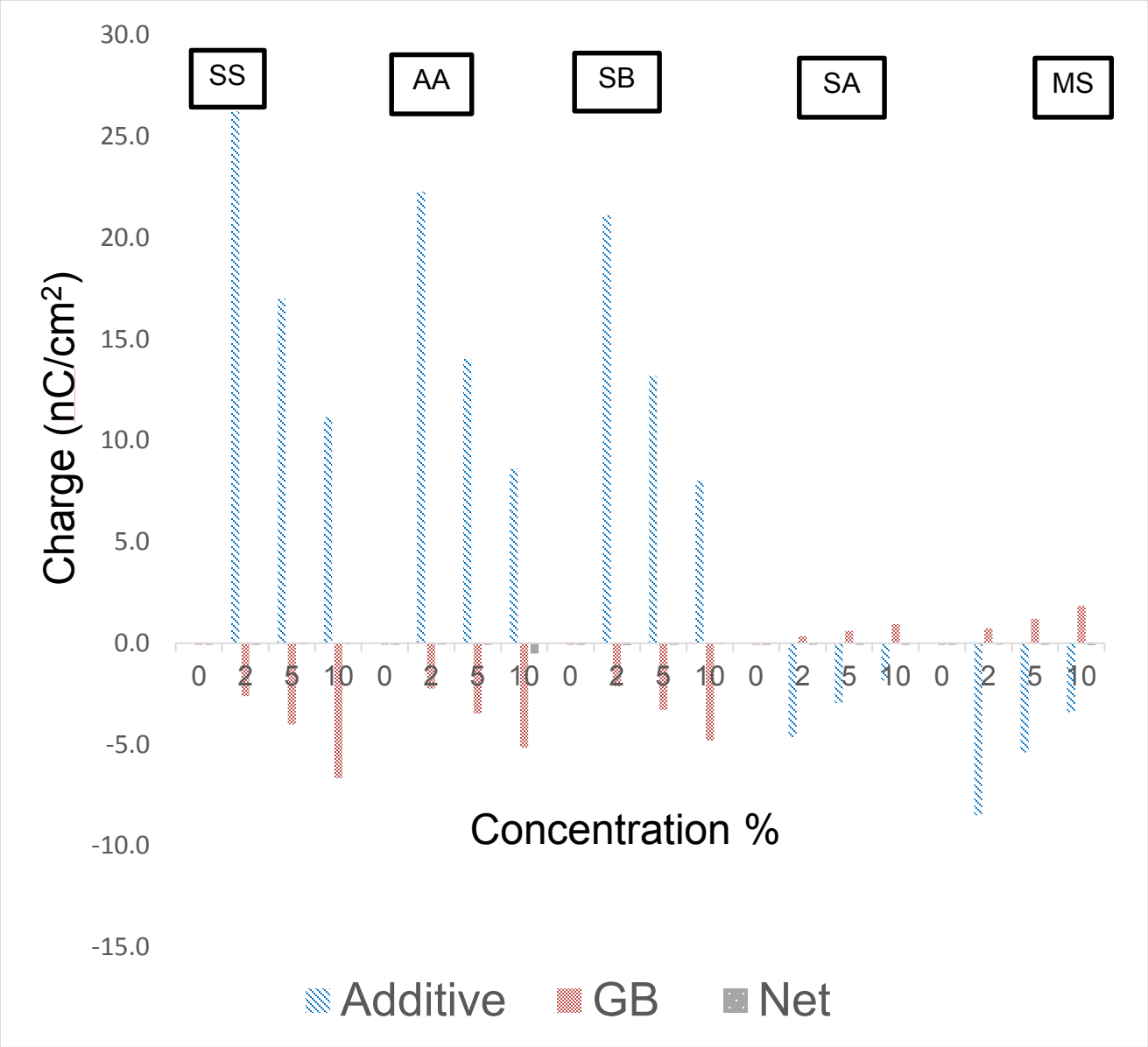

Figure 10. Charge per area on additives, GB, and the overall granular assembly as a function of the additive concentration

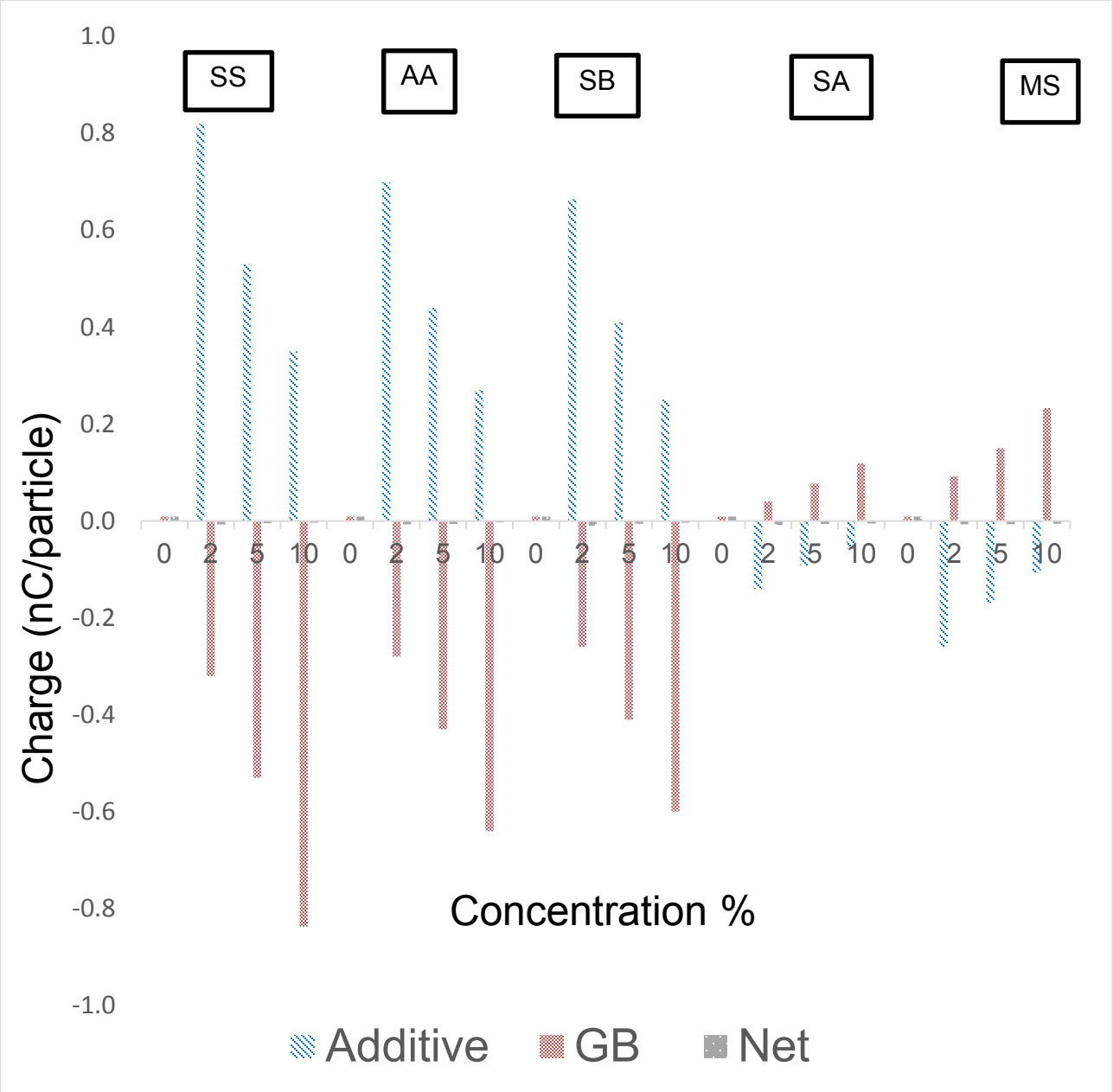

Figure 11. Charge per particle on additives, GB, and the overall granular assembly as a function of the additive concentration

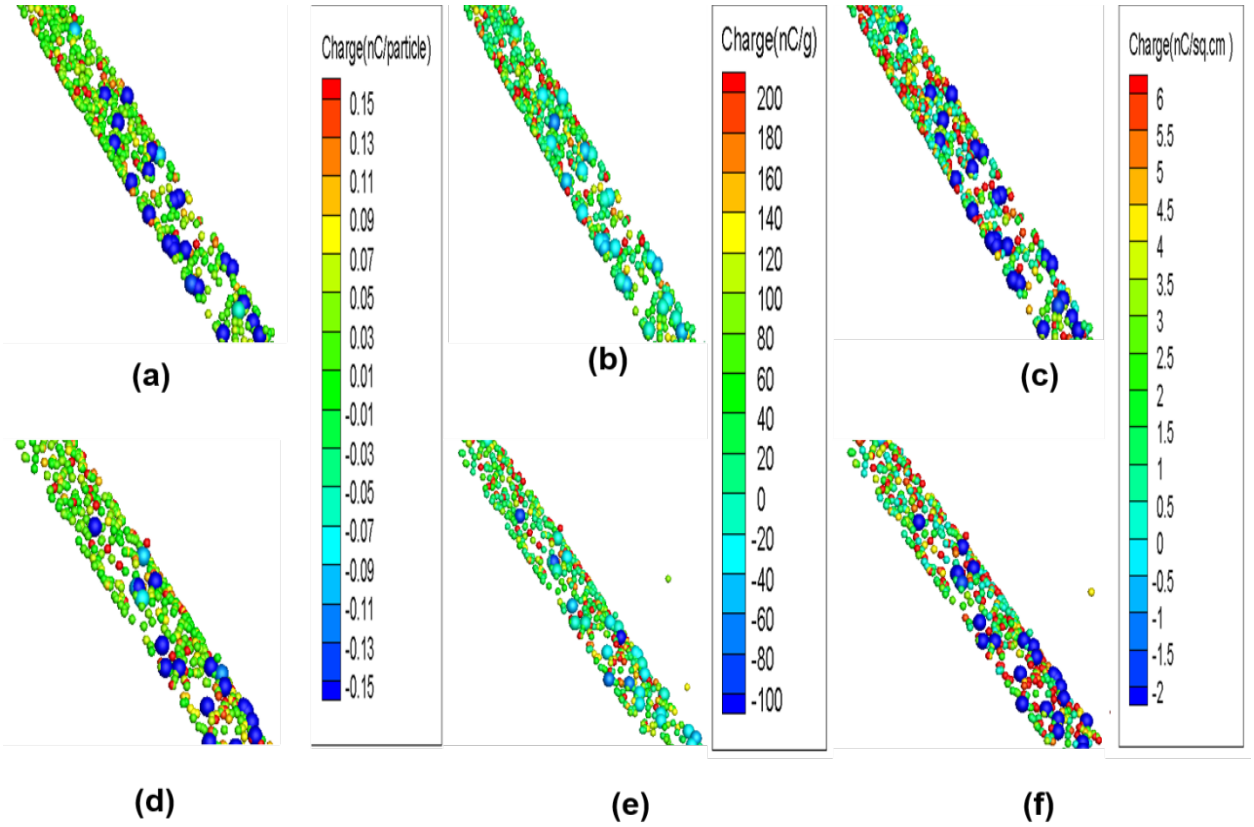

Figure 12. DEM snapshots showing the static charging of the granular assembly at 2 sec for 5% w/w concentration of AA (a-c) and SS (d-f). Different normalizations are used: Charge/mass (b,e), Charge/area (c,f), Charge/particle (a,d)

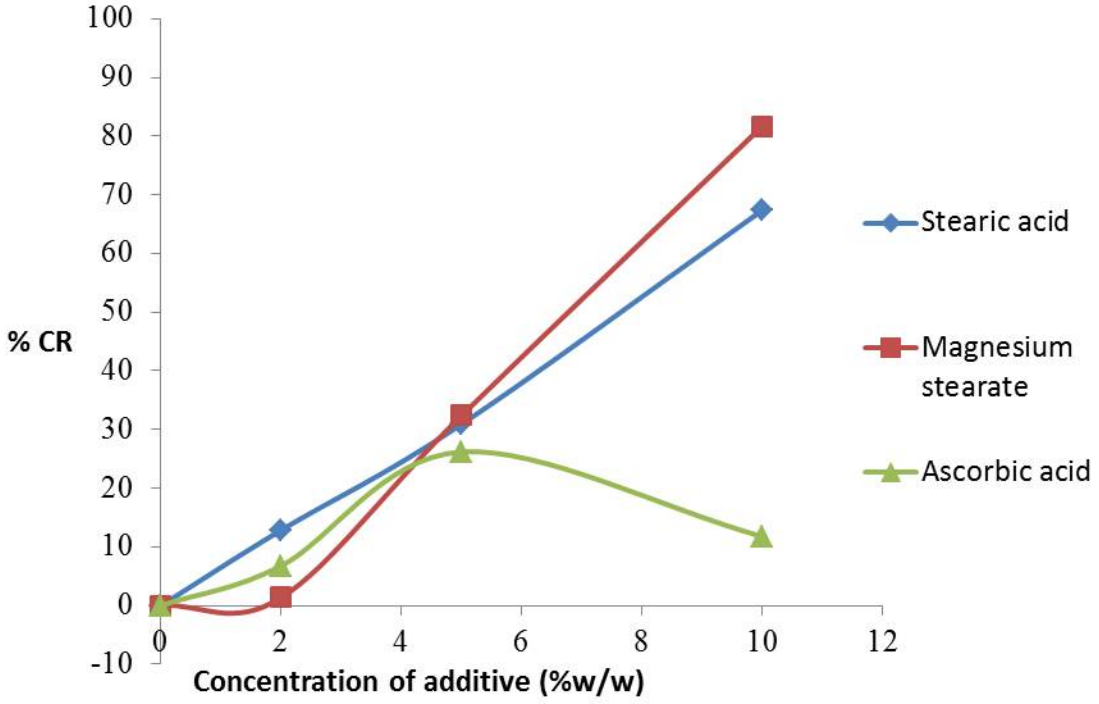

Figure 13. Percentage of charge reduction on the overall granular assembly as a function of the additive concentration obtained from DEM simulations

Chapter 6

Optimization of High Shear Wet Granulation of a Simple System

Abstract

High Shear Wet Granulation (HSWG) is one of the most poorly understood processes with known difficulties in optimization and scale up. The purpose of the current study is to develop a DEM model which can be applied under dynamic process conditions with high predictive capacity. The DEM model would be used to predict agglomeration as a function of impeller speed and liquid addition rate in a high shear granulator. The DEM model tracks dynamic formation and breakage of liquid bridges between particles as water in the system is added, and corrects for the change in material properties as a function of water content. The effect of particle cohesion on formation of capillary bridges in also investigated. The predictions of increasing liquid bridges with increasing liquid addition rate and decreased impeller speed were well correlated between experiments and simulations. In addition, the DEM simulations also predicted increased liquid bridge formation with decreasing particle cohesion and reducing the coefficients of friction, restitution and the elastic modulus of the particles upon addition of water.

Keywords: High shear wet granulation, discrete element method, capillary force, liquid bridges.

1. Introduction

Granulation, a widely used process in pharmaceutical, agriculture, food and paper industry, is the technique of agglomerating particles together into semi-permanent granules (aggregates) made up of easily distinguishable original particles. This size enlargement process is achieved by various means such as (i) compression techniques: bracketing and extrusion (ii) heat bonding: sintering (iii) drop formation: prilling and spray drying and lastly by (iv) process agitation in the presence of a binder or "wet granulation". In wet granulation, the binder liquid is sprayed onto the surface of a mixed granular bed, resulting in the formation of aggregates as the particle is held together by capillary bridge forces. The granules formed offer significant improvement over the ungranulated powder in terms of material properties and behavior such flow, appearance, handling, strength, rate of dissolution while reducing dustiness and segregation.[1] This unit operation is of great commercial importance across a range of industrial sectors like pharmaceutical, food, detergents, defense, energy, fertilizers and ceramics. Often hydrophobic particles, like most typical APIs, do not lend to spreading of liquid due to the thermodynamic barrier of spreading as reflected by their large contact angles. This is overcome by applying mechanical energy through an impeller in a high shear mixer/granulator.

HSWG process can be broadly considered to be interplay of three rate limiting processes: (a) wetting of particles to create nuclei, (b) consolidation and coalescence of these nuclei to give growth and agglomeration, (c) Breakage and attrition of these nuclei under high shear.[1] The progress of wet granulation can be tracked by the following the load on the impeller and generating a power consumption profile. The general power consumption profiles obtained has been traditionally subdivided into the following phases: (1) a first slight increase in the profile, usually related to nuclei formation and moisture sorption, (2) a rapid increase in the profile slope,

due to the attainment of the pendular state (when particles are held by liquid bridges at their contact points), (3) a plateau phase in the profile which indicates the transition from the pendular to the funicular state (particle voids begin to fill with the binder).[2] These rate processes must be controlled in order to achieve granules with acceptable properties. However, despite long history and widespread use of HSWG; the interplay of material, geometric and process variables at different length scales is rather poorly understood which contributes in large parts towards operation on an empirical basis in most manufacturing units,[3] especially with regards to end point determination and scale up. These problems are accentuated for pharmaceuticals formulations, which are multicomponent and present a range of micrometric and material properties. Significant failure rate is often observed during scale up to industrial production, even after successful pilot-scale tests.

Traditionally simulation efforts in the field of HSWG have been dominated by population balance models (PBM).[4-6] These models have several drawbacks such as development of a coalescence kernel which are often empirical in nature and need fitting parameters from experiments. Quite fundamentally, they do not capture the dynamic mesoscale effects which are believed to be transmitted through formation and breakage of discrete capillary liquid between particles. This casts doubts over the ability of PBMs to model dynamic processes.[7] It is often cumbersome to develop governing equations inclusive of process parameters affecting particle size distribution. The discrete nature of capillary bridges and the ability of DEM to model dynamic processing conditions make it an attractive choice to model HSWG. A notable disadvantage is huge computational cost which is further increased once capillary forces are included. Some DEM based efforts have thus modeled motion of wet particles, without explicit inclusion of capillary forces.[8,9] Talu[10] included capillary forces to model agglomeration in a 2D

system while Lian[11] used a 3D box containing 1000 particles to develop a preliminary understanding of particle agglomeration processes. These studies were done in rather small systems and significant process insight cannot be gained. Simulation of larger HSWG systems remains an active area of research within the academia and industry alike.

HSWG process performance depends on a dynamic interplay of several process, material and geometric variables. The mapping of these interactions in a dynamic system is complicated given the nature of capillary forces, which invoke the effects of a 'discrete liquid' coupled with granular flow dynamics making it a difficult multiphase multicomponent multi-scale problem. Recently, it was pointed out that severe assumptions need to be made about binder distribution and surface wetting of the particles.[12] In addition, material properties of the granular phase changes with binder content which presents an additional complexity. The current article attempts to address these issues from experimentally validated numerical simulations in a high shear granulator in a simple system to map the interactions of different process and material parameters. DEM simulations are performed which explicitly incorporate the capillary bridge forces, and provides empirical first order corrections for variation of material properties as a function of binder content.

2. Materials & Methods

2.1 Materials

316 NF grade Fast Flo Lactose (Kerry Inc.) is used as the model compound with water as a binder. In addition to being very frequently used in the pharmaceutical industry, these materials as chosen to allow quick distribution of water over the particle so that the easily wetted.

2.2 Procedure

The wet granulation experiments were performed in a 1L bowl in a KG5 granulator (Key International, NJ). The bowls were loaded with fast flow lactose (d_{50} = 67µm) at a specified fill level and the impeller and chopper were turned on for a dry run of 2 minutes. The telescopic spray pump was then turned on to give a specified volumetric flow rate of the binder till a specified end point based on the liquid volume percentage, which corresponded to a plateau region on the impeller power consumption curve. The liquid addition rate from the pump was calibrated prior to every run. 2-3 g of the wet granules were sampled for particle size measurements every 2 minutes and then dried at 40° C in a laboratory tray oven. The wet granules were dried till the moisture content of 2.5% or lower were achieved as measured using a Sartorius MA 100^{TM} moisture analyzer. The operating conditions were optimized for the lactose –water system by parametrically analysis with respect to processing variables of interest. Table 1 lists the process parameters under investigation in the current study conducted at a 35% fill volume.10% w/w of binder content was added in each of the cases investigated. Progress of the HSWG run was monitored from the temporal evolution of the dynamic strength and particle size of the powder bed.

2.2.1 Dynamic Strength: Load on the main impeller, which represents the resistance to impeller motion at a specified speed, was estimated by measuring the current in DC motor as in our study because the torque generated by the impeller is proportional to the current applied. The dynamic strength of the granules as a function of time was monitored through the ammeter readings recorded manually every 5 seconds from the display unit of the KG5 machine. The ammeter reading was normalized with respect to the average reading during the dry run to account for different mass loading rates, impeller speeds and motor heating effects.

2.2.2 Particle Size Determination: The particle size distributions of the dried samples were determined using a Malvern Mastersizer 2000 E^{TM} laser diffraction instrument fitted with a Sirocco dry powder unit. An air pressure of 0.5 bar and was used to produce uniform powder dispersion for each sample. These conditions were optimized with respect to feed rate and obscuration to achieve a complete dispersion of the primary particles without causing significant particle attrition. Direct visualization of both the raw feed and the granulated mass was done through Scanning Electron Tomography (SEM), as shown in Figure 1.

3. Discrete Element Method (DEM)

3.1 Liquid Bridge Model

The basic implementation of the DEM model is outlined in Appendix Section Sec A2.In addition to the normal and tangential contact forces, the present study incorporates liquid bridge forces between particles. The model liquid bridge is represented earlier in Chapter 2 (Figure 11). These were calculated using the liquid bridge model developed by Lian et al[13] who assumed a toroidal liquid bridge shape when the separation distance of two particles is less than the critical value S_c ,

$$S_c = (1 + 0.5\theta)V^{1/3} \quad [1]$$

Here, θ is the solid-liquid contact angle and V is the volume of the liquid bridge. The capillary force F_c are calculated using the following relation

$$F_c = 2\pi\gamma\rho_2(1 + H\rho_2) \quad [2]$$

where γ is the surface tension of the solvent, ρ_2 is the radius of the liquid bridge at the neck and H is the mean curvature of the liquid bridge. The approximate closed form solution

obtained is used to model the normal component of the viscous force of the liquid bridge between two spheres where the normal component is given by Adams and Perchard[14]

$$F_{vn} = 6\pi\eta R^{*} v_n \frac{R^{*}}{S} \qquad [3]$$

η is the viscosity, v_n is the relative normal velocity between two spheres, S is the separation distance and $R*$ is the reduced radius. There is no rigorous analytical solution for the tangential component of the viscous force but Goldman et al.[15] derived the following asymptotic solution, valid under limiting conditions, for the viscous force for sufficiently small separation distances

$$F_{vt} = (\frac{8}{15} ln \frac{R}{S} + 0.9588) \qquad [4]$$

Where, v_t is the relative normal velocity between two particles and R is the radius of the sphere. At the beginning of the simulation, particles would be started dry. The liquid content would be increased corresponding to the liquid addition rate. Given the high wettability of water over lactose, all the liquid water in the system is considered to be evenly distributed amongst the particles. Considering that an ideal sphere can have a maximum of 12 neighbors of equivalent size, 1/12 of the water content on a given particle is used to form one bridge. Thus, the instantaneous liquid bridge volume V, which is used to calculate S_c in equation 1, is 2/12 or 1/6 of the water volume on one particle. When these particles approach each other to a separation distance less than S_c, a liquid bridge is assumed to be formed between the particles. The bridges are broken if the particles either move close to each other and are in physical contact , or increase in separation by a distance greater than S_c. In the event of bridge rupture, the volume of the broken bridge is assumed to be shared equally between the separating particles, as they are of equal size. Simultaneous capillary and viscous forces are calculated on the particles forming the liquid bridge as discussed above.

In addition to dynamic tracking of the liquid bridge formation, the DEM code is equipped to deal with a change in material properties upon water addition. The coefficients of restitution (e), coefficient of friction (μ) and the elastic modulus (E) of the powder are expected to decrease as water, from observations of lubrication and softening of particles is added.[1] The change in material properties with addition of water is incorporated by assigning a first order correction factor depending upon the moisture content of the particle. For the current simulation, the correction factors or slopes are calculated by assuming *ad-hoc* that e ,μ, E go from evolve from 0.6 to 0.1,0.7 to 0.2 and 6000N/m to 4500 N/m upon addition of water, such that there is 10% water at the end point. Table 2 lists the DEM parameters used for the computational studies. Since the DEM computations are very expensive, the cases are run for 10 seconds (approximately 42 rotations at the default speed of 250 rpm), at which point the simulations appear to reach steady state for the different cases investigated. Running for longer time steps is not feasible as the fluid effects become more pronounced leading to solution instability.

3.2 Post Processing & Visualization

The results were analyzed by tracking the coordination number (CRN), i.e. number of particles surrounding a given particle, and the liquid bridge (LB) count on every particle as a function of time. Evolution of CRN & LB were taken as a measure of size evolution. LB, in particular is more accurate measure of the particle agglomeration size, because the CRN just represents instantaneous physical contact and not stable bonding. Ideally, particles with high CRN and high LB can be considered as “granules”. The DEM visualizations were done by sizing the particles according to their CRN values, so particles contacting other particles due to agglomeration, random contact or material cohesion appear bigger. The particles have been colored according to their LB values, so that the wetter particles can be easily identified. The

trend-lines obtained for different conditions examined experimentally are compared with simulations.

4. Results & Discussion

4.1 Effect of Impeller Speed

The mean impeller power consumption and mean particle size of the lactose-water system are shown in Figure 2a and b respectively for a representative single run. The power increased with the impeller speed in both scales. The trend of the variation of the strength with the impeller speed is in agreement with previous literature studies. The higher impeller speeds cause more intensive mixing and compaction of the granules to a higher degree that leads to higher granule strength. Granulation regimes in high shear granulators have been defined by Lister and Ennis[3] as bumping and roping at low and high shearing rates, where in the former the wet mass is bumped up and down as the impeller passes underneath, whilst in the latter the wet mass is moved as a ribbon. For each scale, the powder flow goes through a wet mass which is bumped up and down as the impeller passes underneath, whilst in the latter the wet mass is moved as a ribbon. The powder flow goes through a transition from bumping to roping as the impeller speed is increased. The roping regime gives a better liquid binder distribution because of good bed turnover and stable flow pattern. The decreased particle size with increased impeller speed is attributed to milling action which promotes a crushing and layering mechanism of growth, which is also predicted to produce stronger granules. DEM simulations display the same qualitative trends obtained experimentally, as seen in Figure 2c though there is not a significant difference between 100 and 250 rpm in terms of capillary bridge formation. Figure 3 displays the DEM snapshots of agglomeration within the high shear granulator.

4.2 Effect of Liquid addition Rate

The lactose-water system is an easily wetted system as characterized by its low wetting angle so that the high affinity of the water and lactose decreases the role of mechanical energy input. The primary particle size growth mechanism is then dictated by the binder supply, corresponding to the drop controlled regime.[16] This is highlighted in Figure 4a, where it can be seen that higher liquid addition rates lead to quicker plateauing corresponding to an end point, but lumps can be easily formed at high liquid addition rates leading to over-granulation and pooling. Figure 4b displays increasing median particle size with increasing liquid addition rate. The DEM visualizations also predict similar trendlines as highlighted in Figure 4c, with increased water addition rate increasing the agglomeration kinetics. It must be noted that for the case of 12 mL/min, the simulation had to be aborted before 10 sec as increased water content led to numerical instability.

4.3 Effect of Material Properties

4.3.1 Particle Cohesion

Particle cohesion was incorporated in the DEM by specifying a Bond number (K) [17], which represents the ratio of cohesive force to the particle weight. The default lactose simulations are at K = 0, while a cohesive material is modeled by arbitrarily specifying K=50. As the particles get more cohesive, liquid bridges are not formed readily as the particles are in continuous contact. This is demonstrated in Figure 5a, which shows that liquid bridge formation is hindered in case of cohesive particles. Figure 5b plots the evolution of CRN vs time for this case, and highlights that the initial material cohesion is more important in agglomeration than the addition of liquid water itself.

4.3.2 Effect of Material Property Correction

The slope of e, μ and E are corrected with water content in the simulations described above to account for "softening" and lubricating properties of water. A slope value of 1 implies that the all particles are corrected for these material properties as described in Table 2, while a value of 0 implies that no corrections are made to the initial values so that the starting values are kept constant. Correcting the material properties with water suggests that liquid bridge formation is facilitated, as the slope value of 1 displays maximum liquid bridge formation (Figure 6). It is hard to attribute a reason for this observation given that 3 properties were varied simultaneously. At the same time, these results are also is also highly suggestive that these effects must be accounted for and studied in greater detail to achieve realistic process understanding. Probably, reduced friction coefficient facilitates increased greater particle contact and the possibility to form liquid bridges. The particle properties must be studied individually for greater insight.

5. Conclusions

An experimentally correlated DEM model was developed which predicted agglomeration performance in a high shear granulator. The effect of process variables like liquid addition rate and impeller speed were examined by tracking dynamic formation and breakage of liquid bridges. The DEM model is set to correct of material properties as the binder is added on to the system, and this was shown to be an important effect. Formation of liquid bridges was found to be hindered for cohesive particles.

6. Acknowledgement

The authors wish to thank Apurva More, Connor Walker, Chris Jensen and Mary Kovacevic, for assisting with experiments. We express our gratitude to PhRMA Foundation for funding this research.

7. References

1. Iveson SM, Litster JD, Hapgood K, Ennis BJ. 2001. Nucleation, growth and breakage phenomena in agitated wet granulation processes: a review. *Powder Technology* **117**(1):3-39.
2. Leuenberger H. 1982. Granulation, new techniques. *Pharmaceutica Acta Helvetiae* **57**(3):72.
3. Litster J. 2003. Scaleup of wet granulation processes: science not art. *Powder Technology* **130**(1):35-40.
4. Adetayo A, Litster J, Pratsinis S, Ennis B. 1995. Population balance modelling of drum granulation of materials with wide size distribution. *Powder Technology* **82**(1):37-49.
5. Chaudhury A, Wu H, Khan M, Ramachandran R. 2014. A mechanistic population balance model for granulation processes: effect of process and formulation parameters. *Chemical Engineering Science* **107**:76-92.
6. Liu L, Litster J. 2002. Population balance modelling of granulation with a physically based coalescence kernel. *Chemical Engineering Science* **57**(12):2183-2191.
7. Cameron I, Wang F, Immanuel C, Stepanek F. 2005. Process systems modelling and applications in granulation: A review. *Chemical Engineering Science* **60**(14):3723-3750.
8. Gantt JA, Gatzke EP. 2005. High-shear granulation modeling using a discrete element simulation approach. *Powder Technology* **156**(2):195-212.
9. Mishra B, Thornton C, Bhimji D. 2002. A preliminary numerical investigation of agglomeration in a rotary drum. *Minerals Engineering* **15**(1):27-33.
10. Talu I, Tardos GI, Khan MI. 2000. Computer simulation of wet granulation. *Powder Technology* **110**(1):59-75.
11. Lian G, Thornton C, Adams MJ. 1998. Discrete particle simulation of agglomerate impact coalescence. *Chemical Engineering Science* **53**(19):3381-3391.
12. Guo Y, Curtis JS. 2015. Discrete element method simulations for complex granular flows. *Annual Review of Fluid Mechanics* **47**:21-46.

13. Lian G, Thornton C, Adams MJ. 1993. A theoretical study of the liquid bridge forces between two rigid spherical bodies. *Journal of Colloid and Interface Science* **161**(1):138-147.

14. Adams M, Perchard V. 1985. Institute of Chemical Engineering Symposium. 147-160.

15. Goldman A, Cox RG, Brenner H. 1967. Slow viscous motion of a sphere parallel to a plane wall—I Motion through a quiescent fluid. *Chemical Engineering Science* **22**(4):637-651.

16. Hapgood K, Litster J, Smith R. 2003. Nucleation regime map for liquid bound granules. *AIChE Journal* **49**(2):350-361.

17. Alexander AW, Chaudhuri B, Faqih A, Muzzio FJ, Davies C, Tomassone MS. 2006. Avalanching flow of cohesive powders. *Powder Technology* **164**(1):13-21.

List of Tables

Parameter	Default value
Impeller speed (rpm)	100, 250 ,500
Liquid Addition Rate (mL/min)	3.5,7,12

Table 1: Process variables in the high shear mixer granulator investigated in the study. 250 rpm and 7 mL/min are the default values.

DEM parameters	
Radius of particle (mm)	3
Number of powder particles	2312
Density of particles(kg/m^3)	1500
Initial Coefficient of Restitution : inter-particle	0.6
Contact Angle (rad)	0.506
Initial Coefficient of restitution: particle-wall	0.6
Half Filling Angle (rad)	0.225
Normal Stiffness : inter-particle (N/m)	6000
Normal Stiffness: particle-wall (N/m)	6000
Coefficient of Friction (particle-particle)	0.7
Time Step (μs)	0.5

Table 2: DEM parameters used for the study of high shear wet granulation.

List of figures

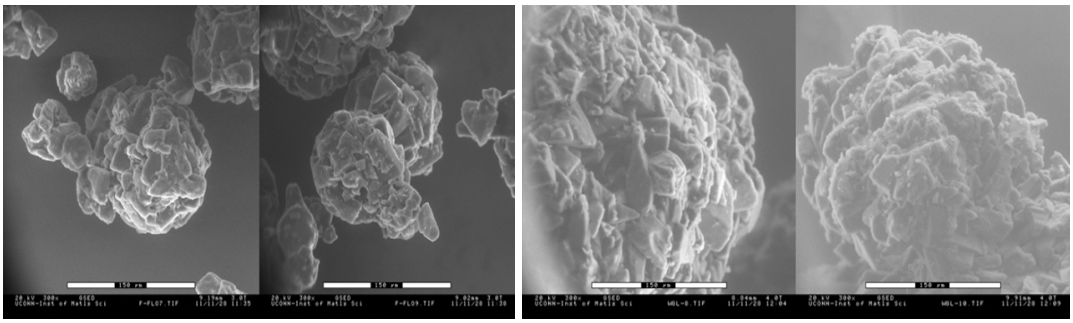

(a) **(b)**

Figure 1. SEM images of (a) ungranulated fast flow lactose , and (b) lactose granules with water as binder

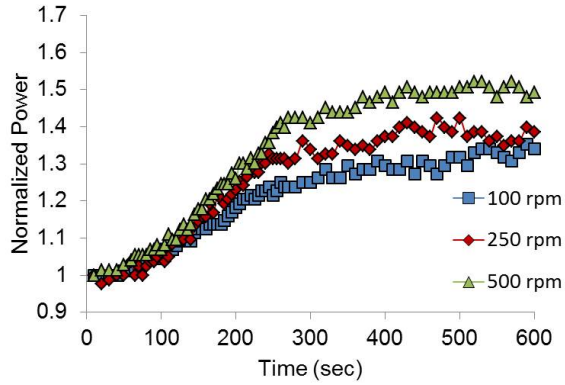

(a)

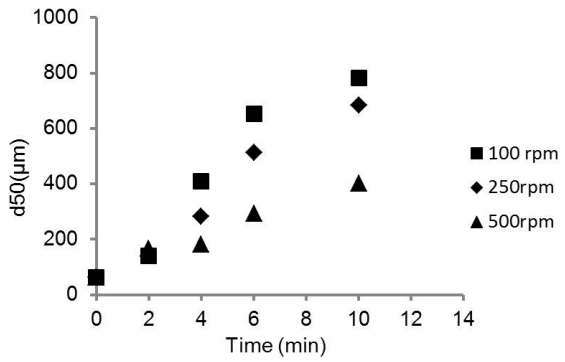

(b)

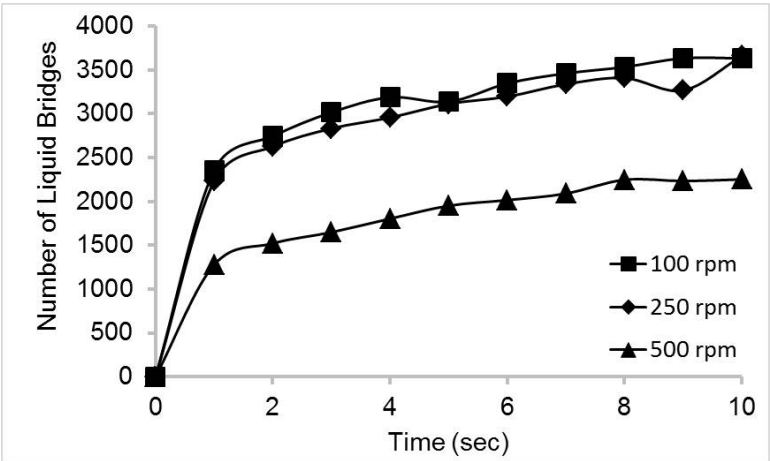

(c)

Figure 2. Effect of impeller speed on agglomeration. (a) Normalized Power Consumption (b) Experimentally observed growth in mean particle size and (c) DEM simulation predictions.

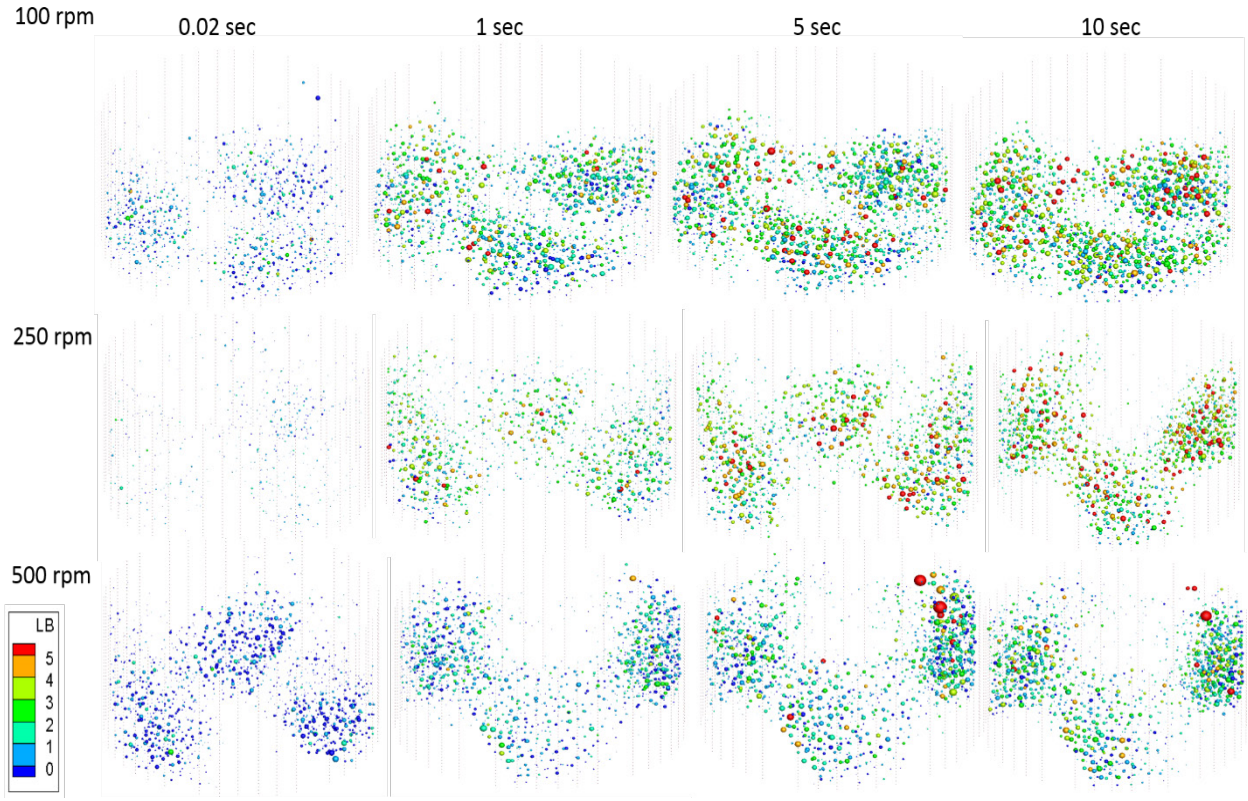

Figure 3. Snapshots from DEM simulations at different time points which show the effect of impeller speed with water being added at 7 mL/min. The particles are sized according to their Coordination number (CRN) and colored by their liquid bridge (LB) count.

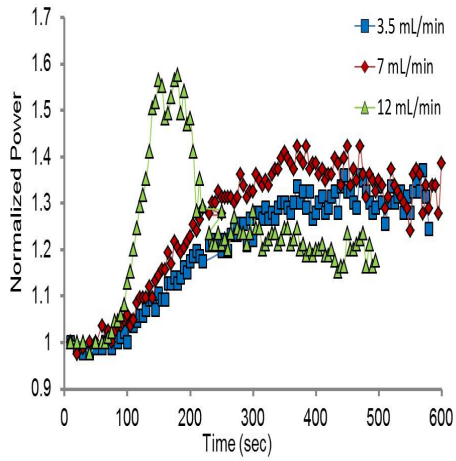

(a)

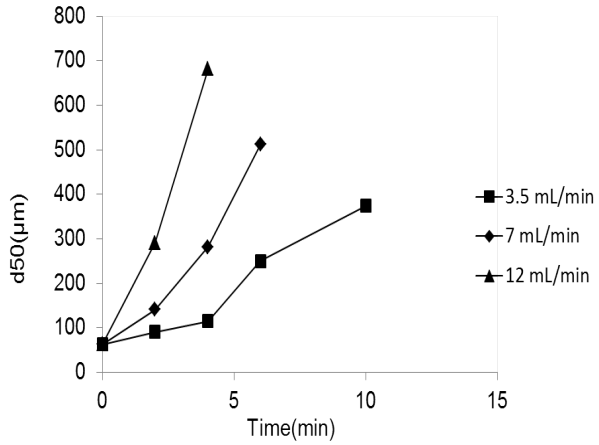

(b)

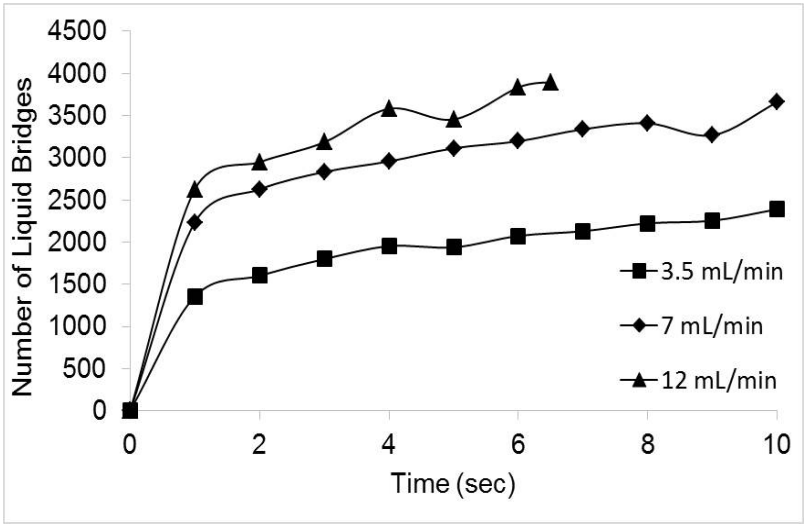

(c)

Figure 4. Effect of Liquid Addition Rate on agglomeration. (a) Normalized Power Consumption (b) Experimentally observed growth in mean particle size and (c) DEM simulation predictions.

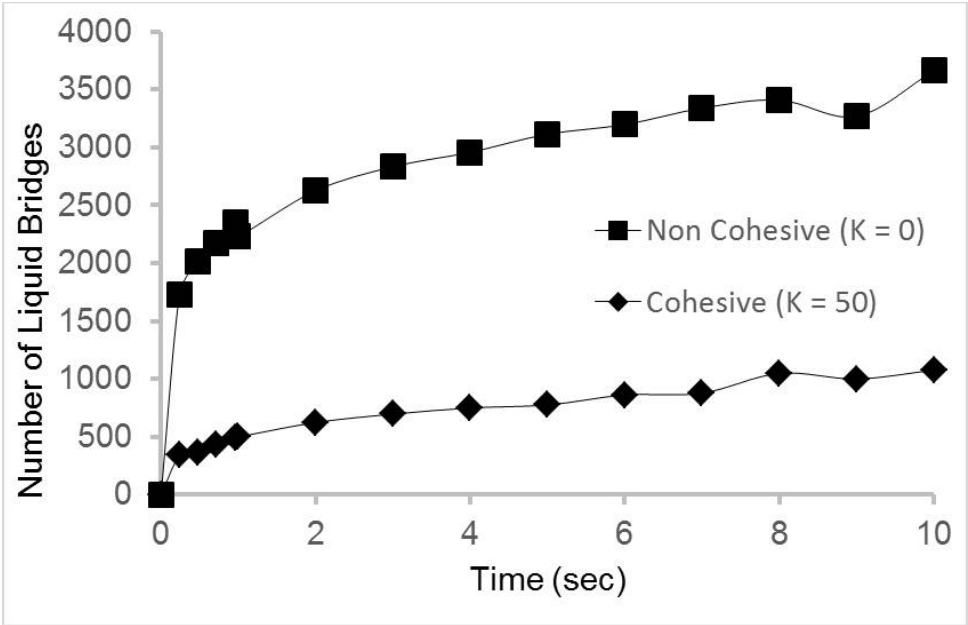

(a)

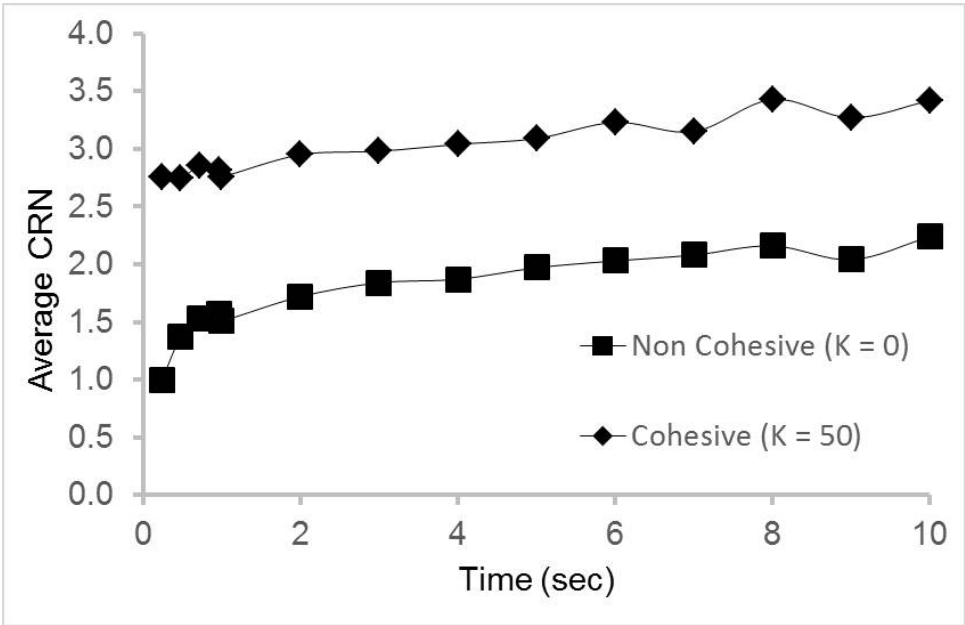

(b)

Figure 5. Effect of particle cohesion in formation of liquid bridges. (a) Higher cohesion restricts capillary bridge formation.(b) Cohesive particles display higher CRN as the agglomeration is dictated by material cohesion

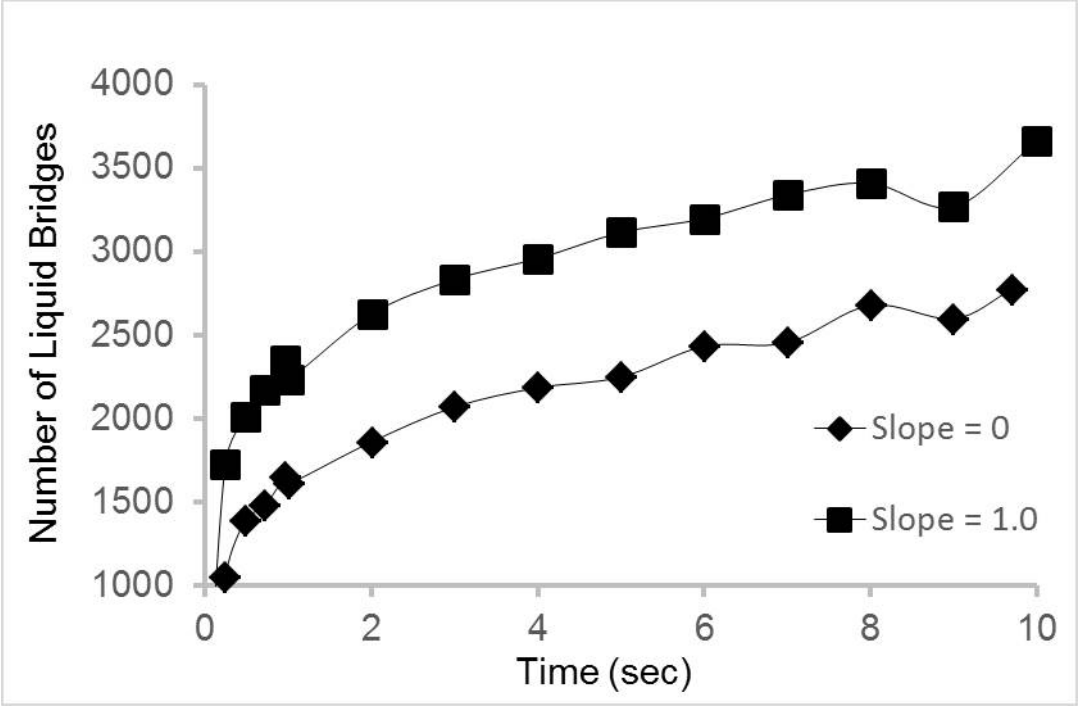

Figure 6. Effect of incorporating change in material properties (coefficients of friction and restitution, elastic modulus) with increasing water content. Slope =1 represents that first order correction factors are applied while Slope = 0 indicates that the initial values for these factors are maintained throughout the simulation.

Chapter 7

Summary and Future Directions

Fundamental understanding of particulate systems is particularly important to design processes and products which are both reliable and cost effective. The current dissertation focusses towards achieving these goals by using experimental and multiscale numerical modeling approaches to improve our insight on some "poorly understood" processes. These processes were chosen from different multiphase multicomponent flow regimes (dilute and dense) to allow for both breadth and depth of scope of the dissertation research. Inter-particulate mesoscale effects were studied in different flow regimes to determine their impact on bulk process performance. These mesoscale effects are driven by fundamental forces, which were identified for each process to govern the dynamic interplay of geometric, process and material variables eventually dictating process and product performance. The objectives of the thesis are achieved through experimentally validated numerical simulations.

Chapter 2 presents a review of the process modeling techniques (DEM, CFD, PBM) used to model dynamic phenomena, and numerical formalisms used to capture forces (fluid, cohesive, electrostatic and capillary) in different areas of academic, industrial and regulatory interest. An introduction to multiphase flows and physical origins of forces in these flow regimes were also described.

Chapter 3 studies the effect of fluid forces which dictate drug deposition behavior in pMDI-spacer systems, whose performance can be quite unpredictable. The performance of these systems, as judged by the drug deposition with the spacer, FPF and MMAD of drug delivered at the end of a model USP throat, was studied as function of spacer geometry and volumetric flow rate of the coaxially flowing air experimentally by the USFDA. Given that the process is in a

dilute flow regime, fluid forces were captured in a commercial CFD code (ANSYS Fluent ™) and systemic numerical studies matching experimental details were carried out. *In silico* results from transient multiphase multicomponent CFD simulations in commercial spacer geometries (Aerochamber Plus ® and Optichamber Advantage®) were found to be in favorable agreement with the experimental determinations. A dimensionless variable, the Recirculation Index (RCI) was developed, which is the ratio of the tendency of a particle to recirculate relative to its tendency to be washed out. A higher RCI was correlated with greater drug deposition within a spacer. Decrease in spacer size and increase in co-flow air were determined to decrease the RCI i.e. decreased spacer deposition. In addition, the deposition of particles (especially bigger particles) was found to be significantly higher near the obstructive bodies, where recirculation and turbulence fields were the strongest. The use of spacers was also revealed to decrease throat wall deposition.

The work presented in **Chapter 4** studies the role of VDW cohesive forces between carrier (LH100) and fine lactose (surrogate API, AZFL**)** in forming ordered mixtures for DPI formulations. These formulations have traditionally low efficacy, quality control attributes determining performance (FPF) are not well established and processing is accompanied by substantial empiricism. The performance of these mixtures, as judged by FPF delivered to the lungs, is critically dependent upon the mixture quality, topographic distribution and press-on forces between the carrier and API. These in turn are dependent upon the bulk and surface properties of both the API and carrier, and the mixing process. Despite significant attention of the pharmaceutical industry in evaluating the role of material properties, the mixing process itself has received little attention. The mixing process was studied in two different blenders: low shear

(DCN) and high shear (HSM) and quality attributes were identified which might be considered critical for performance of adhesive mixtures. The blenders were compared with respect to time needed to form ordered mixtures, press-on forces, wall adhesion of fines, static charging of the blend, abrasion of carrier fines and segregation potential. Increased rotation speed and a central loading configuration were associated with the fastest mixing, but increased speed was also associated with a greater abrasion of fines and wall adhesion of the drug. Ordered mixtures from DCN were formed after a much longer time and were charged more, but had lower abrasion of carrier fines. Press-on forces of the blend from both the blenders were not differentiable. DEM simulations revealed that HSM achieved greater velocities but produced lower chaos, while the inverse was true for DCN. Time taken to adhesive mixtures decreased markedly upon increasing the adhesion between the drug and carrier. In contrast, the effect of material adhesion was not pronounced for HSM. HSM was also predicted to approach the theoretical limit of ideal ordered mixture in contrast to DCN.

Chapter 5 studies the role of electrostatic forces and material properties in determining the static charging or triboelectrification during granular flow. Despite its recognized importance, triboelectrification is not well understood from a theoretical perspective. The interaction of material properties with process variables was explored to holistically explore tribocharging of mixed systems through both experimental and multi-scale numerical modeling approaches. Work function difference, determined by MD calculations, of the contacting material and wall was directly correlated to the static charge generated on the system in experiments done in a hopper-chute assembly for pure systems. The feasibility of reducing net granular charge by using additives with different work functions was explored through

experiments and bulk DEM modeling. It was determined that the charge modulation for mixed systems was related to both material work function and hygroscopicity, with increased water adsorption on a particle increasing the effectivity of charge reduction. DEM simulations also revealed that the local charge distribution patterns in dynamic system, which is not completely represented by the net charge value. Charge per unit area was observed to be a more natural scale for reporting tribocharging of granular systems.

Chapter 6 investigates the dynamics of capillary bridge formation during high shear wet granulation (HSWG) process in a model lactose system. A model was developed which predicted trends in qualitative agreement with experimental observations. The DEM model could account for dynamic process conditions and changing material properties by incorporating toroidal liquid bridge approximation and accounting for the role of water in changing the material properties of the granular solid. Parametric studies were performed experimentally to determine the effect of process and material properties. The process was monitored with respect to size and impeller power consumption. Increasing impeller speed decreased the particle size but produced granules with higher dynamic strength, while increasing the liquid addition rate caused the quickest growth in size owing to ease of spreading water on lactose. *In silico* predictions were well correlated with experimental observations. Additionally, increasing particle cohesion was predicted to decrease liquid bridge. Decreasing the coefficient of restitution, friction and elastic modulus with increasing binder content was predicted to enhance kinetics of liquid bridge formation.

Future Directions

This work provided a fundamental understanding of mesoscale interparticle interactions to determine bulk process behavior. Each case study presented in the thesis can be utilized can a starting template to further explore systems with greater complexity in further detail. Some proposed studies are:

1) With regard to pMDI-spacer interactions, the model can be extended to more combinations by studying more spacer and pMDIs and test the general validity of the developed CFD model and RCI as a predictive parameter correlated with particle deposition behavior.
2) Formation of ordered mixtures should be performed with commonly marketed API, so that the adhesive mixture components are chemically different. This would necessitate simultaneous consideration of electrostatic and cohesive forces which would be a more realistic representation of a commercial formulation.
3) Modifications of material work function with adsorbed moisture should be studied both computationally and experimentally so that tribocharging can be understood for a wider range of environmental conditions to mimic dynamic process and storage conditions. This would also facilitate study of bipolar charging, wherein a different charge polarity is attributed to particles with the same work function but differing sizes. First principle based studies developed in this thesis for a hopper-chute system can also extended to different set-ups and materials.
4) The DEM code incorporating capillary forces should be applied to study the effect of other process ad material variables, and at different length scales. The DEM model developed for HSWG system can be improved by including fluid forces after a certain binder concentration is achieved. Mixed systems, containing bigger and smaller particles should be studied to

determine particle flow behavior especially with respect to their flow, wetting and aggregation tendencies.

5) Modifications to the DEM code can be done to include a combination of two or more fundamental forces are suggested. Computational studies should be directed towards parallelizing the DEM code to simulate bigger and complicated systems.

NOMENCLATURE

Abbreviations

AC	Alternating Current
ACI	Andersen Cascade Impactor
AFM	Atomic Force Microscopy
API	Active Pharmaceutical Ingredient
AUC	Area Under the Curve
AR	Aspect Ratio
AZFL	AstraZeneca Fine Lactose
BET	Brunauer–Emmett–Teller (BET)
CCF	Continuum Capillary Force
CFD	Computational Fluid Dynamics
CI	Carr's Index
CL	Central Loading
CR	Charge Reduction
CRN	Coordination Number
d_{10}	diameter at which 10% of the sample's mass consists of smaller particles
d_{50}	diameter at which 50% of the sample's mass consists of smaller particles
d_{90}	diameter at which 90% of the sample's mass consists of smaller particles
DC	Direct Current
DCN	Double Cone Blender
DEM	Discrete Element Method
DFT	Density Functional Theory
DMT	Derjaguin-Muller-Toporov
DNS	Direct Numerical Simulation
DOF	Degrees of Freedom
DPI	Dry Powder Inhaler
DPM	Discrete Phase Model
ELPI	Electrical Low Pressure Impactor

ESPART	Electrical –Single Particle Aerodynamic Relaxation Time
FEM	Finite Element Method
FPA	Fine particle Aggregate
FPC	Fine Particle Content
FPF	Fine Particle Fraction
GSD	Geometric standard Deviation
HOMO	Highest Occupied Molecular orbital
HPC	Hydroxypropyl Cellulose
HSM	High Shear Mixer
HSWG	High Shear Wet Granulation
HR	Hauser's Ratio
IGC	Inverse Gas Chromatography
JKR	Johnson Kendall Roberts
LB	Liquid Bridge
LH 100	Lactohale 100
LLS	Laser Light Scattering
LPM	Liters per Minute
LSD	Linear Spring & dashpot Model
LUMO	Lowest Unoccupied Molecular Orbital
MMAD	Mass Median Aerodynamic Diameter
NBFE	Normalized Basic Flow Energy
NF	National Formulary
NME	New Molecular Entity
NP	Non Pareils
PA	Provnetil HFA-Aerochamber Plus
PAT	Provnetil HFA-Aerochamber Plus –USP Throat
PBM	Population Balance Method
PCM	Particle Cloud Model
PDA	Phase Doppler Anemometry
PES	Photoemission Spectroscopy

PO	Provnetil HFA- Optichamber Advantage
POT	Provnetil HFA- Optichamber Advantage-USP Throat
pMDI	Pressurized Metered Dose Inhaler
PSD	Particle Size Distribution
PT	Provnetil HFA- USP Throat
PVC	Polyvinyl Chloride
VDW	van der Waals
VHC	Valved Holding Chamber
QbD	Quality by Design
DNS	Direct Numerical Simulation
RANS	Reynolds Averaged Navier Stokes
RCI	Recirculation Index
RH	Relative Humidity
rpm	revolutions per minute
RHF	Restricted Hartree Fock
RSD	Relative Standard Deviation
SEM	Scanning Electron Microscope
SGI	Segregation Index
SIMPLE	Semi Implicit Method for Pressure Linked Equations
TAB	Taylor Analogy Break Up
TFM	Two Fluid Model
TKE	Turbulence Kinetic Energy
TL	Top Loading
USFDA	United States Food & Drug Administration
UPS	Ultra-violet photoelectron Spectroscopy
USP	United States Pharmacopoeia
XPS	X Ray Photoelectron spectroscopy

Symbols

Bo	Bond number

Kn	Knudsen number
Ma	Mach number
Re	Reynolds number
Sc	Schmidt number
St	Stokes number
We	Weber number
Ir	Turbulence Intensity

Subscripts

bb	between big and big particles
bs	between big and small particles
cap	capillary
f	fluid
g	gas
i	i^{th} particle
ij	between i and j particles
LV	Liquid-Vapor
l	liquid
lb	liquid bridge
n	normal component
p	particle
ss	between small and small particle
t	tangential component

Appendix

A1. Computational Fluid Dynamics (CFD): Governing Equations

The governing equations have been taken from ANSYS Fluent Manual. Continuity and Navier Stokes equations are represented are solved in Eq. 1 and 2 respectively RANS k-

$$\frac{\partial \rho}{\partial t} + \frac{\partial \rho u_i}{\partial x_i} = 0 \qquad [1]$$

$$\frac{\partial \rho u_i}{\partial t} + \frac{\partial \rho u_i u_j}{\partial x_j} = -\frac{\partial P}{\partial x_i} + \frac{\partial}{\partial x_j}\left[\mu\left(\frac{\partial u_i}{\partial x_j} + \frac{\partial u_j}{\partial x_i} - \frac{2}{3}\delta_{ij}\frac{\partial u_k}{\partial x_k}\right)\right] + \frac{\partial}{\partial x_j}\left[\mu_T\left(\frac{\partial u_i}{\partial x_j} + \frac{\partial u_j}{\partial x_i}\right) - \frac{2}{3}\left(\rho k + \mu_T\frac{\partial u_k}{\partial x_k}\right)\delta_{ij}\right]$$

[2]

Here u_i is the time averaged velocity in the three coordinate directions (i=1-3), P is the time averaged pressure, ρ is the mixture density, μ is the mixture viscosity, μ_T is the turbulent viscosity and is given as

$\mu_T = \alpha^* k\rho/\omega$ where $\alpha^* = \frac{0.024 + k/6v\omega}{1.0 + k/6v\omega}$

The **RANS** transport equations governing turbulent kinetic energy (k) and specific dissipation rate (ω) are described in Eq. 3 and 4.

$$\frac{\partial \rho k}{\partial t} + \frac{\partial \rho u_j k}{\partial x_j} = \frac{\partial}{\partial x_j}\left[(\mu + 0.5\mu_T)\left(\frac{\partial k}{\partial x_j}\right)\right] + g_k - \varepsilon_k \qquad [3]$$

$$\frac{\partial \rho\omega}{\partial t} + \frac{\partial \rho u_j \omega}{\partial x_j} = \frac{\partial}{\partial x_j}\left[(\mu + 0.5\mu_T)\left(\frac{\partial \omega}{\partial x_j}\right)\right] + g_\omega - \varepsilon_\omega \qquad [4]$$

In the equations above, g_k and g_ω represent generation of k and ω, ε_k and ε_ω represent dissipation of k and ω. The transport of propellant vapor is governed by a convective diffusive mass transfer relation shown in Eq. 5

Species Transport (Diffusive)

$$\frac{\partial \rho Y_v}{\partial t} + \frac{\partial \rho u_j Y_v}{\partial x_j} = \frac{\partial}{\partial x_j}\left[\left(\rho D_v + \frac{\mu_T}{Sc_T}\right)\left(\frac{\partial Y_v}{\partial x_j}\right)\right] + S_v \qquad [5]$$

Where, Y_v is the mass fraction of vapor, S_v is the vapor source generation term, D_v is the Diffusion coefficient in air, Sc_T is the Schmidt Number. For compressible temperature dependent flow, the combined thermal and mechanical energy equation (Eq. 6) must be solved.

$$\frac{\partial \rho e}{\partial t} + \frac{\partial}{\partial x_j}\left(u_j(\rho e + p)\right) = \frac{\partial}{\partial x_j}\left[(\kappa + \kappa_T)\left(\frac{\partial T}{\partial x_j}\right)\right] + \sum_s \hbar_s \left(\rho D_v + \frac{\mu_T}{Sc_T}\right)\frac{\partial Y_s}{\partial x_j} \qquad [6]$$

The diffusion coefficient of propellant vapor (HFA-134a) in air would be a function of temperature as given by $D_v = 5.725646*10^{-6} + 5.265307*10^{-8} * T\ m^2/s$. At 25°C, it works out to be 9.945×10^{-6} m^2/s [12].

In addition, the energy equation (Eq. 7) is also solved.

$$e = \hbar - \frac{P}{\rho} + \frac{V^2}{2}\ where\ \hbar = \sum \hbar_s Y_s \qquad [7]$$

Where, the total enthalapy (h) is mass fraction weighed sum of the constituent enthalpies for each of the species (h_s). The density of this mixture is calculated from multicomponent ideal gas assumptions (Eq. 8).

$$\rho = \frac{P}{R_u T\left(\sum_i \frac{Y_i}{MW_i}\right)} \quad [8]$$

Where MW_i is the molecular weight of each species & R_u is the universal gas constant.

Physical Models

1) Droplet Break Up

This is calculated from the Weber number (We).

$$We = \frac{p_g v^2}{\sigma} \quad [9]$$

Where, V is the between the droplet with a surface tension σ and radius air and a gas of local density p_g. We relates the gas induced drag force to the liquid surface tension which tends to maintain a spherical shape. Above a certain We, significant droplet distortion occurs which is modeled as a forced damped harmonic oscillator with droplet viscosity as the damping force and surface tension as the restoring force. The size of child droplet is based on conservation of surface energy and energy bound in the distortion and oscillation of the parent droplet and surface energy and kinetic energy of the child droplets. This is the basic principle of the Taylor Analogy Break Up (TAB) model.

2) Pressure dependent boiling

When the droplet temperature T_p equals the boiling temperature T_{bp}, the boiling rate law is applied to change the droplet diameter d_p.

$$\frac{d(d_p)}{dt} = \frac{4k_\infty}{\rho_p c_{p,\infty} d_p}\left(1 + 0.23\sqrt{Re_d}\right) ln\left[1 + \frac{c_{p,\infty}(T_\infty - T_p)}{h_{fg}}\right] \quad [10]$$

Where $C_{p,\infty}$ and k_∞ are heat capacity and thermal conductivity of the gas, while h_{fg} is the temperature dependent latent.

3) Inert Heating

$$m_p c_p \frac{dT_p}{dt} = hA_p(T_g - T_p) \quad [11]$$

Where m_p, c_p, A_p, T_p refer to mass, heat capacity, cross sectional area and temperature of the particle, while $T_g$is the local gas temperature.

4) Brownian Motion

Brownian motion is modeled as Gaussean noise where ζ is a Gaussean random number. The Brownian force(F_b)is calculated from Eqn 12 a

$$F_b = \zeta\sqrt{\frac{\pi S_o}{\Delta t}} \quad [12a]$$

Where, k_B is the Boltzmann's constant, ν is the kinematic viscosity at temperature T , and S_o given by Eq. 12b

$$S_o = \frac{216 \nu k_B T}{\pi^2 d_p^5 \rho (\frac{\rho_p}{\rho})^5 C_c} \quad [12b]$$

A2. Discrete Element Method (DEM)

In DEM, the granular material is considered as a collection of frictional inelastic spherical particles, which resembles powder. Each particle may interact with its neighbors or with the boundary only at contact points through normal and tangential forces. Major assumptions for the current DEM simulation include:

1) Particles are spherical in shape.
2) Particles are considered to be uniform in size.
3) Fluid flow effects are ignored.
4) Unless otherwise specified, particle material properties would be kept constant throughout the simulation run.

The forces and torques acting on each of the particles are calculated as following:

$$\Sigma F_i = m_i g + F_n + F_n \quad [13]$$

$$\Sigma T_i = r_i \times F_t \quad [14]$$

The force on each particle is given by the sum of gravitational, contact forces (normal and tangential F_n and F_t respectively) as indicated in Eq. (26).For the dissertation projects, all the relevant forces are added up ,which are given by the sum of capillary, electrostatic and cohesive forces. The corresponding torque on each particle is the sum of the moment of the tangential forces (F_T) (Eq. (13)). The normal forces (F_n) and tangential forces (F_t), also called collisional forces, are calculated using Walton's contact mechanics model[70]. The normal force as mentioned above is calculated as a function of the overlap value. The stiffness coefficients (K_1 and K_2) are chosen to be large enough to ensure that the overlap (α_0 and α_1) values remains small compared to the particles sizes. The normal forces acting between pairs of particles in contact are defined using loading and unloading spring constants K_1 and K_2 respectively:

$$F = K_1 \alpha_1 \quad \text{(loading)} \quad [15]$$

$K_2 (\alpha_1 - \alpha_o)$ (unloading)

To incorporate the inelasticity of collisions, the coefficient of restitution is calculated as:

$e = (K_1/K_2)^{1/2}$ where $(0<e<1)$ [16]

$e = 1$ implies perfectly elastic collision with no energy dissipation.

$e = 0$ implies completely inelastic collision.

Tangential forces (F_T) are calculated employing Walton's incrementally slipping model. After the contact occurs, tangential forces build up nonlinearly, causing displacement in the tangential plane of contact. These forces obey the Coulomb's law i.e. if the magnitude of tangential forces is greater than the product of the normal force and the coefficient of static friction, (i.e. $T \geq \mu F_N$) sliding takes place with a constant coefficient of dynamic friction. The model also takes into account the elastic deformation that can occur in the tangential direction. The tangential force is evaluated considering an effective tangential stiffness k_T associated with a linear spring. It is incremented at each time step as $T_{t+1} = T_t + k_T \Delta s$, where Δs is the relative tangential displacement between two time steps. Figure 4 depicts the DEM algorithm used to calculate the forces.

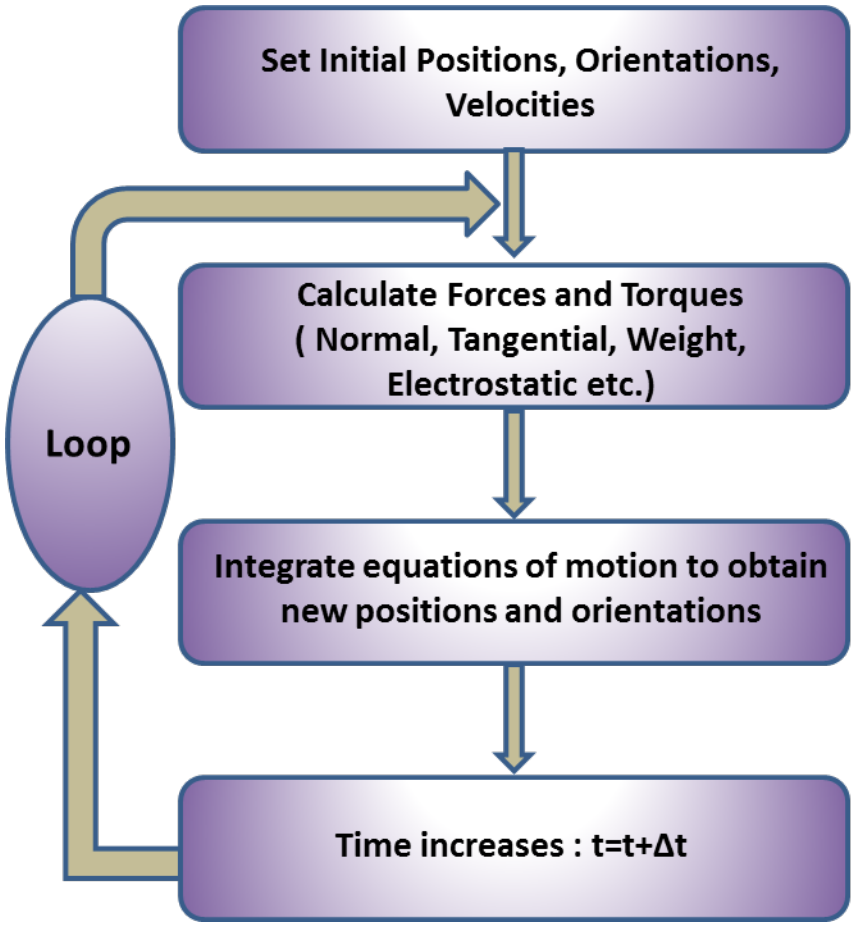

Figure A1. Flow chart of the general soft particle DEM algorithm

The spring constants are function of Yield strength of the material as estimated using, $K_1 = 2\pi YR$ and $K_t = 0.8K_1$, where R and Y are the radius and the Yield Strength of the appropriate material.